PROBING THE NUCLEAR SYMMETRY ENERGY WITH HEAVY ION COLLISIONS

By

Daniel David Schechtman Coupland

A DISSERTATION

Submitted to
Michigan State University
in partial fulfillment of the requirements
for the degree of

Physics - Doctor of Philosophy

2013

ABSTRACT

PROBING THE NUCLEAR SYMMETRY ENERGY WITH HEAVY ION COLLISIONS

By

Daniel David Schechtman Coupland

There are two distinct components involved in using heavy ion collisions to constrain the density dependence of the symmetry energy. On one hand, observables sensitive to the symmetry energy must be identified and measured with enough precision to provide meaningful constraints. On the other hand, nuclear reaction simulations are used to predict those observables for different possible forms of the symmetry energy. Examination of both components and the interface between them is important to improve the constraints. This thesis contributes to both the experimental and theoretical parts of this endeavor.

First, we examine the uncertainties in the simulation of the isospin diffusion observable by varying the input physics within the pBUU transport code. In addition to the symmetry energy, several other uncertain parts of the calculation affect isospin diffusion, most notably the in-medium nucleon-nucleon cross sections and light cluster production. There is also a difference in the calculated isospin transport ratios depending on whether they are computed using the isospin asymmetry of the heavy residue or of all forward-moving fragments. We suggest that measurements comparing these two quantities would help place constraints on the input physics, including the density dependence of the symmetry energy.

Second, we present a measurement of the neutron and proton kinetic energy spectra emitted from central collisions of ^{124}Sn + ^{124}Sn and ^{112}Sn + ^{112}Sn at beam energies of 50 MeV per nucleon and 120 MeV per nucleon. Previous transport simulations indicate that

ratios of these spectra are sensitive to the density dependence of the symmetry energy and to the isovector momentum dependence of the mean field. Protons were detected in the Large Area Silicon Strip Array (LASSA) and neutrons were detected in the MSU Neutron Walls. The multiplicity of charged particles detected in the MSU Miniball was used to determine the impact parameter of the collisions. Several thin scintillators were used to provide the start time for the neutron measurement, determine the charged particle background in the neutron detector, and measure the beam rate.

We construct ratios of the neutron and proton spectra between the two reaction systems and compare them to recent ImQMD-Sky transport model simulations and to previous data, where available. The new data with beam energy of 50 MeV per nucleon represents a substantial increase in precision and an extension to higher kinetic energies compared to the previous data. No previous data exists near a beam energy of 120 MeV per nucleon. The simulations indicate a strong dependence of the spectral ratios on the effective mass splitting and to a lesser extent on the density dependence of the symmetry energy. However, significant differences exist between the simulations and the measurement. We present arguments and coalescence invariant spectra to indicate that a major source of the discrepancy is clustering effects. The theoretical treatment of these effects must be considered in more detail before constraints on the equation of state can be extracted from this or other measurements of proton and neutron emission from heavy ion collisions.

To Lauren and Owen

ACKNOWLEDGMENTS

The work presented here would not have been possible without the help, advice, and support of many people. First, I would like to thank my advisor, Bill Lynch, for his consistent support, advice, and enthusiasm. Whatever I know about being an experimental nuclear physicist, I learned from him. The many people who have been part of the HiRA group during my tenure here have all helped to make this work possible in one way or another. Betty Tsang has been like a second advisor to me, contributing substantially to my ideas of data analysis and presentation among many other things. From close work with post-docs Vlad, Daniela, and Zibi, as well as collaborator Mike Famiano, I learned many of the specifics of nuclear lab techniques, electronics, and data analysis. It was through my interactions with my fellow graduate students Andy, Micha, Mike, Rachel, and Jack that I explored and solidified most of my own ideas about programming, simulations, data analysis, and experimental setup, not to mention graduate school itself.

Special recognition is due to those members of the group and outside collaborators who gave countless hours to the setup and operation of my thesis experiment. It was a huge undertaking, and I could not have managed it without your help. Many NSCL personnel also helped make the experiment possible, from the cyclotron operators and beam physicists to the mechanical design engineers, from the software support to the vacuum system support, and many more in between.

The theoretical work presented here benefited from numerous discussions with Pawel Danielewicz and Yingxun Zhang. My use of the three neutron detector efficiency calculations were made possible by help from Aaron Galonsky, Zach Kohley, Daiki Satoh. Daiki went above and beyond by actually running the calculation when it was unclear how long it would take to make the code available to me.

Mike Youngs deserves a special note. He has been my officemate, group member, co-leader of the experiment and experimental analysis, and partner in mischief. My time in graduate school would have been immeasurably different without him. Where's the water, Mike?

I am blessed to come home to my wife Lauren and son Owen at the end of the day. Your love, support, and understanding even as I have worked longer and longer hours to finish this thesis have been incredible. I love you both.

TABLE OF CONTENTS

LIST OF TABLES

LIST OF FIGURES

Chapter 1

Introduction

One of the main goals of nuclear physics is to determine the characteristics of nuclear matter under various conditions. Stable nuclei exist at zero temperature and an equilibrium or saturation density of 0.16 nucleons per cubic fermi, or about $2.7 \times 10^{14} g/cm^3$, with contributions from lower densities at their surface. At much higher temperatures, nucleons undergo a phase transition, melting into a quark-gluon plasma, which was present in macroscopic quantities during the first 10 μs after the Big Bang, and has been the focus of much recent work at the Relativistic Heavy Ion Collider (RHIC). At another extreme where the macroscopic limit is relevant, neutron stars exist at low temperature and densities possibly extending to nine times nuclear saturation density. Other phase transitions to more exotic forms of dense matter may occur at the center of these astrophysical objects. To connect laboratory nuclear experiments to such astrophysical scenarios, one must connect nuclear experiments to the macroscopic limit where pressure, density, temperature, and other thermodynamic quantities are the relevant properties. In general, the relationship between pressure, energy, temperature, density, and neutron-proton (isospin) asymmetry is called the Equation of State (EoS). In the regime dominated by nucleon degrees of freedom, the pressure P is determined by the partial derivative of the Helmholtz free energy per nucleon f with respect to the nucleon density:

$$P(\rho, T, \delta) = -\frac{\partial F}{\partial V} = \rho^2 \frac{\partial f(\rho, T, \delta)}{\partial \rho} \tag{1.1}$$

where P is the pressure, ρ is the density, T is the temperature, and

$$\delta = (\rho_n - \rho_p)/(\rho_n + \rho_p) \tag{1.2}$$

is the isospin asymmetry that describes the difference between neutron and proton densities ρ_n and ρ_p. In addition, $f(\rho, T, \delta) = \epsilon(\rho, T, \delta) - T\sigma(\rho, T, \delta)$, where ϵ is the energy per nucleon and σ is the entropy per nucleon. Finite temperature effects are less problematic than potential energy effects, and can be approximately constrained by the heat capacities of nuclei. We then consider the zero temperature limit, where

$$P(\rho, \delta) = \rho^2 \frac{\partial \epsilon(\rho, \delta)}{\partial \rho} \tag{1.3}$$

In this case, we can choose to describe the EoS simply by $\epsilon(\rho, \delta)$, which is more intuitively related to the underlying potentials.

The Weizäcker binding energy formula from the liquid drop model can provide some insight into the phenomenological form of the EoS:

$$E_B = a_V A - a_S A^{2/3} - a_A \frac{(N-Z)^2}{A} - a_C \frac{Z^2}{A^{1/3}} + \delta(A, Z) \tag{1.4}$$

The volume and surface terms depend only on the number of nucleons, not their type. Isospin asymmetry enters as a quadratic correction, which is consistent with an energy minimum for symmetric matter. Pairing effects round out the strong force contributions to the binding energy, and the Coulomb interaction completes the formula. Based on the terms in this formula, we can cast the full nuclear EoS into the form:

$$\epsilon(\rho, \delta) = \epsilon(\rho, 0) + S(\rho)\delta^2 + O(\delta^4) \tag{1.5}$$

The density dependence of the symmetric matter term in Equation 1.5 has been constrained near saturation density via investigations of the Isoscalar Giant Monopole Resonance (GMR) [4]. Heavy Ion Collisions (HICs) provide a unique opportunity to study the density dependence of the nuclear EoS, since they are the only opportunity we have in the laboratory to create nuclear matter significantly above and below saturation density. At high densities, the symmetric matter EoS has been constrained by examining kaon production and particle flow from HICs [5,6]. On the other hand, the density dependence of the second term in Equation 1.5 is still uncertain. This correction for the isospin asymmetry is known as the symmetry energy. Fourth-order terms in the isospin asymmetry may contribute, but the effect is generally expected to be quite small.

1.1 Motivation

The density dependence of the symmetry energy plays a role in many different nuclear physics systems at vastly differing size scales. In nuclear structure, it is intimately related to the neutron skin of neutron-rich nuclei [7–10], as well as nuclear masses and isobaric analog states. It also influences the centroid of the Giant Dipole Resonance [11] as well as the relative strength of the Pygmy Dipole Resonance [12, 13]. In astrophysics, nearly every observable property of neutron stars is affected by the density dependence of the symmetry energy [9,14,15], and through this, nucleosynthesis and explosion mechanisms of core-collapse supernovae [16]. It also influences the evolution of nuclear reactions, including the neutron-to-proton spectral ratio from central heavy ion collisions [17], isospin diffusion/charge equilibration [18, 19], isospin fractionation [20], isoscaling [21–23], and the ratio of charged pion yields [24]. Despite this, the density dependence, and even the value at saturation density of the symmetry energy is not well determined. Different microscopic calculations can predict very different forms of the symmetry energy, and even the sign of the slope varies among Skyrme parameterizations [25]. Significant experimental constraints at and below saturation density have emerged only within the past few years [26, 27], and there is still much debate about any constraints extracted above saturation density [28–34].

Efforts to constrain the symmetry energy are ongoing within the structure, astrophysics, and reactions communities. These efforts are hindered by both the difficulty of the measurements and the model dependence of their interpretation. For example, the PREX experiment aimed to measure the neutron skin thickness of ^{208}Pb using parity-violating electron scattering, which is a better understood process than hadronic probes. A precise measurement of the neutron skin thickness would provide a strong constraint on the symmetry energy below saturation density, but the current uncertainty in the data is insufficient for this purpose [35]. On the astrophysics side, the mass-radius relationship in neutron stars is strongly influenced by the symmetry energy, but few neutron stars lend themselves to both mass and radius measurements. Steiner *et al.* extracted symmetry energy constraints from a Bayesian analysis of several neutron stars with both mass and radius measurements [36], but the measurements themselves are strongly model dependent, as is the analysis, and even given that it is unclear what range of densities the constraints most strongly reflect.

Many HIC observables sensitive to the symmetry energy have been identified and are reviewed in Ref. [37]. Like other fields, the experiments are difficult and definitive data is rare. Extracting the symmetry energy from these experiments is dependent on theoretical transport model calculations. Particular observables must be chosen to select for the effects of the symmetry energy. The effects of the symmetry energy on these observables, however, must be separated from the other components of the mean field, in medium nucleon-nucleon cross sections, and cluster formation.

1.2 Transport Models

To extract quantitative information about the symmetry energy from nuclear reactions, experimental data needs to be compared with the predictions of dynamical transport models. Transport models track the time evolution of a nuclear reaction, and may separately treat the nuclear EoS, both symmetric and asymmetric parts, nucleon-nucleon (NN) collision cross sections, and inelastic nucleon collisions that lead to cluster or pion production [38]. These simulations are quite complex, and a full quantum mechanical treatment is not currently possible. The effective nuclear interactions determined by different microscopic theories are also quite complex and differ between theories. Therefore, simplified phenomenological interactions are employed in transport simulations. Experimental observables are calculated from the final states of the simulations and compared to data.

The role of the symmetry energy in these observables is bound up with the other physics inputs. Thus even a perfect measurement of one of these observables does not uniquely determine the symmetry energy. Instead, the sensitivity of the simulation to other uncertain physics must be ascertained, and measurements made to constrain those other uncertainties. This iterative process is not a new phenomenon in EoS studies. For instance, the momentum dependence of the symmetric part of the EoS needed to be determined from elliptic flow studies before the EoS could be constrained at high densities [6,39].

Similarly, to constrain the symmetry energy, the other uncertain quantities in the transport models must either be constrained or shown not to affect a given observable. One such parameter is the isovector momentum dependence of the mean field. A momentum dependent potential modifies the usual non-relativistic relationship between mass, velocity, and momentum, as is evident from one of Hamilton's Equations:

$$\begin{aligned} \dot{x} &= \frac{\partial H}{\partial p} \qquad (1.6) \\ &= \frac{p}{m} + \frac{\partial U}{\partial p} \qquad (1.7) \end{aligned}$$

In this case, it is convenient to define an effective mass m^* such that

$$\dot{x} = \frac{p}{m^*} \qquad (1.8)$$

$$\frac{m^*}{m} = \left(1 + \frac{m}{p}\frac{\partial U}{\partial p}\right)^{-1} \tag{1.9}$$

Applying the chain rule and rearranging yields the equivalent expression

$$\frac{m^*}{m} = 1 - \frac{\partial U}{\partial E}. \tag{1.10}$$

The concept of a nucleon effective mass was introduced by Brueckner [40] to simplify the description of nucleons moving in a momentum-dependent mean field in a nucleus. This description can be expressed instead as nucleons with an effective mass different from their free mass moving in a static potential. The self-consistent potentials derived from this treatment were shown to more attractive at low momentum than at high momentum, leading to $m^*/m < 1$. Early calculations indicated that $m^*/m \approx 0.7$, but data derived from the densities of nuclear energy levels seemed to indicate a value closer to unity [41]. Further studies employing nucleus-nucleon collisions and electron scattering eventually resolved this discrepancy: deeply bound states and scattering states indicate $m^*/m \approx 0.7$, while weakly bound states have a larger effective mass due to coupling with collective surface vibration modes [42]. This suggests that a value of $m^*/m \approx 0.7$ is appropriate for transport calculations. Analysis of elliptic flow data by Danielewicz [39] within a transport calculation eventually supported this value. It should be stressed, however, that a potential that depends nonlinearly on energy, such as those used in transport codes, will not have a constant effective mass. The reported value is the effective mass at the Fermi surface, although the elliptic flow analysis actually constrains the momentum dependence at higher densities.

Differences between the momentum dependence of the potentials felt by protons and neutrons in asymmetric nuclear matter would lead to an effective mass splitting between the two nucleon species. The mass splitting is an interesting parameter in its own right, since it affects some properties of neutron stars and the magnitude of shell effects in nuclei far from stability [43–45]. It also influences the outcome of heavy ion collisions, and can affect observables that are used to constrain the density dependence of the symmetry energy [46, 47]. However, the sign and magnitude of the mass splitting are not well constrained. Some microscopic many-body theories, such as the Landau-Fermi liquid theory [48] and the non-relativistic Brueckner-Hartree-Fock approach [49,50] predict that $m_n^* > m_p^*$ in neutron rich matter while relativistic mean field (RMF) and relativistic Dirac-Brueckner calculations [51–53] predict the opposite. Different Skyrme parameter sets indicate different mass splittings. At maximum, these approaches predict a splitting of order 15% at $\rho = \rho_0$ and $\delta = 0.2$. This uncertainty is large enough to affect some observables that are used to constrain the symmetry energy, so further experimental constraints on the mass splitting are important.

In addition to uncertainties in the physics inputs, transport simulations can be uncertain due to the underlying models. Most of the current nuclear reaction transport models either rely on the Uehling-Uhlenbeck version of the Boltzmann equation (BUU), or on quantum molecular dynamics (QMD) [26,37,38,54]. Both models are semiclassical, evolving particle positions and momenta using Hamilton's equations in a mean field. The residual interactions are handled as nucleon-nucleon collisions, which may have reduced cross sections in the medium compared to their free space values. The implementation is largely classical, with the addition of Pauli blocking.

The BUU approach uses many pointlike test particles per nucleon to approximate the continuous phase-space density matrix, while the QMD approach follows individual nucleons expressed as wave packets with a finite, usually fixed, width. These different treatments affect the calculated dynamics. Nucleon-nucleon collisions rearrange whole nucleons in the QMD approach while only rearranging individual test particles in the BUU approach, leading to larger fluctuations and more restrictive Pauli blocking in QMD. Additionally, fragments form in the QMD treatment due to N-body correlations caused by the overlapping wave packets, but in BUU instead form mostly from mean-field instabilities, and are thus suppressed for many test particles per nucleon [54]. Codes based on both models will be used in this thesis.

1.3 Observables

The dynamic nature of transport models gives access to not just the final state of the collision, but also information about the time evolution of the system. The qualitative description of HICs that emerges from this information can inform the selection and interpretation of EoS observables. The following description focuses on HIC at beam energies between tens and hundreds of MeV.

In reactions where the nuclei do not collide perfectly head on, some nucleons will be directly involved in the collision while others will be sheared off and continue in approximately their original direction of motion. These are referred to as participant and spectator nucleons, respectively. The impact parameter, denoted b, describes the minimum distance between the incoming trajectory of the center of the projectile and the center of the target. The actual distance of closest approach may be modified by coulomb and nuclear forces. In reactions with a small impact parameter, most of the nucleons participate, while in reactions with a large impact parameter, most of the nucleons are spectators. There are respectively referred to as central and peripheral reactions. In both cases, the participant region is compressed to densities above saturation density, then rebounds and expands to densities below saturation density, emitting nucleons and light clusters in the process. The spectator regions continue largely intact at velocities comparable to the original projectile and target velocities, and are often referred to as projectile and target residues. However, the residues are excited, and tend to evaporate nucleons as they deexcite. At longer time scales, all the reaction products are subject to fragmentation and decay as they cool, a process referred to as secondary decay.

In central collisions, the system disintegrates almost entirely into light $Z \leq 2$ and intermediate mass $3 \leq Z < 30$ fragments via a process known as multifragmentation, which is thought to be related to the nuclear liquid-gas phase transition. In more peripheral collisions, the interplay between spectator and participant regions has been used to probe the EoS. A more repulsive mean field leads to the earlier expansion of the compressed region. This is not directly observable due to the small length and time scales involved in the reaction. However, if the beam energy is chosen such that expansion occurs while the spectator regions are still around the participant region, the expansion must take place primarily perpendicular to the plane of the reaction. For less repulsive mean fields, the expansion is slower and the spectators have passed by, leading to transverse emission primarily within the plane of the reaction. The comparison of in-plane to out-of-plane emission, called elliptic flow, has provided constraints on the EoS of symmetric nuclear matter to densities larger than $4\rho_0$ [6]. In this thesis we explore two observables sensitive to the symmetry. The first, isospin diffusion, primarily concerns the transfer of nucleons between the two spectator nuclei and the participant region. The second concerns the emission of protons and neutrons from the participant region.

1.3.1 Isospin Diffusion

Isospin diffusion occurs in nuclear collisions where the projectile and target nuclei differ in their relative isospin asymmetry. Over the course of the reaction, the symmetry energy pushes the system toward isospin equilibrium. Since the reaction takes place over a limited time span, determined by the beam energy, full isospin equilibrium is not reached for sufficiently energetic beams. The degree of isospin equilibration is an observable that is sensitive to the strength of the symmetry energy. Usually isospin diffusion is discussed for semi-peripheral collisions, where large portions of the initial nuclei are spectators. As these projectile-like and target-like residues separate in the expansion phase of the reaction, a low density neck connects them, and it is through this neck that isospin diffusion occurs. Isospin diffusion has been measured for collisions of ^{124,112}Sn + ^{124,112}Sn at beam energies of 50 MeV/nucleon, and that measurement provides one of the strongest HIC-based constraints on the symmetry energy. However, the transport model calculations used in those constraints did not calculate exactly the same observable as was used in the experiment, and the sensitivity of the calculations to other physics inputs was not explored, raising questions about the validity of the constraints. These issues are addressed in Chapter 2.

1.3.2 Transverse Emission of Protons and Neutrons

In a neutron-rich system, the symmetry potential has opposite signs for protons and neutrons, attracting protons and repelling neutrons. In a HIC, this has an effect on the energy of emitted nucleons. After the participant region has compressed and expanded, nucleons are emitted from the low density region at the edge of the nuclear fireball. If the symmetry energy is large at these densities, the likelihood of neutron emission is increased while the likelihood of proton emission is decreased. Similarly, neutrons will be preferentially emitted at higher energy. Therefore, the ratio of the neutron to proton energy spectra is an observable of the symmetry energy. Experimentally, however, the neutron/proton (n/p) spectral ratio is difficult to determine. Intermediate energy neutrons have a low probability of interacting with a detector, and the detection efficiency is often uncertain. Protons and neutrons are also detected with different detectors, which can introduce another source of uncertainty in the n/p ratio having to do with the overlap of the acceptance of these detectors. To account for this, the n/p ratio from a neutron-rich system is compared to the n/p ratio from a symmetric system by constructing the double ratio

$$DR(n/p) = \frac{(n/p)_{asymm}}{(n/p)_{symm}} \tag{1.11}$$

.

The detection efficiencies are thus removed from the observable.

Two selections are employed to ensure that the detected particles are emitted from the expanding edge of the participant region. First, only central events are considered, so that most of the nucleons in the collision are participants. Theoretical studies have shown that the ratio is not particularly sensitive to the precise details of the centrality cut [55]. Second, the spectra are constructed from nucleons emitted in the transverse direction, generally between 70° and 110° polar angle in the center of mass frame, to avoid contributions from the evaporation of projectile or target residues.

The effect of the density dependence of the symmetry energy on the double ratio is largest for beam energies around 50 MeV per nucleon. However, a study by Rizzo *et al.* showed that at beam energies around 100 MeV per nucleon, the n/p ratio is also sensitive to the in-medium effective mass splitting [47]. If $m_n^* < m_p^*$, then high momentum neutrons experience a more repulsive potential and a higher acceleration than do protons with the same momentum, leading to a larger n/p ratio at high energies. If $m_n^* > m_p^*$, the reverse is true. Thus a measurement of the n/p ratio in this energy range could constrain the mass splitting and reduce the model uncertainties in the determination of the symmetry energy.

Despite the utility of the n/p ratio in EoS studies, few measurements have been made due to the difficulties involved in such complicated experiments. Previous work by Famiano *et al.* measured the double ratio from collisions of $\mathrm{Sn}^{124} + \mathrm{Sn}^{124}$ compared to collisions of $\mathrm{Sn}^{112} + \mathrm{Sn}^{112}$ at $E_{beam} = 50$ AMeV, but the uncertainties in the high energy data points preclude any strong constraints on the density dependence of the symmetry energy [17]. At much higher energy, Russotto *et al.* analyzed proton and neutron flow from Au + Au collisions at 400 AMeV [32,34]. The elliptic flow observable is somewhat different than the simple n/p ratio in that it describes the amount of the transverse nucleon emission in the reaction plane compared to out of plane, but the ratio of the neutron to Hydrogen flow is still sensitive to the symmetry energy. Again, the uncertainties in the data are of similar size as the expected sensitivity to the symmetry energy. No measurements exist near 100 AMeV to constrain the effective mass splitting.

1.4 Organization of Thesis

The remainder of this thesis is organized as follows. Chapter 2 details a study of the dependence of the isospin diffusion observable on the physics inputs in a particular transport model code. The effects of the symmetry energy, symmetric matter EoS, in-medium cross sections, and cluster production are explored in detail. Additional observables are suggested to remove ambiguities in the comparison between theory and experiment. The following chapters concern an experiment that measured the transverse emission of protons and neutrons from central HIC with the intent to constrain both the density dependence of the symmetry energy and the in-medium effective mass splitting. Chapter 3 provides the details of the experimental setup, including the beams and targets, detectors, and the associated electronics. Chapter 4 then describes the analysis of that experiment. The detector calibrations, event reconstruction, and efficiency analysis are detailed separately for the major detection systems. Following this, Chapter 5 presents the results of the analysis and comparison to transport simulations. Finally, Chapter 6 provides conclusions and a summary.

Chapter 2

Sensitivity of Isospin Diffusion to Physics Inputs[1]

Let us briefly discuss simple qualitative expectations regarding the effects of different ingredients on isospin diffusion. All other effects being equal, a stronger symmetry energy in the low-density region of the neck will lead to more isospin diffusion, while nuclear collisions will tend to slow down the diffusion by locally trapping the asymmetry. In fact, Shi and Danielewicz derived an expression for the diffusion constant from an analytic solution to the BUU equations, and found it to be proportional to the strength of the symmetry energy and inversely proportional to the neutron-proton cross section [57]. Collisions are not expected to be the driving force in the energy regime studied here because of Pauli blocking. Diffusion is expected to increase with decreasing impact parameter due to the larger overlap region and longer reaction time. For central impact parameters, however, a heavy residue generally does not survive, and some diffusion

---

[1] This chapter reproduces parts of a previous published article [56], which is copyright 2011 by the American Physical Society.

observables may not be well defined at the beam energy we studied.

In the case of two colliding nuclei, however, other aspects of the system dynamics may complicate the above simple picture. The symmetric matter mean field is not expected to affect isospin diffusion directly, but changes that affect the stability of nuclei or favor the creation of intermediate mass fragments (IMFs) may affect the dynamics of the system enough to enhance or suppress diffusion processes. Baran et al. point out that density gradients will also lead to isospin transport, causing the low-density neck to become preferentially neutron-rich [58]. Some of this matter is not transferred between nuclei but is expelled as free nucleons or light fragments, decreasing the total asymmetry of the remaining residues. Other effects may change the role of nucleon-nucleon collisions. Some collisions may be needed to remove nucleons from one nucleus into the momentum space corresponding to stable and unstable orbits about the other nucleus. In-medium clustering effects may increase the nucleon-nucleon cross section by increasing the available phase space.

Isospin diffusion was measured for the systems of ^{124}Sn +^{112}Sn and ^{112}Sn+^{124}Sn at beam energies of 50 MeV/nucleon at NSCL/MSU [18, 19]. The symmetric reaction systems, ^{124}Sn+^{124}Sn and ^{112}Sn+^{112}Sn were also studied to remove the contribution from non-isospin diffusion effects. This was done by utilizing the isospin transport ratio (also called the imbalance ratio):

$$R_i = 2\frac{X - (X_{124+124} + X_{112+112})/2}{X_{124+124} - X_{112+112}}, \tag{2.1}$$

first introduced in Ref. [59]. The ratio (2.1) normalizes the amount of diffusion observed through an isospin sensitive observable X to the value in the symmetric systems, such that in the absence of diffusion R_i = 1 for a neutron-rich projectile, and R_i = -1 for a neutron-poor projectile. Complete equilibration occurs near $R_i = 0$. The ratio also reduces the sensitivity to pre-equilibrium emission, although it does not remove it entirely [58]. In the MSU data, the isoscaling parameter α and the ratio of light mirror nuclei were both used to construct isospin transport ratios. Another advantage of this ratio is that observables that depend linearly on each other produce the same ratio, allowing for easier comparison between data and transport models. Transport models are generally not able to realistically handle sequential decays of the residues, which occur over long timescales and can depend n the structure of the residue. However, these models can calculate the isospin asymmetry δ of the excited residues. Statistical and dynamical calculations as well as experimental tests have shown that the isoscaling parameter α relates linearly to the δ of the excited residues, so the experimental and theoretical results may be directly compared through the isospin transport ratio [19]. It should be noted, however, that it is uncertain if the yields used to construct α always come from the decay of the residue, as opposed to the breakup of the neck.

The MSU data from Ref. [18] has been analyzed by several groups using different models to extract constraints on low density behavior of the symmetry energy. Two of the most prominent results come from Ref. [60], which used the BUU code IBUU04, and Ref. [26], which used the QMD code ImQMD05. Even through the constraints established by these two groups overlap, as shown in Fig. 3 of Ref. [26], there are real differences in the simulation results. Aside from differences between the Boltzmann and molecular dynamics models, physics quantities are parameterized differently in the codes. The form of the in-medium NN cross section reduction in particular was quite different [55].

IBUU04 includes isovector and isoscaler momentum dependencies of the mean field, while ImQMD05 includes only isoscaler. More importantly, ImQMD05 can produce complex nuclei from the neck region, while IBUU04 cannot. The relative importance of these transport properties on isospin diffusion appears to vary between the two models, but direct comparisons are difficult because of the differing nature of the models and the implementation of the codes.

The goal of this work is to explore the effect of transport quantities and assumptions on isospin diffusion within a BUU transport model, henceforth referred to as pBUU [39,61,62]. We explore many of the basic properties of the system, including the density dependence of the symmetry energy, the value of the symmetry energy at saturation density, the curvature of the symmetric part of the EoS, the momentum dependence of the symmetric EoS, and in-medium nucleon cross sections. The pBUU model can optionally produce light clusters in the medium, which is a process not native to the BUU framework and may make the system behave more similarly to the ImQMD05 work. Due to its complexity, the momentum dependence of the isovector mean field is not studied here. A similar, though not as extensive, study has also been carried out using the ImQMD05 code [55].

2.1 Description of Model

The pBUU code is of the class of Boltzmann-Uehling-Uhlenbeck models, which are one of the main types of dynamic transport models used to study nuclear reactions, particularly of heavy nuclei. The model includes as degrees of freedom both stable and excited baryons, pions, and light nuclear clusters. It calculates the time evolution of the Wigner transform of the semiclassical one-body density matrix, i.e. the semiclassical one-body phase space distribution of those particles, following a set of Boltzmann equations, modified to include Pauli blocking [38]. Many test particles per nucleon are used to approximate the continuous phase space distribution. The mean field is calculated self-consistently from the phase space distribution. The symmetric matter EoS has been extended to include momentum dependence, which can account for non-localities in the N-N interaction and from the Fock term. This code has been extensively tested against experimental data, including single particle distributions [61, 62], elliptic flow [39], and stopping observables [63]. It has been used to constrain the high density behavior of the symmetric matter EoS [6], and was used in early isospin diffusion calculations to demonstrate the sensitivity of the isospin transport ratio to the density dependence of the symmetry energy [18].

2.1.1 Mean field

The symmetry energy used in this code takes the form:

$$E_{sym}(\frac{\rho}{\rho_0}) = S_{kin}(\frac{\rho}{\rho_0})^{2/3} + S_{int}(\frac{\rho}{\rho_0})^{\gamma_i} \tag{2.2}$$

where the kinetic term arises from the Fermi motion of the nucleons, resulting in $S_{kin} = 12.5 MeV$. We will examine the variation of isospin diffusion with potential interaction term, varying both the value at saturation density (S_{int}) and the density dependence (γ_i). The form of the symmetric matter EoS is described in Ref. [39] for both momentum independent (MI) and momentum dependent (MD) forms. As was done there, we choose parameter values that provide a curvature K=210 MeV, near the currently accepted value of 231 ± 5 MeV [37], and K=380 MeV for comparison. We will show that the stiffness (curvature) of the symmetric matter EoS does not affect isospin diffusion. We also study the momentum dependent case that best fits the elliptic flow data in Ref. [39], which is characterized by an effective mass $m^* = 0.7m_N$. Our study shows that the momentum dependence changes the dynamics of the reaction such that intermediate mass fragments are produced from the breakup of the neck and the interaction time is lengthened, both of which affect the isospin diffusion signal.

2.1.2 In-medium Cross sections

The residual interactions between nucleons are represented by nucleon-nucleon collisions, which are parameterized separately from the mean field. The cross sections of these collisions are known to be reduced in the nuclear medium compared to their free-space values [64], but the form of this reduction is not yet established. Starting from the free space cross section parameterization of Ref. [65], we examine two forms of the in-medium cross section reduction. The screened cross section is derived from the geometric reasoning that the geometric cross section radius should not exceed the inter-particle distance, and is implemented in the form:

$$\sigma = \sigma_0 \tanh(\sigma_{free}/\sigma_0) \tag{2.3}$$

$$\sigma_0 = y\rho^{-2/3}, y = 0.85 \tag{2.4}$$

This screened reduction is strongly dependent on the density, and is very much reduced compared to free-space cross sections. Since this form has a maximum cross section σ_0, large cross sections have a larger fractional reduction than small cross sections. The free neutron-proton (np) cross section is larger than the free neutron-neutron (nn) or proton-

proton (pp) cross sections in the relevant energy range, so the in-medium np cross section is suppressed more than the nn or pp cross sections.

In contrast, the Rostock cross section is parameterized from the results of Brueckner-Hartree-Fock calculations [66,67], and is implemented in the form:

$$\sigma = \sigma_{free} \exp(-0.6 \frac{\rho}{\rho_0} \frac{1}{1 + (T_{c.m.}/150MeV)^2}) \tag{2.5}$$

where $T_{c.m.}$ is the center of mass kinetic energy of the nucleon pair. It is less dependent on density than the screened cross section, and results in less reduction at the energy of interest. Both cross sections were tested versus stopping data within the pBUU model in Ref. [63]. The screened cross section showed somewhat better agreement with data, but both were an improvement compared to free-space cross sections. Neither cross section reduction corresponds exactly with the reductions used in the IBUU04 or ImQMD05 codes, but the amount of reduction in those codes is more similar to the Rostock cross section than to the screened. We will show that the choice of cross section reduction can greatly affect the diffusion signal.

2.1.3 Cluster Formation

Production of light clusters in the pBUU code is implemented as an option up through cluster mass 3, with the production rate derived through the inverse process of cluster breakup. In pBUU these clusters are produced by the interaction of test particles in the nuclear medium. Since the clusters are test particles themselves, they may exist as part of the density distribution that represents a nucleus, residue, or fragment. In this analysis, this makes them distinct from intermediate mass fragments (IMFs), which are distinguished by distinct peaks in the phase space density distributions that are spatially separated from the heavy residues and each other, and are the result of the interplay between density fluctuations and the mean field. While this is far from a complete clustering model, missing in particular the formation of α particles, it can give an indication of the importance of clustering in the nuclear medium. Even though the QMD model includes a method of forming clusters, it is difficult to remove the cluster formation mechanism entirely from the QMD model in order to quantify the effects of clusters on the reaction dynamics. With the cluster option in pBUU, we are able to compare isospin diffusion results with and without cluster formation.

2.2 Identification of Residue

Several methods of extracting the projectile-like residue from the results of a transport simulation have been put forward in the literature. These methods generally fall into two categories. Within the first method, employed exclusively in BUU approaches providing single-particle density, the residue is defined as consisting of cells in the computational grid that match a particular average velocity cut and average density cut, regardless of the cells' relative locations [18,60]. Within the second method, spatially contiguous fragments are identified, either by examining the single-particle density directly or through a tree-spanning method. Thereafter, cuts on the average velocity and size of those fragments are applied to either include only the largest fragment (the residue), or all fragments that match particular mass and velocity criteria, sometimes including free nucleons [26,55,68]. In both cases, the velocity cut tends to be half of the initial projectile velocity in the center of mass, and if a density cut is employed, it can range from 0.2 to 0.05 of saturation density. Obviously, these two methods will produce the same result for a simple reaction that does not produce any intermediate mass fragments. Nonetheless, the first method has the advantage that it allows fragments to be traced through the timescale of the reaction, while the second can only define fragments once the system has sufficiently spread out. On the other hand, the second method allows for a more precise description of the final state of the system when intermediate mass fragments form, and it does it not break up a spatially contiguous fragment if some rotation or other collective motion exists within that fragment. Whatever method is chosen to define the projectile-like residue, the isospin asymmetry can be determined and used as the isospin sensitive observable within the isospin transport ratio.

In our analysis, we chose to use the second method, since there are systems produced in this study that emerge either with IMFs or collective motion in the residue regions. We identified contiguous areas above a given density threshold as fragments, and we tested the effect of the density cut, of the time chosen to stop the reactions, and of velocity cuts on the extracted isospin asymmetry and isospin transport ratio, using several combinations of physics inputs examined here. The density cut was varied from $\rho_0/20$ to $\rho_0/5$. Lower density cuts led to a more asymmetric residue, indicating a low-density neutron skin on the fragment, but this effect was almost entirely removed by the isospin transport ratio. Likewise, after the main reaction is completed (when all fragments have spatial separation), the residues continue to evaporate neutrons, becoming more symmetric, but this effect exists in the symmetric systems as well and ultimately does not affect the isospin transport ratio significantly. The time for the fragments to separate spatially depended on the density cut and on the physics inputs, but was complete by 220 fm/c after the start of the simulation in every case. For the remainder of this chapter, the analysis was conducted at 270 fm/c with a density cut of $\rho_0/20$, unless otherwise indicated.

Some combinations of physics inputs yielded results that were sensitive to velocity cuts. As will be discussed later, some choices of mean field parameters affect the formation of intermediate mass fragments (IMF). Systems that produced large IMFs sometimes had significantly different results for the isospin transport ratio if those large fragments were included in the analysis. These effects will be discussed in more detail in the next section. Systems without IMFs or with many small IMFs showed no dependence on whether the highest mass fragment was considered alone or whether all fragments matching a particular velocity cut were considered together, for any forward-moving velocity cut from 0 to 1/2 of the initial velocity of the projectile in the center of mass. For the remainder of this chapter, our analysis will focus on either the asymmetry of the largest forward-moving fragment without IMFs, or on the asymmetry of all forward-moving fragments. Free nucleons are not included in the analysis.

2.3 Results

2.3.1 Mean field effects

We start with a simple momentum independent (MI) description of the mean field. As has been done in Ref. [39], we use a mean field with an isoscaler compressibility of K=380 MeV, a screened cross section, and no light cluster production. We vary the coefficient (S_{int}) and density dependence coefficient (γ_i) of the symmetry energy in Eq. 2.2. The results when following the heavy residue are shown in Fig. 2.1(a) for the ^{124}Sn +^{112}Sn

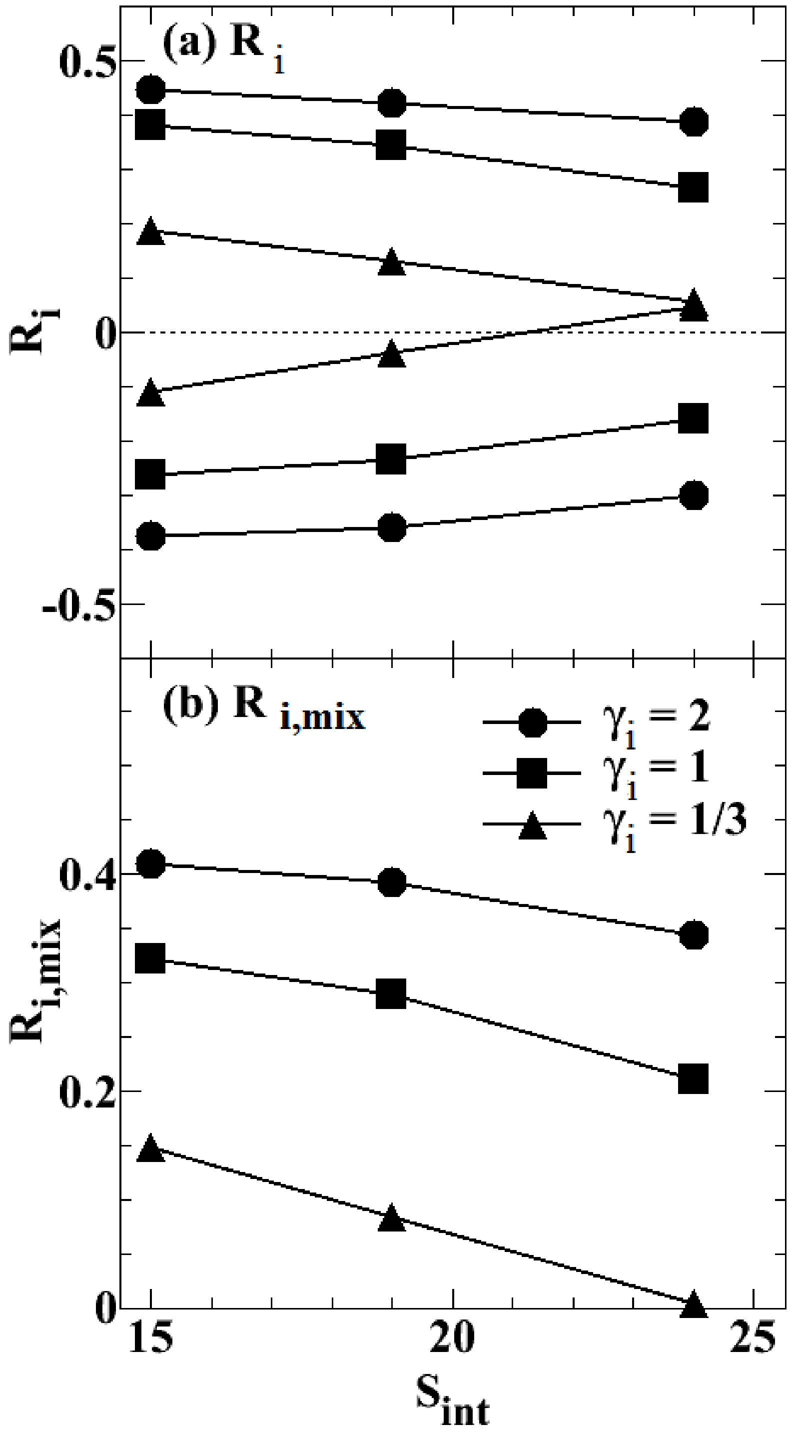

Figure 2.1: (a) The isospin transport ratio of the ^{124}Sn +^{112}Sn and ^{112}Sn+^{124}Sn systems as a function of the symmetry energy interaction coefficient from Equation 2.2, for a momentum independent (MI) mean field. (b) Results from combining the two systems. As expected, a larger coefficient leads to a smaller isospin transport ratio, indicating more equilibration. In addition, a smaller exponent γ_i also leads to more equilibration, which is consistent with a sensitivity to low densities.

(positive R_i) and ^{112}Sn+^{124}Sn (negative R_i) systems at an impact parameter of 6 fm. The x-axis represents the strength of the interaction term, S_{int}, in Eq. 2.2 at saturation density. Three different density dependencies γ_i = 1/3, 1, and 2 are shown with triangles, squares, and circles. Lines are drawn to guide the eye. For all γ_i, larger S_{int} leads to an isospin transport ratio closer to zero (horizontal dotted line), which matches the expectation that a stronger symmetry energy leads to more diffusion and faster isospin equilibration. Consistent with that expectation, the most equilibration occurs for the smallest value of γ_i (triangles), which corresponds to a stronger symmetry energy at sub-saturation densities. This confirms that isospin diffusion is sensitive to the strength of the symmetry energy in the sub-saturation neck region, as anticipated.

The isospin transport ratios for the ^{124}Sn +^{112}Sn and ^{112}Sn+^{124}Sn systems converge for $\gamma = 1/3$ and $S_{int} = 24$, indicating complete equilibration, but the value of R_i at these points is definitely different from zero. This offset can be attributed to the mass asymmetry of the system, as may be demonstrated with a very simple calculation. Assuming that nucleons are only transfered between the nuclei and none are lost to free space or to light fragments, simple algebra shows that complete equilibration leads to $R_{i,eq} = (A_1 - A_2)/(A_1 + A_2)$. This result will be modified by preequilibrium emission, but the effect on the transport ratio will be small. In our system this calculation leads to $R_{i,eq} = 0.051$, which is consistent with the observed equilibration in Fig. 2.1a. However, $R_{i,eq} = 0$ is more intuitive, and noting that the two systems provide similar information, we can restore the expectation of a zero for complete equilibration by combining information from both systems:

$$R_{i,mix} = (R_{i,124+112} - R_{i,112+124})/2$$

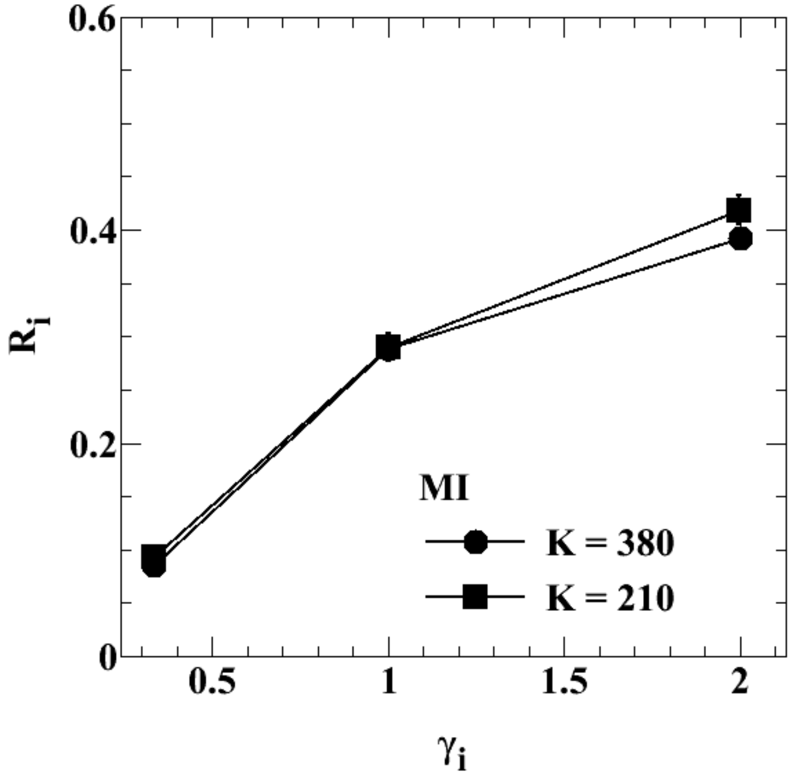

Figure 2.2: The effect of the compressibility of the symmetric EoS on isospin diffusion, as a function of the exponent γ_i that determines the density dependence of the symmetry energy in Equation 2.2. The effect of the compressibility on this observable is quite small.

as demonstrated in Fig. 2.1(b). Unless stated otherwise, we use the quantity $R_{i,mix}$ for the remainder of this chapter, and for simplicity we relabel it as R_i. Having established that varying either S_{int} or γ_i produces changes resulting only from the overall strength of the symmetry energy at subsaturation densities, for the calculations discussed in the remainder of this work we vary only γ_i and set $S_{int} = 19 MeV$ ($E_{sym}(\rho_0) = 31.5 MeV$), as for the middle set of points in Fig. 2.1.

Next we examine the effect of changing the isoscaler compressibility, still using a momentum independent mean field. In Fig. 2.2, the simulations with compressibility K=210 MeV are shown with squares and K=380 MeV with circles, as a function of the density dependence of the symmetry energy. Recall that the accepted value of K is 231 ± 5 MeV [37], so K=380 MeV lies well outside the accepted uncertainties. However, varying the compressibility even this much produces very little change in the isospin transport ratio, although there is slightly less diffusion for the K=210 MeV case than for the K=380 MeV case.

In elliptic flow data at higher energies, including momentum dependence had an effect similar to increasing the stiffness of the mean field. That is why the momentum dependent (MD) mean field with curvature K=210 MeV was often compared to the momentum independent (MI) mean field with K=380 MeV [39]. However, for isospin diffusion at 50 MeV/nucleon, the momentum dependence has a much different effect than the compressibility. First, it changes the dynamics of the reaction, enhancing the likelihood of IMF production, and in particular leading to the production of larger IMFs. This arises because the depth of the attractive potential is lower at large relative momenta, and it is easier for groups of particles to escape. A density profile of the momentum independent and the momentum dependent systems is shown in Fig. 2.3 at t=270 fm/c, highlighting the difference in IMF production.

The emerging IMFs have a large effect on the diffusion signal. When all forward-moving fragments are used as the isospin tracer, including both the projectile-like residue and IMFs, a MD EoS gives rise to more diffusion than a MI EoS (Fig. 2.4, open triangles and filled circles, respectively), resulting in smaller values of R_i. Only very small IMFs are produced in MI simulations. The isospin diffusion results are essentially unchanged when the small IMFs are included, so the respective result is not shown separately in the figure. By contrast, when looking just at the largest residue, inclusion of momentum

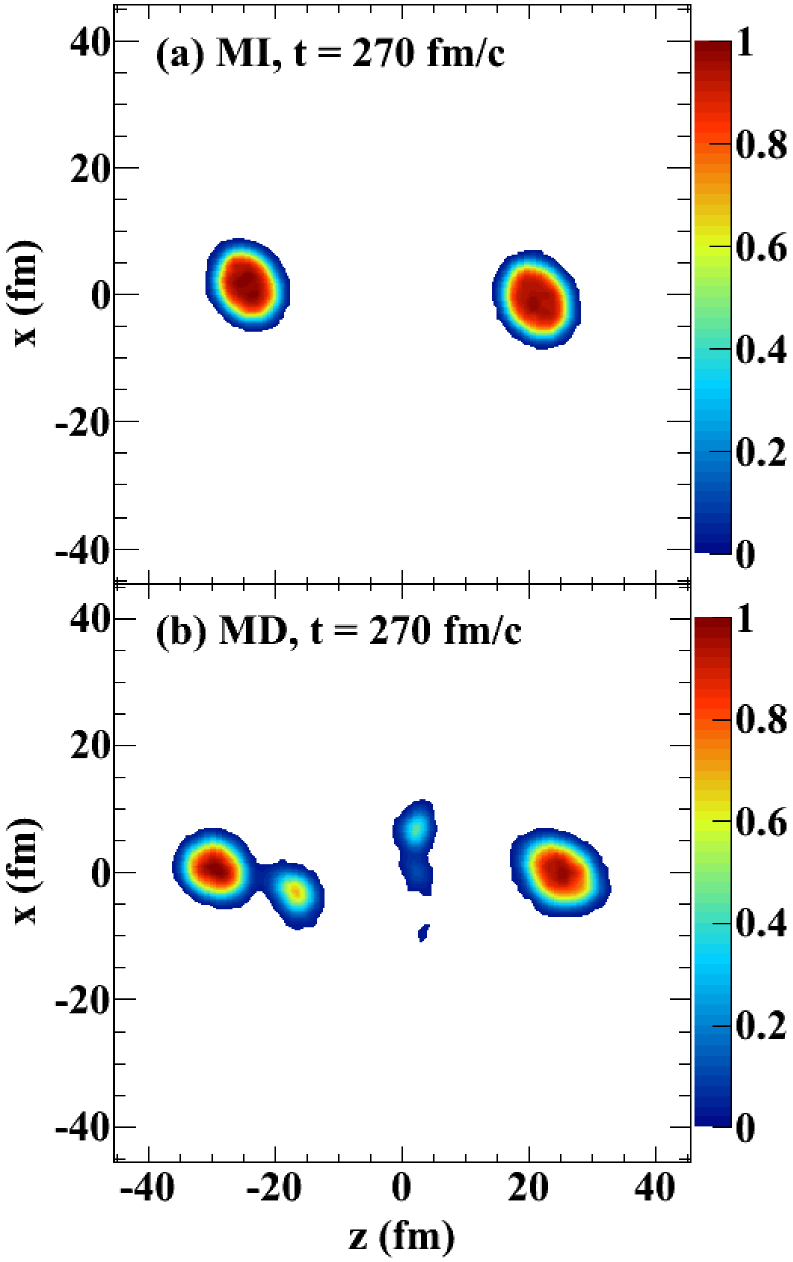

Figure 2.3: Density profiles from sample calculations within the reaction plane at t=270fm/c, after the residues have separated, following an EoS that is (a) momentum independent and (b) momentum dependent. The z axis is the beam direction, and the color scale represents density, normalized to saturation density. The momentum independent interaction leads only to two large residues, while the momentum dependent interaction also gives rise to intermediate mass fragments. For interpretation of the references to color in this and all other figures, the reader is referred to the electronic version of this dissertation.

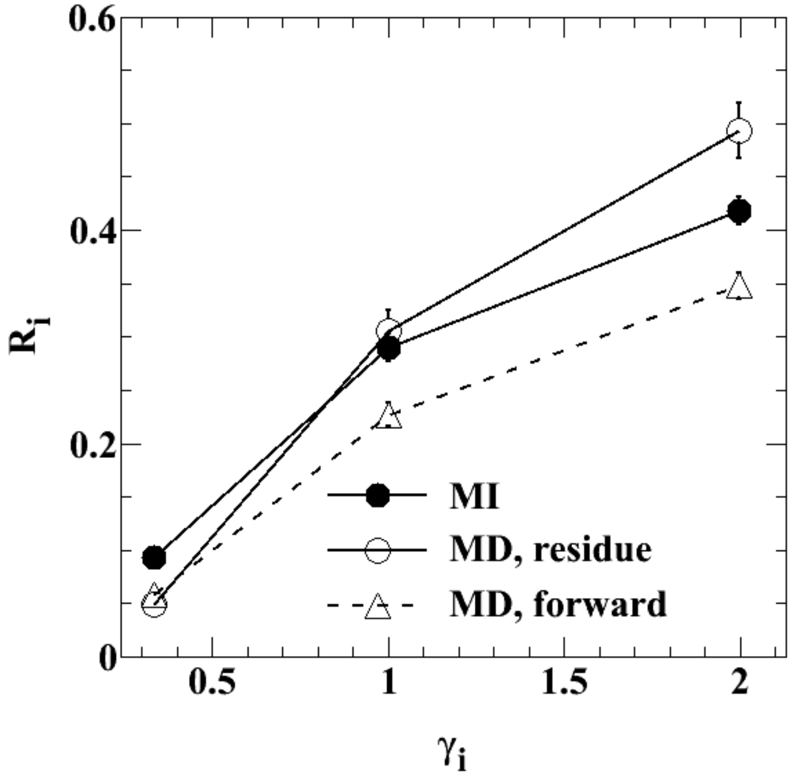

Figure 2.4: The effect of momentum dependence on isospin diffusion, as a function of the density dependence of the symmetry energy. The diffusion into the largest residue is compared to the diffusion into all forward-moving fragments. The diffusion signal is quite different depending on whether the intermediate mass fragments are considered.

dependence (open circles) decreases the amount of diffusion, resulting in larger R_i values for large γ_i and smaller for small γ_i. Thus, inclusion of the momentum dependence of the mean field has two effects on the diffusion signal. It increases the overall rate of isospin diffusion, but if the overall rate of diffusion is slow, as is the case for large γ_i, many of the diffused particles are stuck in the neck and contribute to the IMFs rather than to the heavy residue. If the diffusion rate is fast, as is the case for small γ_i, the neck and the residue reach equilibrium, and the inclusion of IMFs does not change the diffusion signal. This is similar to an effect of IMFs reported by Zhang *et al.* in Ref. [55] following the ImQMD code, although the dependence on γ_i is different there.

On the other hand, the increase in diffusion due to the momentum dependence contradicts the results of Rizzo *et al.* in Ref. [68], who report the opposite effect within the stochastic mean field (SMF) model. They report that the inclusion of momentum dependence in the mean field, which causes greater isoscaler repulsion, increases the rate at which the residues separate and thus reduces the interaction time. The momentum dependence corresponds to a reduction of the effective mass compared to the free mass, which means that particles with a given canonical momentum will be moving faster in a momentum dependent mean field than in a momentum independent mean field. This speeds up the interaction of the colliding nuclei. Our simulations do show that the residues move apart from each other more quickly when isoscaler momentum dependence is included. However, the formation of density clumps in the neck, which results in emission of IMFs after the neck snaps, anchor the neck, causing it to persist longer and allowing more diffusion to occur. This effect is visible in the density profiles of the system at 162 fm/c, when the neck in the MI case (upper panel) has already broken up but the MD case (lower panel) has not, as shown in Fig. 2.5. This effect occurs even when the density fluctuations in the neck do not persist as IMFs at the end of the reaction. This suggests that the major effect of the symmetric mean field in isospin transport is to influence the time and manner of the neck breakup. The explicit inclusion of stochastic effects in the SMF model produces density fluctuations leading to IMFs even for MI mean fields, which may cause the neck to break up similarly regardless of the momentum dependence of the mean field. The amount of time during which the residues interact would then depend only on the velocity of the residues, producing the different trend in their calculations.

This same dependence on manner of the neck breakup is evident in the impact parameter dependence of the isospin transport ratio. Fig. 2.6 shows the transport ratio as a function of impact parameter. Line style corresponds to density dependence of the symmetry energy. As expected, less diffusion takes place (larger R_i) at large impact parameters where the overlap region is smaller and the residues continue to move faster. The amount of diffusion changes monotonically in the MI case (Fig. 2.6(a)). When momentum dependence is included, however, this monotonicity disappears (Fig. 2.6(b)) for central and mid-peripheral collisions. This is again due to the large IMFs, which are only created if there is a sufficient overlap region. For peripheral collisions ($b > 7fm$), the density fluctuations in the neck extend the lifetime of the neck, increasing the interaction time and the amount of equilibration, but not creating large enough IMFs to carry away the asymmetry. For mid-peripheral collisions ($5fm \leq b \leq 7fm$), the residue equilibration varies significantly but flattens out on average. When including all forward moving fragments (Fig. 2.6(c)), the monotonicity is restored in this region. For the smallest impact parameter ($b = 4fm$) shown in Fig. 2.6, the amount of equilibration indicated by both

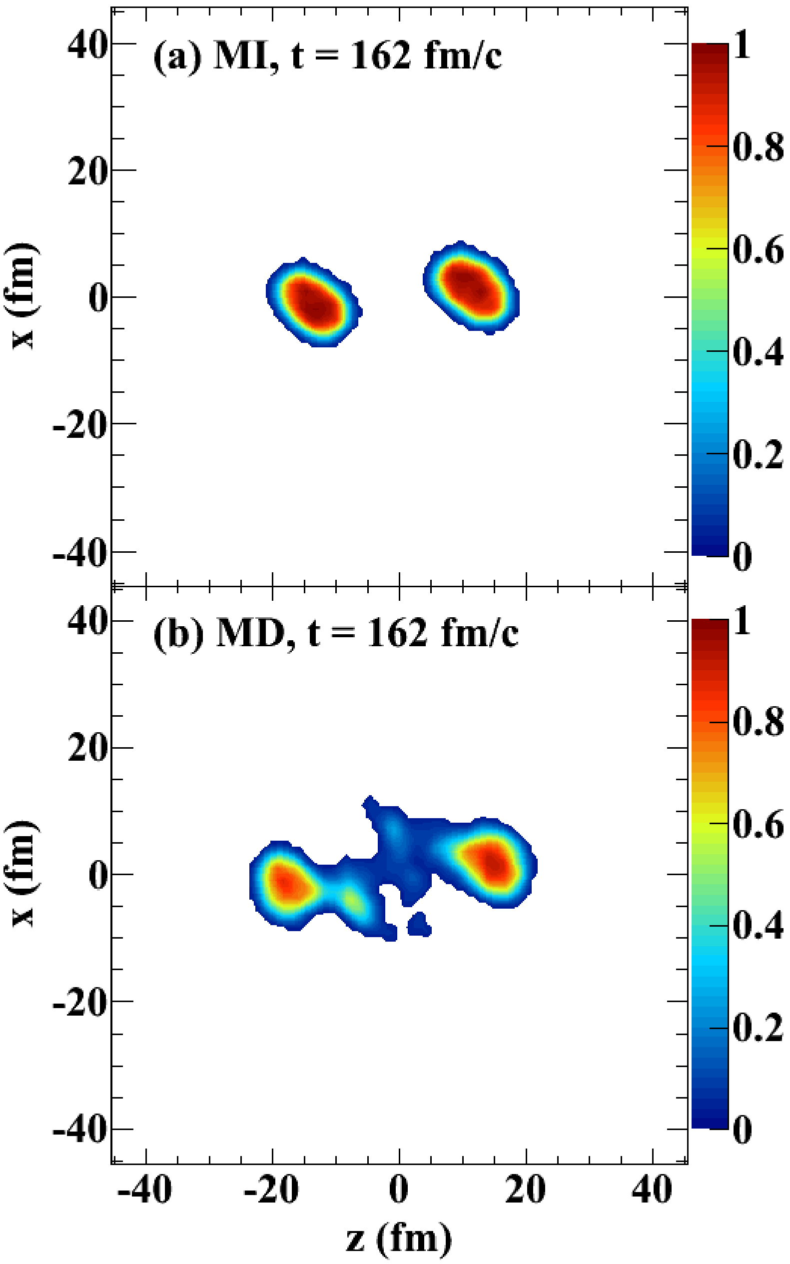

Figure 2.5: Density profiles within the reaction plane at t=162fm/c, normalized to saturation density. (a) When following a momentum independent (MI) EoS and (b) when following a momentum dependent (MD) EoS. The neck is seen to persist at longer times with the momentum dependent interaction, due to the effect of the fledgling intermediate mass fragments. This leads to more diffusion when the entire forward-moving system is considered, but the diffusion to the heavy residue can also be limited by the nearby light fragment. These explain the effects seen in Figure 2.4

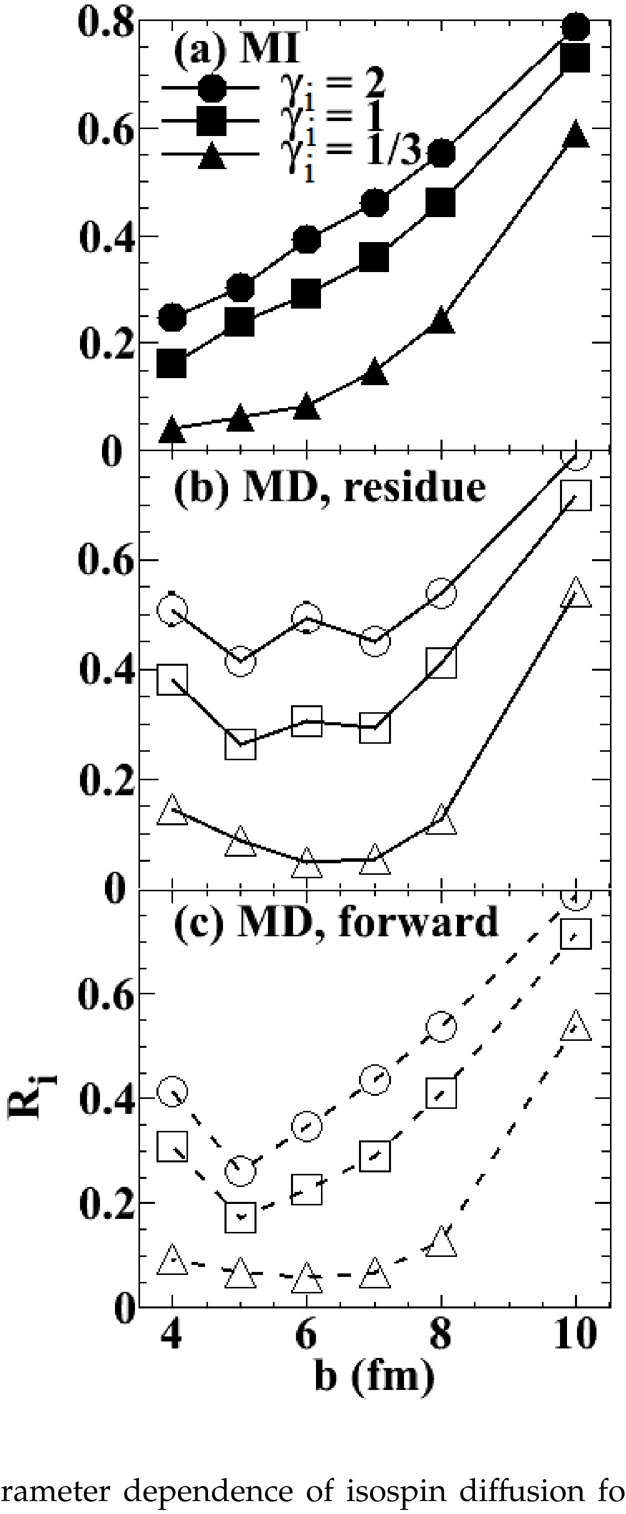

Figure 2.6: Impact parameter dependence of isospin diffusion for: (a) momentum independent EoS, (b) momentum dependent EoS, to the heavy residue, (c) momentum dependent EoS, to all forward-moving fragments. A large impact parameter leads to a shorter interaction and a smaller neck, which reduces the amount of diffusion. However, there is quite a bit of variation between the MI and MD interactions and between observables at smaller impact parameters.

tracers decreases (larger R_i values). In this region, the motion of matter squeezed out from the overlap region competes with the diffusion process. Comparison of the three panels reveals the smallest effect from the momentum dependence of the mean field at large impact parameters, while still being sensitive to γ_i. For mid-peripheral collisions, the dependence on the mechanism of neck breakup due to the momentum dependence of the mean field is reduced when looking at all forward-moving fragments.

2.3.2 In-medium cross sections

We now move in our considerations from the mean field to the in-medium nucleon cross sections. As discussed in section 2.1.2, we examine free cross sections and two parameterizations of in-medium reductions. Prior to this point in the chapter, we have been using the screened cross section.

The effect of the different cross section parameterizations is shown in Fig. 2.7, when following the MI EoS. Clearly, less diffusion occurs for the free cross section (triangles) than for either reduced one, and this effect is most pronounced for small γ_i. This contradicts the conclusion arrive at within the IBUU04 code in Ref. [60], where it was found that the free cross section produced more diffusion than the reduced cross section for very stiff symmetry energies ($\gamma_i > 2$), with less effect in the range of γ_i considered here. Similarly, the ImQMD05 code is largely insensitive to the cross section over a similar range of density dependencies as considered here [55]. However, both of those results were obtained with MD mean fields, which will be considered here only later in Fig. 2.9. In Fig. 2.7, the difference between the Rostock and screened cross sections, shown as squares and circles, respectively, is larger than the difference between the free and the Rostock. More

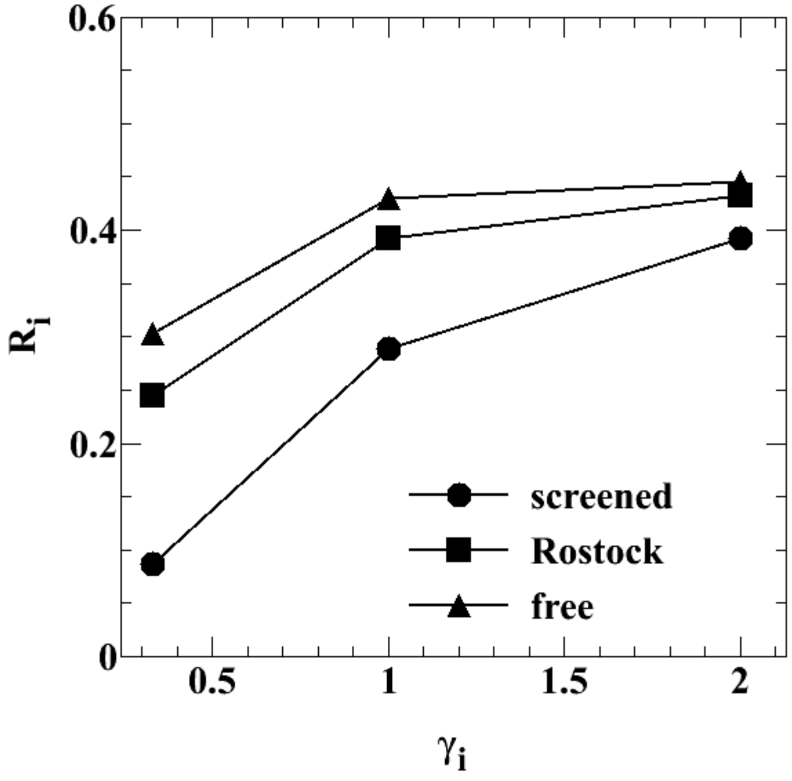

Figure 2.7: Effect of different cross section parameterization on isospin diffusion. The three cross sections were introduced in Section 2.1.2. The screened cross section, which is the most reduced, leads to the most diffusion.

importantly, the sensitivity to γ_i is strongly affected by the cross section.

The screened and Rostock cross sections lead to similar stopping in heavy ion collisions because they produce similar viscosities [63]. However, they suppress the overall number of nucleon-nucleon collisions by different factors, and as discussed in section 2.1.2, the screened cross section reduces the np cross section more than the nn or pp. In these simulations, $N_{Rostock} \approx \frac{3}{4}N_{free}$ while $N_{nn,pp,screened} \approx \frac{1}{4}N_{free}$ and $N_{np,screened} \approx 0.15N_{free}$, where N is the total number of nucleon-nucleon collisions over the course of the simulation. It is not simply the number of collisions that affects the isospin transport. From Shi and Danielewicz [57], we expect the isospin diffusion rate to depend inversely on the np cross section, without depending on the nn or pp cross sections at all. However, Ref. [57] studied diffusion in nuclear matter near equilibrium, and the dependence on cross sections may be different in heavy ion collisions. Fig. 2.8 shows the isospin transport values when the np cross section is reduced by a constant factor relative to the free cross sections. As expected, changing the nn and pp cross sections leads to only very small changes, so these are not shown. The x-axis is the employed reduction factor, with the limit of no collisions at the left of the axis ($\sigma_{np}/\sigma_{np,free} = 0$) and free-space cross sections at the right. Line and marker styles represent the density dependence of the symmetry energy, γ_i. The trend of each line indicates that collisions have two major effects on the amount of isospin diffusion. For nearly free cross sections on the right side of the plot, increasing the cross section decreases the amount of diffusion. This matches the intuition, formally derived in Ref. [57], that collisions impede isospin diffusion. A nucleon that undergoes a collision or series of collisions with large momentum transfer forgets its original direction of motion, which impedes the equilibration effects of the mean field.

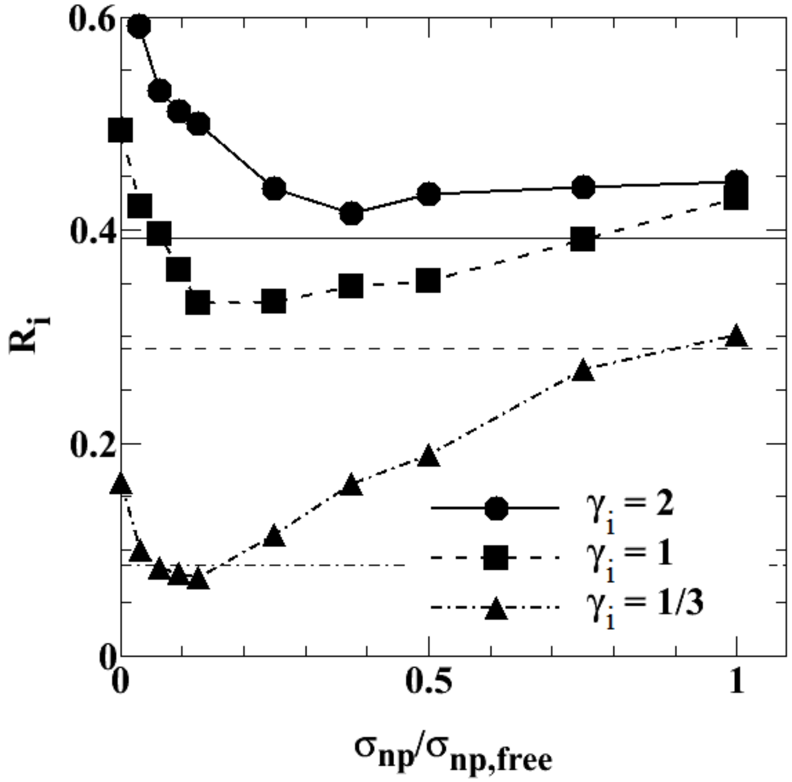

Figure 2.8: Sensitivity of isospin diffusion to np cross section reduction by a constant factor. The x-axis is the fractional reduction relative to free cross sections. Horizontal lines represent the results obtained using the screened cross section, from Fig. 2.1. While reducing the cross section increases the amount of diffusion to a degree, this trend does not continue indefinitely. Particularly small cross sections lead to less diffusion.

For the very small cross sections on the left side of the figure, however, increasing the cross section increases diffusion. The nucleon-nucleon collisions can cause isospin transport by knocking nucleons out of the momentum space of one nucleus, causing them to be transferred to the other nucleus or expelled as free nucleons. This process is largely isospin independent, but will contribute to isospin equilibration via simple mixing. The hook at low end of the $\gamma_i = 1/3$ (triangles, dot-dashed) line shows that this yields a finite contribution to isospin diffusion for even a strong symmetry potential at subsaturation densities. For $\gamma_i = 2$ (solid line), this is the dominant contribution, and is approaching the point where diffusion would increase by increasing the cross section at any point on the curve. For even stiffer symmetry energies, this could easily lead to the free cross section producing more diffusion, as was seen in the IBUU04 study. For reference, three horizontal lines are drawn to indicate the value of R_i from the screened cross section. Except for the $\gamma_i = 1/3$ case (dot-dashed), a uniform reduction of the free cross section never produces as much diffusion as the screened cross section. This indicates that the strong density dependence of the screened cross section is particularly favorable for overall isospin equilibration. Therefore, the exact form of the in-medium cross section is the important quantity, not merely the viscosity or the net collision number.

A similar hierarchy of cross section effects is evident with a momentum dependent EoS, with the stipulation that one takes the IMFs into account. As shown in Fig. 2.9, the IMFs included in the forward moving fragments modify the signal differently for the different cross sections. The screened cross section (circles) is strongly affected by the inclusion of IMFs (panel (b)), while the Rostock (squares) is affected modestly and the free cross section (triangles) is affected little. This may open an avenue to experimentally constrain

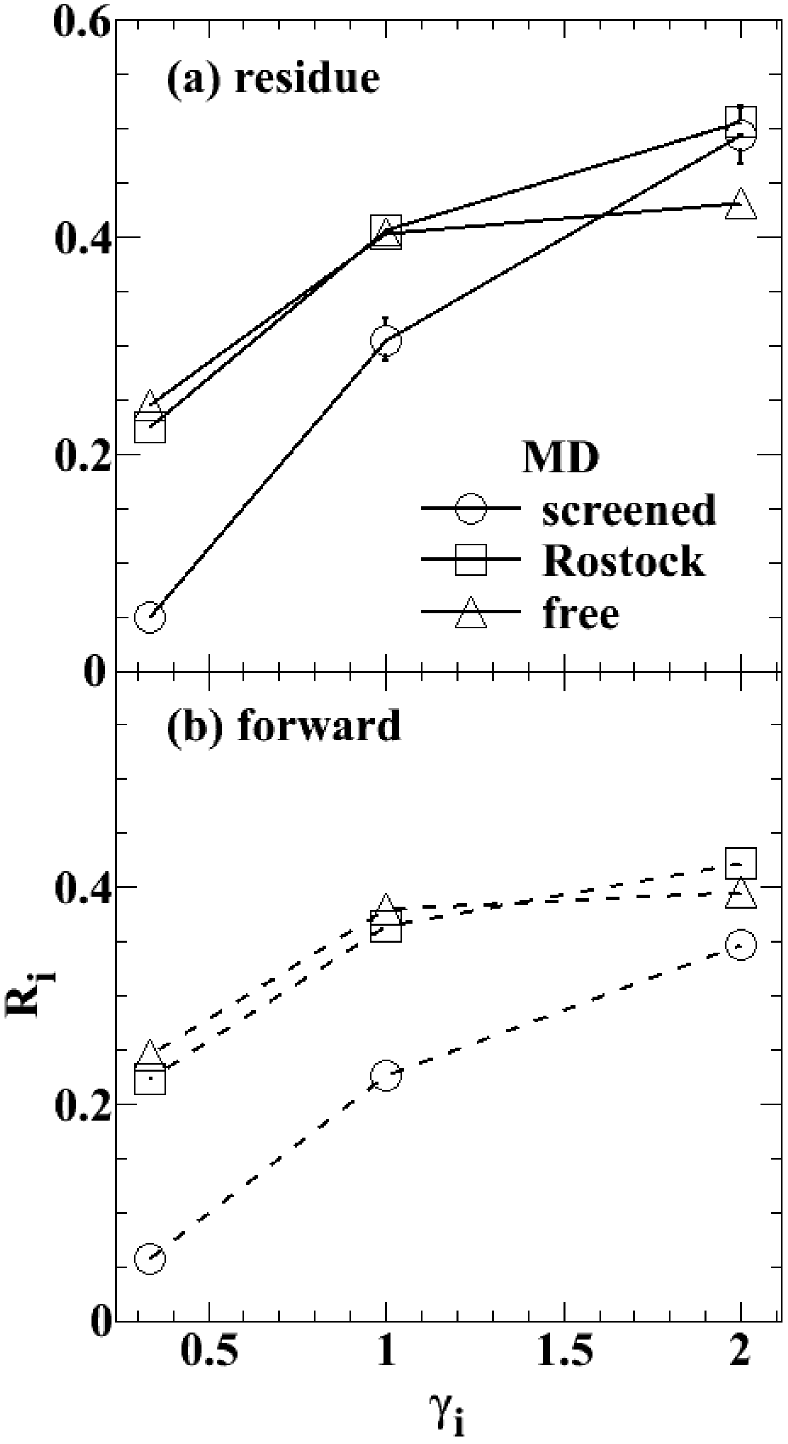

Figure 2.9: Isospin equilibration for a momentum dependent EoS with in-medium cross section reductions. Panel (a) shows results from the heavy residues only, while panel (b) shows results from all forward-moving fragments. With the slightly weaker momentum-dependent interaction, the dependence of diffusion on cross section reduction does not display the clear trend as with the momentum independent interaction shown in Figure 2.7.

the cross sections. A careful comparison of Fig. 2.9 to Fig. 2.7 also reveals that the results obtained using the screened cross section are most strongly modified by using a mean field with momentum dependence. This can be understood as the competition between the collisions and the mean field: as the importance of the collisions grows, the changes in the mean field become less important. This figure also shows that with a momentum dependent mean field, the Rostock and free cross sections produce very similar results, except for the very stiff symmetry energy $\gamma_i = 2$. This is consistent with the results of [60].

The difference in dynamics that gives rise to the different IMF dependencies is evident in Fig. 2.10, where the asymmetry of all fragments greater than mass two at the final time of the ^{124}Sn +^{112}Sn simulations are plotted against their rapidity in the reaction center of mass, accumulated over many simulations. The two different symbols represent two different γ_i values in the EoS used in the simulations, and panels (a) and (b) show results for the screened and Rostock cross sections, respectively. The tight clumps of fragments at the largest absolute rapidities are the large residues, and all other points represent IMFs. While the fragment asymmetry is similar between the two cross sections for a given γ_i, the IMFs are more evenly spread in rapidity with the Rostock cross section (Fig. 2.10(b)), whereas they are more likely to be concentrated at larger absolute rapidity with the screened cross section (Fig. 2.10(a)). This indicates less stopping for the IMFs from the screened cross section, even though the residue rapidity is unchanged. Related to this, but not illustrated, is that the produced IMFs tend to be larger in the screened case compared to the Rostock case, but of quite similar asymmetry. Note that there are no IMFs close to the residue in rapidity. Since this is a snapshot taken on the timescale of the nuclear reaction, the effect cannot be attributed to the long-term impact of Coulomb

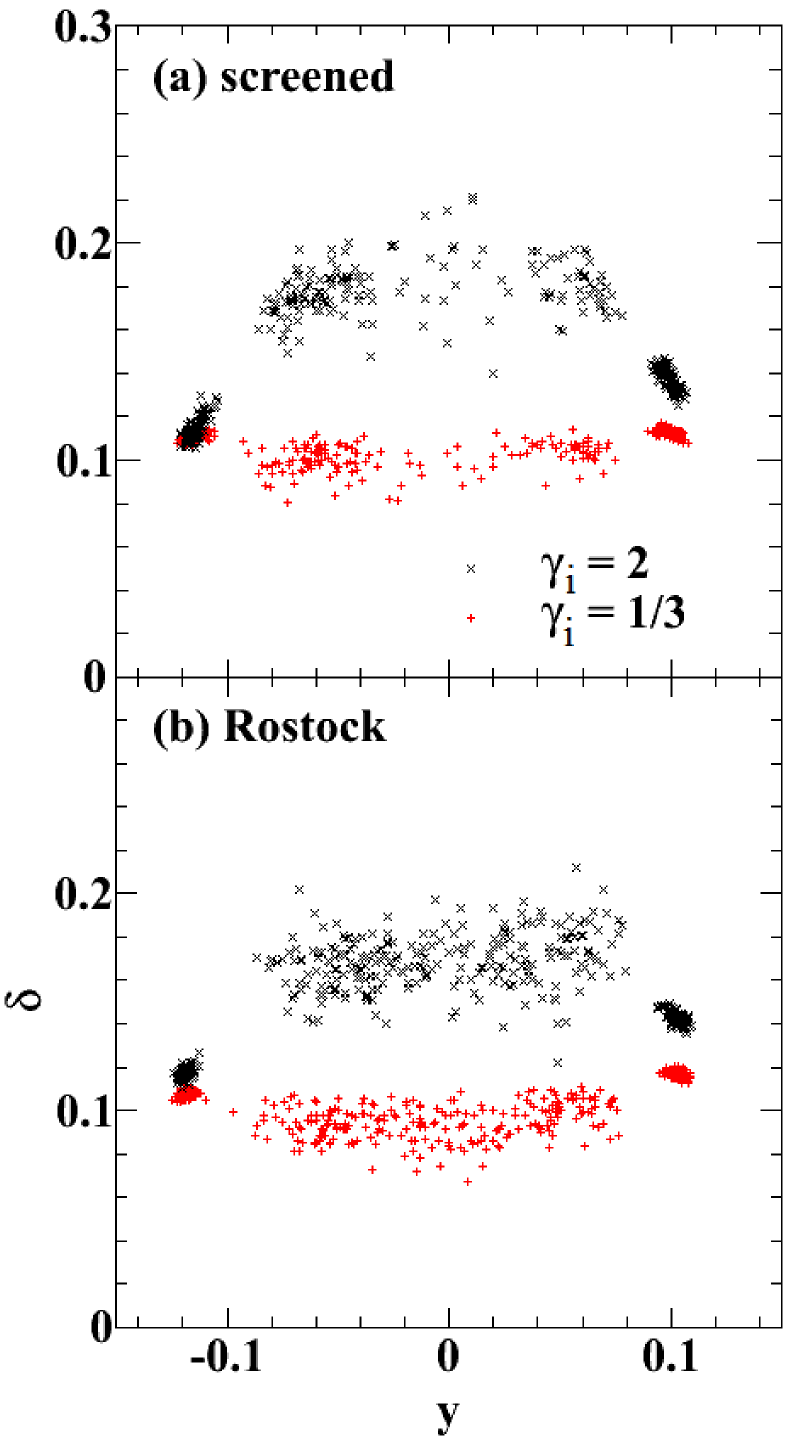

Figure 2.10: Distribution of fragments in isospin asymmetry δ (see Equation 1.2) and rapidity, using (a) screened and (b) Rostock in-medium cross sections. The rapidity distributions of the intermediate mass fragments depend strongly on the cross section, which the rapidity of the heavy residue does not. Also note the strong sensitivity of the IMF asymmetry to the symmetry energy.

repulsion. Rather it is the effect of the residue "gobbling up" nearby fragments. Because the IMFs are moving faster in the screened case, they are closer to the residue and are more likely to be absorbed. This, combined with the mass difference of the IMFs, causes the different degree of response to the inclusion of IMFs in the isospin transport ratio. The dependence on IMF mass and rapidity distributions can be measured, and this may provide additional constraints on the in-medium cross section reduction.

2.3.3 Cluster Production

Next we examine the effects of light cluster production in the nuclear medium. This is a distinct process from the formation of IMFs during the breakup of the neck. IMFs are the result of density fluctuations, whereas cluster production is a fast nucleation process, the result of inelastic particle collisions. It is unclear how to combine the information about light fragments produced from these two mechanisms; nevertheless, it is interesting to examine the change in dynamics that results. Fig. 2.11 shows the changes in the isospin transport ratio caused by including cluster production, when examining all forward moving fragments. Specifically, the figure compares the results of simulations with and without clustering when employing a MI mean field (panel (a)), and when employing a MD mean field (panel (b)). In both cases, the inclusion of cluster production (squares) reduces the amount of diffusion and decreases the sensitivity of the diffusion to the symmetry energy. The increased value of the isospin transport ratio for small γ_i better matches the predictions of ImQMD05 [55], bolstering the idea that clustering in a BUU model is required for comparison to results from QMD models and to experimental data. However, the maximum isospin transport ratio for large γ_i here is still significantly less than that

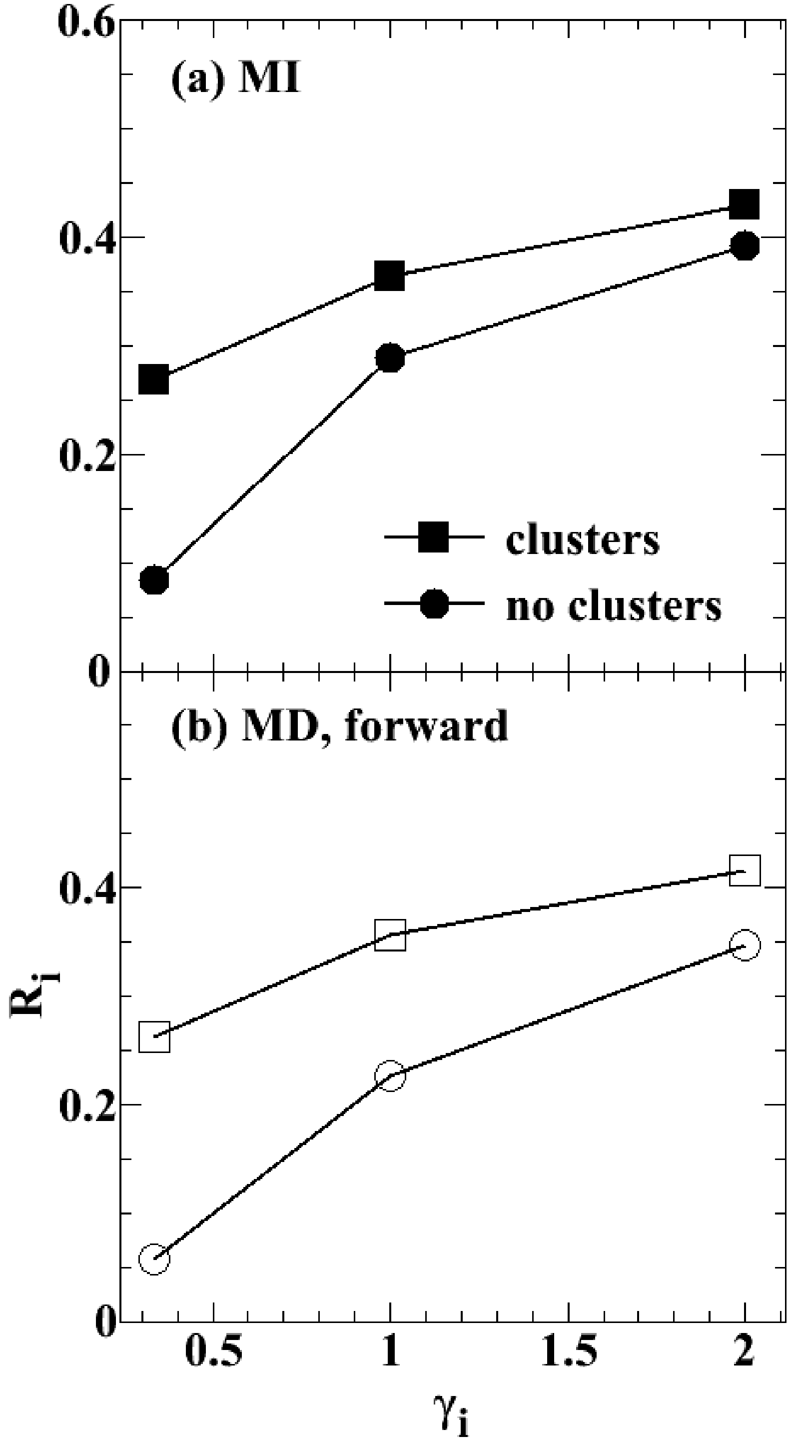

Figure 2.11: Effect of in-medium cluster production on isospin equilibration for a momentum independent mean field (a) and a momentum dependent mean field (b). Clustering greatly reduces the amount of diffusion, regardless of the EoS employed.

reported in ImQMD05. The effect of clustering is very similar to the effect of increasing the cross section in section 2.3.2. In fact, with this new collision channel open, more collisions occur. This reduces the influence of other effects. Comparing the two panels in Fig. 2.11, there is little difference between the momentum dependent and independent simulations, once clustering is included. Similarly, the differences between cross section parameterizations are reduced when clustering is included, compare Figs. 2.12 and 2.9. The difference between the residue and forward moving fragment tracers is also less with the inclusion of cluster production, and for the free and Rostock cross sections, it becomes a small, nearly constant offset in the value of the isospin transport ratio. Interestingly, the simple dependence on collisions number, that was lost when momentum dependence was included, has been restored.

However, the effect of including clustering goes well beyond the increased number of collisions. The extra kinetic energy released by the cluster formation causes the neck to fragment into many smaller pieces rather than a few large IMFs, as seen in the density plot at t=270 fm/c in Fig. 2.13. The fragmentation process also continues longer, as evidenced by the shape of the residues, which have not yet reached a spherical shape. Additionally, the whole neck region tends to expel its asymmetry with less dependence on γ_i, as shown in Fig. 2.14 (compare Fig. 2.10). This effect was predicted by Shi and Danielewicz [69]. They argued that the clusters modify the liquid-gas phase transition, forming droplets in the low-density gas phase and causing it to behave more like the liquid phase. This results in less isospin migration to the neck, and thus less diffusion taking place through the neck. Another result is that the IMFs are smaller and have asymmetries similar to the residue, and both these effects reduce the importance of including them in the isospin

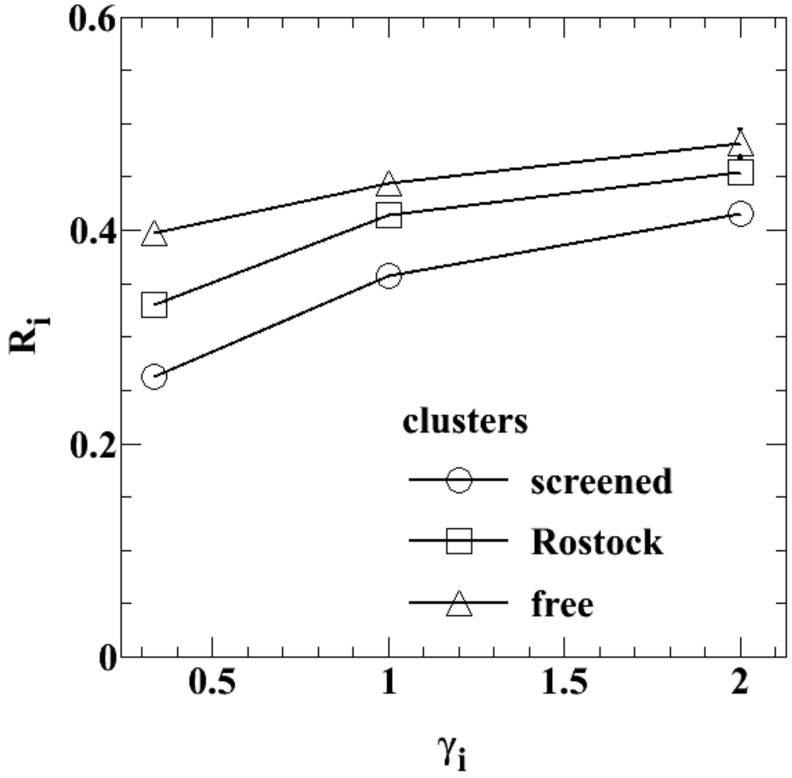

Figure 2.12: Effect of cluster production and of in-medium cross section reductions on isospin equilibration, when using a momentum dependent mean field. The strong influence of clustering on the isospin diffusion observable reduces the sensitivity to the cross section.

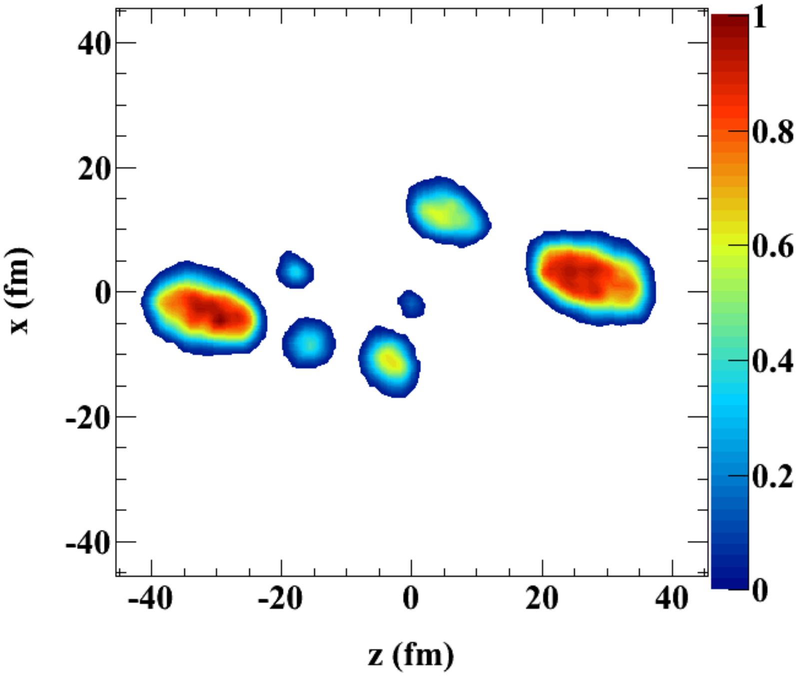

Figure 2.13: Density profile within the reaction plane at t=270fm/c, normalized to saturation density, when cluster production is incorporated and a momentum-dependent mean field is employed. This demonstrates that the breakup of the neck is much more violent when clustering is employed, due to the heating of the neck. This is part of the reason why clustering leads to reduced diffusion.

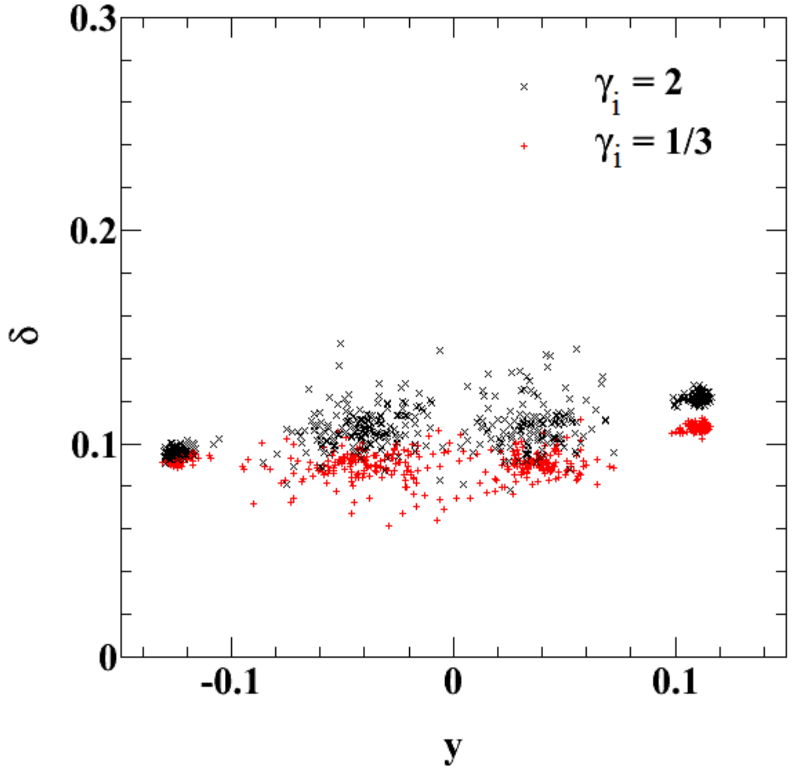

Figure 2.14: Distribution of fragments in isospin asymmetry and rapidity, when cluster production is incorporated and a momentum dependent mean field is employed, for two choices of symmetry energy. Compared to Figure 2.10, the asymmetry of the neck fragments is much less sensitive to the symmetry energy.

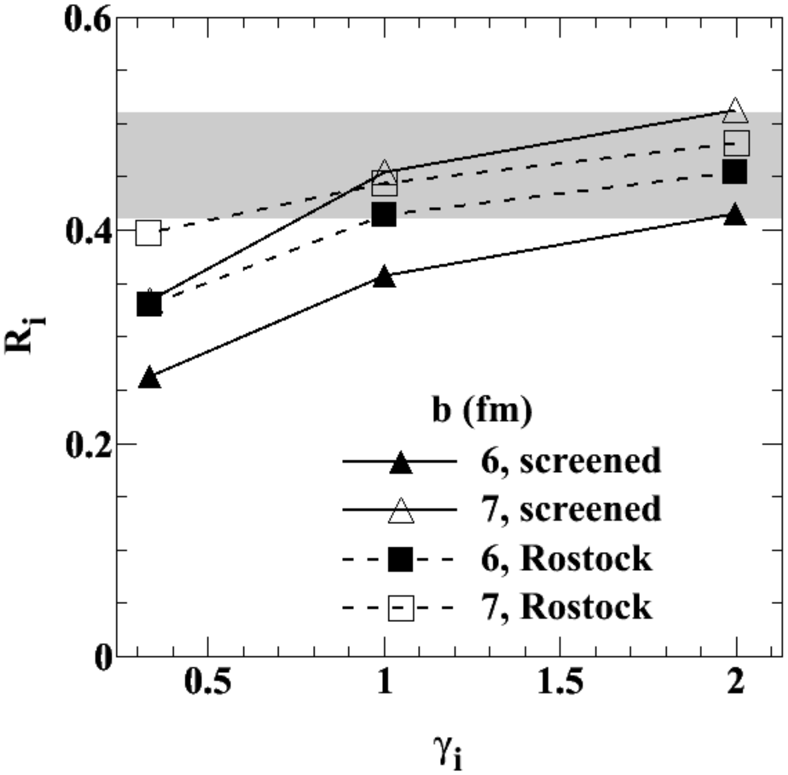

Figure 2.15: A comparison of isospin equilibration data to results of simulations that incorporate a MD mean field, cluster production, and one of two parameterizations of in-medium cross section reductions.

transport ratio. Note that the isospin distribution of the IMFs in Fig. 2.14 is similar to that in Fig. 2.10 for $\gamma_i = 1/3$, while the diffusion represented in Fig. 2.12 is more similar to that previously displayed for $\gamma_i = 2$. This indicates that the effect of clustering on isospin diffusion may be distinguished from the effect of the symmetry energy by examining both the IMFs and the projectile-like residues.

Finally, it is interesting to consider a comparison to data, with all the discussed effects included. Fig. 2.15 includes simulation results using a momentum dependent mean field, cluster production, and both cross section reductions, compared to the experimental data (shaded region) from Ref. [18]. The simulations are carried out at impact parameters of both 6fm (solid symbols) and 7fm (open symbols), to represent the uncertainty in the impact parameter in the data. The results compare well with the data, but unfortunately do not tightly constrain the density dependence of the symmetry energy, γ_i especially when the Rostock cross sections (squares) are used. This calls for further investigation into the uncertainties in the transport model. As presented here, many of those uncertainties affect the distribution of mass, isospin, and rapidity between IMFs and heavy residues, which can be experimentally measured. The decreased dependence on γ_i once all effects are included, as compared to previous BUU results, also argues for more precise experimental measurements. Isospin diffusion experiments were proposed at both the National Superconducting Cyclotron Laboratory and the Rare Isotope Beam Facility at RIKEN to measure the isospin signals from both IMFs and heavy residues with high precision. The experiment at the NSCL was recently completed, but no results are yet available from this experiment. The RIKEN experiment is expected to run in the summer of 2013.

Chapter 3

Experimental Details

As discussed in the Chapter 1, the goal of this experiment was to measure the transverse emission of protons and neutrons from neutron-rich heavy ion collisions and compare them to the emission of the same from symmetric collisions. We chose to use collisions of ^{124}Sn on ^{124}Sn for the neutron rich system and collisions of ^{112}Sn on ^{112}Sn for the symmetric system. These are the most neutron-rich and neutron-poor stable isotopes of Sn. While isospin-dependent effects would be larger for more neutron-rich unstable isotopes, only stable beams were available at MSU with sufficiently high rates for this experiment. For each system, we used both 50 AMeV and 120 AMeV beams to determine the energy dependence of the spectra, which should constrain both the symmetry energy and the isovector nucleon effective mass. The beams were produced at the NSCL Coupled Cyclotron Facility at Michigan State University and transported to an experimental setup in the S2 vault. The collisions occurred on approximately 5 mg/cm^2 Sn targets with approximate dimensions of 2cm x 2cm. The exact target thicknesses are given in Table 3.1. The target ladder was situated at the center of a 52 inch diameter round vacuum chamber.

Target	Thickness (mg/cm^2)
^{112}Sn	5.57
^{124}Sn	5.30

Table 3.1: Thicknesses of targets used in the experiment.

The chamber was large enough to house the MSU Miniball plus other necessary charged particle detectors, and the aluminum walls were thin enough to minimize the possibility of neutron reactions on the way to the external neutron detectors. In addition to the reactions of interest for the measurement, ^{16}O beams with energies of 16.8 AMeV and 29.4 AMeV were impinged on CH_2 targets to provide energy calibrations for the charged particle detectors.

The transverse emission of protons and neutrons from central heavy-ion collisions were measured simultaneously during the experiment. Most of the measurements required specialized detectors. In particular, we detected protons and other light charged particles with the Large Area Silicon Strip Array (LASSA). We measured neutron spectra with the Large Area Neutron Area (LANA), also known as the Neutron Walls (NW). The NW are also sensitive to charged particles and gamma rays in addition to neutrons. While gammas have a distinct signature in the walls and can be distinguished from neutrons, charged particles do not. To identify and remove the charged particles from the neutron spectra, we placed an array of thin plastic scintillators between the reaction target and the neutron walls. We referred to this array as the Proton Vetoes (PV). Because neutron energy is determined by time of flight (TOF), we placed an additional array of thin plastic scintillators just downstream of the reaction target to provide a start time. Due to its location, we called this the Forward Array (FA). The final piece of event-by-event

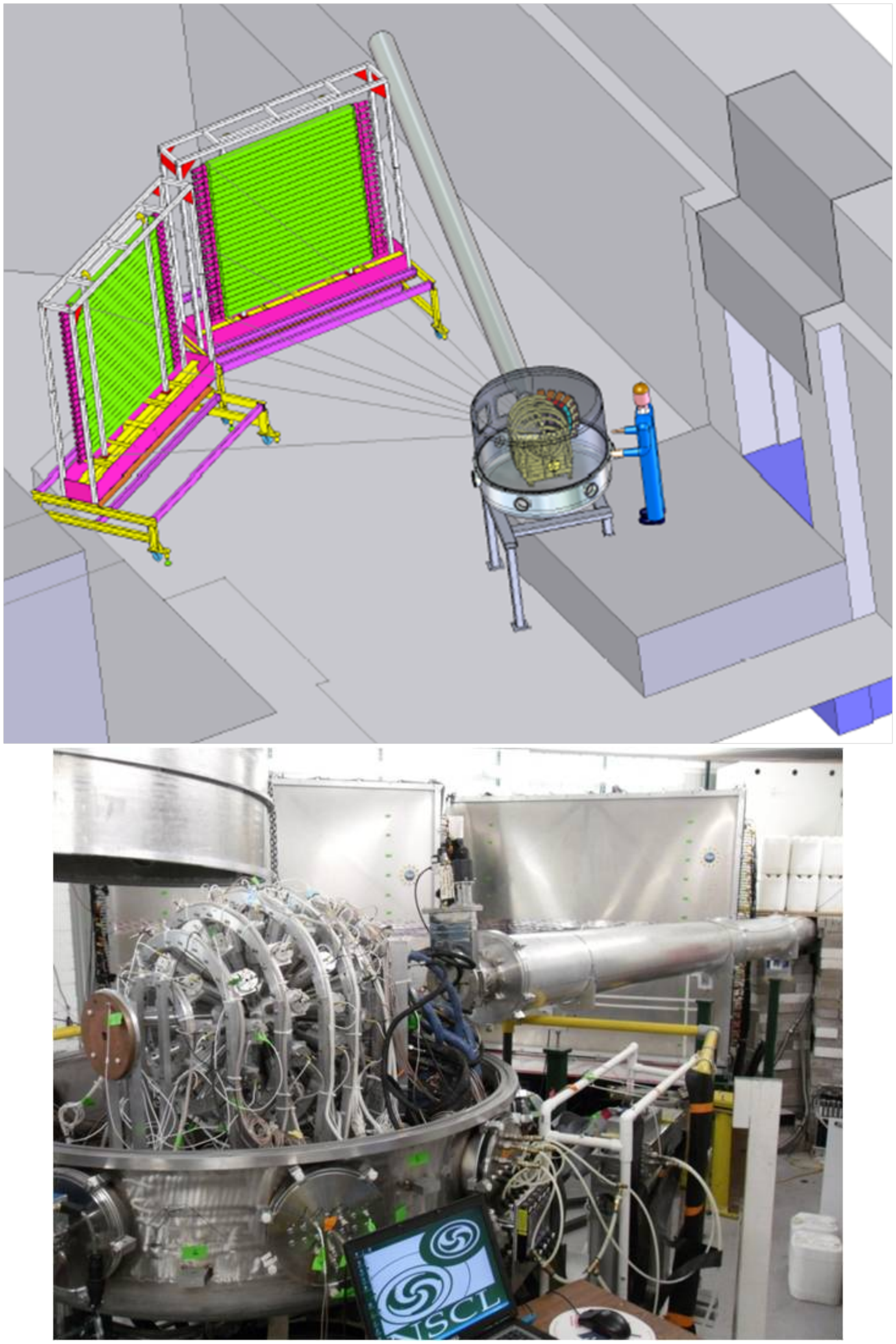

Figure 3.1: Layout of the full experimental setup in the vault. The beamline leads to a downstream beam dump that is not shown in the figure. The most prominent detectors are the two neutron walls, which are five and six meters away from the target to the left of the beamline, and the MSU Miniball array that occupies the majority of the reaction chamber. Smaller detectors are mostly obscured in this image. During experimental operation, the reaction chamber is closed and at vacuum.

information required for this experiment was the reaction impact parameter, which we determined from the multiplicity of charged particles in a 4π charged particle detector, the MSU Miniball (MB). A fast scintillator was placed downstream of the reaction target during a few calibration runs, and provided a beam rate measurement need for an absolute cross section determination. This Downstream Scintillator (DS) was retracted and not used during normal data taking.

Each detector required its own set of electronics to digitize and store the electronic signals it generated, but the whole system had to communicate for a coordinated readout. To allow fast self-triggering for some subsystems and to facilitate easier operation and debugging, we adopted a modular approach to the electronics. We kept the subsystems for the different detectors as separate and self-contained as possible, communicating only through a master logic circuit and a few reference times. Each subsystem generated its own digitization gates, delays, busy signals, submaster triggers, and, if necessary, fast clears. The subsystems passed their submaster triggers and busies to the master logic, which returned a master trigger and global busy to each subsystem, and triggered the computer to read out the event.

In the next several sections, I will discuss the design and operation of the detectors and their associated electronic subsystems in more detail. I end the chapter with a description of the master trigger logic.

3.1 Miniball

The MSU Miniball [70] is a granular charged particle detector with large solid angle coverage. In its full configuration, it consists of 188 CsI(Tl) phoswich detectors covering

89% of 4π. The individual phoswich detectors are arranged into eleven rings, each of which spans the azimuthal direction at a different polar angle with respect to the beam axis. The polar angles and number of detectors in each ring are shown in Fig. 3.2. In the current experiment, we removed many of the forward detectors to make room for LASSA and the forward array, and to reduce the material between the target and the neutron walls. The number of detectors remaining in each ring are shown in Table 3.2.

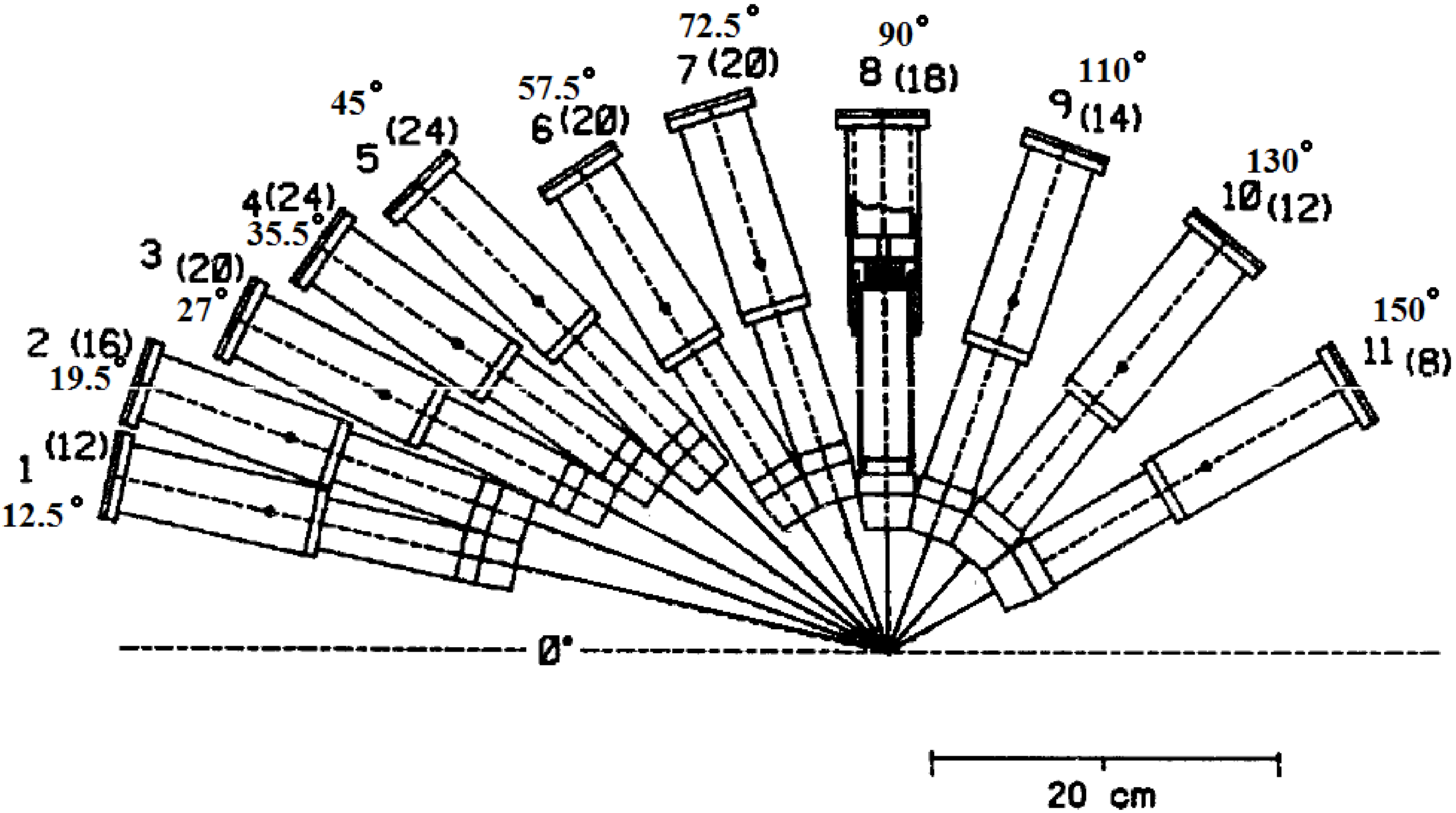

Figure 3.2: The polar angle and number of detectors in each Miniball ring in the full Miniball setup. The polar angles are in the laboratory frame.

Ring	$\theta(^\circ)$	$\Delta\theta(^\circ)$	Detectors used/total
5	45	10	15 / 24
6	57.5	15	14 / 20
7	72.5	15	19 / 20
8	90	20	16 / 18
9	110	20	13 / 14
10	130	20	11 / 12
11	150	20	8 / 8

Table 3.2: Detectors used in the Miniball setup for this experiment, by ring. The forward rings and parts of the intermediate rings were removed to make space for other detectors.

The individual phoswich detectors, as shown in Figure 3.3 are composed of a thin (usually 40 μm) plastic scintillator spun from Bicron BC-498X scintillator solution backed by a 2 cm CsI(Tl) scintillator crystal. The CsI crystal is attached, via two pieces of UVT Plexiglas, to a Burle Industries model C83062E photomultiplier tube (PMT). This arrangement leads to a single electronic signal from the detector that contains three distinct time components: one from the thin scintillator characterized by a 2.4 ns decay time, and two from the CsI crystal with decay times in the hundreds of ns and few μs, respectively. These different time components are exploited for particle identification. The thin scintillator is covered by an aluminized mylar foil, which in turn is covered by a 5 mg/cm^2 Sn-Pb foil that suppresses hits from electrons.

The electronic signal from the PMT was further amplified for the detectors from the backward rings, and then passively split using custom Miniball splitters to pick out the different time components of the signal, called fast, slow, and tail as shown in Figure 3.4. The integration times for these different components are 30 ns, 400 ns, and 1.5 μs, respectively (see Figure 3.5), so the split fraction is lopsided to provide a similar integrated charge for each signal: 92% for the fast signal, 4% for the slow, and 4% for the tail.

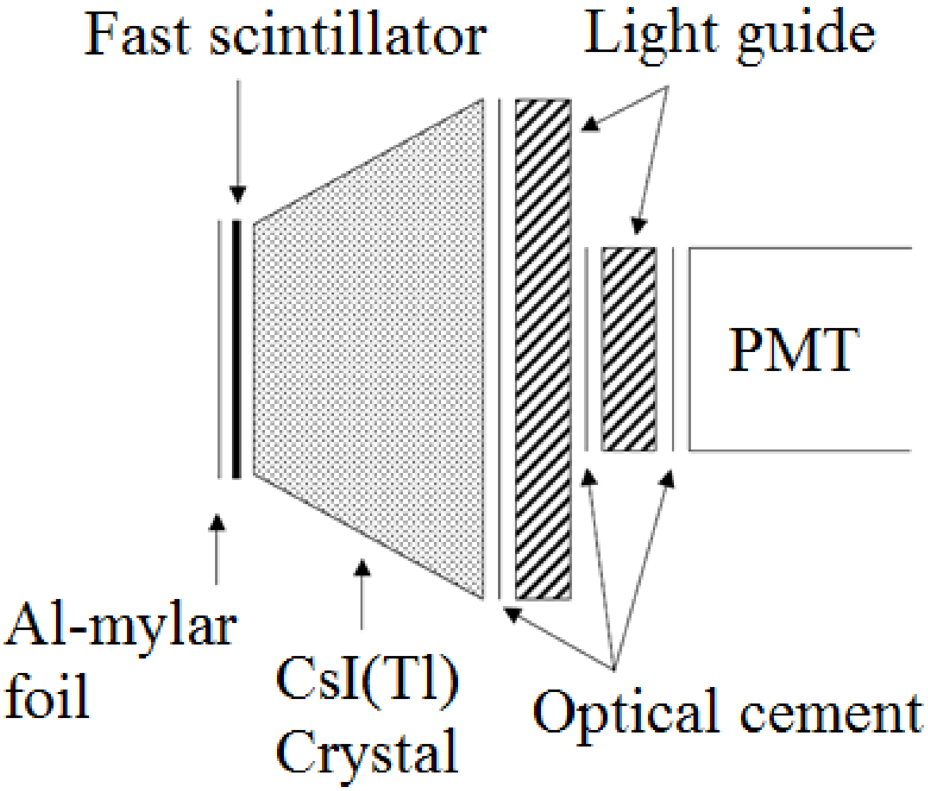

Figure 3.3: Diagram of an individual Miniball phoswich detector. The thin fast scintillator backed by a thick CsI crystal allows particle identification through pulse shape discrimination.

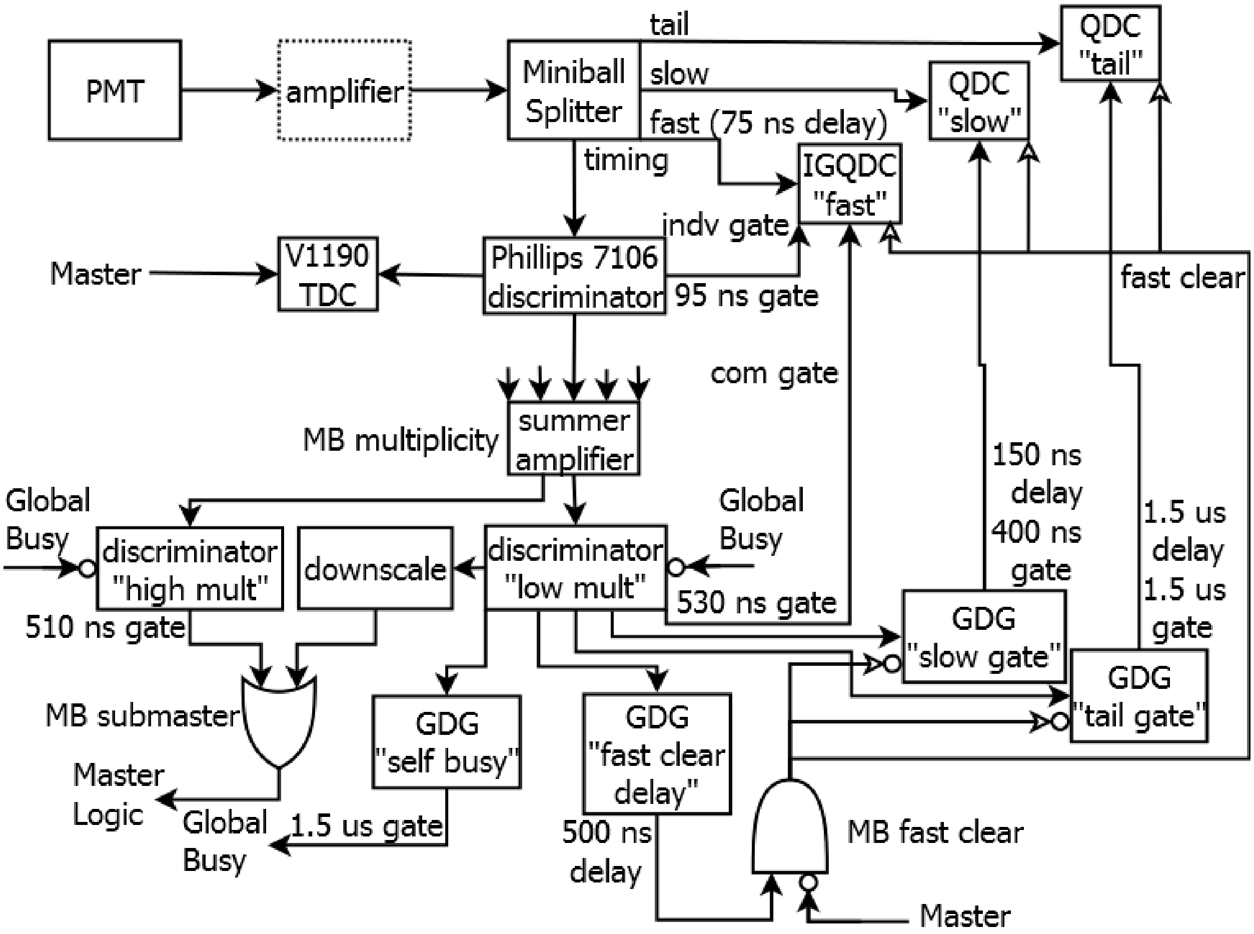

Figure 3.4: The Miniball electronics subsystem. The start of the ”fast” integration is determined by the common gate on the QDC, while the stop is determined by the individual channel gates. Arrows with open heads are used to distinguish the fast clear signal from other signals.

An additional amplified output is sent to a modified Phillips 7106 discriminator, which provides time information and forms the basis of the Miniball logic. The discriminator was modified to prevent retriggering earlier than 1.5 μs. The timing requirements of the PSD meant that the Miniball subsystem had to be triggered before the master logic could produce a trigger. To account for this the subsystem triggered itself, and if no master trigger was received within 500 ns it produced its own fast clear to abort digitization and prematurely close the QDC integration gates. A Miniball-busy gate was sent to the global busy and fanned out to all subsystems to prevent triggering on another event during this fast clear window. This gate is 1.5 μs long to include not just the 500 ns fast clear decision but also the QDC internal busy from the fast clear.

Because we are interested in central collisions with corresponding high charged particle multiplicity in the Miniball, the Miniball submaster is triggered only by high multiplicity events. This was achieved by adding the SUM outputs from the all the discriminators using a summer/amplifier module, which produced a 50 mV/hit signal. This signal was sent to discriminators which determined if the multiplicity was large enough to be interesting. The statistics were limited by data rate rather than beam rate, so we adopted a setup using two discriminators to increase statistics for the highest multiplicity events while still taking some data for events with moderate multiplicity. Both discriminators were blocked by the global busy to prevent triggering while the system was busy. The low multiplicity trigger was downscaled and ORed with the high multiplicity trigger to create the Miniball submaster trigger, which was sent to the global trigger logic. The fast QDC needed to be triggered prior to the creation of the Miniball submaster to provide good PSD, so the QDCs were triggered by the low multiplicity trigger rather than the

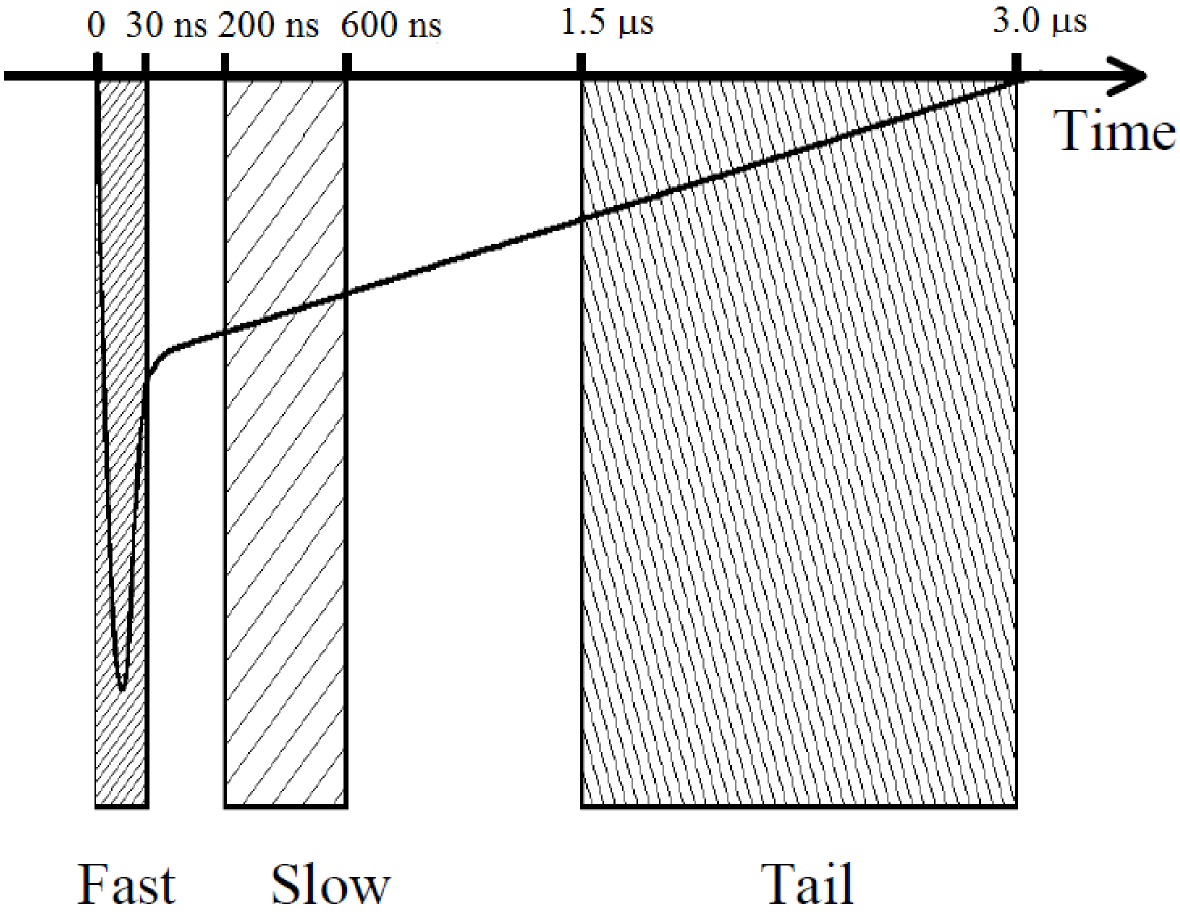

Figure 3.5: Timing of Miniball integration gates compared to PMT signal. Comparison of the charge collected in the three integration gates can identify the incident charged particle. Adapted from [1].

submaster.

3.2 Neutron Walls

The Neutron Wall Array [71] is a time of flight (TOF) detector for intermediate energy neutrons. Neutrons with kinetic energies in the tens or hundreds of MeV have a low likelihood of interacting with matter. When a neutron in this energy range interacts with a detector at all, it collides with a nucleus in the detector material and transfers some fraction of its kinetic energy to that nucleus. If the collision is elastic, the recoiling nucleus deposits its energy in the detector, and if that detector is a scintillator, some of that energy is converted into light and detected. If the collision is a more complicated reaction, then other particles, such as α particles, are emitted and produce light in the scintillator. Because the neutron does not transfer a fixed fraction of its kinetic energy to the recoil nucleus, neutron energy must be determined by TOF rather than pulse height.

Pulse height is still important, however, because it needs to be large enough to be detected. Simple two body kinematics gives the maximum energy the neutron can transfer to the recoil nucleus as

$$E_{R,max} = \frac{4A}{(1+A)^2} E_n \tag{3.1}$$

which indicates that detectors composed mostly of Hydrogen are preferable. This is true for a second reason as well: heavier elements of a given kinetic energy produce less light in a scintillator than light elements of the same kinetic energy.

Energy resolution in a TOF detector is determined by the magnitude of the TOF and the time resolution. Non-relativistically, this takes the form

$$E = \frac{1}{2}m\left(\frac{d}{TOF}\right)^2$$

$$\frac{\delta E}{E} = 2\frac{\delta TOF}{TOF}$$

$$\delta E = md^2\frac{\delta TOF}{TOF^3}$$

Detection efficiency is determined by the areal density of nuclei in the detector and the solid angle coverage. A thick detector sacrifices time resolution for efficiency, and a distant detector sacrifices coverage for energy resolution. The dimensions of a detector have to find a balance between these effects. While the above equations are not strictly accurate for the energies considered in this experiment, the considerations are the same.

The NW Array consists of two walls, each with an area of 2x2 m^2 divided into 25 horizontal detector bars. A cut-away of one wall is shown in Figure 3.6, and a single cell is shown in Figure 3.7. The detector bars consist of 2 m long Pyrex shells which contain the liquid organic scintillator NE-213. In each bar, the scintillator is 7.62 cm tall and the Pyrex shell is 3 mm thick. Space was left between the bars to account for the stainless-steel bands used to attach the bars to the wall frame and variations in the Pyrex. The result is a 8.6 cm bar spacing, corresponding to 11% inactive area. A Phillips Photonics model XP4312B/04 PMT is affixed to each end of the bar to detect the scintillated light.

The time of an event is determined by the average of the times from the two PMTs, and the position is determined by the difference in PMT times. The nominal time resolution is 1 ns, and with a nominal 7.65 cm/ns position calibration, this leads to a horizontal position resolution similar to the vertical resolution determined by the bar height. The light output

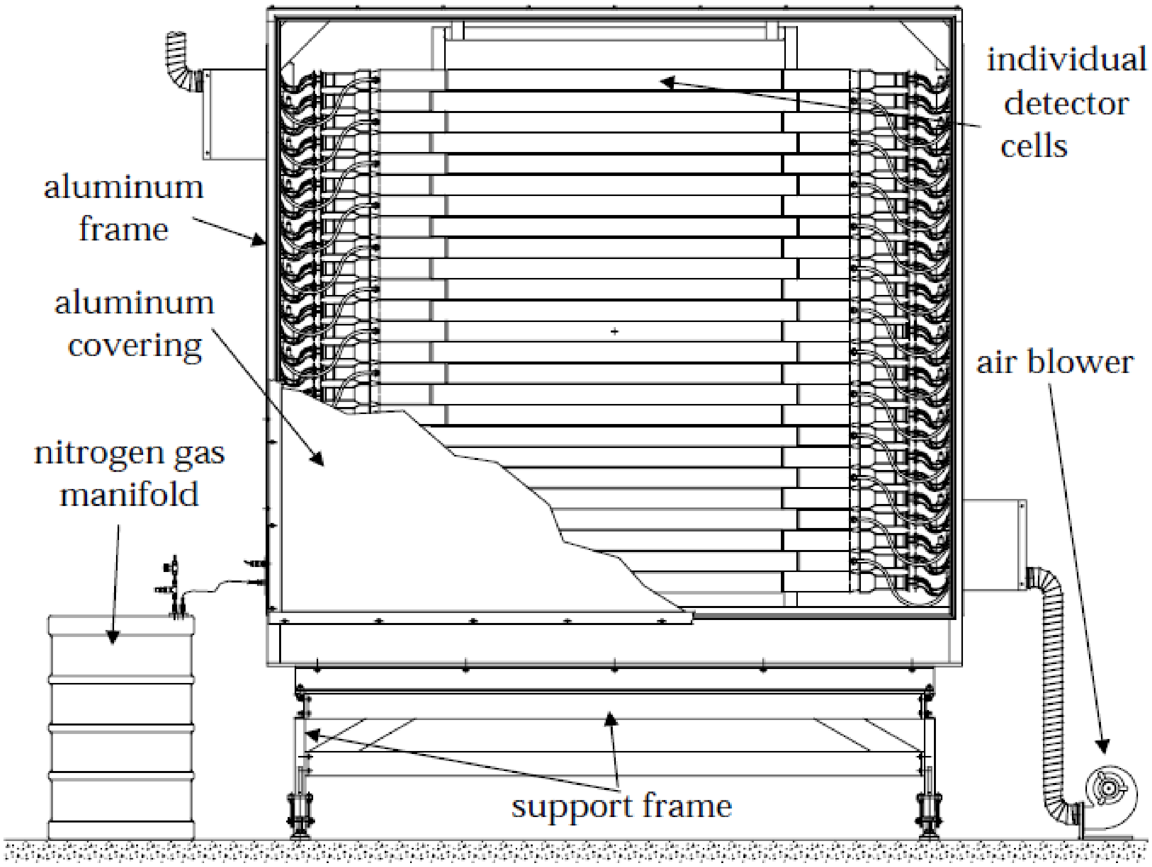

Figure 3.6: Cut-away of one neutron wall [2].

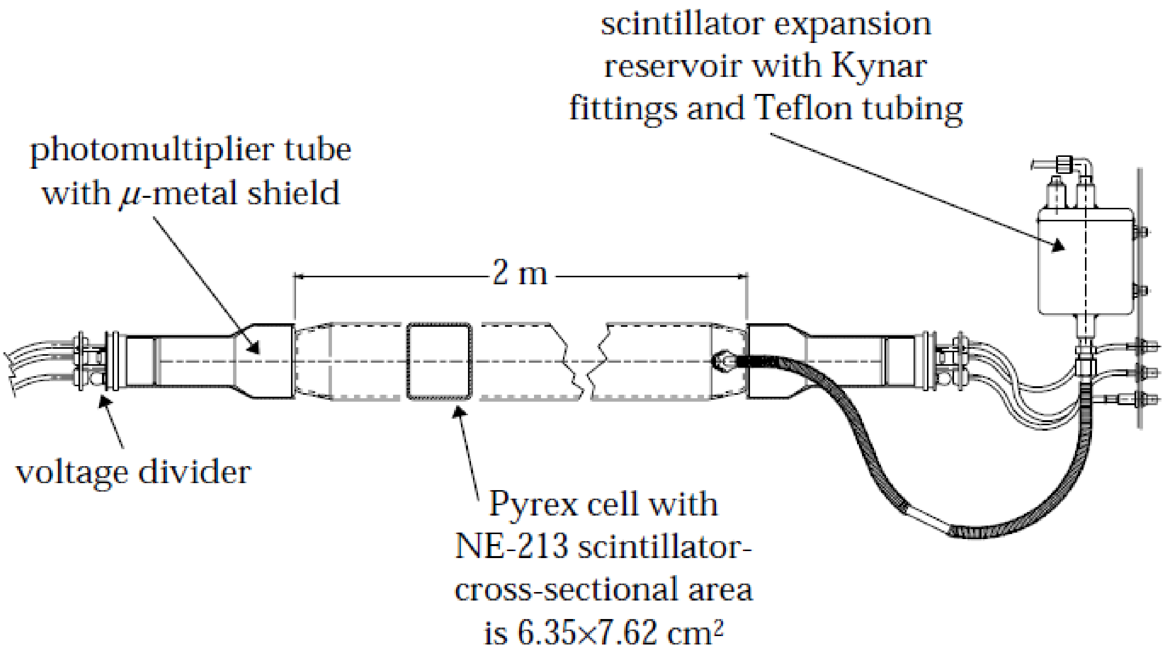

Figure 3.7: Diagram of one of the detector bars in the Neutron Walls [2].

is measured using the geometric mean of the integrated signal from the two PMTs. The two walls were placed 6 m and 5 m away from the target with the more distant wall closer to the beamline as shown in Figure 3.1, leading to the angular coverage shown in Figure 3.8. Only 24 bars in each wall are used, due to the number of available electronics channels.

The Neutron Walls cannot measure the incident angle of the detected neutrons, so neutrons that scatter off material in the vault and reach the walls via an indirect path contribute a background to the measurement. To determine that scattered background, 30 cm thick brass shadowbars were placed midway between the target and Neutron Walls to prevent neutrons from taking a direct path to reach the walls, leaving only the scattered background in the shadowed region. The shadowbars were moved to shadow different locations on the walls over the course of each beam-target combination, providing a map of the background over the surface of the detector. A shadowbar is shown in Figure 3.9, and several shadowbars are shown in location in Figure 3.10.

Like any organic scintillator, NE-213 has a high concentration of protons, in this case 4.82x10^{22} per cubic cm [72], making it useful as a proton recoil neutron detector. The distinguishing feature of NE-213, however, is the ability to distinguish neutrons from gammas using PSD. This arises from two contributions to the scintillation light spectrum with very different decay times. The fast contribution proceeds via prompt fluorescence from the S_{10} excited singlet state [73] and has a characteristic time of 32.3 ns [72]. The slow component arises from phosphorescence from the T_{10} triplet state, which has the much longer lifetime of 270 ns.

The light output from highly ionizing particles is always quenched relative to lightly

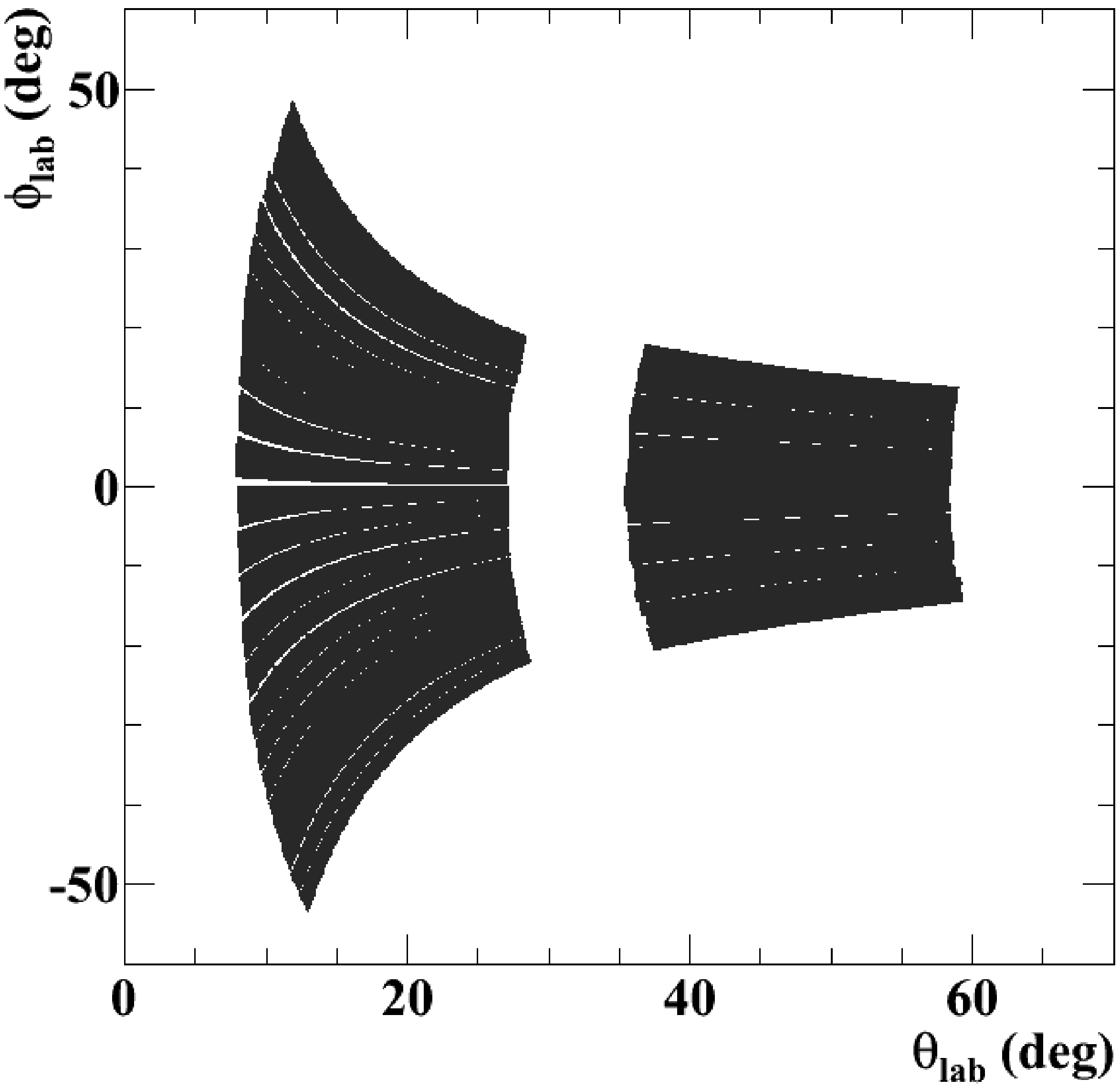

Figure 3.8: Angular coverage of the Neutron Wall array in the lab frame. Note that only 24 bars are used in each wall. The separation between the two walls and between wall elements is visible.

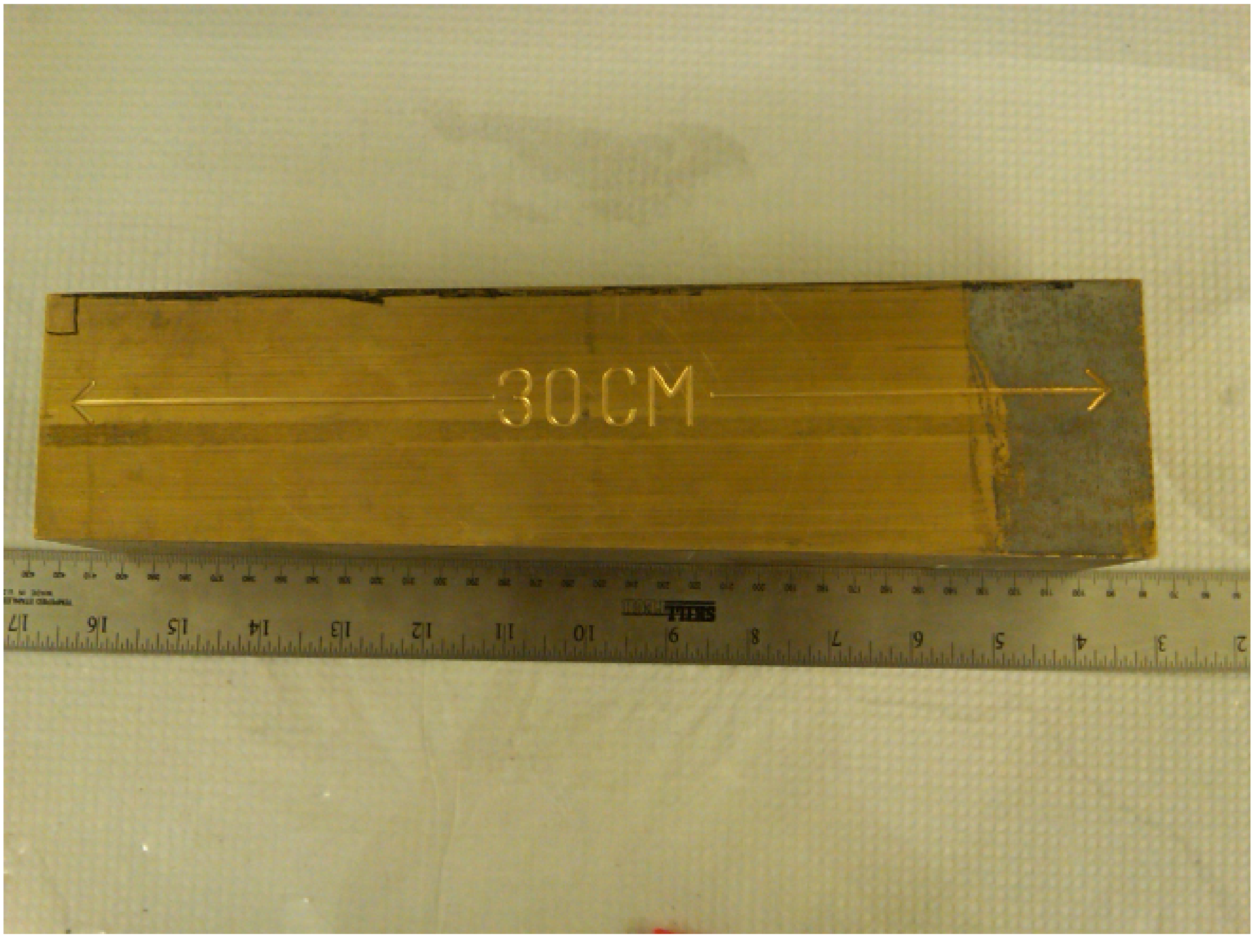

Figure 3.9: One brass shadowbar. The shadowbar is thick enough to stop neutrons that take a direct path to the Neutron Walls, which provides a measurement of the scattering background.

Figure 3.10: Four shadowbars in one of the configurations used in the experiment.

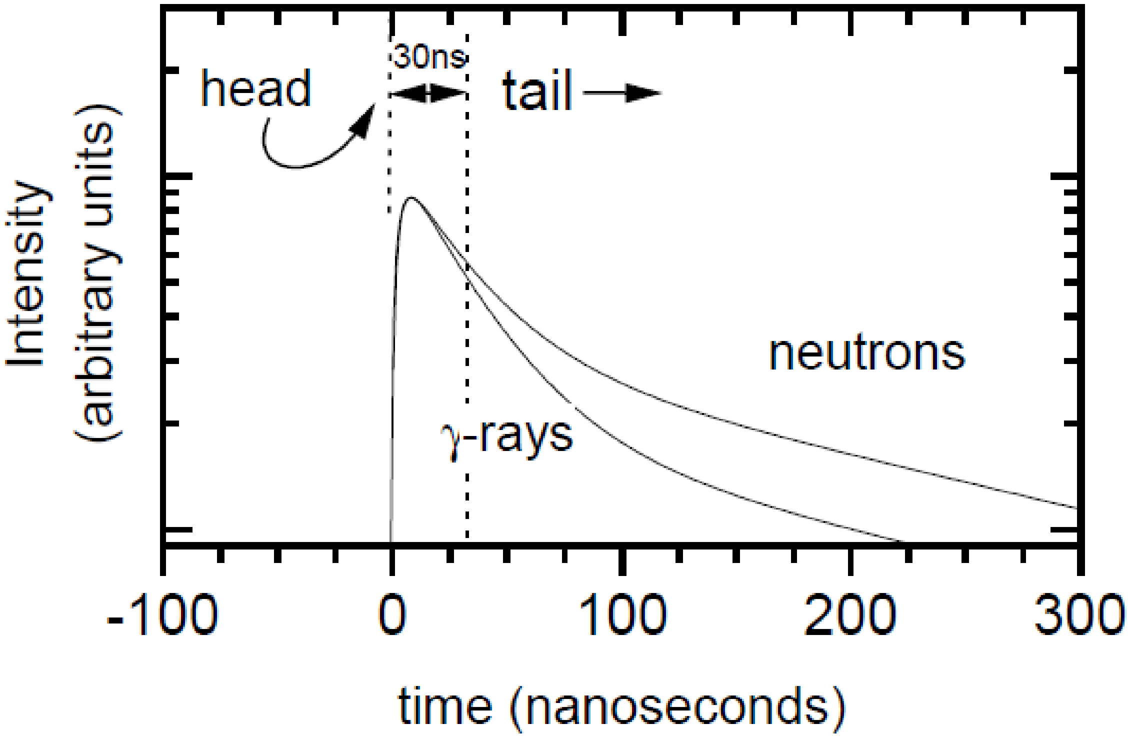

Figure 3.11: Schematic of different pulse shapes for γ-rays and neutrons in NE-213, where the peak heights are normalized to be the same [2]. Like the Miniball, the readout of the Neutron Walls exploits this pulse shape difference to identify the source of the signal.

ionizing particles such as electrons, but the quenching is weaker in the slow component. Thus when the peak height of the pulse is the same, a signal arising from a neutron scattering off a proton will have a larger tail component than a signal arising from a gamma scattering off an electron, as depicted in Figure 3.11. In our setup, PSD was accomplished by comparing the integral of the first 30 ns of the signal to the total integral. The result for an AmBe source, shown in Figure 3.12, clearly distinguishes between neutrons and gammas. One should note, however, that many of the energetic pulses in the AmBe spectrum originated from cosmic ray muons. These have the same pulse shape characteristics as the gammas and appear in the gamma-ray PSD line.

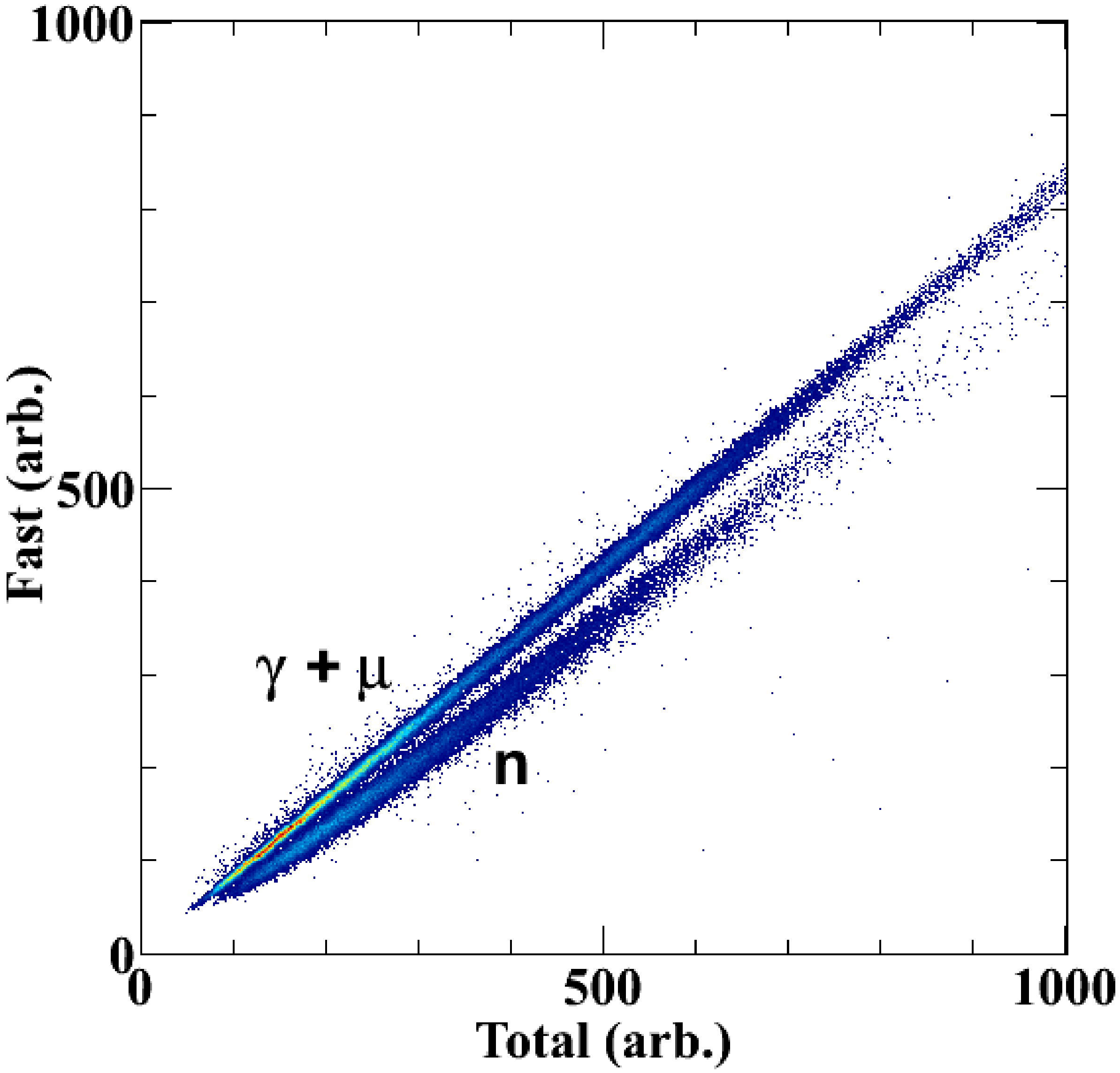

Figure 3.12: Example pulse shape discrimination from an AmBe source. The two lines are derived from the different pulse shapes produced by incident gammas and neutrons in the detector, as indicated in Figure 3.11.

To accomplish the PSD, the PMT anode signal was resistively split as shown in Figure 3.13. The total signal was integrated in a QDC with a 340 ns wide gate common to all channels on the QDC, while individually-gated QDCs (IGQDC) were used to capture the fast signal. This is similar to the Miniball subsystem. The PMT dynode signal was used in a CFD to acquire times and to start the subsystem logic. Individual discriminator signals were reshaped to provide constant-width 60 ns gates for the IGQDCs, while all channels associated with a given QDC were ORed to start the common gate. The common gates were vetoed both by the local self veto to prevent refiring and by the global busy to keep the Neutron Wall subsystem inactive when another subsystem or the data acquisition computer were busy. The OR of the three common gates was the Neutron Wall submaster. As in the Miniball subsystem, the Neutron Wall QDCs needed to start integration before the master signal could be received, so the submaster started a fast clear circuit that was cancelled if a master trigger arrived. The CAEN V1190 TDC stores hits in buffer and can read out events that were stored prior to the trigger, so it was not necessary to connect it to the fast clear circuit.

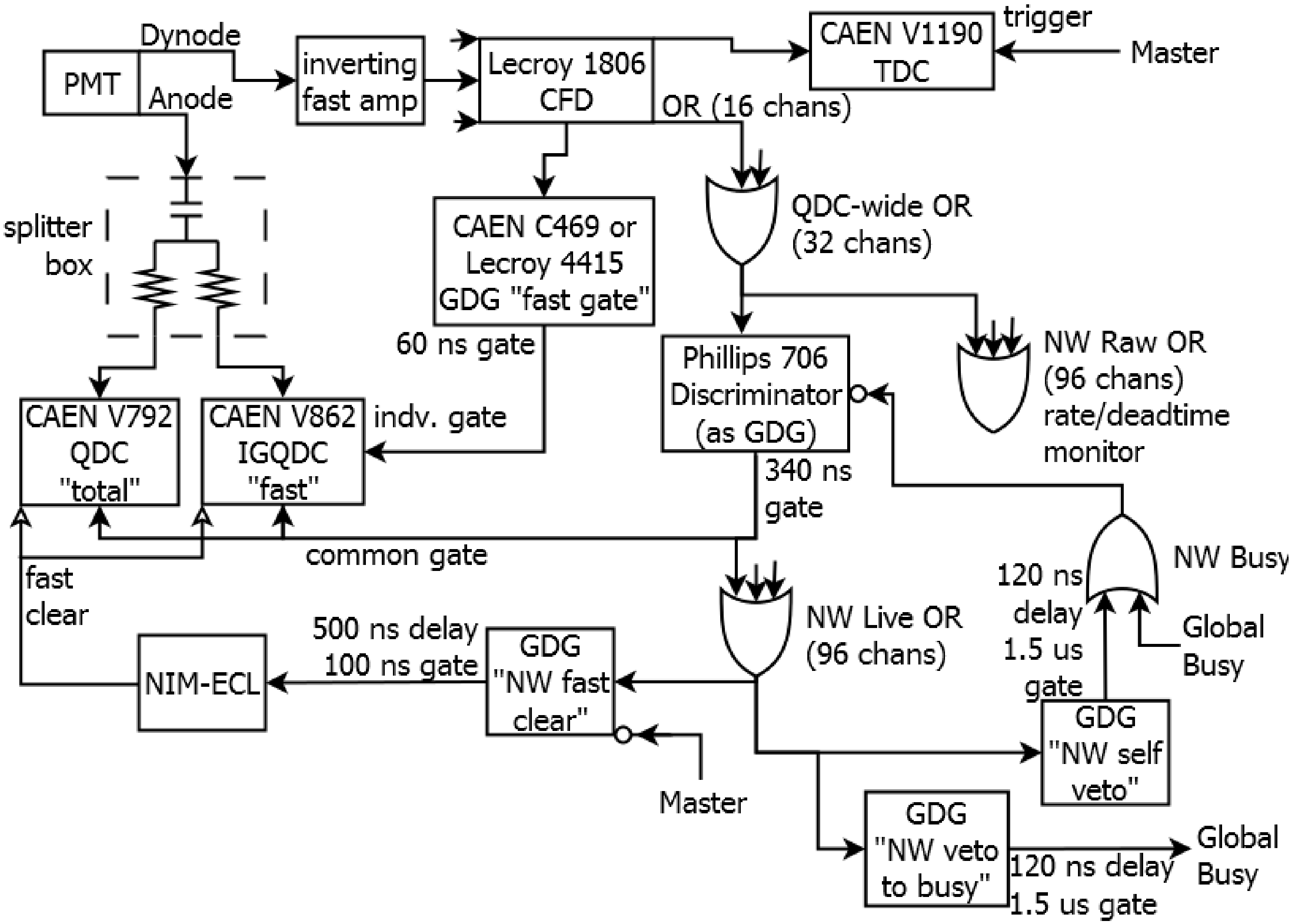

Figure 3.13: The Neutron Wall Array electronics subsystem.

3.3 LASSA

LASSA is a charged particle detector that was designed to deliver good energy resolution, good angular resolution, and isotopic resolution for elements ranging from Hydrogen through Oxygen [74]. The array is divided into telescopes, each containing a 500 µm double-sided silicon strip detector (DSSD) backed by four tapered 6 cm thick CsI(Tl) crystals, all housed in an trapezoidal aluminum casing. In previous measurements of low energy particles, a 65 µm single-sided silicon strip detector was placed in front of the DSSD, but that was not used in this setup.

For this experiment, the full array consisted of six telescopes that sampled polar angles from 16° to 58°, a similar range as the neutron walls but on the opposite side of the beam axis. The setup is shown in Figure 3.14. The front of each telescope was covered with aluminized mylar foil and 15 µm of SnPb foil to make a Faraday cage and protect against low energy electrons coming from the target.

As shown schematically in Figure 3.15, the front and back segmentation of the DSSD allow the hit position to be localized to one pixel. The strip pitch of the DSSD is 3 mm, and the interstrip SiO_2 isolation is 100 µm wide, leading to approximately 0.9° angular resolution at the design distance of 20 cm. In addition, multiple particle readout is possible within one telescope due to the segmentation of the CsI, which is important when the reaction multiplicity is high. For the particles of interest, the correlation between the energy loss in the thin DSSD and the total energy deposited in the CsI uniquely determines the particle type. An example particle identification (PID) is shown in Figure 3.16. This technique works as long as the particle stops in the CsI, which limits the detected proton energy to 147 MeV.

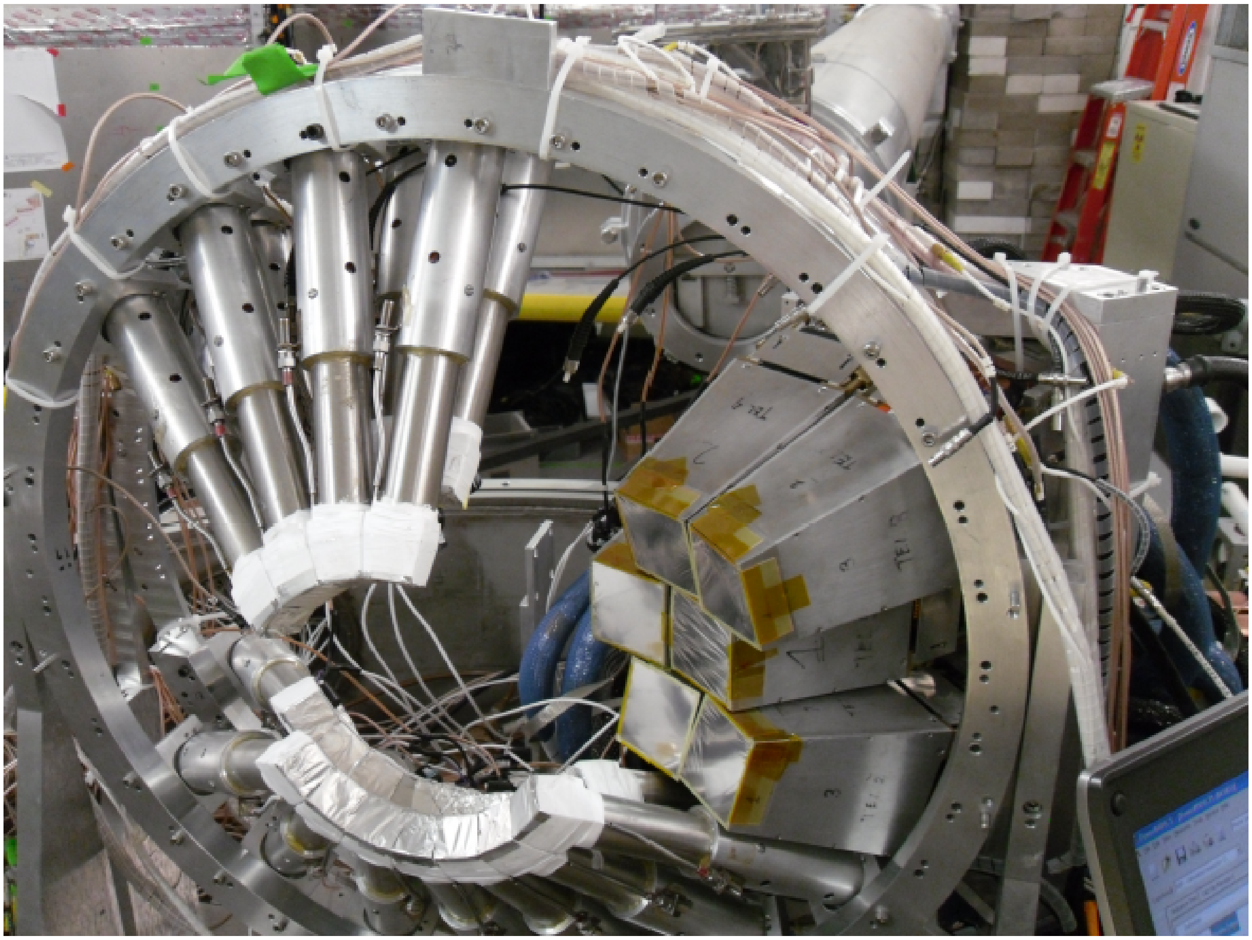

Figure 3.14: A photo of the six LASSA telescopes (center-right) and several Miniball telescopes. LASSA is used to detect the protons and light charged particles for this analysis.

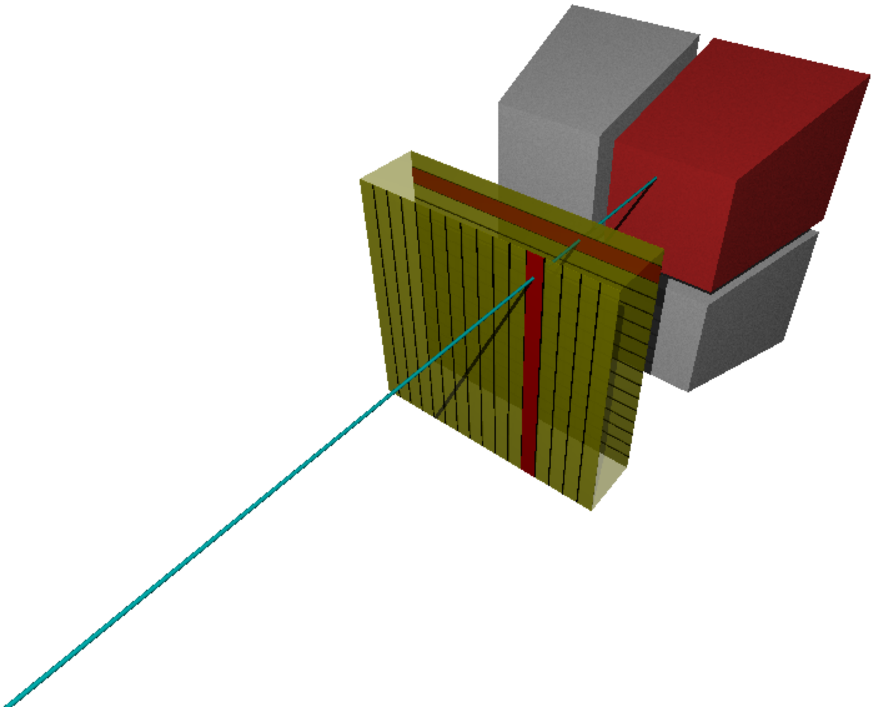

Figure 3.15: A schematic of the detectors in a LASSA telescope, showing how front and back strips are used to determine a hit location. Not to scale.

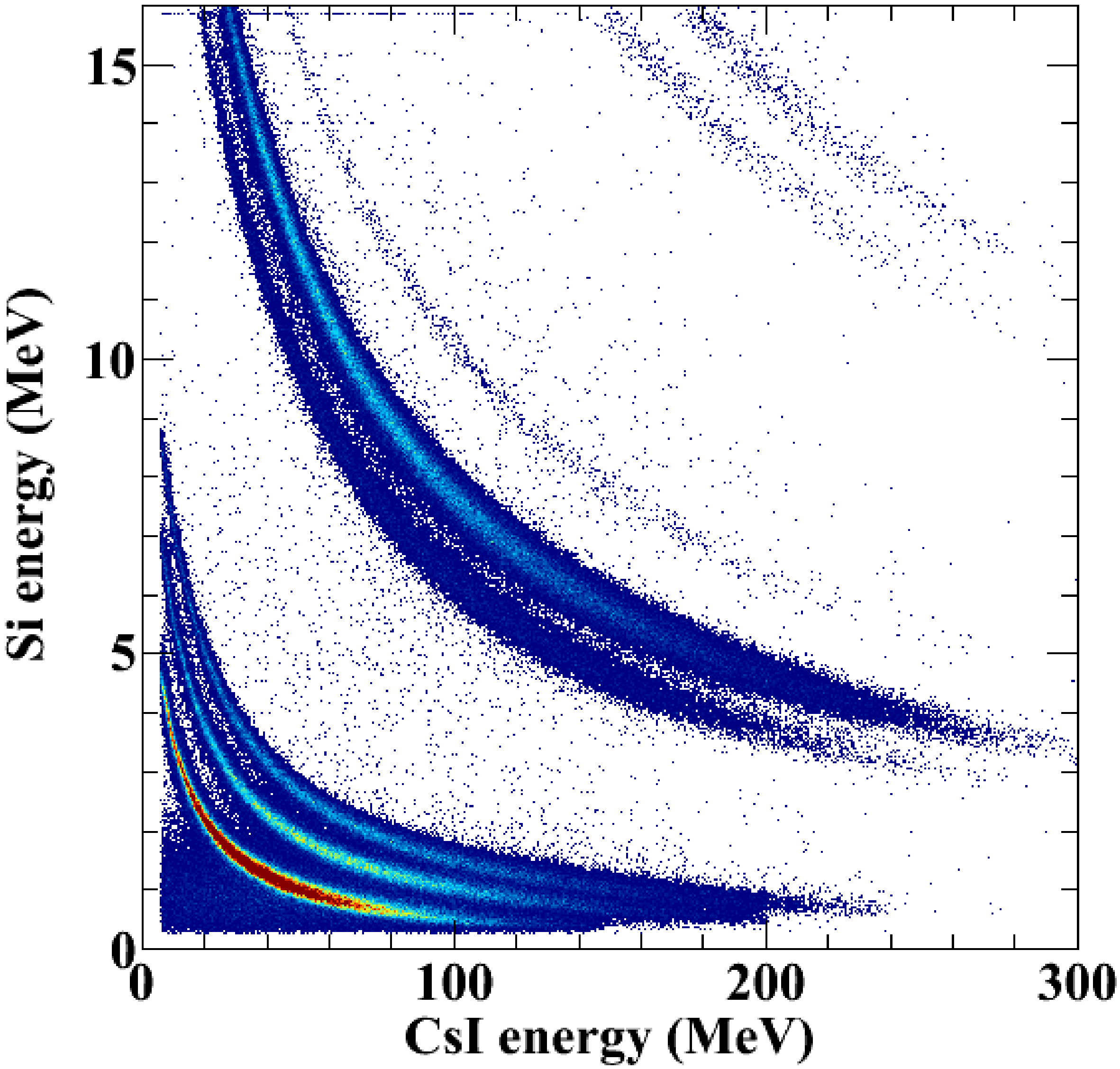

Figure 3.16: Particle identification in LASSA using the ΔE-E technique. From bottom left, bands are proton, deuteron, and triton, followed by Helium isotopes.

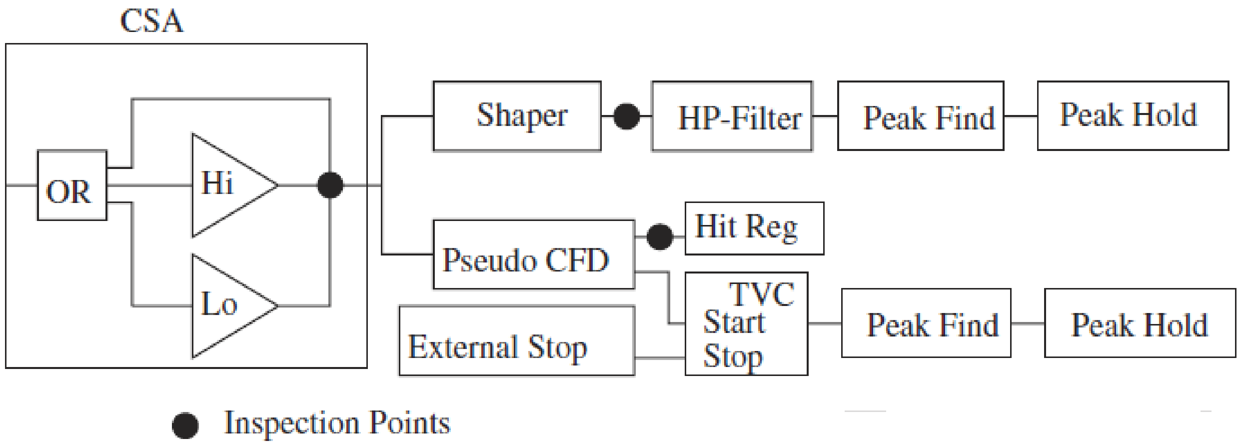

Figure 3.17: A diagram of one channel on the HiRA ASIC [3].

The DSSD and CsI are read out using separate electronic subsystems. The Si subsystem is unique in this setup in that it uses an application specific integrated circuit (ASIC) rather than conventional nuclear electronics. The HINP16C chip [75] that forms the basis of this system was developed to read out the Si in HiRA [3], another array of Si and CsI telescopes. The electronic processing on each channel is actually quite similar to that discussed in the other subsystems in this experiment, as shown Figure 3.17.

First, the incoming signal is passed through a charge sensitive amplifier (CSA), of which two internal options are available. In this setup, we instead chose to use external pre-amplifiers to maximize the gain. The signal is then split, with one path going to a Nowlin pseudo constant fraction discriminator (CFD) to determine if a hit has occurred, and then on to a time-to-voltage converter (TVC). The other path goes to a shaper with a shaping time around 1 µs. The time and energy are then stored for readout. If a trigger is not received within the allotted time, the stored values are cleared. This is similar to the fast clear circuits in the Neutron Wall and Miniball subsystems, except it operates for each individual channel separately. The major virtues of this system as compared to a

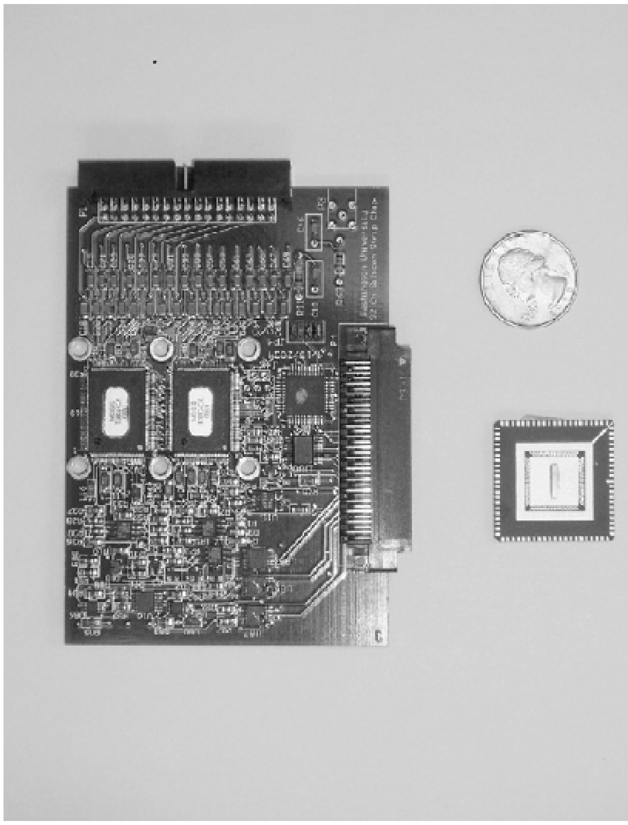

Figure 3.18: Image of a HiRA chipboard with a US quarter for reference. A prototype chip is also shown. The two chips on the chipboard each contain sixteen channels of the circuit shown in Figure 3.17.

conventional electronics system are the size and cost. This system can be produced for about $50 per channel. Conventional electronics cost about a factor of ten more. Each chip processes sixteen signal channels, and two chips fit on a small chipboard as shown in Figure 3.18, minimizing the ”foot print” of the electronics. Another major advantage is the ability to remotely monitor the signals and change settings channel by channel, as partially indicated by the inspection points in the block diagram in Figure 3.17.

In addition to the ASIC chips, the chipboards contain resistors and decoupling capacitors to pass the bias voltage to the Si, and a complex programmable logic device that handles the chip logic. In principle, up to sixteen chipboards can be connected to a motherboard, which provides power and communication to the chipboards. A motherboard filled with the six chipboards required for this experiment is shown in Figure 3.19. The motherboard contains a field programmable gate array (FPGA) that controls the communication between the chips and the outside world. It provides multiplexed access to the inspection points on each chip, and can generate up to three ORs from any combination of channels. Two linear outputs on the motherboard send the energy and time determined on the ASIC channels to a SIS3301 flash ADC, one of two VME modules required for this setup. The other module is a JTEC XLM universal logic module, which controls the readout and stores the addresses of read channels. The XLM is also the access point between the Si subsystem and the master logic, accepting the master trigger and signalling when digitization is complete so a computer read can occur. Overall, this system is optimized for sparse readout from a large number of channels.

One advantage of treating each channel separately on the ASIC chips is that noisy channels do not tie up the whole system, so long as they are not in the trigger. The disadvantage on the flip side of this is that there is no external information about the electronics dead time of each channel when it is not in the trigger. The electronics dead time can be significant at low thresholds because of noise and because of analog-digital cross talk within the system. To account for this, every Si channel was pulsed at 2 Hz during the experiment. A busy channel does not read out during these events, so this method determines the dead time fraction of each channel. The electronics for this pulser setup are described in Section 3.7.

The CsI electronic subsystem is much simpler than the others mentioned so far in part because there are few channels, and in part because there are no timing requirements.

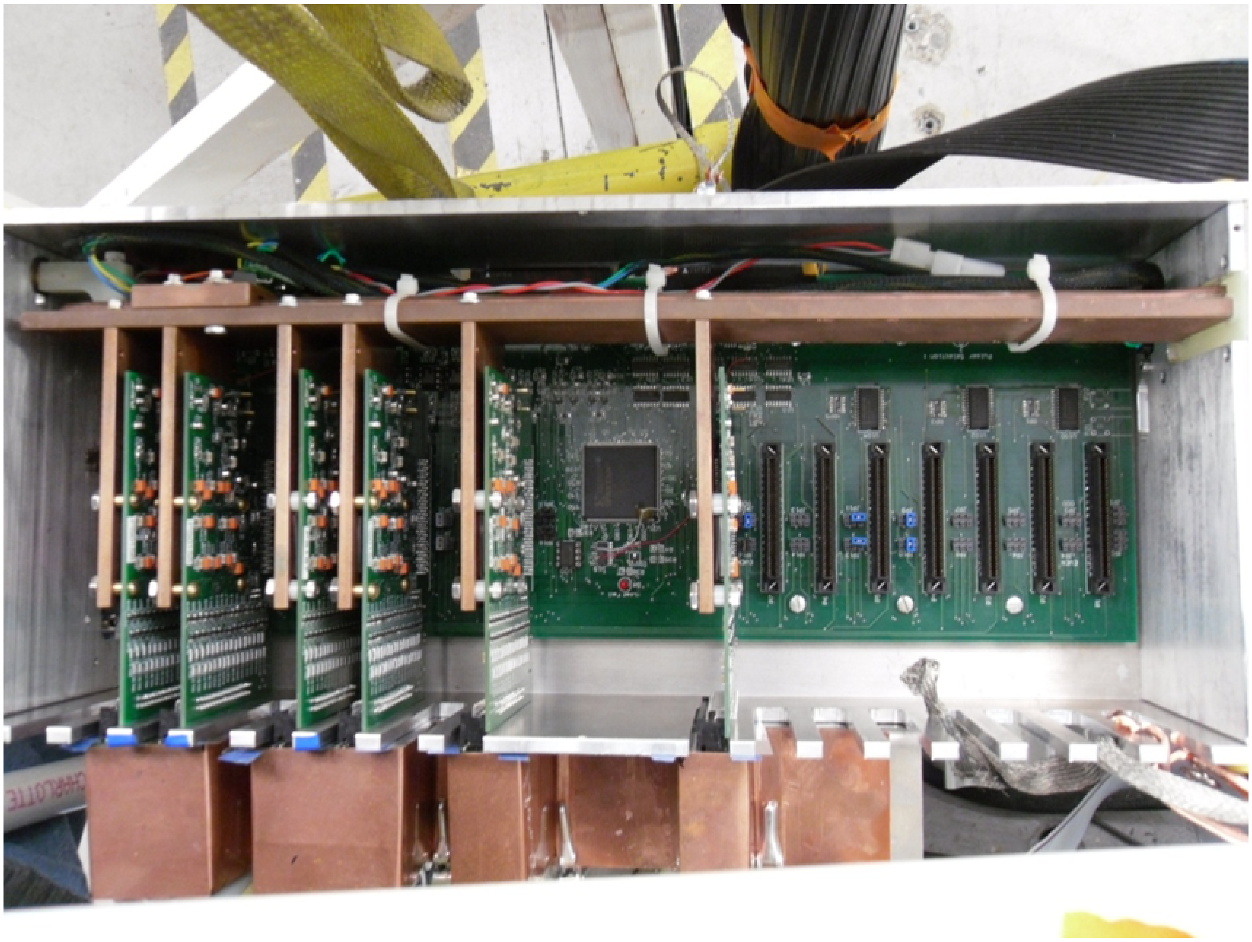

Figure 3.19: The HiRA motherboard used in this experiment, filled with six chipboards.

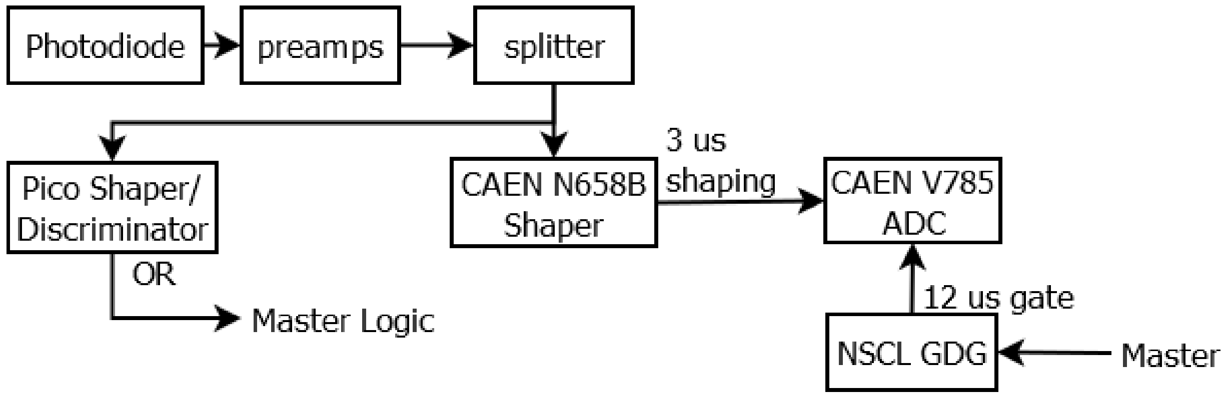

Figure 3.20: The CsI electronics subsystem.

The times are not even digitized. As indicated in Figure 3.20, the light from the crystal is collected by a photodiode, amplified by preamps onboard the telescope, then split into time and energy paths. The time path produces a raw OR and passes it to the master logic. The energy path is shaped then digitized in an ADC. The times involved are long enough that the master trigger starts the ADC gate; neither subsystem busy nor fast clear is required.

3.4 Forward Array

The Forward Array was built to provide a start for the neutron TOF measurement. It consists of sixteen thin NE-110 plastic scintillator wedges arranged in a partial annulus with a one inch inner diameter and a 4.5 inch outer diameter. The array is centered on the beam 10 cm downstream of the target, and contains a 72° cutout that leaves space for the most forward LASSA telescope. Because this experiment is focused on central collisions, a shower of charged particles will spray forward from the target at approximately beam velocity, generally hitting several elements in the FA. The small size of each element was chosen to optimize the time resolution. Each wedge is painted with Bicron BC-620 reflective paint to improve light transmission and wrapped in aluminized mylar foil to prevent external light contamination or cross talk. The scintillated light is detected by Hamamatsu R5600U PMTs attached to the outside of each wedge with optical epoxy. The model E5780 base is used with the PMTs. The wedges are attached to an aluminum plate that has the same dimensions as the array. Figure 3.21 shows the forward array in place.

The electronic signal from the PMT base follows a similar path as in the CsI subsystem, as shown in Figure 3.22. However, the FA times are read out. The TDC was set to common stop mode to avoid the need for a fast clear circuit. Also of note is that the FA TDC is self timing: the FA OR sets the time of the common stop. The FA OR is also passed to the Neutron Wall and Miniball TDCs as a time reference, making it one of the only signals that is passed directly between different subsystems.

3.5 Proton Vetoes

The Proton Veto array is composed of thin plastic scintillators placed on the outside of the reaction chamber between the target and the Neutron Walls. Neutrons are unlikely to interact with the array on their way to the Neutron Walls, while charged particles will deposit energy and be detected. This distinguishes the charged particle background from the neutron signal in the walls. Four existing square scintillators, designated paddles, covered the neutron wall at backward angles of $35^\circ \leq \theta \leq 60^\circ$. Thirteen narrow rectangular bars covered the neutron wall at forward angles of $8^\circ \leq \theta \leq 30^\circ$ in order to achieve higher granularity at small polar angles where the charged particle multiplicity was expected to be large. An image of the veto array is displayed in Figure 3.23.

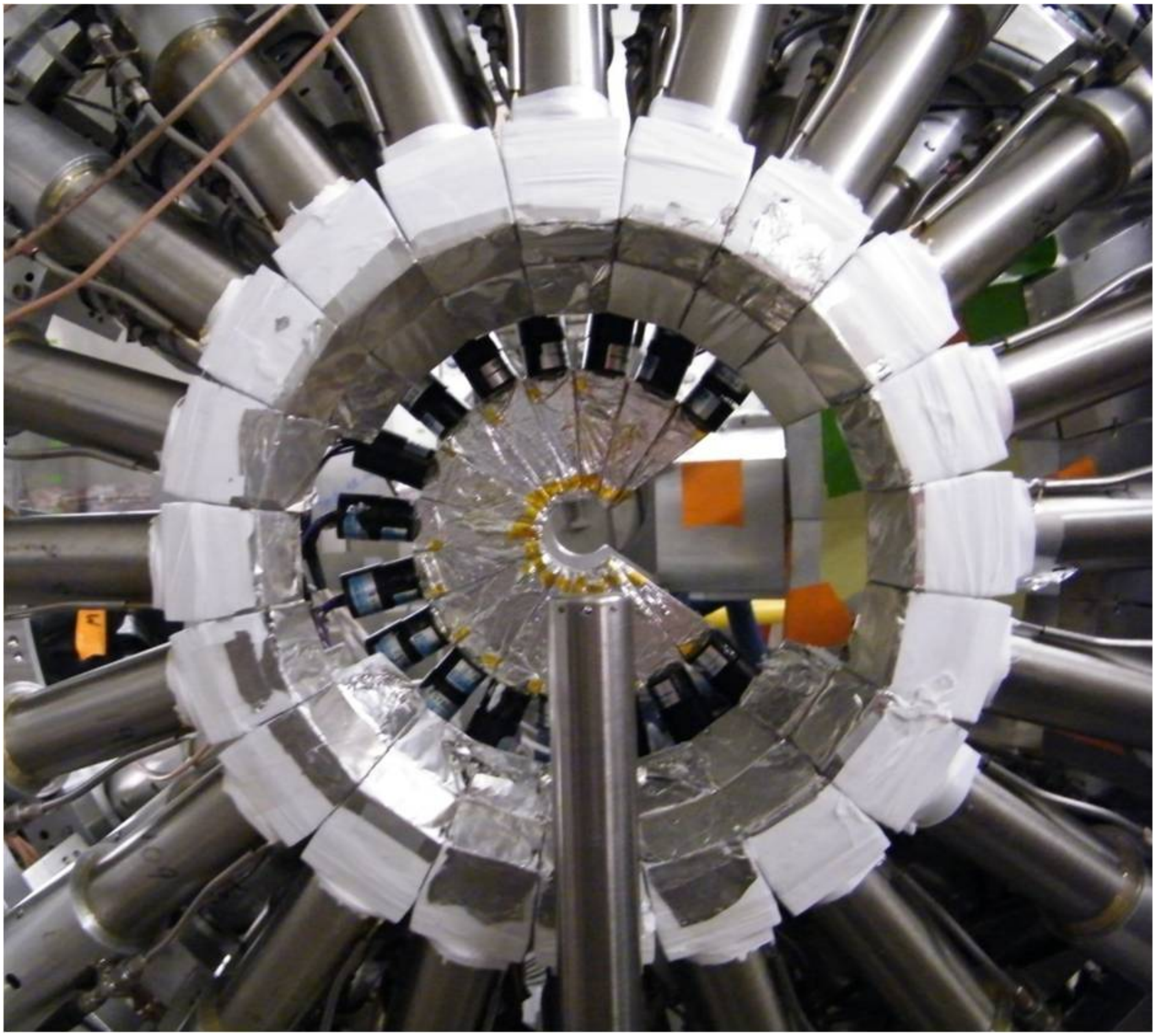

Figure 3.21: Image of the Forward Array in place (center) looking downstream from the target position. The aluminum support plate is behind the wedges, and not visible in this image. The cutout in the array, beam right, makes room for a LASSA telescope, which has a protective cover in this picture. In this image, the array is surrounded by two rings of Miniball telescopes.

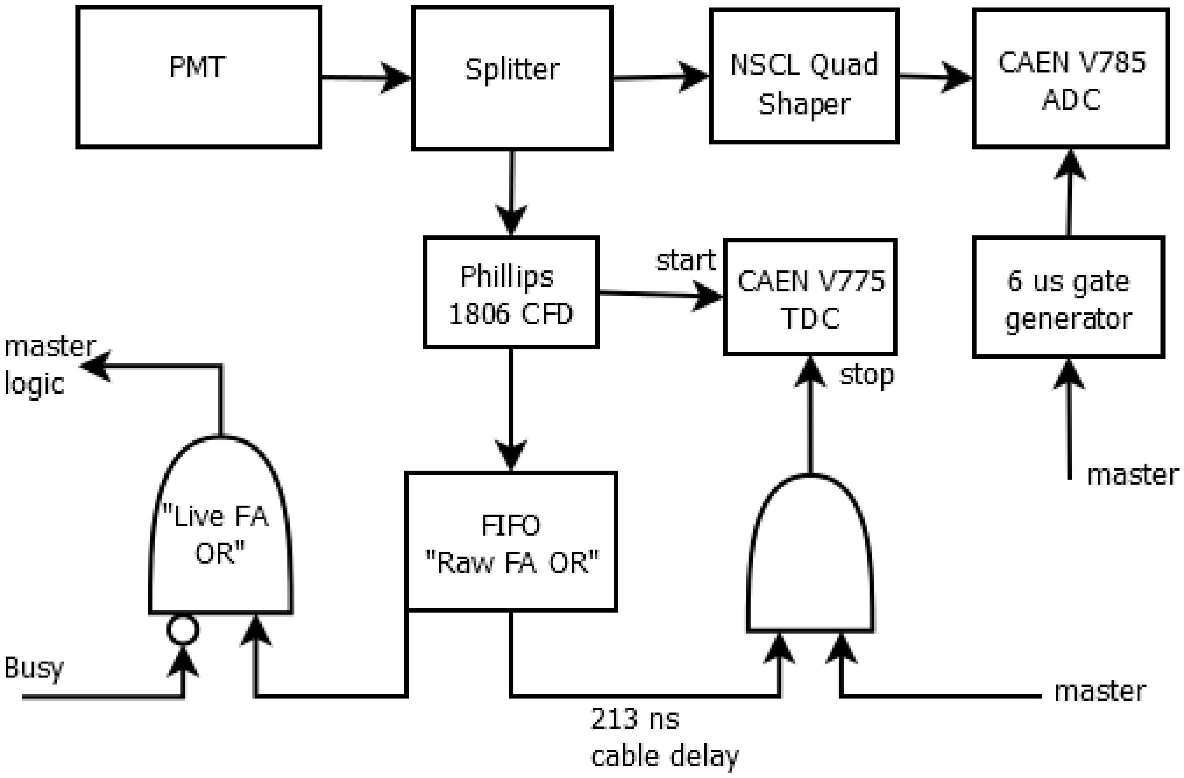

Figure 3.22: The Forward Array electronics subsystem.

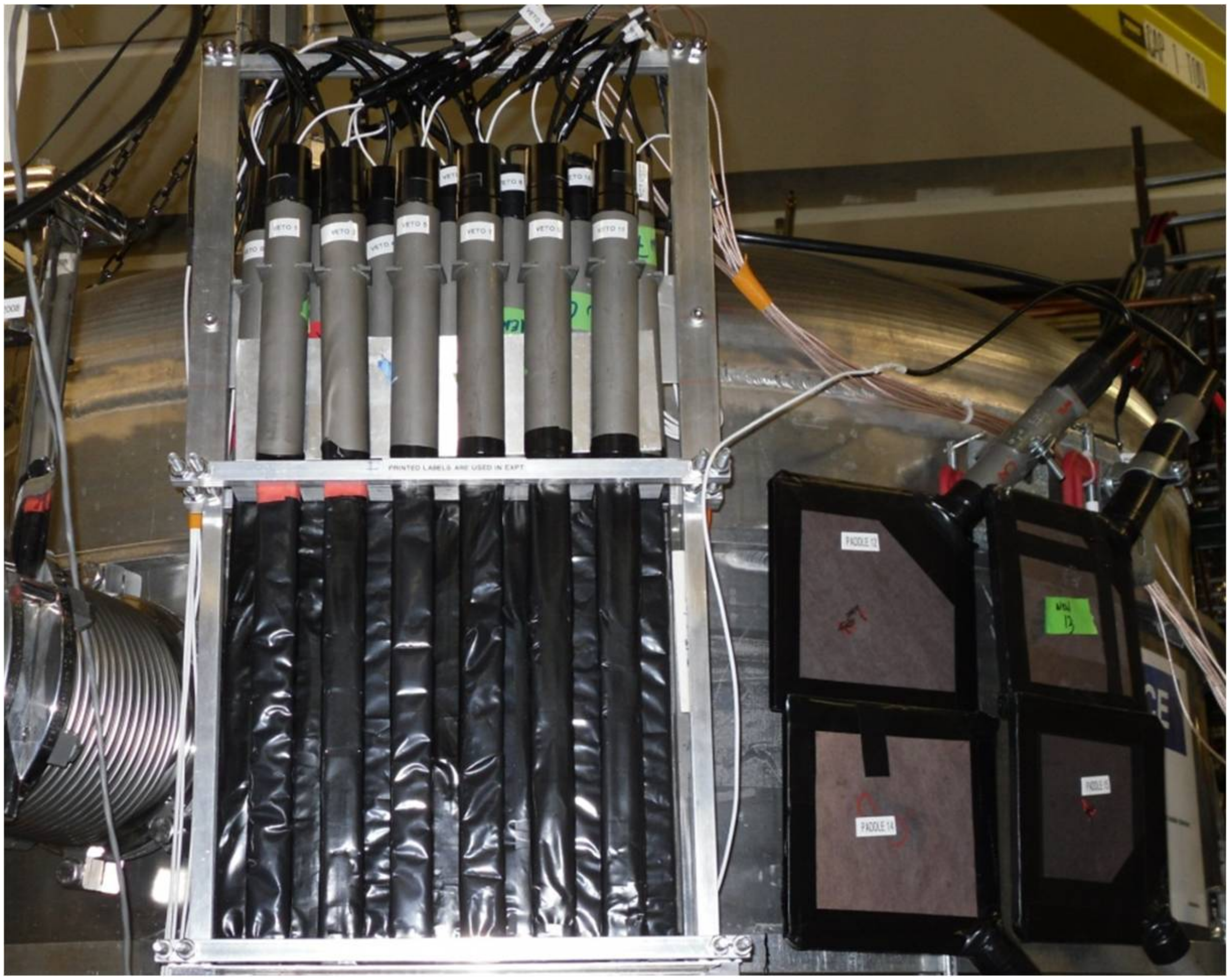

Figure 3.23: Image of the proton veto array attached to the outside of the reaction chamber. The vertical bars shadow the forward Neutron Wall, and the square paddles shadow the backward wall. The thin plastic scintillators detect charged particles that travel to the Neutron Walls.

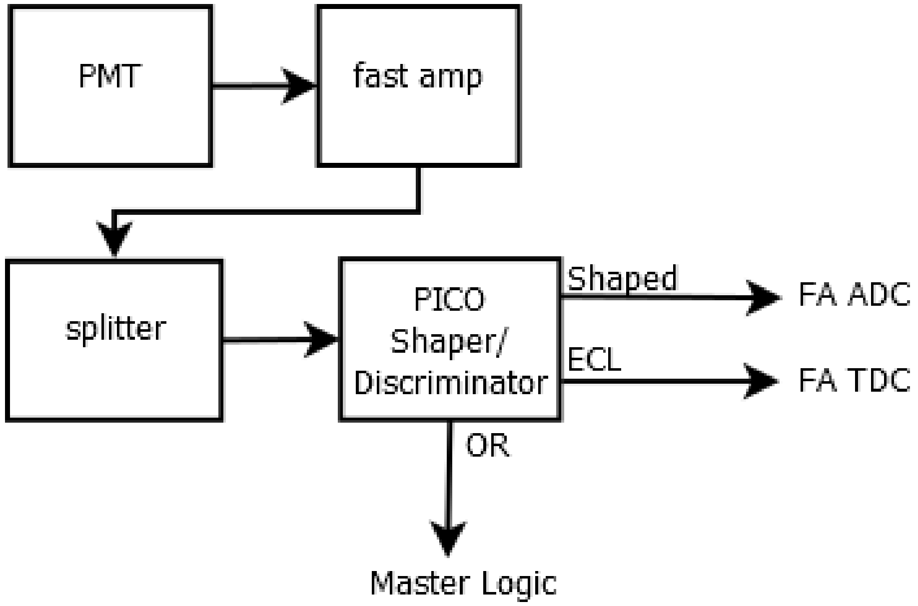

Figure 3.24: The Proton Veto electronics subsystem.

Both types of veto are made of Bicron BC-408 scintillator. The paddles are $^3/_8$ inch thick, while the bars are $^1/_2$ inch thick. The face of each veto paddle has dimensions 16cm x 16cm, and the face of each veto bar measures 23.5 mm by 27.4 cm. A UVT light guide attaches one corner of each paddle to a PMT, and a similar setup is attached to one end of the bars. The surfaces of each scintillator were polished to maximize light transmission. In addition, the paddle light guides and the entire length of the bars were wrapped with reflective tape to further improve transmission. Both geometries are covered in black plastic to prevent light contamination and optical cross talk. The PV electronics subsystem, presented in Figure 3.24, is similar to the FA and CsI subsystems. The time and pulse height information are read out through the same TDC and ADC used for the Forward Array.

3.6 Downstream Scintillator

The Downstream Scintillator was used to determine the beam rate in certain calibration runs. The scintillator itself was a 3.5 inch square, $^{1}/_{8}$ inch thick piece of Bicron BC-404 plastic scintillator. This was coupled to a Thorn EMI 4011 PMT via two pieces of UVT lightguide. The assembly, shown in Figure 3.25, was located just downstream of the Miniball, and retracted from the beam path during normal data taking to reduce background and protect the scintillator. The PMT signal was discriminated, then counted in a CAEN V830 scaler. The energies and times were not digitized.

3.7 Master Logic

The master logic system determines the trigger condition for computer readout and coordinates the detector electronic subsystems. During normal data taking, the AND of the Forward Array and Miniball submasters was required to generate a trigger and the other systems were run as slaves. The multiplicity requirement rejected uninteresting peripheral events, and the FA requirement guaranteed a time start for the neutron measurement. However, any of the logical signals in the dotted box displayed in Figure 3.26 could be inserted or removed from the trigger by the movement of a single cable. This flexibility was necessary to provide the trigger conditions for various calibrations without tearing apart the data acquisition.

Due to timing requirements, a trigger associated with the LASSA pulser system operated separately from the trigger determination described above, and the OR of these two triggers, widened to 20 μs to prevent retriggering, formed the master trigger. The

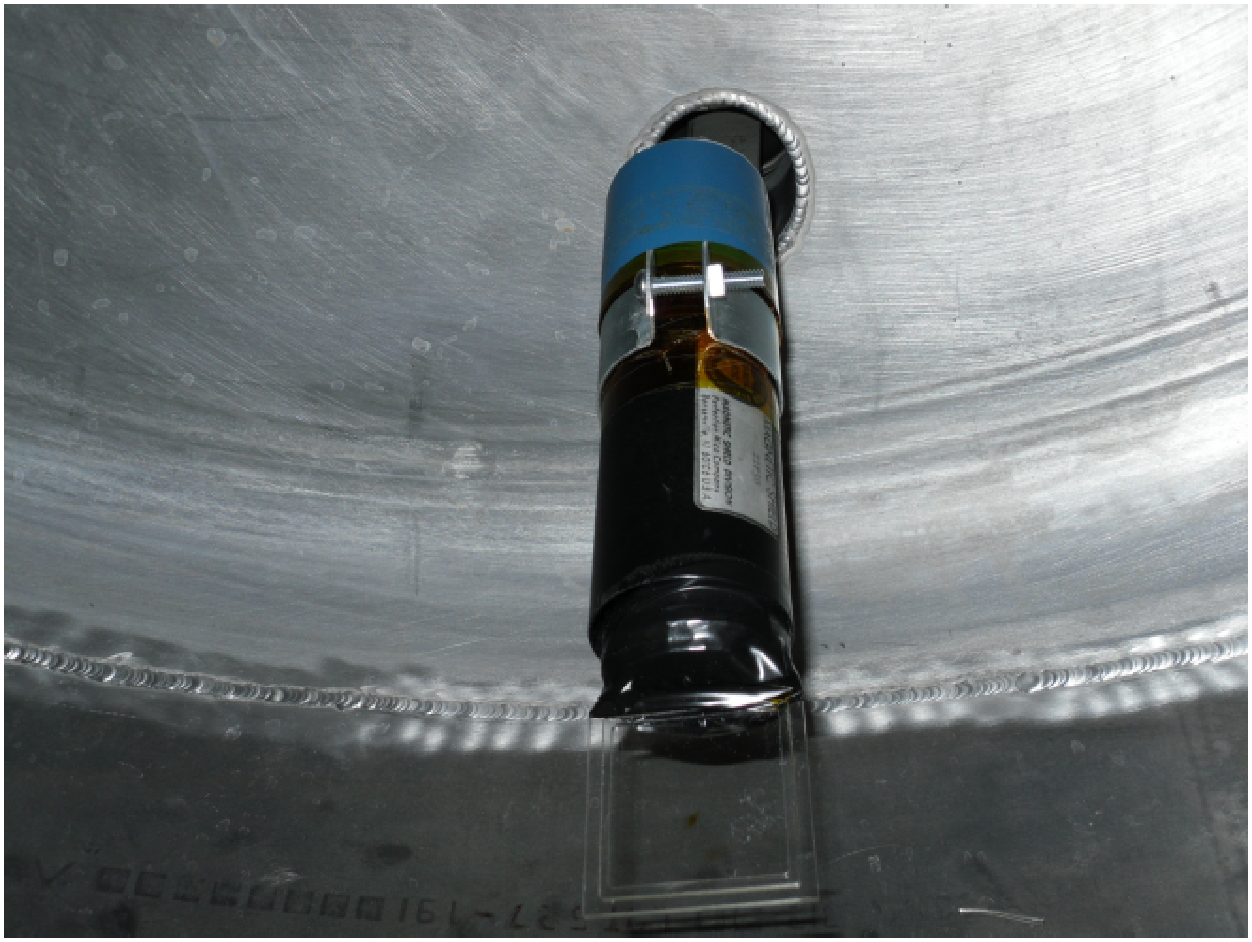

Figure 3.25: Image of the Downstream Scintillator, which was used to measure the beam rate during calibration runs. The scintillator was retracted during normal data taking.

master was fanned out to trigger the individual subsystems. After a short resolving time delay, the master started a latch indicating that the computer was busy, but the computer trigger itself was delayed by 20 μs before being passed to the I/O module to allow time for ADC digitization. As mentioned in Section 3.3, the Si ASIC electronics are optimized for sparse readout, which is not the case when every channel is triggered during a pulser event. The serial signal digitization is quite slow in this case, so a during a pulser event, computer trigger was delayed by an additional 786 μs. When the computer was triggered, data acquisition proceeded through the NSCL DAQ system. At the end of acquisition, a signal from the I/O module cleared the computer busy latch and the internal LASSA XLM busy latch, returning the electronics to a ready state.

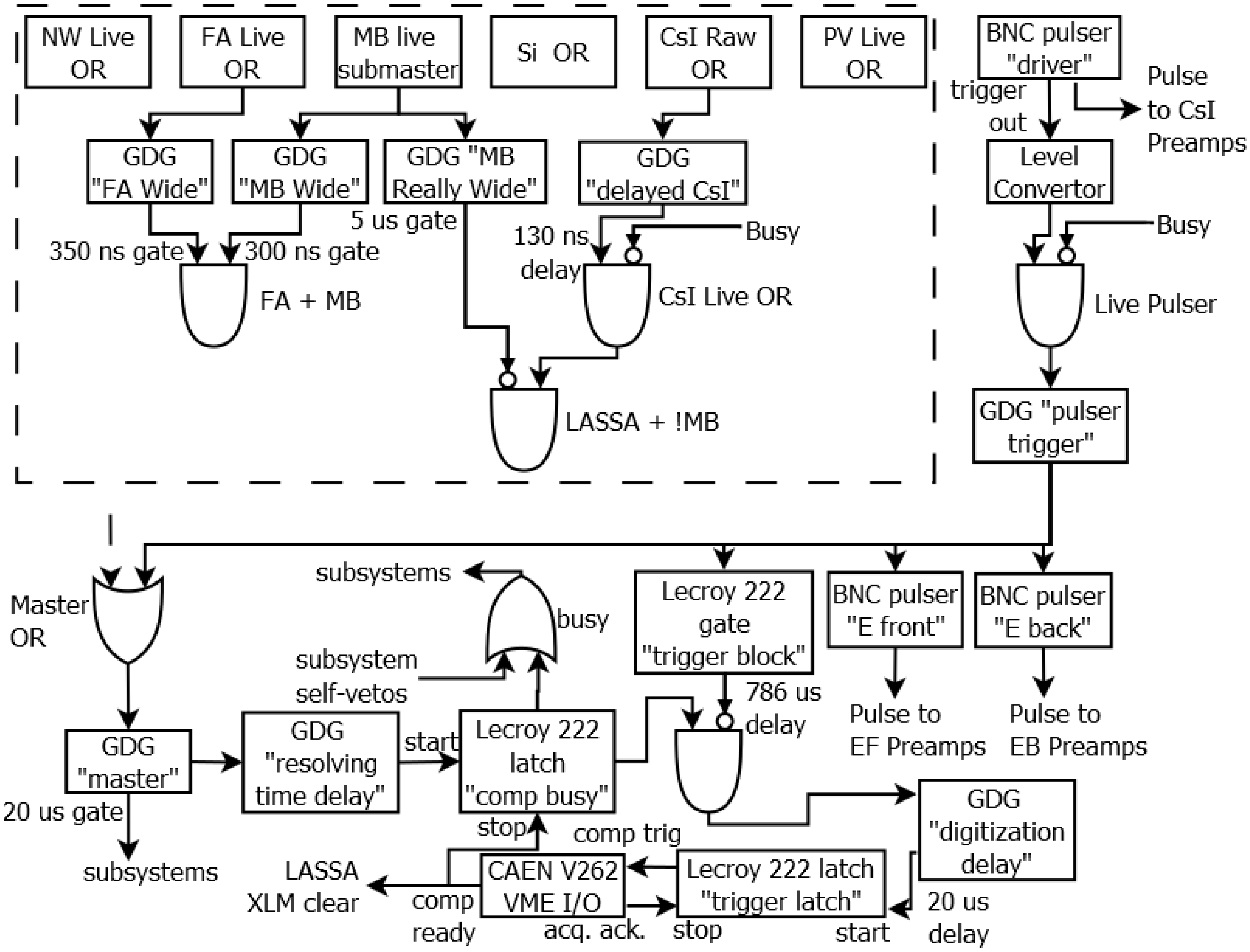

Figure 3.26: The electronic master logic.

Chapter 4

Analysis

The data produced in a nuclear physics experiment is in the form of digitized electronic signals from the various detector systems. These digitized signals have units assigned during, known as channels, whose meaning must be assigned by the experiment's calibration procedures. In the NSCL DAQ system, the digital values are written to a computer file as a string of hexadecimal words, with additional hexadecimal words indicating the electronics module that produced the data. One goal of experimental analysis is to assign meaning to this raw data, and put it into a useful and physically meaningful format.

For this experiment, the analysis is done within the ROOT analysis framework. Each detector component is represented by a C++ class, which includes structures that hold the data and functions for basic processing. Following the framework set up by Rogers [76], the data processing is conducted in several stages. First, the raw data file is converted into the ROOT file format. In this stage, the data is mapped onto C++ structures that have physical meaning, as a neutron wall element rather than a QDC. However, the data is left in its original digitized values.

Analyzing the raw calibration data in the ROOT file for each detector system leads to the development of functions that calibrate the data into physical units, such as the energy deposited in a given detector. This calibrated data is written to a new file. Separate calibrated files are written for the separate detector systems. An additional processing stage is necessary to turn this data into a physical description of the detected particle, e.g. a neutron of a particular energy detected at a particular angle. This data is written into a new file for each detector system. Finally, the data from the separate detectors are merged into a ″physics″ file that describes the full event. In the rest of this chapter, I will describe the calibrations and processing that are used to transform the raw data into particle spectra.

4.1 Centrality Determination

The reaction centrality is determined using the charged particle multiplicity in the Miniball, which is an indicator of the violence of the reaction. The cross section for events in which at least N_c charged particles are detected is:

$$\sigma(N_c) = \frac{I_r(N_c)}{I_i N} \tag{4.1}$$

where $I_r(N_c)$ is the rate of reactions where at least N_c charged particles are detected, I_i is the beam rate, and N is the areal number density of the target. N is calculated from the target thickness given in Table 3.1. Assuming that the charged particle multiplicity is a monotonically decreasing function of impact parameter b, one infers that collisions at b lead to the detection of $N_c(b)$ charges on average. A more central collision with smaller b

leads to a larger average value for the multiplicity, and a less central collision leads to a smaller average value. Relating the cross section to its geometric interpretation

$$\sigma(N_c) = \pi b^2 \tag{4.2}$$

determines the average b value corresponding to the detection of N_c charged particles [77].

Complex triggers can complicate the cross section measurement, so the multiplicity was calibrated in terms of the impact parameter in runs that only require a hit in the Miniball array. A trigger that accepts all data with N_c greater than or equal to a chosen minimum value is referred to as a minimum bias trigger. Occasional scattering from the target frame or the downstream scintillator gives rise to a low multiplicity background with a maximum multiplicity less than $N_c = 7$. This is quantified by repeating the measurement with a blank frame in place of the target. The downstream scintillator can measure the beam rate when the rate is 10^5/s or less, but it does not function properly at higher beam rates. To obtain enough statistics for the high end of the multiplicity spectrum, an additional set of runs is performed at a higher beam rate and with the downstream scintillator retracted. The shape of the background-subtracted multiplicity spectra above multiplicity 7 is the same in the high rate and low rate runs. The dead-time corrected ratio of the integral of the two background-subtracted spectra above this multiplicity is also the ratio of the beam rates. Using this information, one can obtain the cross section $\sigma(N_c)$ for every value of N_c, allowing values for the corresponding impact parameter to be accurately calculated as a function of Miniball multiplicity for all four reaction systems. The results are displayed in Figure 4.1.

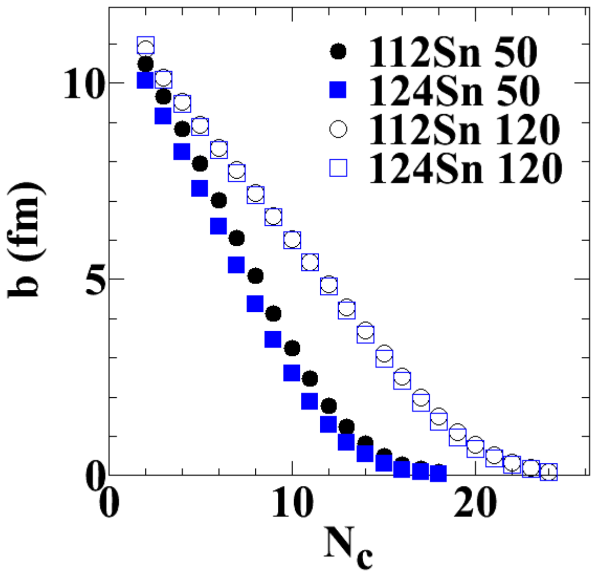

Figure 4.1: Impact parameter as a function of Miniball multiplicity for all four reaction systems

4.2 LASSA Analysis

The LASSA analysis consists of three parts. First, the individual detector components are calibrated. Then the component information is combined to determine what particles were detected in an event. Finally, the detection efficiency is investigated to determine the true spectra.

4.2.1 Detector Calibrations

The Si and CsI calibrations contain the same two pieces: matching the spectrum to several energy references, and accounting for any nonlinearity in the readout electronics. The nonlinearity is determined using a PB-5 pulser made by the Berkeley Nucleonics Corporation, which has a very linear output. Pulsing either the Si or the CsI preamps and varying the pulse height in many equal steps produces a map between the digitized output of the electronics and the input signal. Both electronic systems are linear over most of their range, but nonlinearities are present for small signals in the Si and large signals in the CsI. The Si nonlinearity is fit by a fourth-order polynomial that transitions to a linear relationship, while only a second-order polynomial is required to match the CsI nonlinear region.

The energy deposited in the Si is determined using a ^{228}Th source, which produces alpha particles at five well-separated energies as it follows its decay chain, as shown in Figure 4.2. Here the data have been binned according to the digitized values for the pulse height. The location of the peaks are used to relate these digitized values to the corresponding energies. Notably, the highest energy alpha has 8.78 MeV of kinetic energy, which is larger than is available in other common sources. The alphas lose energy in intervening material before stopping in the detector, so that the deposited energy is not the original decay energy at the source. The LISE++ computer program [78] is used to calculate the energy loss in the 50 μg/cm^2 window on the source, the 1.9 micron aluminized mylar foil, and the dead layer of the silicon detector to determine the energy collected in the detector. The five peaks in the linearized spectrum are then fit onto the known energies to arrive at a calibration.

The CsI cannot be accurately calibrated with a radioactive source because the light output is too small for such low energies. Instead, protons are identified in the reaction data using calibrated Si energy vs uncalibrated CsI energy, similar to Figure 3.16. The expected energy in the CsI is calculated in LISE++ from the known energy in the Si. This technique works well when the Si energy varies quickly with CsI energy as it does for lower energy particles, but it is not useful when the Si energy plateaus. Signals below

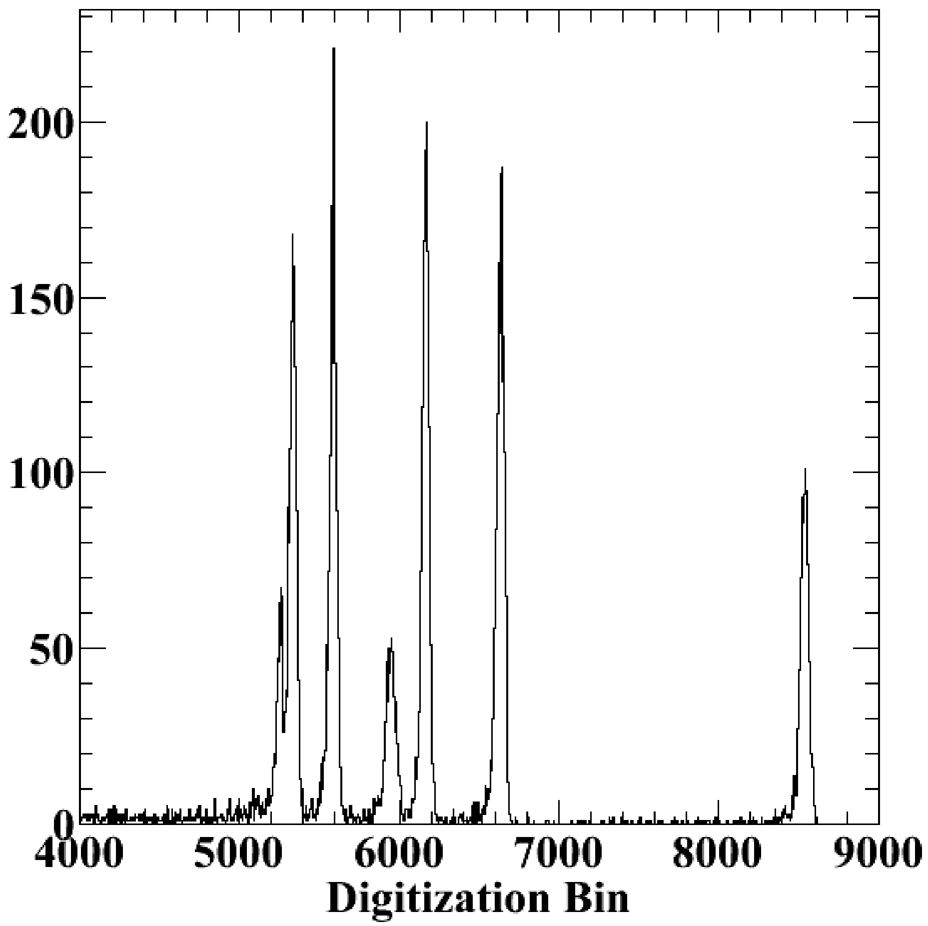

Figure 4.2: ^{228}Th alpha source spectrum in a LASSA silicon detector. The five main peaks provide calibration points.

2 MeV in the Si are excluded from the fit. Additional information is needed to fix the calibration at higher energies. Once a proton has enough energy to punch through the CsI without stopping, it deposits less energy in the CsI with increasing kinetic energy. This leads to a clear end of the proton PID line at known energy, called the punch-through point. Scaling the calibration to match the punch-through point at 146.8 MeV in the CsI and 0.51 MeV in the Si completes the proton energy calibration. Additional energy corrections are made for other particle species during the event reconstruction.

4.2.2 Event Reconstruction

The Si electronics thresholds were set low to make sure to include the entire proton line out to the punch-through point. This also meant that channels would sometimes fire on electronic noise. During this experiment, LASSA was run as a slave. That is, it did not contribute to the master trigger, and so these noise events did not tie up the system. However, the first task of event reconstruction is to identify and remove these spurious signals. The pedestal values, the pulse height associated with noise events, are identified channel by channel and a software threshold is put in place to exclude them. In all cases, these thresholds were below the proton punch-through value. Another source of low-energy pulses is bleed-over from a large pulse coming from a highly ionizing particle that traverses a neighboring strip near the boundary of the two strips or in the 100 μm wide interstrip gap. This decreases the measured energy on the main strip, so a gluing procedure is employed to combine the energies of neighboring strips to get the correct energy.

The next step is to determine which pixel a particle primarily passes through, that is, to match the front strip to the back strip for the same particle. The same pulse size is collected on the front and back of the silicon detector, so the calibrated energies should be similar. Hit pixels are identified by requiring that the front and back energies match to within 40% if the pulse is below 3 MeV and within 10% if it is larger, and requiring that a hit is observed in the CsI behind the identified pixel. When more than one silicon pixel is identified in front of a given CsI crystal, it indicates that multiple particles have interacted with that crystal. In this case, which happens in less than 5% of hits, the hit is discarded because the particles cannot be distinguished.

With pixels assigned, particle identification is determined using the ΔE-E method. Two additional corrections are needed to assign the energy of the particle. The light output of the CsI crystals are quenched for heavier particles relative to protons. Following a previous analysis of LASSA by Liu [1], we adopt the following ionization corrections as a function of particle mass and charge:

$$E = aL + b \qquad Z = 1 \tag{4.3}$$

$$E = aL + bA^{c}\left(1 - e^{dL}\right) \qquad Z = 2 \tag{4.4}$$

$$E = a\sqrt{AZ^2}L + b\left(1 + cAZ^2\right)L^{1-d\sqrt{A}Z} \qquad Z = 3 \tag{4.5}$$

$$E = aAZ^2L + b\left(1 + cAZ^2\right)L^{1-d\sqrt{A}Z} \qquad Z = 4 \tag{4.6}$$

where a,b,c, and d are parameters with values defined in Table 4.1.

The final energy correction is for the energy deposited in material that is not part of an active detector. This is determined by working back from the final energy deposited

Z	a	b	c	d
1	0.2010	-0.9587		
2	0.1696	4.575	0.3380	-0.05772
3	0.01783	0.2456	0.09743	0.06358
4	0.0006680	0.4493	0.01015	0.02626

Table 4.1: Parameter values used in LASSA CsI ionization correction.

in the CsI out through an aluminized mylar foil, the active part of the Si detector, the Si dead layer, more mylar, SnPbSb foils and finally half the target, assuming that the reaction happened at the target center. Note that the target is aligned with the beam rather than the detector, and the effective target half-thickness accounts for this. All losses are computed using LISE++.

4.2.3 Efficiencies

LASSA does not cover the entire solid angle in the angular range of interest, so the fractional coverage must be taken into account. The geometric efficiency is determined by summing the angular coverage of all pixels used in the final analysis, as shown in Figure 4.3. Some pixels are removed because the strip, Si preamp, or CsI preamp was broken. Others are partially shadowed by part of the Miniball or Forward Array. The most forward two CsI crystals are removed because the hit rate was too high to get an accurate representation of the detection efficiency.

The detectors and associated electronics are also subject to an efficiency adjustment. Multiple hits in a given CsI crystal cause all associated particles to fall outside the PID lines and be lost. These events are specifically noted and rejected during the pixel assignment. Assuming Poisson statistics, the hit rate in a given crystal is used to determine the efficiency correction. The Si detector does not suffer the same fate due to the higher segmentation,

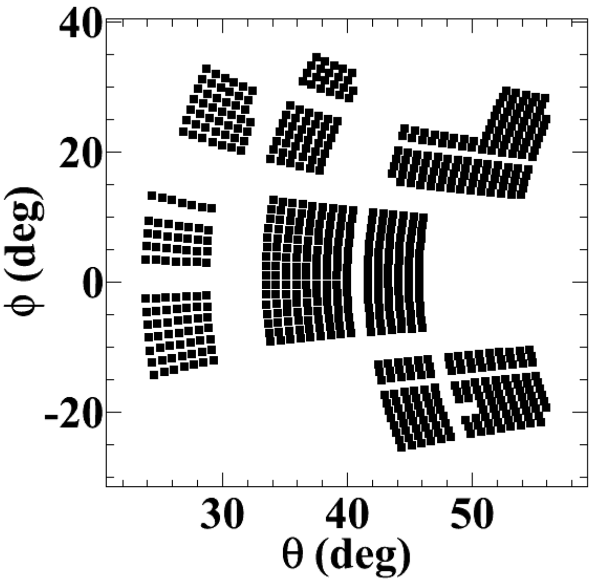

Figure 4.3: The center location of each LASSA pixel used in the final analysis. Several unconnected strips are visible on from the silicon detector. Some regions were also removed due to shadowing from other materials or detectors.

but the electronics channels are susceptible to dead time effects. No external measure of this electronic dead time is available, so a pulser was used to trigger all channels at 2 Hz during normal data taking. If a given channel is busy, it will not read out during the pulser event. The dead time fraction of each channel for a particular run is the number of missed pulser events divided by the total number of pulser events.

4.3 Neutron Analysis

The purpose and basic setup of the Neutron Walls, the Forward Array, and the Proton Vetoes were covered in Sections 3.2, 3.4, and 3.5, respectively. These detectors require separate calibrations but need to be combined to produce a physical description of an event.

4.3.1 Detector Calibrations

4.3.1.1 Time Calibrations

The energy of neutrons detected in the Neutron Wall is determined by measuring the time of flight, so obtaining an accurate time calibration is obviously important. The two components of this are the timing start in the Forward Array and the timing stop in the Neutron Wall. The signals from both detector arrays are measured relative to the OR of the signals from the sixteen FA detectors, the timing of which is determined by the first signal to reach the discriminator. If the FA OR was a perfect indicator of the start time, then only the NW TDC would need to be calibrated. However, the timing of the FA OR can vary due to slight cable length differences between different FA elements, and due to walk in the discriminator. Some corrections are necessary to achieve the best TOF resolution, and this requires a time calibration of the individual FA elements.

The time calibration for both the Neutron Wall and Forward Array is obtained using an Ortec 462 time pulser. The time pulser outputs a start and a stop signal with a precise time difference of $n \times I$, where I is the base time interval and n is an integer that varies within a given range. The result, accumulated over many events, is a series of peaks of known spacing I that can be used to calibrate the TDC. For the Neutron Wall TDC, the time pulser spectrum revealed a linear relationship between digitization channel and true time with a slope of about 100 ps per channel. However, this spectrum is not enough to set the offset of the calibration. The offset is determined with experimental data, in particular the signal from gamma rays traveling directly from the reaction to the detector. These prompt gammas form a sharp peak at the earliest possible TOF, as shown in Figure 4.4. Because this TOF is known once the position is known, it sets the offset for the time calibration.

The Forward Array time calibration is also mostly linear, with a slope of about 85 ps per channel. At high channels the linearity fails, but this is outside the region of interest. The calibration offset was chosen to set the self-timing peak at time zero. This peak occurs in the channel that starts the FA OR and is thus being timed against itself. With this offset, the earliest FA signal in an event is the most likely start channel. Cable length differences between FA elements lead to shifts in the OR, which appear as shifts in the prompt gamma peak in the NW spectrum when gating on a particular start channel. However, the start channel is ambiguous when several FA elements have signals near their self-timing peaks, as was often the case. Corrections based just on the start channel are thus impossible.

Subtracting a given FA element time from the NW time removes the FA OR from the TOF. The offset associated with that element is then evident as a shift in the prompt gamma peak, and correcting this offset does not rely on the flawless identification of the start channel. However, the offset may not be constant. Walk in the discriminator gives rise to a time displacement that depends on pulse height. Plotting the digitized pulse height of the FA element vs the subtracted time spectrum, as shown in Figure 4.5, reveals the discriminator walk. The fit to the peak centroid as a function of pulse height is used to correct the walk and offset.

The best start time is that which minimizes the FWHM of the prompt gamma peak. However, comparisons to the prompt gamma peak are complicated by a wider secondary gamma peak shortly after it. The relative strength of the secondary peak depends on the FA multiplicity and thus the reaction multiplicity, and the time of the peak is earlier for higher velocity beams, suggesting that the peak comes from gamma production from charged

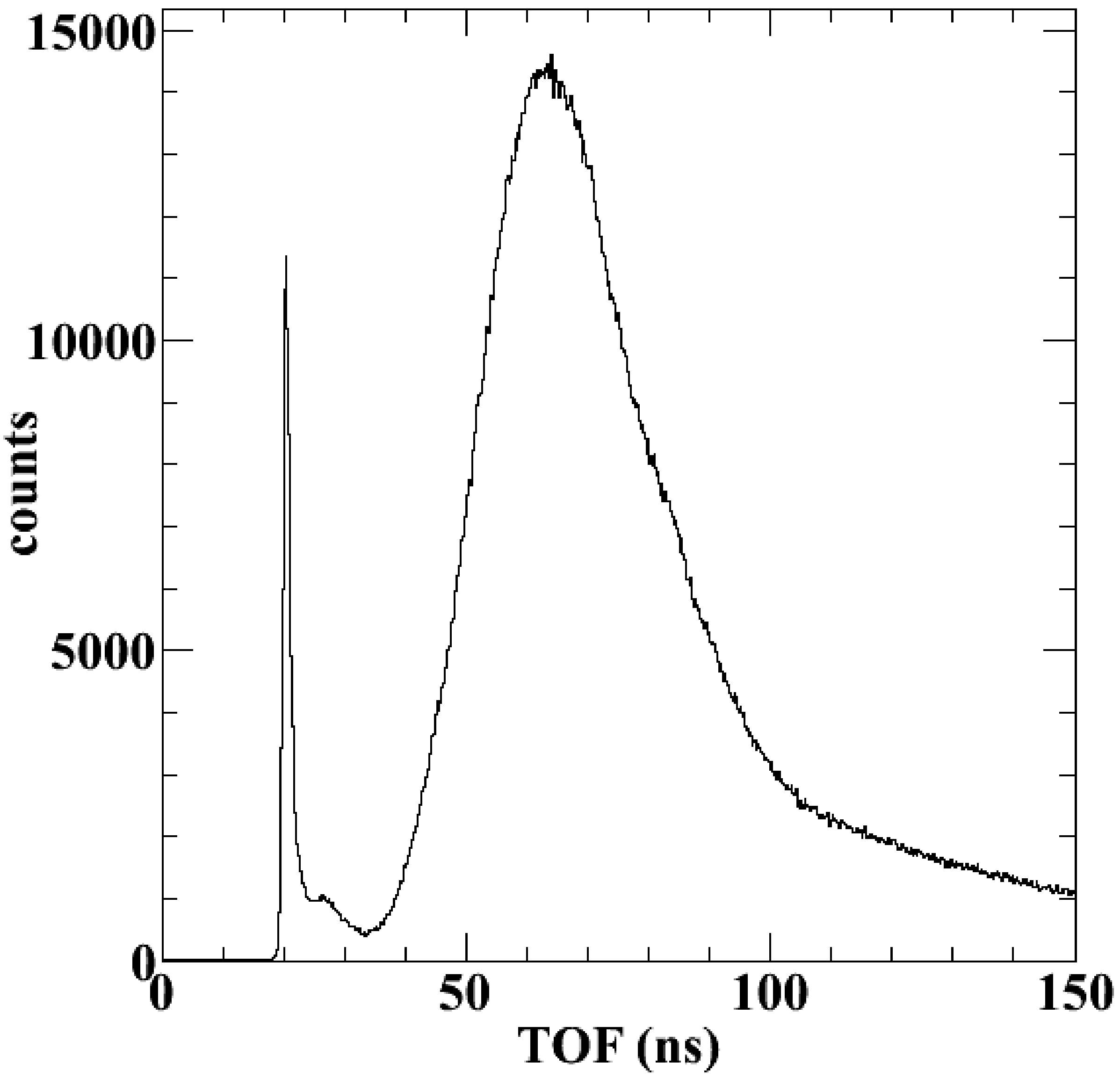

Figure 4.4: A time of flight spectrum from the Neutron Walls. The narrow peak at the start of the spectrum is from prompt gammas, while the rest of the spectrum is due to a combination of massive particles and delayed gammas.

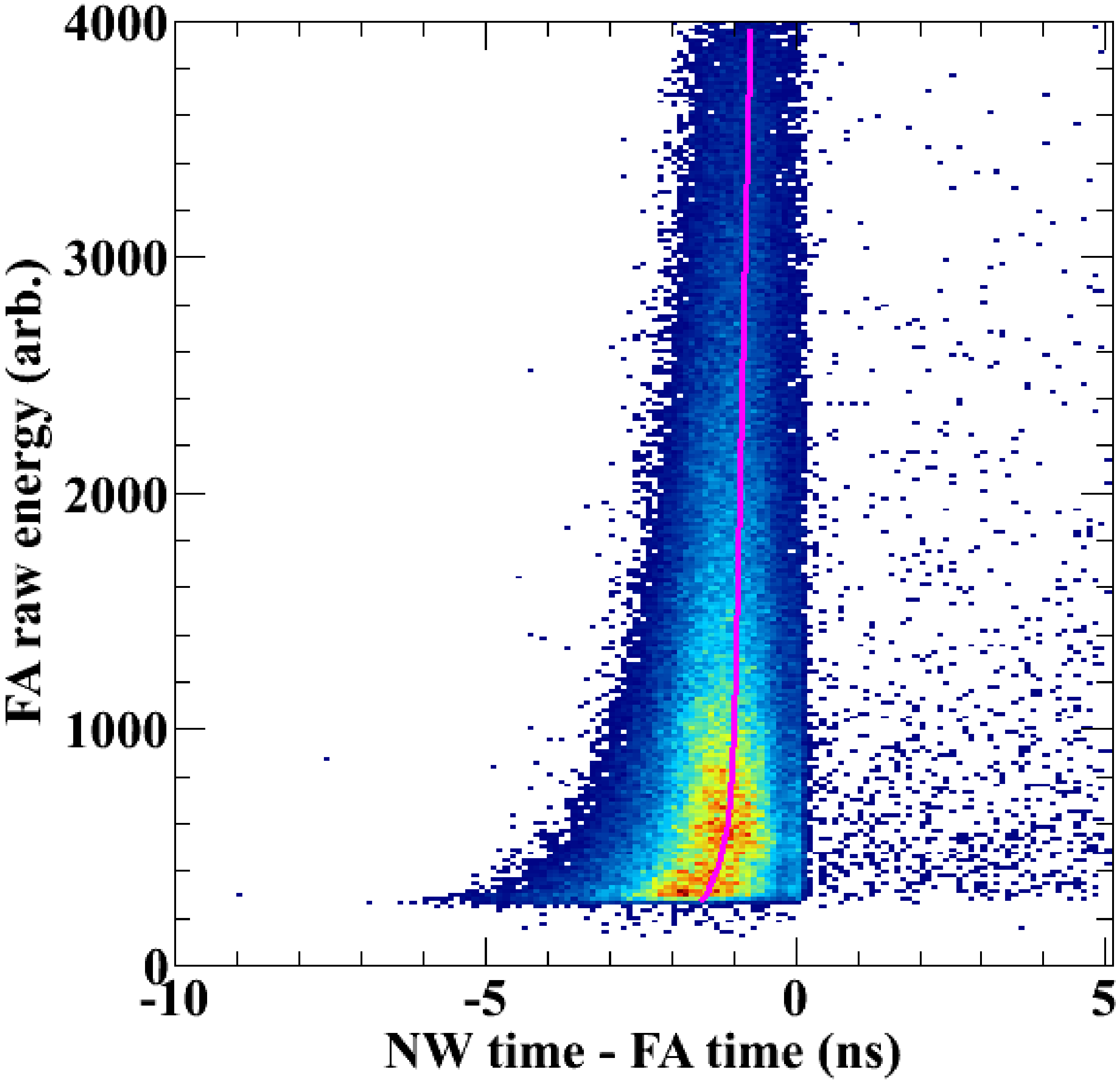

Figure 4.5: The prompt gamma peak in the Neutron Wall time spectrum plotted as pulse height in a forward array element vs neutron wall time measured with respect to that element. Walk in the Forward Array discriminator results in the pulse height dependence of the peak centroid, which is fit by the magenta line. The spectrum would peak at 0 ns if there was no channel-dependent offset.

particles or neutrons interacting with material in the reaction chamber. Choosing low multiplicity events to minimize this secondary peak increases the accuracy of comparisons to the prompt gamma time and width.

Two methods of constructing the start time were considered. The first method is to use the earliest FA element. The second is to determine the resolution of the prompt gamma peak referenced to each FA element as a function of the FA pulse height, and then use the average of the best few elements in an event as the start time. The comparison of these two methods to the uncorrected spectrum in Figure 4.6 demonstrates that these two methods are comparable, but the second method is slightly better than the first. The final time resolution is 1.2 ns.

The same algorithm is used to determine the start time regardless of the reaction. However, the start time shifted based on the beam energy, because the average time for charged particles to reach the forward array changes. Once again, the time of the prompt gamma peak is used to determine this offset.

4.3.1.2 Position Calibrations

Laser measurements by Dr. David Sanderson of the NSCL provided the locations of the reaction target, the shadowbars, and the corners of each Neutron Wall bar. The raw hit position in a neutron wall bar, defined by the time difference between the left and right signals, needs to be mapped onto these locations in real space. Some position information is available from the proton veto array. Even without further processing of the PV array, events with one hit in the proton veto array and one hit in the neutron wall produce an image of the proton veto elements on the wall behind them. The vertically aligned

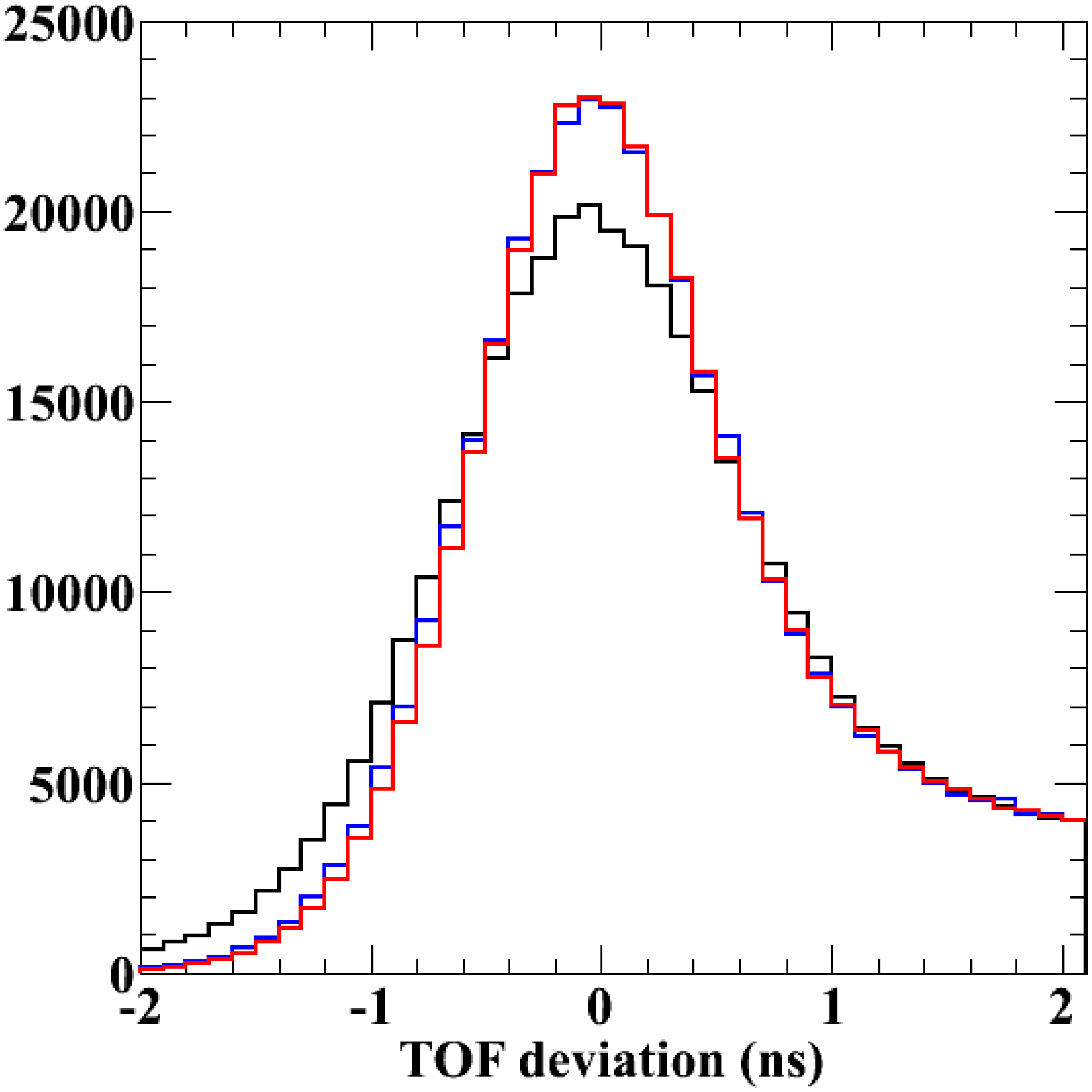

Figure 4.6: NW prompt gamma peak, using the FA OR (black), the first FA hit (blue) or the average of good hits (red) as the start time. Both corrected times have a higher resolution than the uncorrected time. The average correction is slightly better than the first hit correction, and is employed for the subsequent analysis.

PV elements in front of the forward neutron wall provide reference points at the same positions along each neutron wall bar, shown in Figure 4.7. All the bars are matched to each other using these points, but the absolute location of the proton veto elements was not measured with enough accuracy to produce a final calibration from this information. The final calibration is obtained using the location of the shadow of the brass shadowbars, which were well measured. Interestingly, this analysis indicates that the neutron wall elements have different time to position calibrations, which was not noted in previous analysis [71]. One bar had a bad position spectrum, and is removed from subsequent analysis.

The lack of several vertically aligned PVs in front of the backward wall makes matching the bars more difficult. One reference point is available from the edge of the proton vetoes, but this is not enough data to determine the slope. Additional information is available from cosmic ray data, which produce a flat position spectrum with sharp edges. The cosmic ray position spectrum edges extend past the edge of the calibrated bars in the forward wall, due to the tapered section that connects the rectangular bar to the PMT. However, the width of the raw spectrum correlates with the calibration slope, as shown in Figure 4.8. Assuming a similar correlation in the backward wall, the bars are matched by fitting the edge of the cosmic position spectrum to the known position of the bar edges and requiring that proton veto edge is at the same position in each bar. The final calibration is again obtained using the known positions of the shadowbars. The average time to position calibration is 8.06 cm/ns, which is larger than the previous value of 7.65 cm/ns.

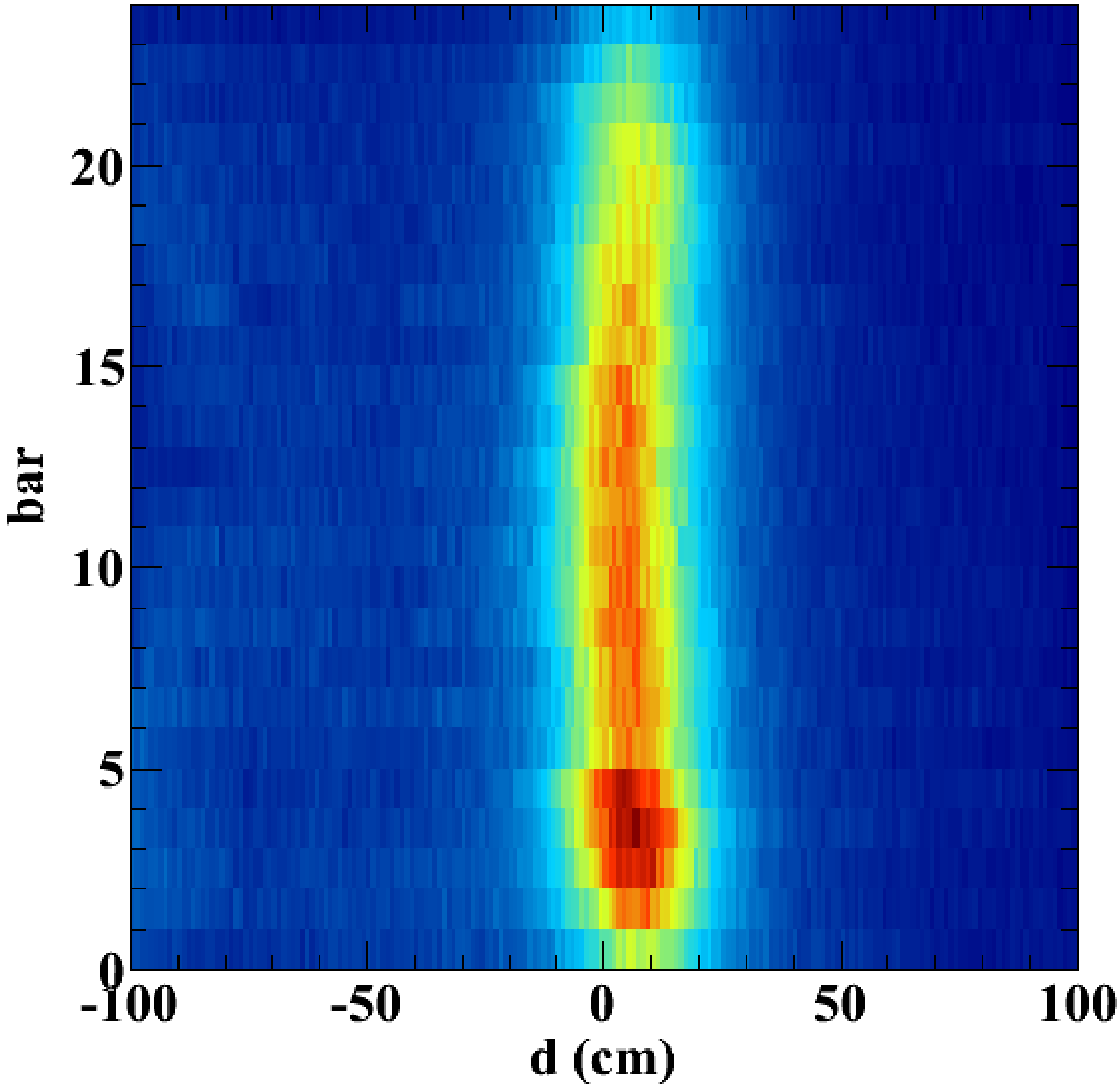

Figure 4.7: Bar number versus position along a neutron wall, gated in hits in coincidence with a particular proton veto element. Red regions have many hits and blue have few. The shadowed position of the proton vetoes was used to match the postion spectra of the neutron wall bars.

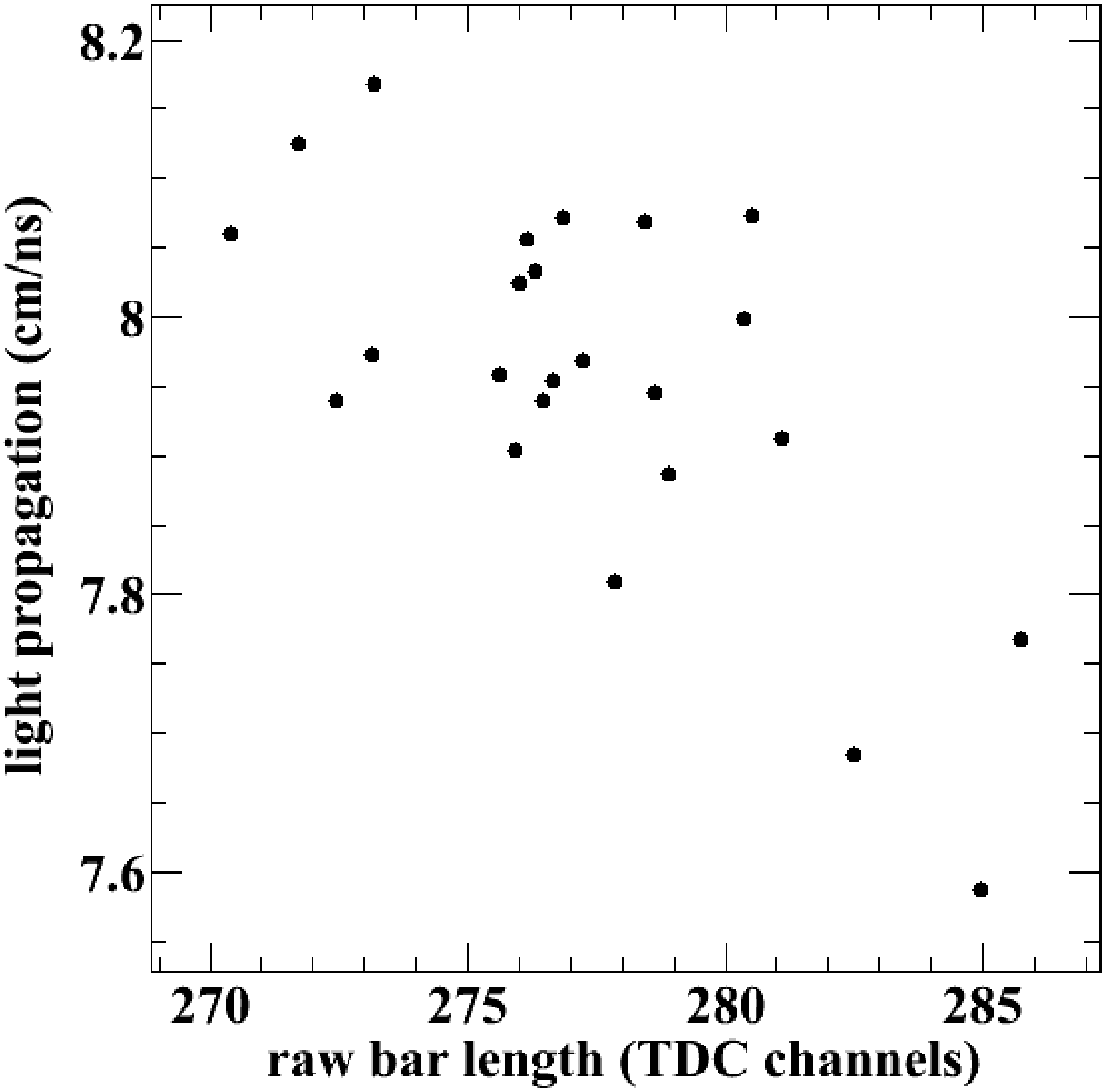

Figure 4.8: The correlation between the position calibration and the cosmic spectrum width in the forward neutron wall. In the absence of narrow proton veto bars for the backward wall, this correlation indicates that the cosmic ray spectrum can be used to match the position spectra of the neutron wall bars.

4.3.1.3 Neutron Wall Pulse Height Calibration

Fast neutrons do not deposit a fixed fraction of their energy when they interact in the neutron walls, and thus time of flight, rather than energy deposited, is used to determine neutron energy. Nevertheless, a pulse height calibration is necessary to account for the effect of pulse height cuts, such as detection thresholds, on detection efficiency. As mentioned in Section 3.2, integrated total charge is measured on both sides of a neutron wall bar. The signal is attenuated as it passes through the bar, so the detected pulse height has an approximately exponential position dependence. This position dependence can be removed by taking the geometric mean of the signals detected on both sides of the bar. The geometric mean light can then be calibrated by comparing to known gamma sources. These sources produce a light calibration in MeV electron equivalent (MeVee), which is the light emitted by an electron depositing one MeV of energy. The light output from more massive particles is quenched, so they will produce less light when they deposit the same energy.

An Americium-Beryllium (AmBe) source produces 4.439 MeV gammas from the deexcitation of ^{12}C. The Compton edge of this spectrum at 4.196 MeV is readily identifiable in the neutron walls, but it exhibits an additional quadratic position dependence as shown in Figure 4.9. The proton stopping line in the wall, gated on a narrow range of velocities, confirms that the same position dependence occurs in larger pulses. The Compton edge in the position-corrected energy spectrum is then one calibration point, as shown in Figure 4.10. Another is obtained from a ^{60}Co source, which emits gamma rays of energy 1.333 MeV and Compton edge 1.119 MeV.

A final calibration point is obtained from cosmic rays. At ground level, the most

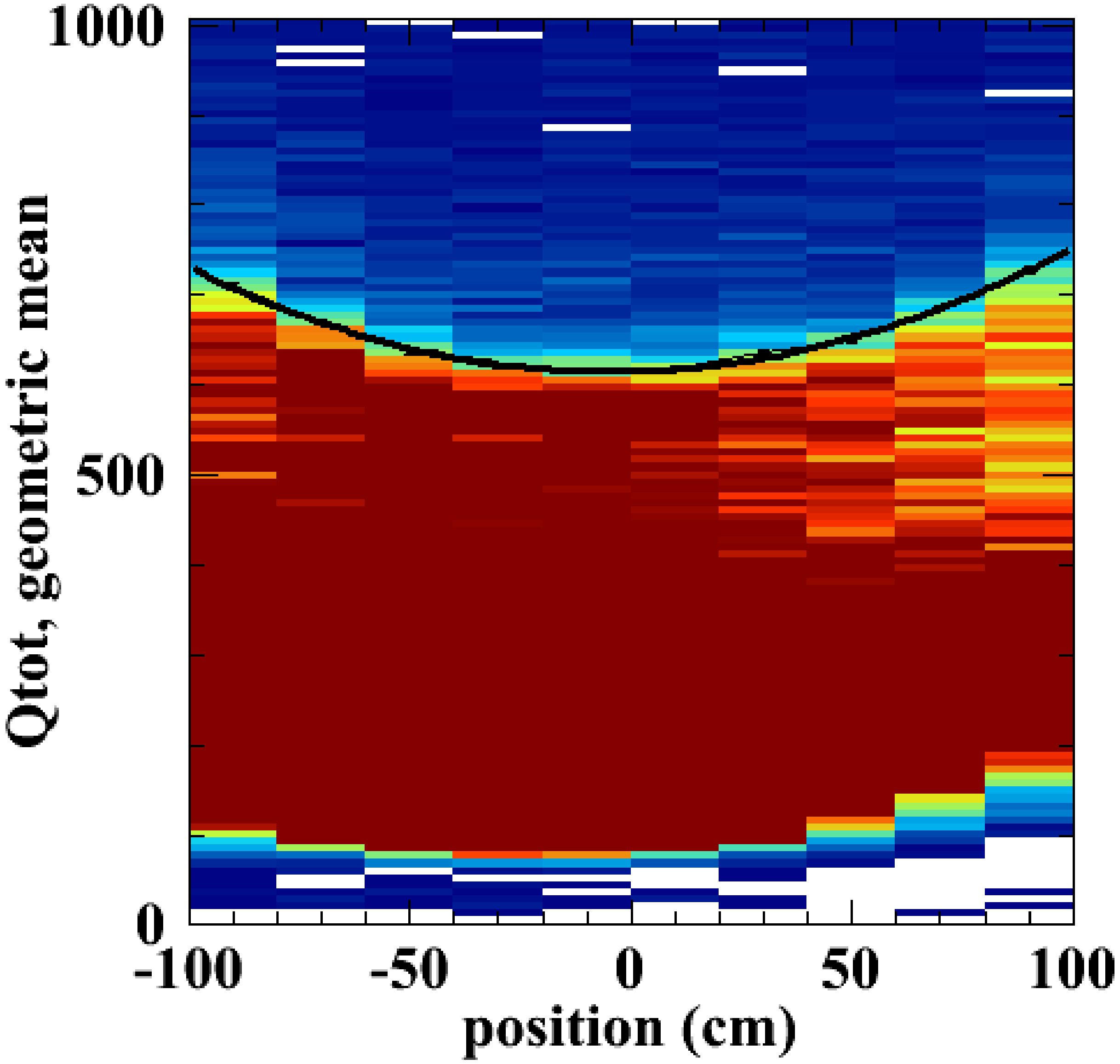

Figure 4.9: The position dependence of the geometric mean pulse height in a neutron wall bar, from the 4.2 MeV Compton edge of an AmBe gamma spectrum.

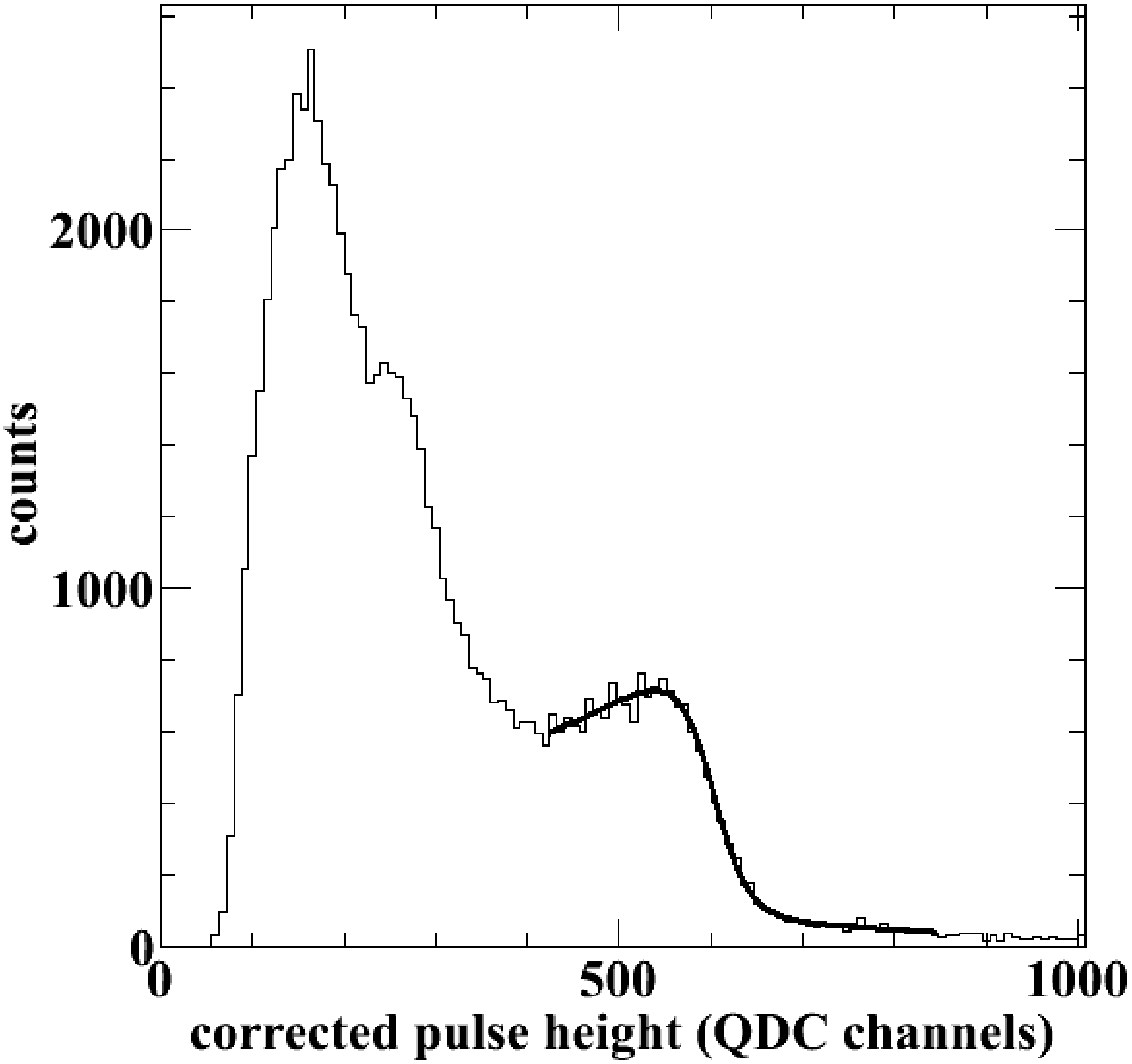

Figure 4.10: The pulse height spectrum in the neutron wall from an AmBe source. The edge is fit with a fermi function between the background and the signal. The Compton edge provides a calibration point for the neutron wall light.

prominent cosmic ray component is muons with approximately 4 GeV kinetic energy. High energy muons were simulated passing vertically through a neutron wall bar in the GEANT simulation described in Section 4.3.3.4. The energy deposited followed a landau function with a most probable value of 11.02 MeV. A similar distribution is observed in the cosmic ray data, for events that pass through all 24 bars at a given incident angle. To determine the calibration for completely vertical events, the spectrum is divided into 5 degree bins and each bin is fit with a landau function. Finally, the most probable value from the landau functions is fit as a function of incident angle and extrapolated to the value for vertical events, as shown in Figure 4.11.

The maximum calibrated geometric mean varies with position, because it requires that the signal detected on both sides of the wall is above the discriminator threshold and below the QDC overflow. This means that the maximum calibrated light output is larger at the center of the bar than at the sides. However, by finding the position dependence of the light collected on one side of the bar, the expected geometric mean can be reconstructed when one side overflows. The maximum detectable light output is then at the sides of the bars. Using this reconstruction, most neutron wall bars could detect between 2 and 24 MeVee light pulses independent of the hit position. Two bars in the forward wall were removed due to higher thresholds.

4.3.1.4 Pulse Shape Discrimination

The pulse shape discrimination described in Section 3.2 and Figure 3.12 is achieved by plotting the integral of the first 30 ns of signal against the integral of the total signal. Both are taken as the geometric mean of the signals from the opposite sides of the bar, to remove

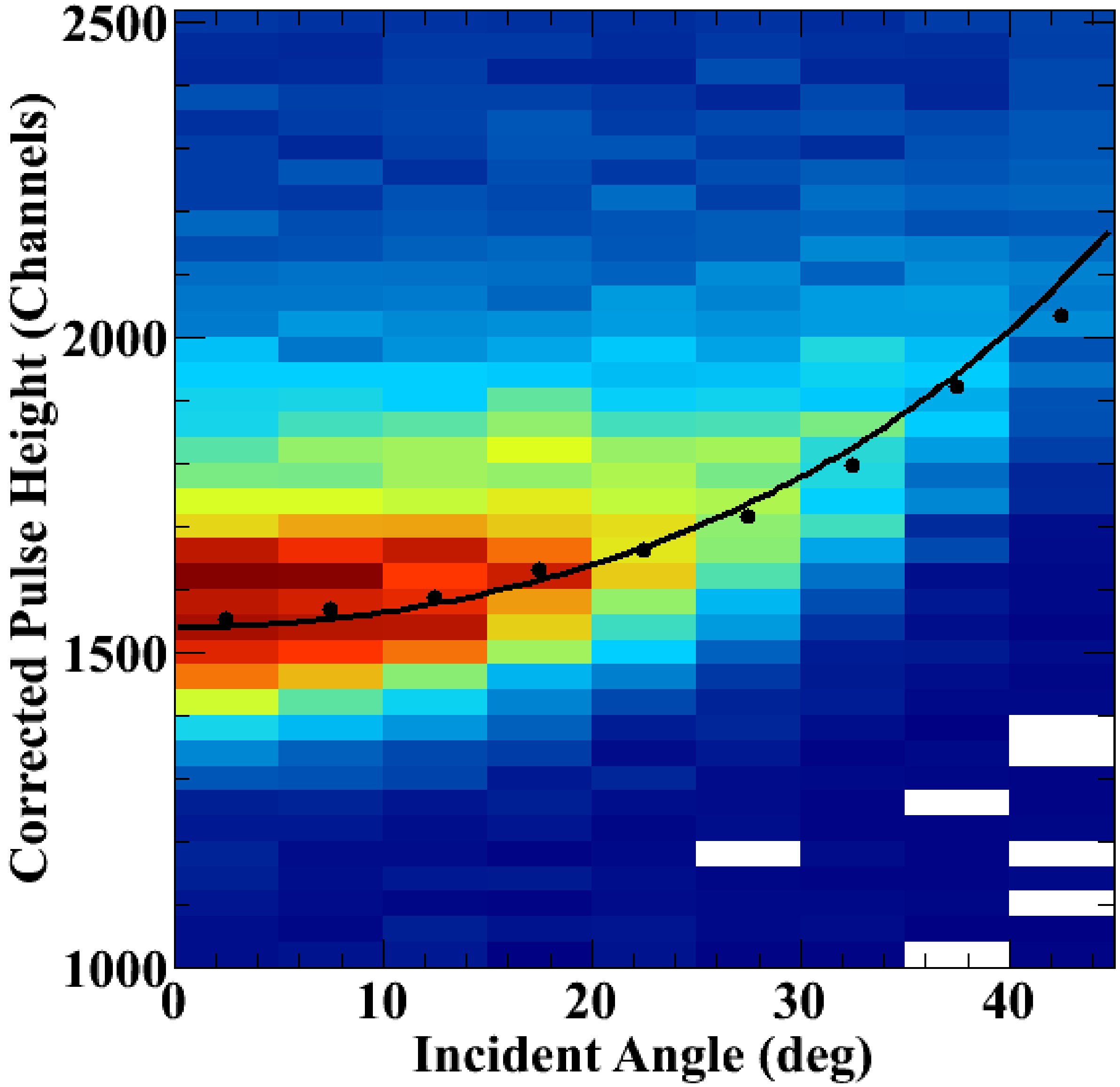

Figure 4.11: Uncalibrated pulse height in a neutron wall element vs the incident angle of cosmic rays. The black points are the most probable value from a landau function fit of each angle bin, and the line is a 1/cos(ϑ) fit to those points.

position dependence. A flattened PSD spectrum is created by subtracting a portion of the total signal from the fast signal, so that the distance between lines is a larger fraction of the ordinate axis. Figure 4.12 displays a sample flattened PSD spectrum, which contains three lines rather than the canonical two. The top line contains the least ionizing particles, which include both electrons scattered by gamma rays and charged particles that escape from the detector without stopping. The middle line is the result of protons that stop in the detector, either directly from the reaction or recoiling from neutrons. The bottom line is the most ionizing, containing alphas from the reaction or from neutron collisions on Carbon in the detector.

4.3.1.5 Proton Veto Matching

The pulse height in the proton vetoes is not calibrated into deposited energy. However, the energy deposited in the PV combined with the time of flight to the neutron walls provides element identification by the dE-TOF method. The light collection in each PV is position dependent. The PV itself provides no position information, but the location of the hit on the neutron wall determines the position of the PV hit. The Hydrogen PID lines are profiled and matched as a function of position with a PV element, and between the elements in the array. For the narrow PV bars in front of the forward wall, matching is only necessary in the vertical direction, indicated by neutron wall bar. For the square PV paddles in front of the backward wall, both vertical and horizontal matching is necessary. The wall is divided into twelve horizontal cuts of equal size to approximate the resolution of the PV bars. Near the PMTs in the PV paddles, the PID lines became very wide and unusable, indicating a partial breakdown in the coupling of the light guide to the PMT.

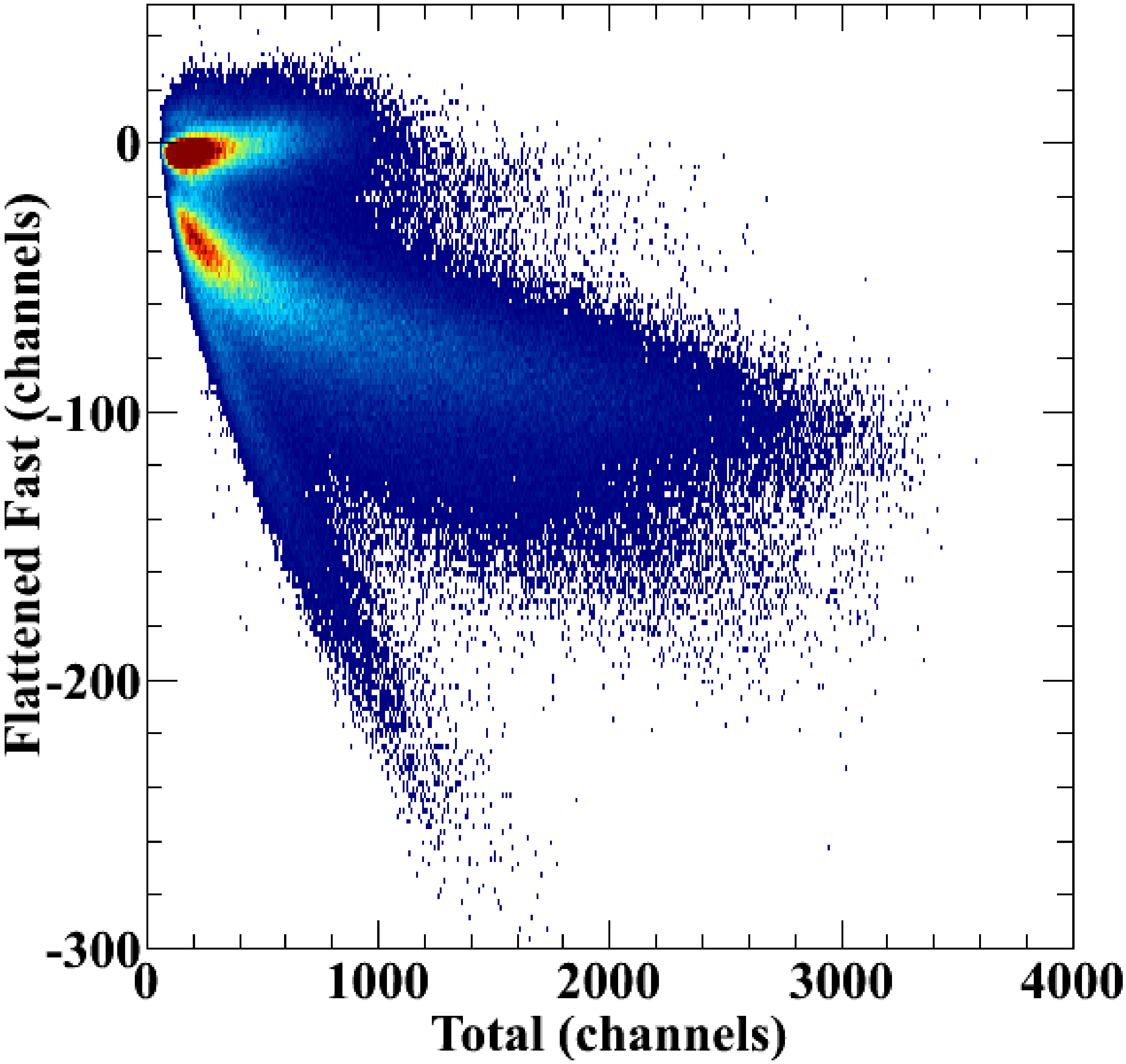

Figure 4.12: A flattened neutron wall PSD spectrum. The three distinct lines are, from top to bottom, gamma rays, neutrons and protons, and alphas.

These regions are not usable for PID, and were excluded from further analysis. Where heavier elements were identifiable, matching the Hydrogen line caused those lines to match within a given PV element but across the array, indicating differing thicknesses or effective thicknesses (rotations) between the elements. The matched PID plot in Figure 4.13 shows the resolution improvement relative to the unmatched spectrum.

Gating on events within the Hydrogen PID band of a particular proton veto reveals the image of that veto in the position spectrum of the wall behind it. For the vertical veto bars in front of the forward wall, this is a broad gaussian on top of a background. For event identification, the edges of the position gates include 95% of the gaussian. Including the tails is more detrimental than beneficial because more neutrons are included in the gate.

The PVs do not cover the whole area of the neutron walls. In particular, the edges of the walls are not well covered. This is apparent from charged particle stopping lines in the NW, which are shown in Figure 4.14. These lines overlap with the neutron spectrum and cannot be distinguished above the 24 MeVee light cutoff so they cannot be used in place of the proton vetoes, but they provide an independent check of the proton veto efficiency. A neutron wall position spectrum gated on the proton stopping line reveals that the top and bottom bars and the edges of the walls are incompletely shadowed. This is considered a bad region during event reconstruction.

4.3.2 Event Reconstruction

Events are reconstructed by examining NW PSD and possible PV PID for a given hit, which together encode the information needed to identify what particle caused a signal in the neutron wall. This becomes more difficult when there are multiple hits in the wall or in

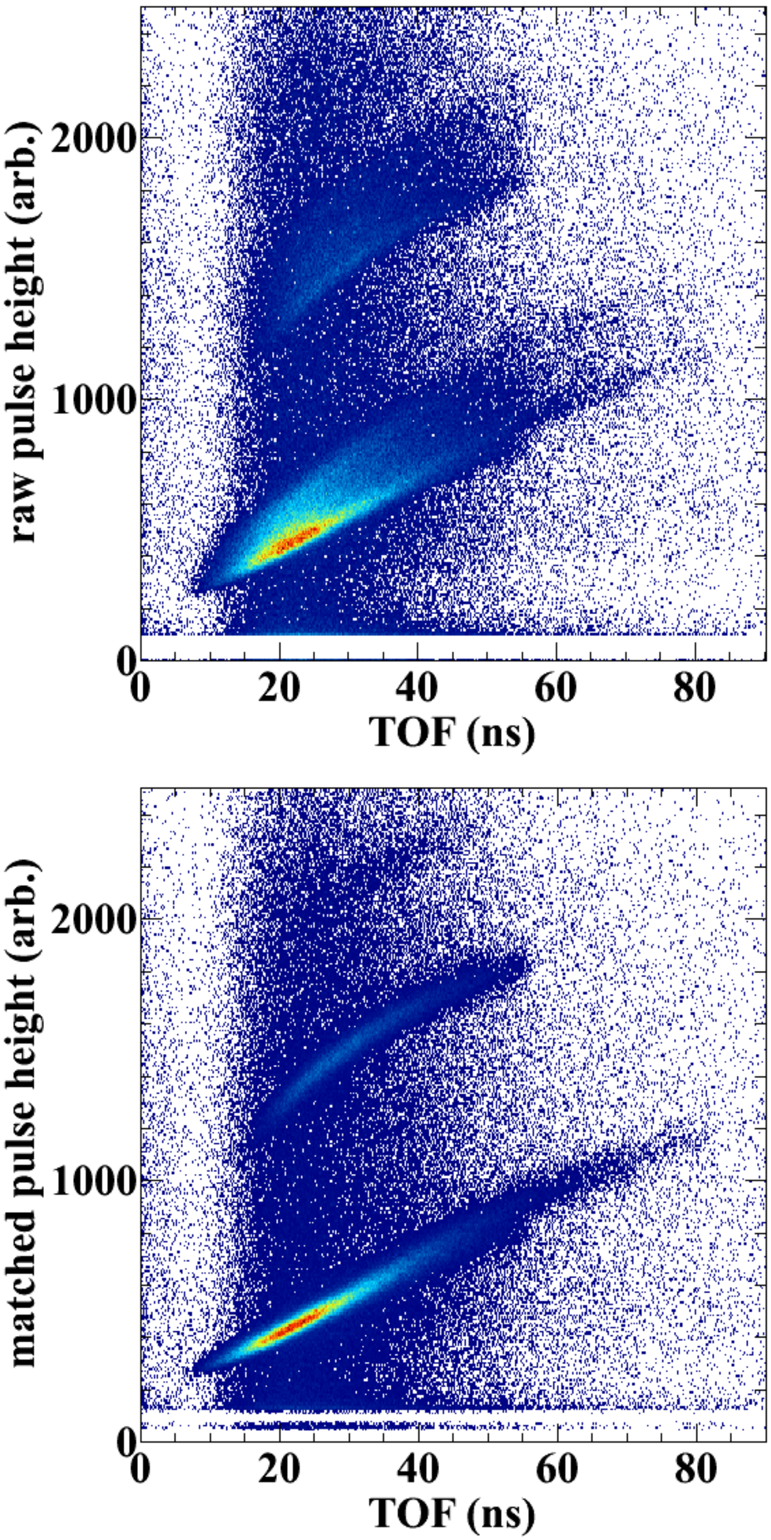

Figure 4.13: (top) Raw proton veto PID. (bottom) Matched PV PID. Here TOF is the time of flight for the observed particle to travel between the target and the neutron wall minus the corresponding time of flight for prompt γ rays.

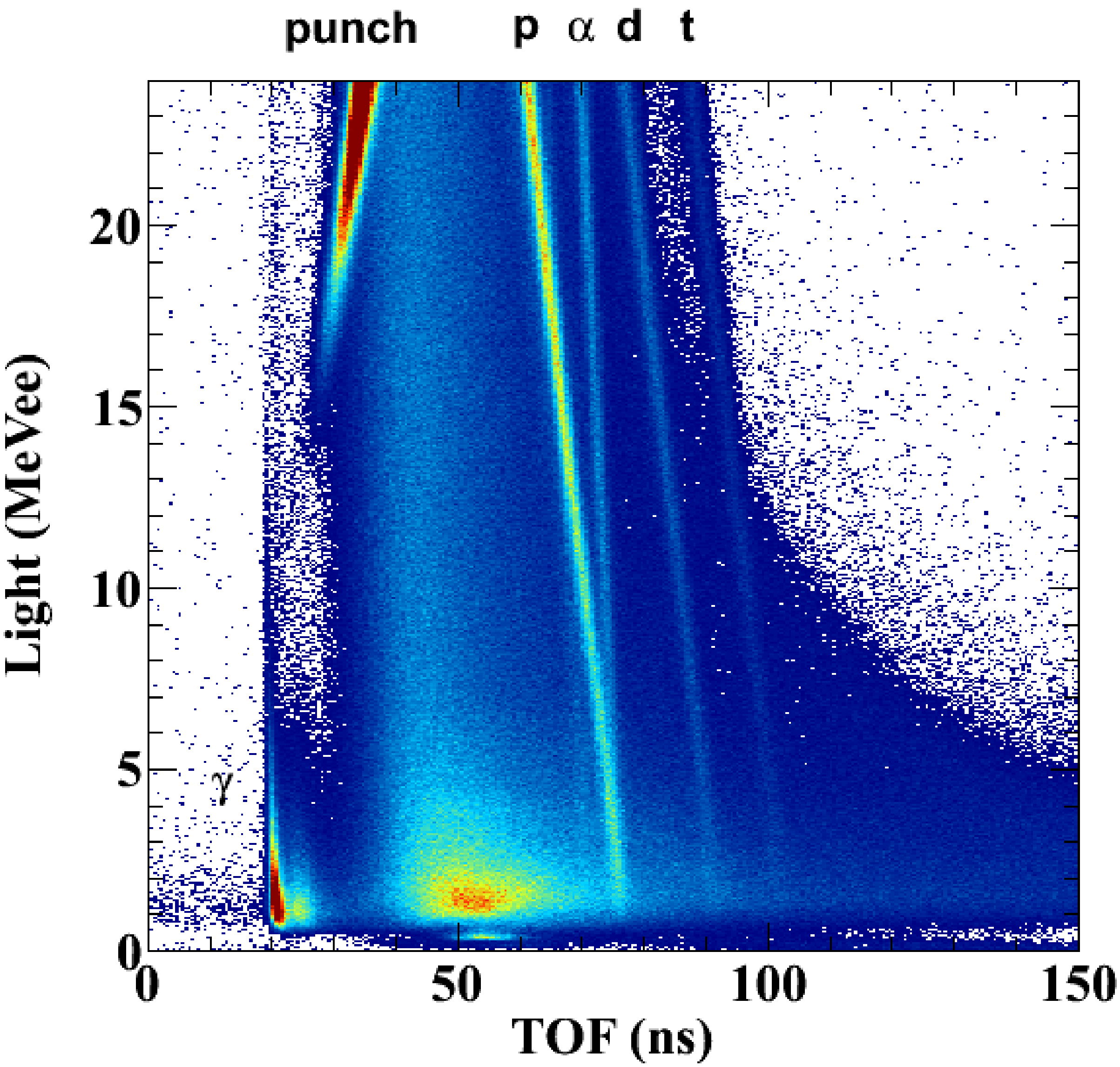

Figure 4.14: Neutron Wall light vs TOF, where TOF is the time of flight for the observed particle to travel to the neutron walls. The prompt γ ray peak, charged particle punch-through, and charged particle stopping PID lines are marked.

the vetoes. All possible PV-NW matches where the NW hit is in the region shadowed by the given PV are checked. The position-dependent PV energy is reconstructed, and a hit is only considered a match if the it falls in a known PV PID line. If more than one PV could match a given NW signal, or more than one NW could match a given PV signal, the hit is considered ambiguous and is rejected. The rejection rate varies similarly to the hit rate, so it depends primarily on the TOF and to a lesser extent on position. In the backward wall, the maximum rejection rate is 15% for the 120 AMeV systems and 8% for the 50 AMeV systems. The variation between reaction systems of the same energy no more than a few percent. Regions of the wall that are poorly shadowed are included in this analysis since a hit there may still pass through a PV. These hits are then discarded. Similarly, the regions that do not provide particle identification in the backward wall veto paddles are counted as charged particle hits, which they very well may be, and later discarded. Hits that are not tagged as charged particles are assigned as gammas or neutrons based on their PSD.

4.3.3 Efficiencies

4.3.3.1 Reconstruction Efficiency

The multihit reconstruction in Section 4.3.2 does not correctly identify all neutrons. There are two major contributions to this. First, the PV array was not completely efficient, even in regions that it completely shadowed. The cause of this is unknown, but is assumed to be the result of a problem in the readout electronics. Second, the rejected particles include neutrons.

The efficiency of the vetoes can be tested using charged particle PID lines in the NW light vs TOF spectrum as shown in Figure 4.14. In this plot, proton, deuteron, and triton lines are clearly separated and have the same slope. The Hydrogen lines can be straightened by defining the parameter:

$$H_{strt} = TOF + c_H L \tag{4.7}$$

where the time of flight has units of ns, the light has units of MeVee, and the Hydrogen straightening parameter c_H is 0.735 ns/MeVee for the forward wall and 0.613 ns/MeVee for the backward wall. After removing γ-rays using PSD cuts, the straightened and projected spectrum produces the peaks in Figure 4.15. The parts of the spectrum that are vetoed and unvetoed are displayed separately. Clearly, charged particles remain in the unvetoed spectrum. In addition, incorrectly vetoed neutrons are evident between the peaks in the vetoed spectrum. It is important to note, however, that Hydrogen scattering out of the detector will not fall into the correct PID line, and this can contribute significantly at early times when the flux is large.

To quantitatively assess the veto efficiency and the loss due to mistakenly vetoed hits, the stopping peaks in the vetoed and total spectra are fit with gaussians on top of a linear or quadratic background, as shown in Figure 4.16. The total spectrum is used rather than the unvetoed spectrum to more easily fit the peaks. The efficiency, ϵ_{PV}, is the ratio between the integral of the peak in the vetoed spectrum to the same same peak in the total spectrum. Similarly, the integral of the region between the deuteron and triton peaks is used to determine the loss fraction, f_{lost}. In the data with E_{beam} = 120 MeV, the punch-through line at short times provides another data point. The efficiency determined from the different peaks varies, and this variation is used as a measure of the systematic uncertainty. The true neutron spectrum S_n can then be calculated from the measured total

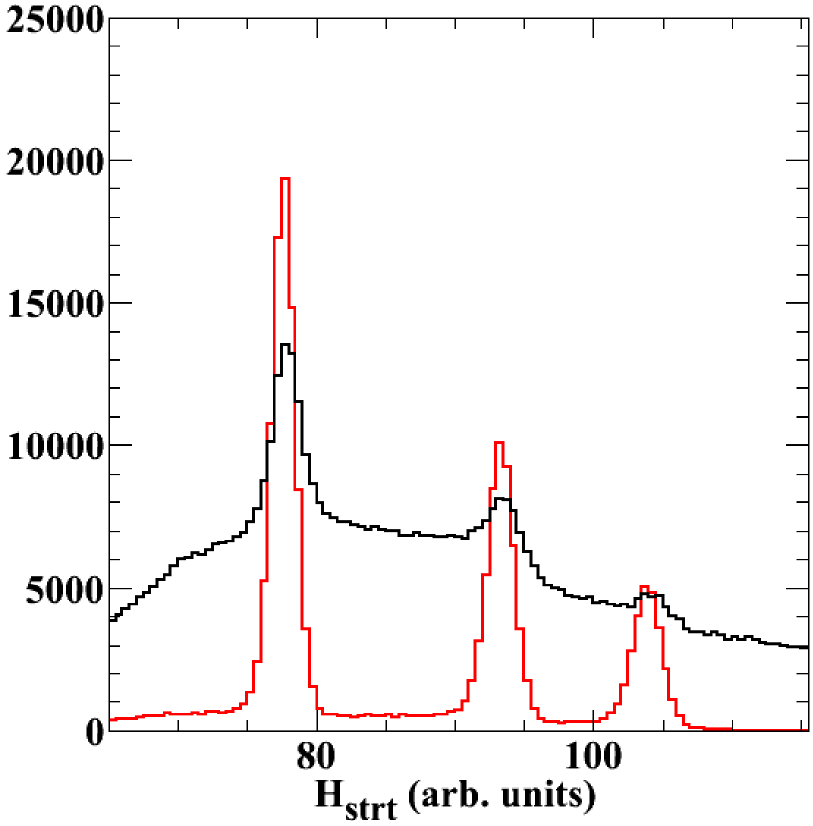

Figure 4.15: Straightened Hydrogen stopping lines in the Neutron Wall, from left to right, proton, deuteron, triton. Events in coincidence with a PV are in red, those not in coincidence are black. Clearly a sizeable fraction of charged particles are not in coincidence with a PV.

and vetoed spectra S_t and S_v as follows.

The total spectrum consists of neutrons and charged particles, but is measured as unvetoed and vetoed components:

$$\begin{aligned} S_t &= S_n + S_c \qquad (4.8) \\ &= S_u + S_v \end{aligned}$$

The vetoed spectrum consists of the charged particles detected by the PVs and the incorrectly assigned neutrons, while the unvetoed spectrum is the complement:

$$S_v = \epsilon_{PV} S_c + f_{lost} S_n \qquad (4.9)$$

$$S_u = (1 - \epsilon_{PV}) S_c + (1 - f_{lost}) S_n \qquad = S_t - S_v \qquad (4.10)$$

Solving for S_n and S_p in terms of S_t and S_v, one gets

$$S_n = \frac{\epsilon_{PV} S_t - S_v}{\epsilon_{PV} - f_{lost}} \qquad (4.11)$$

$$S_c = \frac{S_v - f_{lost} S_t}{\epsilon_{PV} - f_{lost}} \qquad (4.12)$$

Pulse height information is only available up through 24 MeVee in the Neutron Walls. Applying the PV efficiency correction from that data to the events above this cutoff results in a negative neutron spectrum at some values of the time of flight. This suggests that the efficiency correction is not constant, and perhaps varies as a function of TOF. Unfortunately, the charged particle PID lines do not provide enough information to search for and determine a time-varying efficiency. This makes it difficult to analyze the neutron

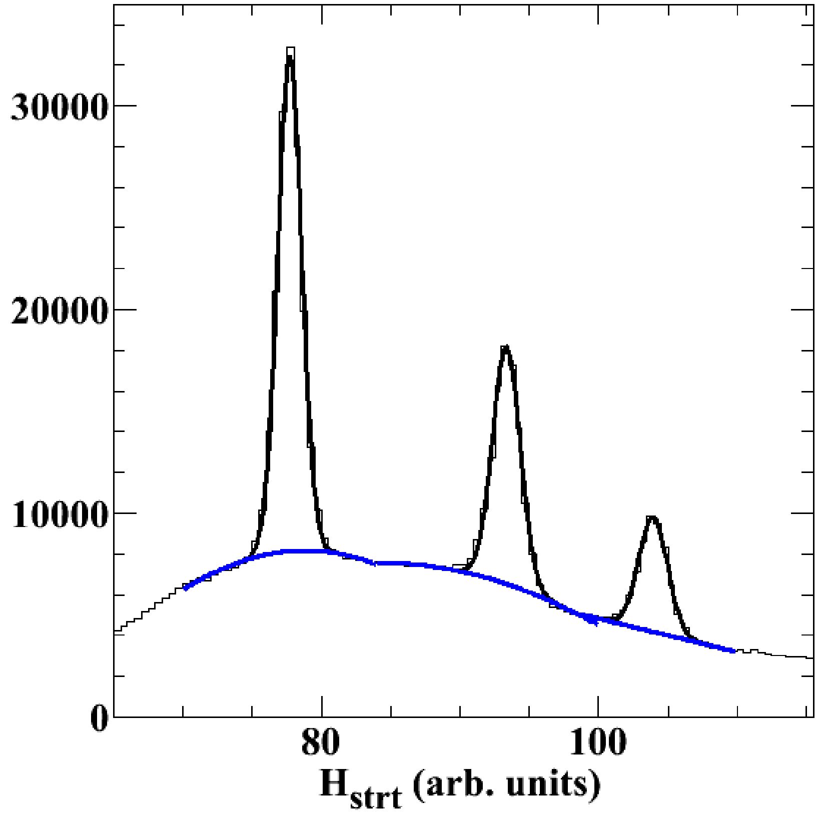

Figure 4.16: Straightened Hydrogen stopping lines of the total spectrum, showing gaussian plus background fit in black and the fit background in blue. Comparing the integrals of these fit peaks to the peaks in the vetoed spectrum measures the efficiency of the proton vetoes.

wall above the 24 MeVee light amplitude. In addition, the charged particle background is much larger for pulse heights above 24 MeVee, and it becomes very risky to include these data because we have no way to crosscheck and constrain the values of ϵ_{PV} and f_{lost}. To reduce the sensitivity to the uncertainties in the charged particle subtraction, we therefore discard the data above the 24 MeVee cutoff. This removes a larger fraction of the charged particle spectrum than of the neutron spectrum, but it does reduce the neutron detection efficiency for higher-energy neutrons.

The final step is to account for the rejected events. The TOF spectrum of rejected neutron wall hits within the 2-24 MeVee light cut is divided by the TOF spectrum of all hits within the same cut, producing a rejection fraction f_{rej} as a function of TOF. Fitting f_{rej} with a high-order polynomial provides a scaling factor $1 - f_{rej}$ that can be applied event-by-event to the spectrum determined above to get the true neutron spectrum. Both the efficiency and rejection rate were determined separately for the different walls for different reactions and using rough bins in Miniball multiplicity to account for variation with reaction impact parameter. As noted in Section 4.3.2, f_{rej} does not exceed 15% in the backward neutron wall, which provides most of the data of interest.

4.3.3.2 Scattering Background

Neutrons that scatter off material in the vault and travel to the Neutron Walls via an indirect path contribute a background to the neutron spectrum. To extract the true neutron yield at a given angle and energy, we measured this scattered background by placing brass shadowbars between the walls and the target to block direct neutrons. Figure 4.17 displays a position spectrum of all types of hits on one of the walls, showing the shadows of these bars. In the figure, the four corner locations are shadowed and have fewer counts than the surrounding regions, while the center location is not shadowed and has more counts. This is due to low energy charged particles stopping in the thin aluminum shadowbar mount but passing through the empty central shadowbar location. The neutron spectrum is mostly unaffected by this material. Also visible at the bottom of the figure are the shadows from the two legs of the mount. This material is thicker and blocks some neutrons, so these regions are excluded from the neutron spectra.

Ideally, the position spectrum of a shadowed neutron wall element would include a square gap with a flat bottom, where the bottom of the gap shows the background, and outside the gap is the result of both background and signal. In reality, the edges of the gap are smeared due to the position resolution of the detector. An example spectrum from the experiment is displayed in the first panel of Figure 4.18. Fitting the region around the gap with a line produces the expected shape of the spectrum in the absence of the shadowbar. The second panel of the figure shows the spectrum scaled by this fit. The value of this spectrum at the bottom of the gap is then the fractional background. To extract this quantitatively, the spectrum is fit with a square gap convoluted with a gaussian:

$$\left(1 + 0.5\mathrm{erf}\left(-\frac{x - x_0}{\sqrt{2}\sigma_0}\right) + 0.5\mathrm{erf}\left(\frac{x - x_1}{\sqrt{2}\sigma_1}\right)\right) \times s + b \tag{4.13}$$

In Equation 4.13, $x_{0,1}$ and $\sigma_{0,1}$ are the locations and resolutions of the gap edges, erf is the Gauss error function, s is the signal fraction and b is the background fraction.

To determine the background as a function of TOF, each shadow spectrum is divided into six TOF bins with equal statistics. Later times had larger backgrounds, as did the higher energy reactions. In many cases with larger backgrounds, the gap edges were

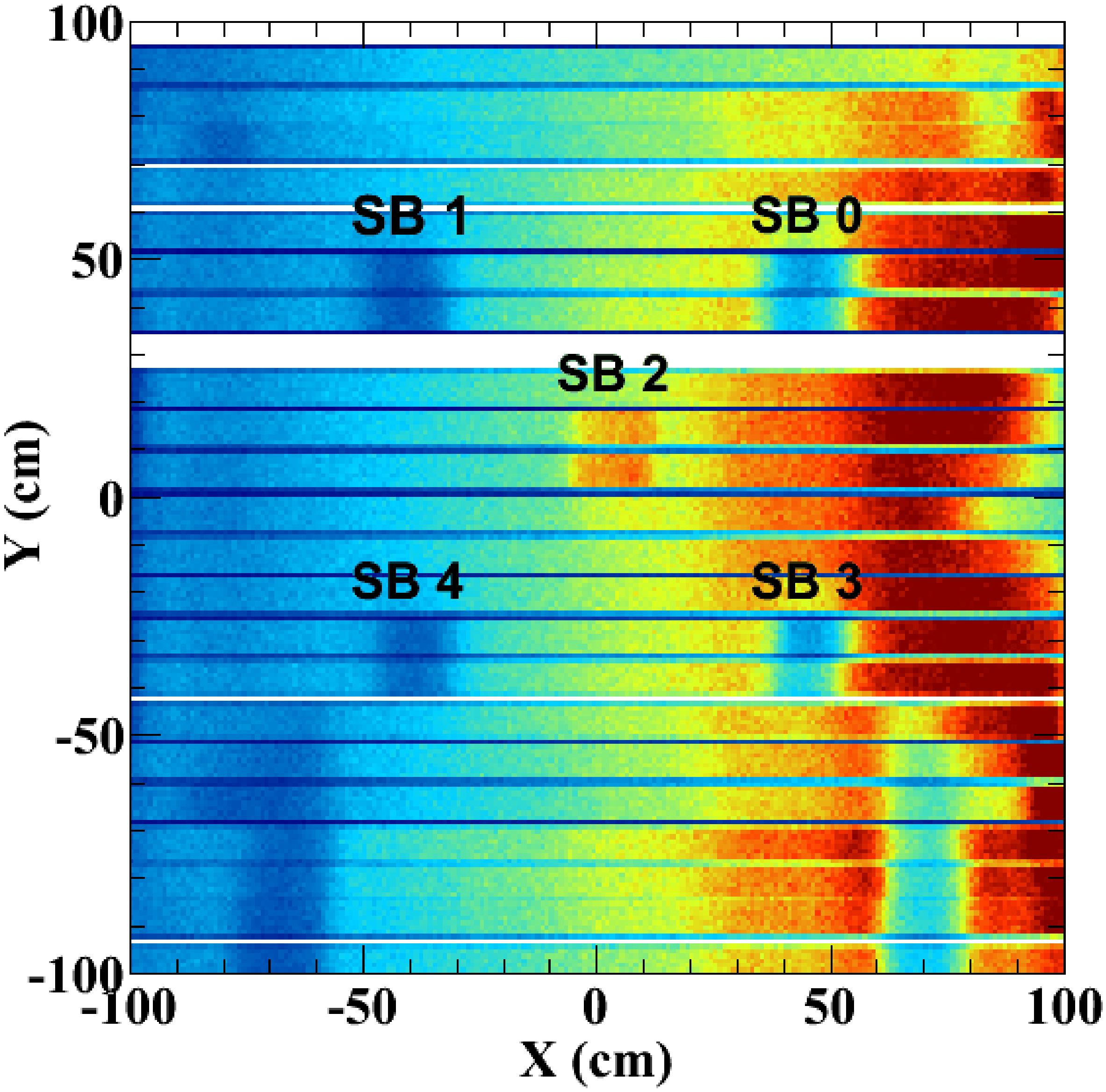

Figure 4.17: A position spectrum of all hits in one Neutron Wall with shadowbars (SB) in place. The beam axis is to the right of the figure. Red indicates many hits and blue indicates few.

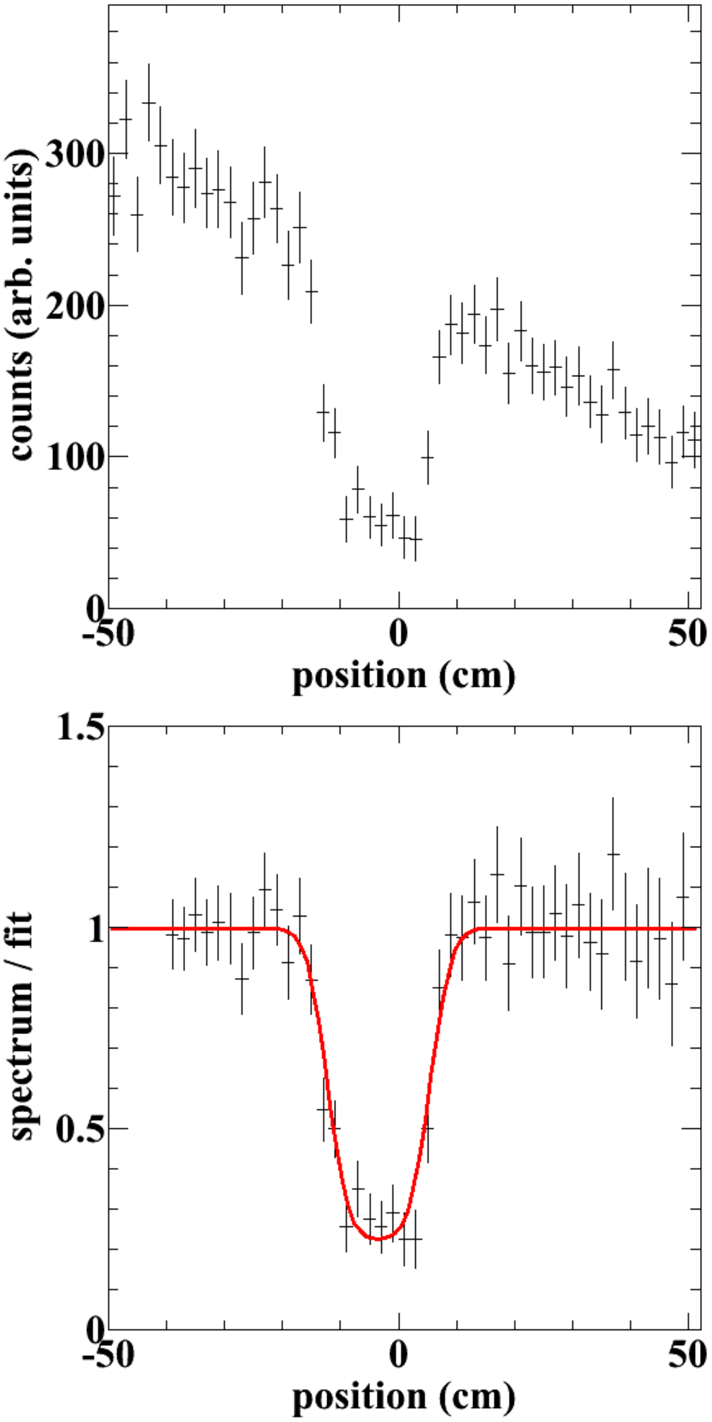

Figure 4.18: a) A neutron position spectrum of one neutron wall element that is shadowed by a brass shadowbar. b) The same spectrum, scaled by the expected spectrum to and fit to indicate the background fraction.

not as well defined as they are in Figure 4.18. As an added complication, the shadowed region in the backward wall is smaller than in the forward wall, because the wall is closer to the shadowbars. The resulting position spectra did not always have a clear bottom. To account for this, the shape parameters of the fits are determined by averaging the values from the most reliable spectra. In the forward wall this led to the edge resolution $\sigma = 2.8$ cm and a gap width of 17.7 cm. Applying the same resolution to the backward wall yielded a gap width of 14.5 cm. From the NW position to time calibration (Section 4.3.1.2), this resolution corresponds to an intrinsic time uncertainty of 0.82 ns FWHM, which is similar to the expected value. The widths are 5% and 3% larger than expected from the measured locations of the NW and SB for the forward and backward walls, respectively. All fits are then repeated with these fixed parameters, so that only the signal and background levels are free. To assess any systematic effects of these parameter choices, additional fits are done for each spectrum using ± 0.5 cm resolution and ± 2 cm width.

When three neutron wall elements are shadowed by the same shadowbar as on the left in Figure 4.19, it is clear that the center element is fully covered in the vertical direction. The fractional coverage of the neighboring bars can also be determined, and the measurements from neighboring bars can then be combined with the center bar measurement to better determine the true background. In this case, the fractional coverage is simple:

$$f_i = \frac{1 - \beta_i}{1 - \beta_0} \tag{4.14}$$

where f_i is the fractional coverage of a partially shadowed bar, β_i describes the depth of the minimum in the fraction spectrum (see Fig. 4.18b), and β_0 is the true background. When the bar is fully covered, $\beta_i = \beta_0$ to within the fit uncertainties, so f_i can be estimated

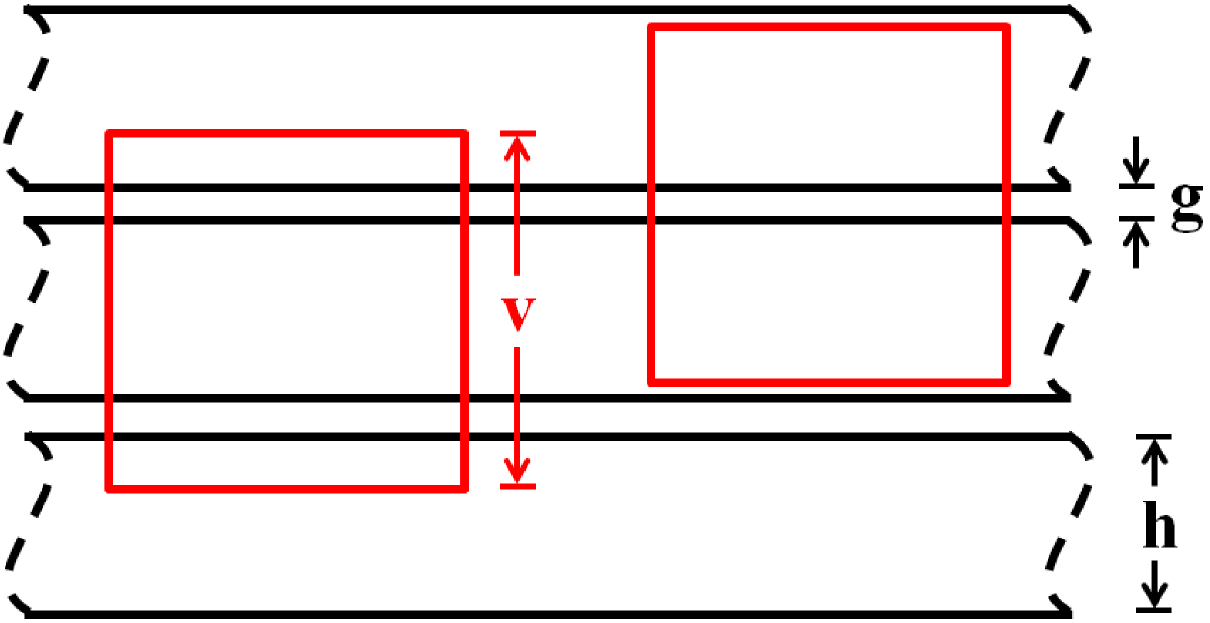

Figure 4.19: Diagram of neutron wall bars (black outlines) and shadows cast by the shadow bars (red outlines) to illustrate background calculations.

for the partially shadowed bar by using the background determined in the neighboring fully shadowed bar. The best f_i for a given bar is obtained by repeating this calculation for every TOF cut and reaction and finding the best fit to all of them, accounting for the uncertainty in the background determination. The vertical extent of the shadow for three bars is then

$$v = \left(\sum_{i=1}^{3} f_i\right)h + 2g \tag{4.15}$$

where h is the height of the active area of one bar and g is the size of the gap between bars as shown in Fig. 4.19.

The height of the active area of a Neutron Wall bar is 7.62 cm, and the measured bar spacing is 8.6 cm. Assuming that the vertical extent of the shadow is 4% larger than measured, similar to the horizontal shadow, the expected shadow height is 18.2 cm on the forward wall and 15.3 cm in the backward wall. In the forward wall this is consistent with the height calculated using Equation 4.15; no cases exist in the backward wall to apply that calculation. Fixing the shadow height places an additional constraint on the fractional coverage in each three bar case and can change the best fit.

In the case that only two bars have visible shadows as on the right in Fig. 4.19, the fractional coverage of each bar can still be determined using the known extent of the shadow v, which does not change between the two and three bar cases, and finding the best fit for the ratio of apparent signals between bars i and j.

$$v = (\sum_{i=1}^{2} f_i)h + g \tag{4.16}$$

$$\frac{f_j}{f_i} = \frac{1-\beta_j}{1-\beta_i} \equiv f_{ji} \tag{4.17}$$

Then

$$f_i = \frac{v-g}{h}\frac{1}{f_{ji}+1} \tag{4.18}$$

$$f_j = \frac{v-g}{h}\frac{f_{ji}}{f_{ji}+1} \tag{4.19}$$

Note that Equation 4.16 differs from Equation 4.15 in that only one gap between bars is shadowed.

The shadow may be shifted between the two cases depicted in Figure 4.19, so that it extends into the gap between the lower bars or even slightly shadows the bottommost bar without producing a noticeable dip in the position spectrum of that bar. This would appear to be a two bar case, but the sum of fractional coverages would be smaller than in Equation 4.16. Then the term $(v - g)/h$ in Equations 4.18 and 4.19 becomes $(v - g - s)/h$, where s is the distance that the shadow extends below the bottom of the middle bar, which is unknown. Note that the values of f_i and f_j calculated with this correction are smaller than the values calculated from the unmodified Equations 4.18 and 4.19. However, the true fractional coverage of the middle bar is one, so using the unmodified Equations 4.18 and 4.19 produces a nonsensical fractional coverage greater than one. This identifies these in-between cases, and the excess in the calculated fractional coverage determines s and thus the corrected fractional coverages.

With all fractional coverages known, the best fit for the background for each reaction and each TOF bin is improved by including the information from neighboring partially shadowed bars. The resulting backgrounds were examined as a function of TOF using the average TOF within a TOF bin. These curves do not display noticeable differences between shadowbar locations on a given wall for a given reaction. This also held when using only three TOF bins, which reduced the errors for each bin but did not provide sufficient information at short TOF. To reduce the uncertainties, the final background fraction is assumed not to vary over the face of a wall. An example of the extracted background fraction is shown in Figure 4.20. There are small but noticeable differences between the background fractions extracted from the two walls, so these are not combined.

The background fraction increases with increasing TOF, but of course can never exceed unity. The data also indicate a decreasing slope with increasing TOF. This suggests a fit of the form:

$$\beta(TOF) = A\left(1 - exp\left(-\frac{TOF - B}{C}\right)\right) \tag{4.20}$$

where A, B, and C are fit parameters. To determine not just the most likely value of the background at a given TOF but also the uncertainty, we scanned over many values of the fit parameters. For each parameter set, we determined the chi-squared of the fit and the corresponding probability from the chi-squared probability distribution:

$$\chi^2 = \sum(\frac{\beta_i - \beta(TOF)}{\sigma_i})^2 \tag{4.21}$$

$$P(\chi^2, \nu) = \frac{1}{2^{\nu/2}\Gamma(\nu/2)}(\chi^2)^{(\nu-2)/2}e^{-\chi^2/2} \tag{4.22}$$

The probability of a given background for each TOF bin was filled into a two-dimensional histogram and normalized. An example of the chi-squared analysis is shown in Figure 4.20 along with the corresponding data. Similarly, the corrected center of mass neutron spectrum was computed for each parameter set. The correction factor f_{SB}, defined as the ratio of the corrected spectrum to the uncorrected spectrum for a given kinetic energy bin, was weighted by the chi-squared probability and filled into a two-dimensional histogram. This was first done for each wall separately, then the corrections were combined. In bins where both walls contribute, each possible new corrected value of the spectrum was computed, sampling over the probability distributions of both spectra, and the new correction factor was weighted by the product of the separate probabilities. Examples of the combined correction spectrum at both beam energies are shown in Figure 4.21. The markers indicate the most probable correction factor, and the errors enclose the central 68% probability.

4.3.3.3 Geometric Efficiency

When constructing the neutron spectrum, we want to express it as a differential multiplicity per event per unit energy and solid angle in the center of mass frame:

$$\frac{dM}{dE_{cm}d\Omega_{cm}} = \frac{dM}{dE_{cm}d\phi_{cm}\sin(\theta_{cm})d\theta_{cm}} \tag{4.23}$$

.

For an infinitesimal bin in the center of mass polar angle vs kinetic energy plot, dE_{cm} and $d\theta_{cm}$ are defined by the bin widths, $\sin(\theta_{cm})$ by the polar angle of the center of the bin, and $d\phi_{cm} = d\phi_{lab}$ is the coverage in the azimuthal direction, which is independent of the frame. $d\phi$ is most easily expressed in the lab, since there it depends only on the polar angle, whereas in the center of mass frame it depends on both energy and angle. The coverage in the lab frame is displayed in Figure 4.22, removing all regions that are incompletely covered by the proton vetoes, are shadowed by the shadowbars or their mount, or have a problem in the Neutron Wall element. The black line shows the fractional azimuthal coverage $f_\phi = d\phi/2\pi$ as a function of lab polar angle. Our differential multiplicity is then

$$\frac{dM}{dE_{cm}d\Omega_{cm}} = \frac{dM/f_\phi(\theta_{lab})}{dE_{cm}2\pi\sin(\theta_{cm})d\theta_{cm}} \tag{4.24}$$

.

By making this substitution, f_ϕ can be used to weight the data event-by-event. The remaining quantities depend only on the center of mass polar angle and kinetic energy coverage, allowing the coverage to be expanded beyond the infinitesimal bin described

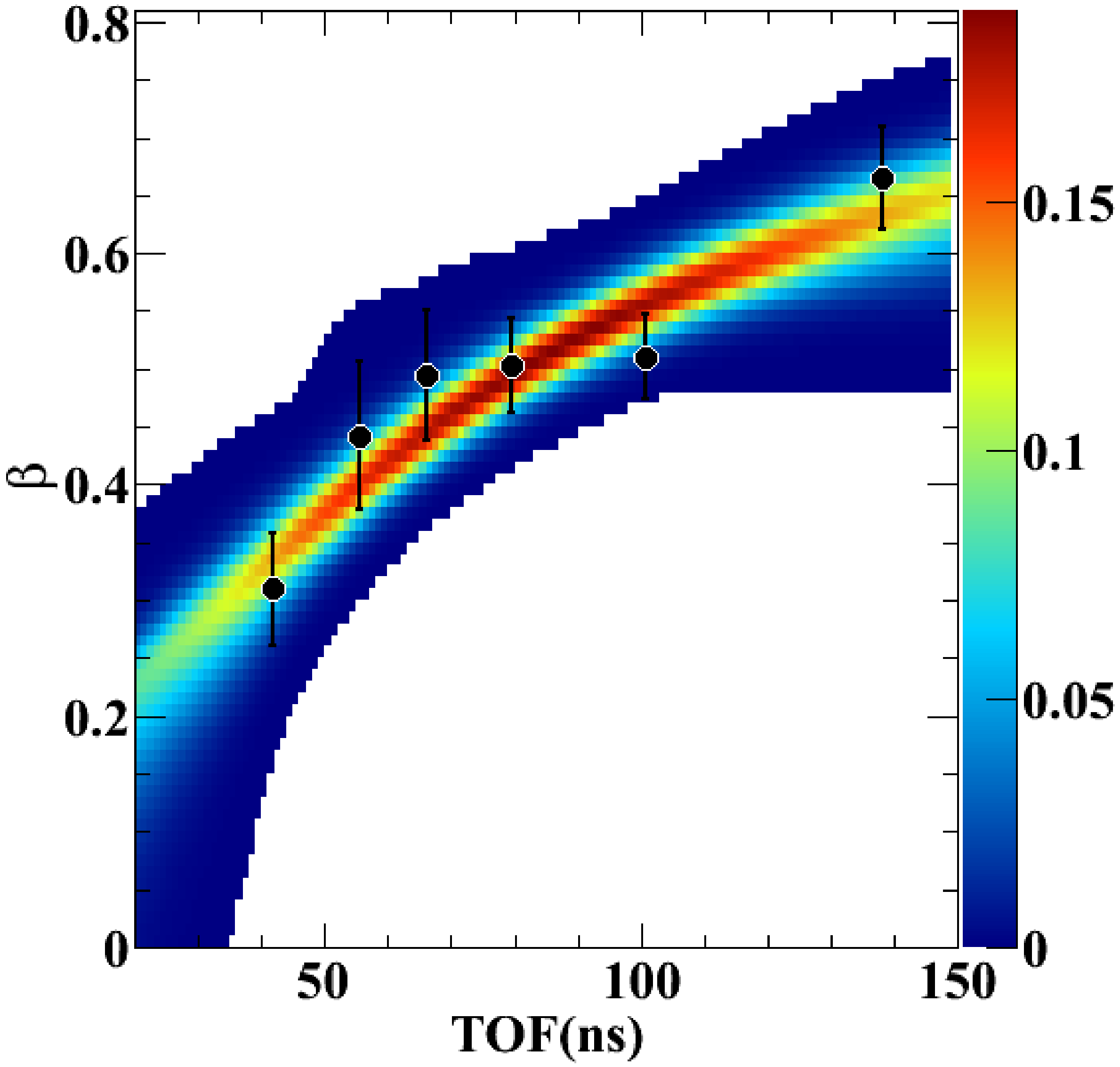

Figure 4.20: An example of the scattering background fraction as a function of time of flight determined by the shadowbar analysis, from the backward wall in the ^{124}Sn 120 MeV dataset. The black points are the data from the background fits and the colors represent the probability of a particular background at a given TOF from a chi-squared analysis.

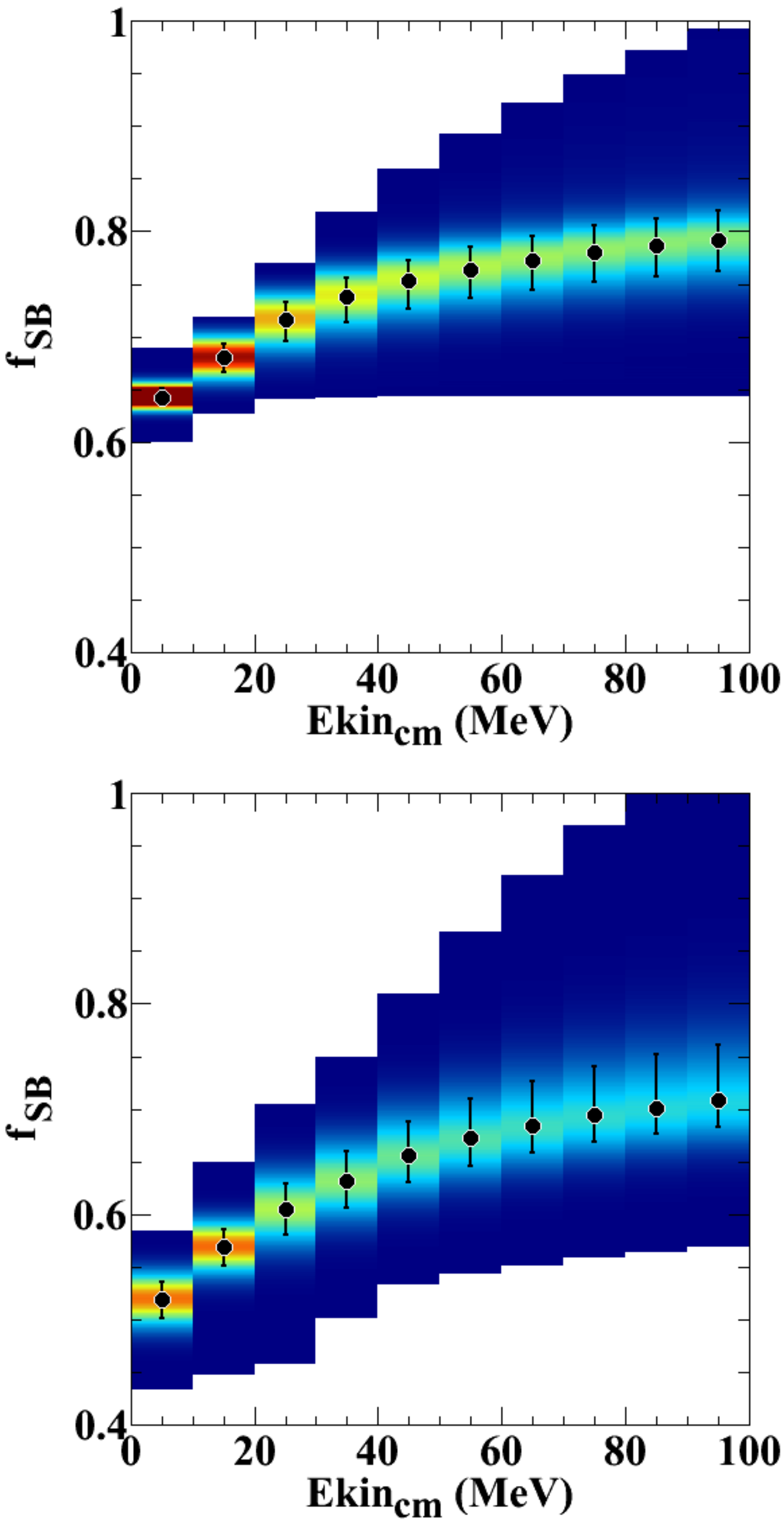

Figure 4.21: The shadowbar background correction factor for the energy spectrum in the center of mass system, for ^{124}Sn at 50 AMeV (top) and 120 AMeV (bottom). The colors represent the probability of a particular correction factor. The markers indicate the most probable correction factor, and the errors enclose the central 68% probability.

previously. A problem with this procedure arises when a rare event occurs near the edge of the distribution where f_ϕ is very small. For instance, if $f_\phi = 0.001$, then that data point will be weighted by a factor of 1000, which is not appropriate when statistics are small. To account for this, data in regions where $f_\phi < 0.03$ are not considered.

Figure 4.23 displays the polar angle coverage vs neutron kinetic energy in the center of mass frame for each beam energy. Because we are most interested in transverse neutron emission, we only examine the polar angle range between 70°and 110°in the center of mass system. The black line shows the adjusted coverage $2\pi\sin(\theta_{cm})d\theta_{cm}$ within that cut, which forms most of the denominator in Equation 4.24. The spectrum is evaluated for $dE = 1$ MeV. When the spectrum is displayed with a courser binning, the 1 MeV bins have been averaged together. This is equivalent to determining the expected multiplicity in each kinetic energy bin prior to rebinning as if it fully covered the polar angle range of interest. This maintains the correct weighting within each displayed bin.

4.3.3.4 Detector Physical Efficiency

Neutrons with kinetic energies of tens or hundreds of MeV have a low probability of interaction in matter. To determine true neutron spectra, the energy-dependent detection efficiency needs to be determined. This factor obviously does not change between different reactions, and so does not contribute to the ratio of spectra.

The dominant neutron reaction at low energies is an elastic collision with a proton. If this were the only relevant reaction, then the efficiency would be given by

$$\epsilon = 1 - exp(-N\sigma_s d) \tag{4.25}$$

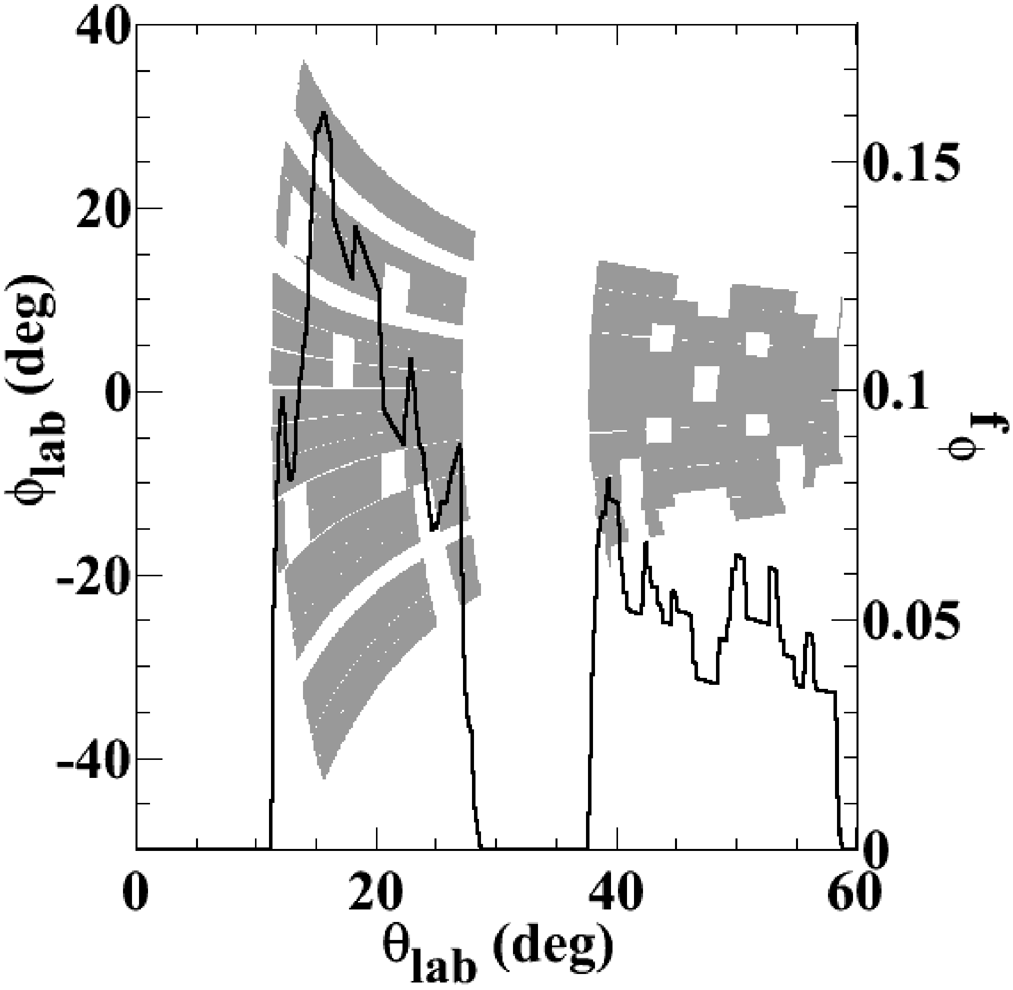

Figure 4.22: Neutron Wall coverage in the lab frame. Gray filled areas represent azimuthal vs polar angle coverage. The black line is the fractional azimuthal coverage as a function of polar angle. See text for explanation.

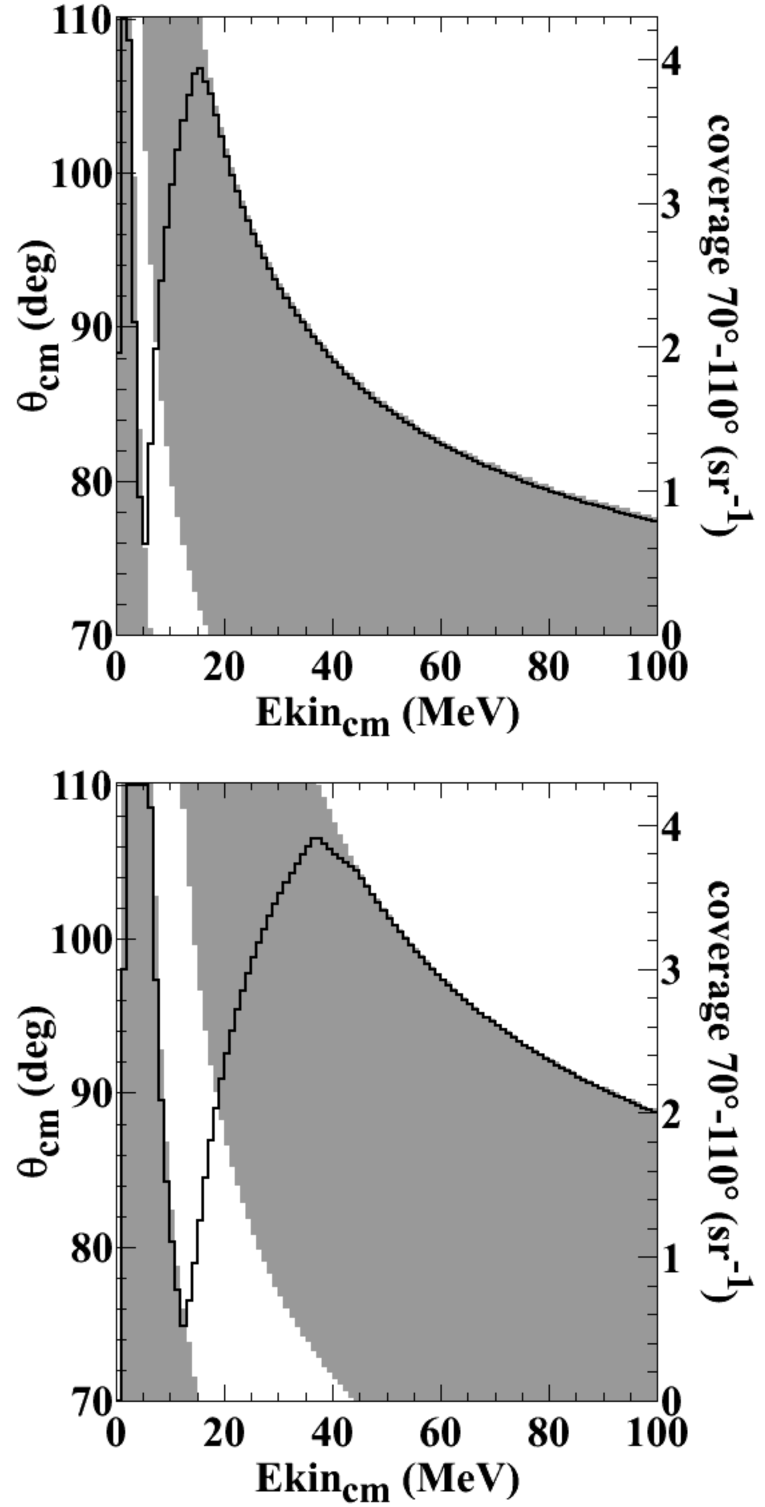

Figure 4.23: Neutron Wall coverage in the center of mass for E_{beam} = 50 AMeV (top) and 120 AMeV (bottom). The gray bands represent the coverage in polar angle vs kinetic energy, with a gap between the two walls. The black line is the solid angle coverage between 70° and 110°.

where N is the proton number density in the detector, σ_s is the scattering cross section, and d is the depth of the detector. Equation 4.25, however, is the probability that scattering occurs, not the probability that it is observed. To be detected, the light resulting from the recoil proton must be above threshold, and below any cutoff. Following Knoll [73], an approximation of the energy distribution of recoil protons dN/dE at a fixed neutron energy is a constant c up to a sharp cutoff, and the light response $L(E) = kE^{3/2}$ for some proportionality constant k. Then, the distribution of the light response

$$\begin{aligned} \frac{dN}{dL} &= \frac{dN}{dE}\frac{dE}{dL} \\ &= \frac{2}{3}\frac{c}{k}E^{-1/2} \\ &= k' L^{-1/3} \end{aligned}$$

which is peaked at low light.

A full treatment of the detector efficiency includes other reactions and other effects. In a large detector, multiple scattering can occur, increasing the light output from a single neutron. Elastic scattering on Carbon in the detector only deposits at maximum 28% of the neutron kinetic energy (see Equation 3.1), and the light output of a recoil carbon is very strongly quenched so it does not contribute. However, it does modify the neutron energy, leading to modified light response in the event of multiple scattering. Inelastic collisions on Carbon contribute strongly in the energy range of interest, and these are shown in Table 4.2. Some of these produce recoil protons, others produce recoil alphas which have a reduced light response and different pulse shape. For high energy recoils or small detectors, the recoil particle can escape the detector without depositing all of its

Reaction	Q (MeV)	Threshold (MeV)	TOTEFF	MENATE_R
p(n, n)p	0	0	yes	yes
^{12}C(n, n)^{12}C	0	0	yes	yes
^{12}C(n, n'γ)^{12}C	-4.44	4.8	yes	yes
^{12}C(n, α)^{9}Be	-5.70	6.2	yes	yes
^{12}C(n, n'3α)	-7.27	7.9	yes	yes
^{12}C(n, p)^{12}B	-12.59	13.6	yes	yes
^{12}C(n, np)^{11}B	-15.96	17.3	no	yes
^{12}C(n, 2n)^{11}C	-18.72	20.3	no	yes

Table 4.2: Reactions involved in neutron detection using the Neutron Walls, and whether they are included in the calculations TOTEFF and MENATE_R

energy, leading to a reduced pulse height and a modified pulse shape (see Section 4.3.1.4). Several computer codes have been developed to account for these and other effects on the efficiency.

One such code is TOTEFF [79], a program originally designed to determine the neutron detection efficiency of a plastic scintillator for neutron energies up to 300 MeV. It includes the cross sections for the reactions in Table 4.2, rescattering based on the mean escape distance from the given detector, and a parameterized light response as a function of deposited energy. Doering [80] modified the built-in detector composition and light response for NE-213, using fits from Verbinski [81] for the latter. He also updated the reaction cross sections based on newer data. The resulting program has been used repeatedly for NE-213 detectors and for the Neutron Walls in particular [2, 80, 82–84]. The output describes the contribution from each of the various reactions and rescattering processes to the efficiency, allowing a separate determination of the proton-like and alpha-like pulse shape contributions. However, it does not indicate what fraction of recoil particles escape from the detector and result in a gamma-like pulse shape. The version of the program at our disposal also suffers at high neutron energies, eventually producing negative efficiencies above 100 MeV. We do not know whether there are improved versions of TOTEFF that do not have this problem.

Another approach is to use a Monte Carlo simulation to determine the detector efficiency. A full simulation of the Neutron Wall geometry has been built using GEANT4 [85]. However, the stock GEANT4 neutron processes are known to be problematic, largely due to the treatment of inelastic collisions on Carbon. Recognizing this, a model called MENATE_R was developed to directly include known neutron cross sections on Hydrogen and Carbon into GEANT4 [86]. Used in a simulation of the Modular Neutron Array (MoNA) [87, 88], MENATE_R produced excellent agreement with data, while the stock GEANT4 processes did not. Importing MENATE_R into the Neutron Wall simulation and modifying the detector composition and light output to match the MoNA simulation allowed me to reproduce those results. The MoNA simulation calculated the light output step-by-step using Birks formula rather than using a parameterization of the entire track as TOTEFF does. To conform to this approach, NE-213 Birks parameters from Mouatassim et al. [89] are adopted. Using the parameterization of the entire track from Verbinski does not qualitatively affect the results.

Another Monte Carlo code named SCINFUL-QMD has been written specifically to determine the efficiency of NE-213 scintillators [90]. At low energies it includes a similar set of reaction cross sections as MENATE_R, but above 80 MeV it transitions to a quantum molecular dynamics model coupled with a statistical decay calculation. The code can only simulate cylindrical detectors, which is a disadvantage compared to GEANT4. However, the trade-off is a code designed with pulse shape discrimination in mind, so that it can ignore gamma-like PSD from escaping protons.

Data from this experiment cannot give insight into the true neutron efficiency, but it does provide the response function or light curve for neutrons of a given energy. Figure 4.24 compares light curves from fully corrected neutron data to those from TOTEFF and MENATE_R at 15 MeV and 65 MeV. These energies were chosen to avoid possible contamination from charged particle PID lines in the data. The escaping protons determined in MENATE_R and SCINFUL-QMD are removed because of their gamma-like pulse shape. TOTEFF does not make this distinction. The simulation curves are normalized to show the efficiency per MeVee light. Since the data is not available in units of efficiency, we only compare the shape of the data to the calculated curves. To put the data on the same scale as the simulations, the data is normalized to match the integral of the TOTEFF curve over a subset of the range. The data is only available between 2 and 24 MeVee, so we do not make comparisons between the simulations outside that range.

At 15 MeV, all three simulations (solid colored lines) reproduce the data (dotted black line) reasonably well. This is in the energy regime still dominated by elastic proton scattering, which is well known. On the other hand, at 65 MeV the shape of the TOTEFF and SCINFUL-QMD curves are similar to the data, but the MENATE_R curve has entirely the wrong shape. Also at this energy, the TOTEFF curve exhibits oscillations that may indicate an instability in the calculation, although these are only of order 0.1% total efficiency. The TOTEFF response function also starts to diverge from the data for the largest light outputs. The SCINFUL-QMD response function is quite similar to the data in this region.

Figure 4.25 displays the detector efficiency as a function of neutron kinetic energy determined by the three calculations, for light pulses between 2 and 24 MeVee. No

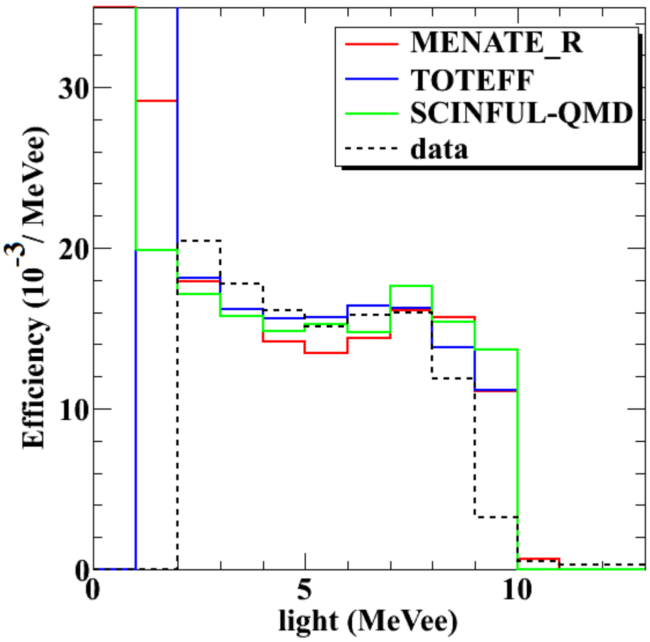

(a) Light response function from 15 MeV neutrons.

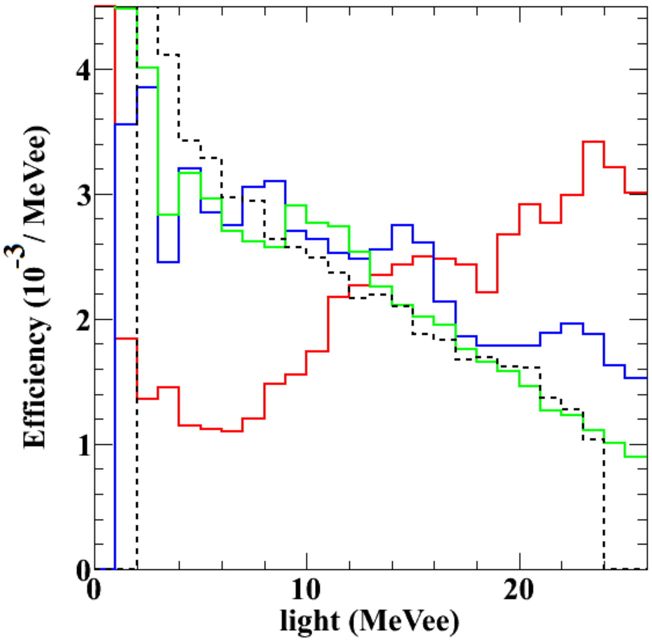

(b) Light response function from 65 MeV neutrons.

Figure 4.24: A comparison of the light curves from TOTEFF (blue), MENATE_R (red), SCINFUL-QMD (green), and data (dashed black) at different neutron energies. The curve indicates the probability that a neutron of the given energy will produce a certain amount of light in the detector, so the y-axis is a differential efficiency.

direct comparison to data is possible. To account for the escaping protons in the TOTEFF calculation, I apply the fraction of escaping protons determined by the GEANT calculation to the TOTEFF calculation. As in the light curves, the MENATE_R efficiency includes a spike that is not matched in the the other calculations. At high energies, TOTEFF and MENATE_R are very similar, while SCINFUL-QMD indicates a much larger efficiency. The light curves in Figure 4.24 make it clear that MENATE_R does not compare well to data at those energies, but it is not certain from those plots whether TOTEFF or SCINFUL-QMD is a better choice. However, the TOTEFF calculation becomes nonsensical at high energies. To consider it further, I extend the TOTEFF efficiency above the energy where TOTEFF becomes unreasonable, by creating a combined efficiency that relies on TOTEFF below 80 MeV, MENATE_R above 100 MeV, and smoothly transitions between the two in the intermediate region. This combined efficiency can then be further tested against the SCINFUL-QMD calculation.

The data from the current experiment provides one more check on the detector efficiency. Each reaction studied is symmetric in the center of mass, meaning that the spectra should be symmetric about $\theta_{cm} = 90°$. Different center of mass angles at the same center of mass kinetic energy sample different energies in the lab, with a wider spread for a larger beam energy. For example, the lab energies sampled by different center of mass angular cuts in the 120 AMeV reactions are shown in Figure 4.26. If the ratio of the detector efficiencies sampled by symmetric angular cuts is correct, then the corrected spectra in those cuts should be the same.

Neutron spectra for a few angular cuts are shown in Figure 4.27 without any detector efficiency correction, corrected with the extended TOTEFF efficiency, and corrected with

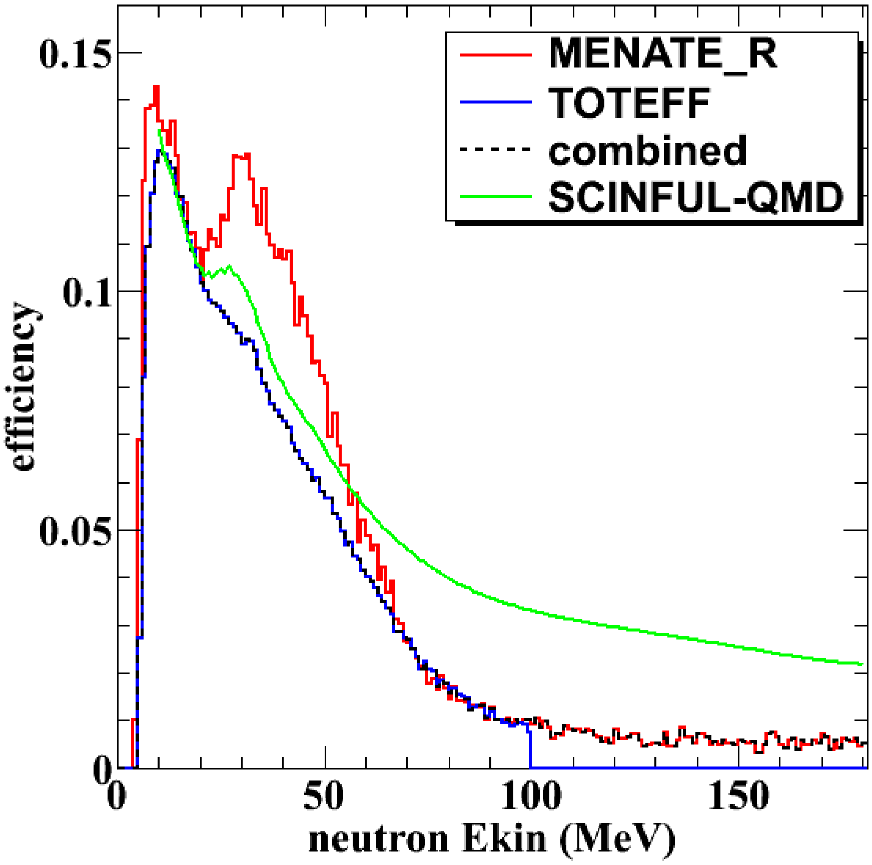

Figure 4.25: Neutron wall efficiency determined by three calculations, with a 2 MeVee light threshold and a 24 MeVee light cutoff.

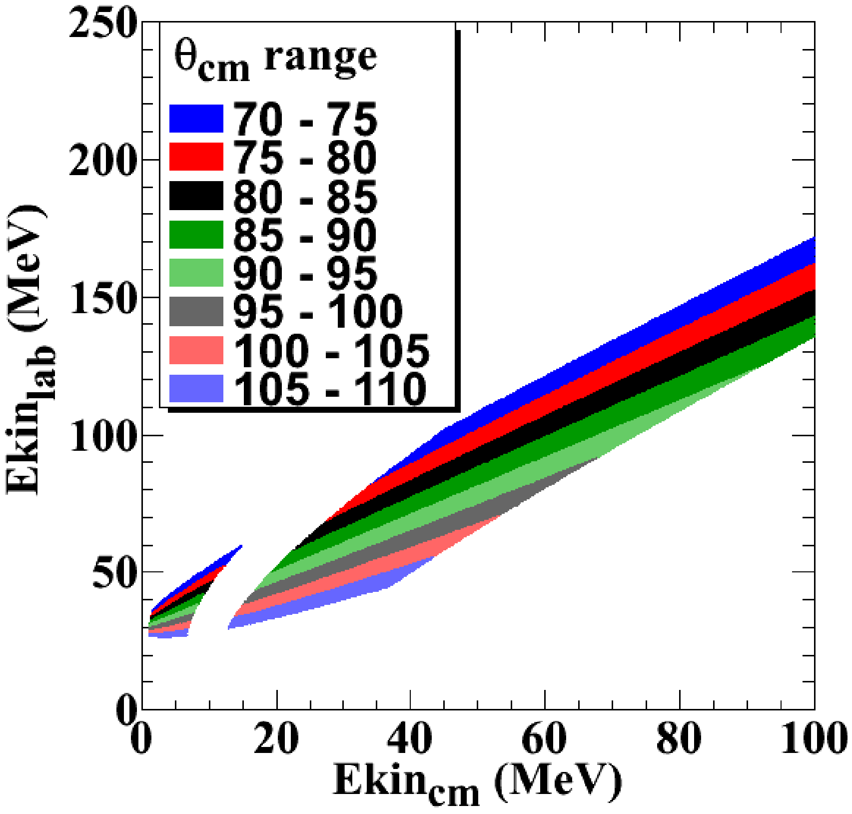

Figure 4.26: The kinetic energy of neutrons in the lab system vs the kinetic energy in the center of mass system, separated by polar angle in the center of mass.

the SCINFUL-QMD efficiency. The MENATE_R efficiency is not considered due to the poor response function comparison in Figure 4.24b. Note that these spectra are for illustration of the detector efficiency only, and do not include all the other corrections. Spectra that have angular cuts symmetric around 90° have the same color, which should be equal where both cuts have reasonable coverage. This is clearly not true in the raw spectra in the top panel, where the backward angle spectra are larger throughout. This affirms what we already know: a flat detector efficiency is not reasonable. The different angles, at different lab energies, must have different corrections. However, the corrected spectra in the middle panel show that the TOTEFF detector efficiency in Figure 4.25 does not fix this problem. Instead, the corrected forward spectra are much larger than the backward spectra in the region from Ekin_{cm} = 30 - 60 MeV. This indicates that the ratio of the correction at the respective lab energies is wrong, and that the TOTEFF efficiency cannot be trusted. The bottom panel, which uses the SCINFUL-QMD calculation, looks better but not perfect. The forward and backward spectra do not match exactly, but they have moved closer together without overshooting each other. As a result, I use the efficiency determined by the SCINFUL-QMD calculation to correct the neutron spectra. It is difficult to assess a reasonable uncertainty for this efficiency. I will include a 10% systematic uncertainty for illustrative purposes, but this likely understates the effect. However, this single-neutron detection efficiency divides out in ratios of neutron spectra, so that uncertainty does not contribute.

The multiple-hit efficiency will not necessarily divide out in the same fashion. However, the hit rate in any given element in the backward neutron wall is of order 1%. In this case, there is only about a tenth of a percent difference between the multi-hit efficiencies for two reactions. The effect in the forward wall can be much higher, but due to coverage cuts, it does not contribute to the data presented in the next chapter.

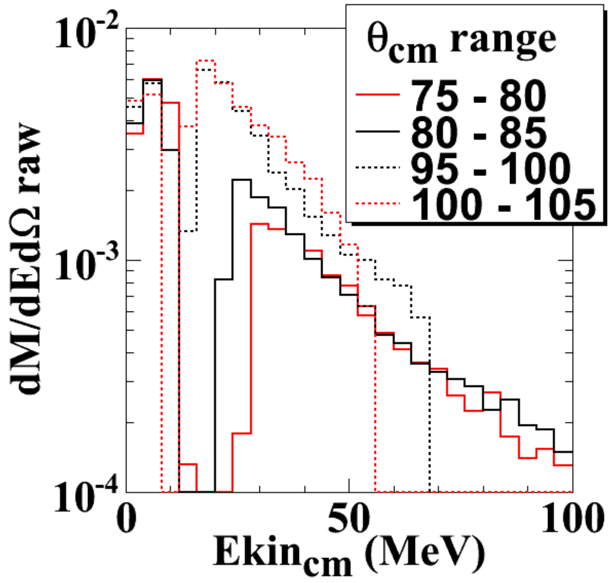

(a) Uncorrected

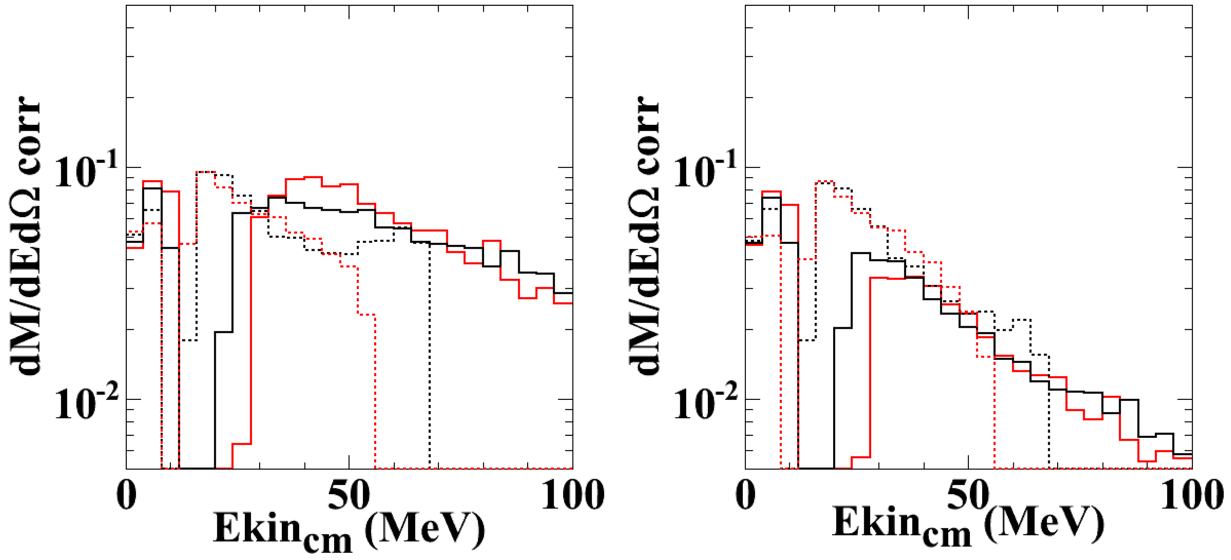

(b) Corrected by the combined efficiency

(c) Corrected by the SCINFUL-QMD efficiency

Figure 4.27: Sample neutron spectra, with and without the detector efficiency correction for different center of mass angular cuts.

Chapter 5

Experimental Results

We now examine the spectra and ratios of spectra produced by the analysis in the preceding chapter. We will consider only the neutron and proton kinetic energy spectra in the center of mass frame, with the requirement that the center of mass polar angle is between 70 and 110 degrees. This transverse cut selects on particles emitted from the participant region of the collision. The charged particle multiplicity in the MSU Miniball is used to construct two impact parameter cuts: very central events with $b < 3$ fm, and mid-peripheral events with 3 fm $\leq b <$ 6 fm. The corresponding multiplicities, which are extracted from Figure 4.1, are indicated in Table 5.1.

Reaction	$b < 3$ fm	3 fm $\leq b <$ 6 fm
^{124}Sn, 50 AMeV	$N_c \geq 10$	$7 \leq N_c < 10$
^{112}Sn, 50 AMeV	$N_c \geq 11$	$7 \leq N_c < 11$
^{124}Sn, 120 AMeV	$N_c \geq 16$	$11 \leq N_c < 16$
^{112}Sn, 120 AMeV	$N_c \geq 16$	$11 \leq N_c < 16$

Table 5.1: Miniball charged particle multiplicity N_c corresponding to the impact parameter cuts used to construct the spectra.

5.1 Systematic Uncertainties

The neutron spectra are presented with systematic as well as statistical uncertainties, as are the ratios involving neutron spectra. Systematic uncertainties in the spectra are derived from uncertainties in the Proton Veto efficiency, uncertainties in the scattering background, and uncertainties in the detector efficiency. The systematic uncertainty due to the proton veto efficiency is determined by constructing the spectra with the largest and smallest values of the efficiency determined in Section 4.3.3.1. The uncertainty is then the difference between these spectra and the spectrum constructed from the best value of the efficiency. These efficiencies were determined using the subset of the data from each reaction system that does not have the shadowbar mounts in place, since these distort the Hydrogen stopping peaks. Using only part of this data produces a similar efficiency but with additional statistical uncertainty, however, the systematic uncertainties do not appear to be run dependent. The uncertainty due to the scattering background is determined in the chi-squared analysis in Section 4.3.3.2. Again, the whole dataset was used to produce the best efficiency determination, but there is no evidence of run dependence in subsets of the data. The uncertainty due to the detector efficiency is harder to quantify, so it is assumed to be 10% of the value of each point in the spectrum. These three uncertainties are combined in quadrature to determine the total systematic uncertainty. No systematic errors are included in the proton spectra, so only the neutron systematic errors contribute to the neutron/proton (n/p) spectral ratio. The fractional systematic error in the n/p ratio is the same as the fractional systematic error in the neutron spectrum.

When constructing ratios of neutron spectra, only the PV and scattering uncertainties contribute to the systematic uncertainties; the uncertainty in the detection efficiency divides out. The full chi-squared probability of the scattering background is propagated to the ratio, assuming that the uncertainties of the two spectra are independent. The proton veto uncertainties are also conservatively assumed to be independent, and thus the uncertainty in the ratio is determined through simple propagation of errors from the original spectra. Again, these two components are combined in quadrature to determine the total systematic error in the ratio. The fractional systematic error in the DR(n/p) is the same as the fractional systematic error in the neutron/neutron (n/n) ratio, because the systematic uncertainty arises primarily from the neutron spectra.

5.2 Comparison to Theory

The spectral ratios will be compared to recent simulations by Zhang, which were done with the newly updated ImQMD-Sky transport code [91]. ImQMD is one of the offshoots of the Quantum Molecular Dynamics formalism that was described in Section 1.2. Nucleons are treated as Gaussian wave packets of fixed size, which are propagated through time and space via the classical Hamilton's equations. The nucleons move under the influence of a self-consistent mean field, the local part of which can be directly related to the standard Skyrme potential without the spin-orbit term. In the previous version of the code, ImQMD05 [92–94], the momentum dependent interaction was taken from Aichelin *et al.* [95], who did not include isospin-dependent effects. The current ImQMD-Sky version instead uses an isospin dependent momentum dependent interaction that can be related directly to Skyrme coefficients, which enables the study of the effective mass splitting.

In addition to the mean field interaction in the ImQMD-Sky code, nucleons collide with each other with cross sections that are reduced from their free space values, and the scattering can be blocked by the Pauli principle. The interaction between nucleons leads to the formation of light clusters and intermediate mass fragments, which are identified by the proximity of nucleons to each other in position and momentum space in the final state of the simulation. These clusters are more realistic than those produced in standard BUU approaches, but they do not contain any structure information.

The ImQMD05 version of the code has been used to extract constraints on the symmetry energy from the existing isospin diffusion and neutron/proton double ratio data [26], and the sensitivity of those observables to many of the physics inputs has been studied with the code [55]. These studies were unable to include isovector momentum dependence of the mean field. The calculations discussed in this work were done with the current ImQMD-Sky code, using four Skyrme potentials that sample different combinations of symmetry energy and mass splitting. The four potentials and their relevant properties are listed in Table 5.2. S_0 is the value of the symmetry energy at saturation density, and L is related to the slope at that density:

$$L = 3\rho_0 \left. \frac{dS(\rho)}{d\rho} \right|_{\rho_0}$$

The effective masses are evaluated at $\rho = \rho_0$ and $\delta = 0.2$. The mass splitting is between 5% and 8% in each case. These parameters indicate that the SkM* and SLy4 parameterizations employ similar density dependences of the symmetry energy but opposite mass splitting, and the same is true of Gs and SkI2. All the simulations were performed with a 2 fm impact parameter, comparable to the most central cut on our data. We emphasize that the mean field parameterizations used in these simulations were chosen to study the sensitivity of the n/p single ratios and double ratios to the effective mass splitting and the

Name	S_0 (MeV)	L (MeV)	m_n^*/m_n	m_p^*/m_p
SkM*	30	46	0.82	0.76
SLy4	32	46	0.68	0.71
Gs	31	93	0.81	0.76
SkI2	33	104	0.66	0.70

Table 5.2: The density dependence of the symmetry energy and the effective masses of the four Skyrme potentials used in the ImQMD simulations.

density dependence of the symmetry energy, not to place constraints on those quantities through comparison to data.

5.3 Presentation of Data

Center of mass neutron energy spectra for all four reaction systems are presented in Figure 5.1 as differential multiplicity per event

$$\frac{dM}{dE_{cm}d\Omega_{cm}}.$$

Systematic errors are indicated by curved lines above and below the central impact parameter data. For clarity they are omitted from the mid-peripheral data, but there is little difference between the systematic errors for the two impact parameter cuts. Statistical errors are indicated by traditional error bars, though these are generally hidden by the data markers. The systematic uncertainties have a larger magnitude than the statistical uncertainties, but they do not change the basic trends. The dominant uncertainty is the 10% that was assessed for the detector efficiency. The spectra are only presented for center of mass kinetic energies between 20 MeV and 100 MeV. Below this range the data is of low quality, and there may be contamination from the spectator sources. Above this range the

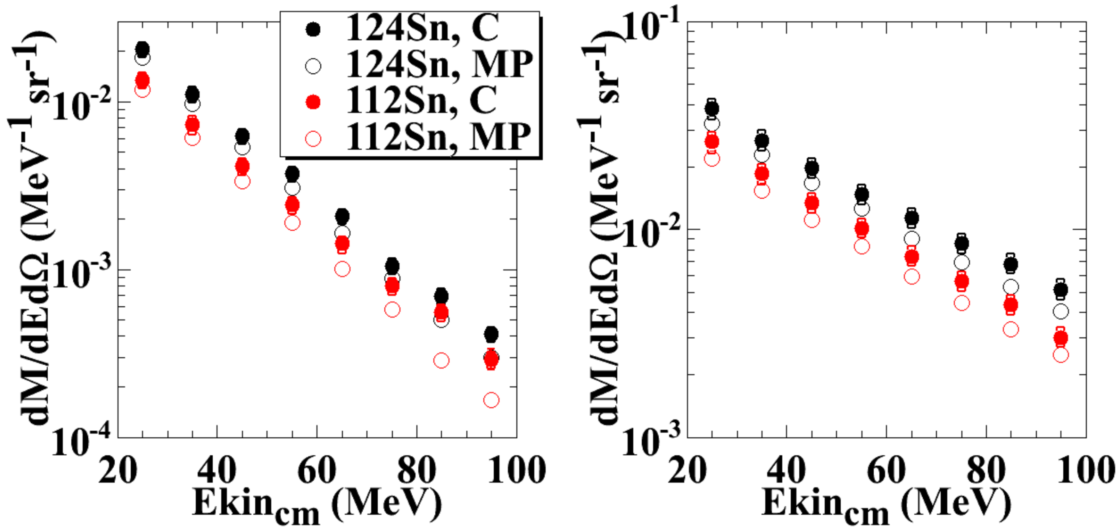

Figure 5.1: Neutron spectra for the 50 AMeV reactions (left) and 120 AMeV reactions (right) for the central (C) and mid-peripheral (MP) impact parameter selections that are given in Table 5.1.

data is limited by low statistics.

The features of the spectra match simple expectations. The spectra all fall off exponentially, as would be expected from a statistical model. In this interpretation, the slope of the log plot is associated with the inverse of the spectral temperature $-1/T$, so the shallower slope of the 120 AMeV data is consistent with the higher expected temperature. Before discussion the fits more extensively it is important to recognize that the spectra also reflect the effects of collective motion, which can significantly influence the slope of the spectrum and temperature derived from fits to it. The temperatures extracted from exponential fits to the spectra are shown in Table 5.3. Interestingly, the 50 AMeV mid-peripheral data has a noticeably steeper slope and thus lower temperature than the corresponding central data. This effect is more pronounced in the ^{112}Sn data than the ^{124}Sn data. In the 120 AMeV data, the mid-peripheral data also implies a lower temperature than the central data, but the effect is within systematic uncertainties.

Reaction	b	T (MeV)	70°-110°	4π	S-P
^{124}Sn, 50 AMeV	$b < 3$ fm	17.7 ± 0.6	6.2	18.1	127.5
^{124}Sn, 50 AMeV	3 fm $\leq b < 6$ fm	16.9 ± 0.5	5.7	16.7	87.8
^{112}Sn, 50 AMeV	$b < 3$ fm	18.4 ± 0.8	3.9	11.4	106.0
^{112}Sn, 50 AMeV	3 fm $\leq b < 6$ fm	16.4 ± 0.5	3.7	10.9	71.4
^{124}Sn, 120 AMeV	$b < 3$ fm	35.6 ± 2.4	11.0	32.2	127.5
^{124}Sn, 120 AMeV	3 fm $\leq b < 6$ fm	33.9 ± 2.1	9.4	27.4	87.8
^{112}Sn, 120 AMeV	$b < 3$ fm	33.3 ± 2.0	7.7	22.4	106.0
^{112}Sn, 120 AMeV	3 fm $\leq b < 6$ fm	32.3 ± 1.9	6.3	18.5	71.4

Table 5.3: Temperatures and total neutron multiplicity from exponential fits to the neutron spectra shown in Figure 5.1. The multiplicity is obtained from the integral of the fit over the energy range from 0 to 1000 MeV, multiplied by the appropriate solid angle coverage. The final column is the expected multiplicity from a simple spectator-participant model.

Extrapolating the exponential fits of the spectra down to 0 MeV and up to very high energy allows an estimate of the total number of neutrons emitted in the transverse direction. If the participant source was isotropic, the total number of emitted neutrons would then be a factor of 2.9 larger than this value. Both multiplicities are given in Table 5.3. The 4π multiplicity can be compared to a simple geometric spectator-participant calculation, where the nuclei are assumed to be spheres of constant density that pass through each other without deflection and any overlapping matter becomes part of the participant source. A perfectly head-on collision would then produce a participant source containing all matter from both of the original nuclei. Since the data samples a range of impact parameters, the expected neutron multiplicity is reduced compared to this limit. Calculating the expected multiplicities at a range of impact parameters and weighting the result by b^2 produces an expected neutron multiplicity, which is also indicated in Table 5.3. Note that it does not depend on the beam energy of the collision.

Clearly, the actual detected multiplicity is greatly reduced compared to this simple model. This is expected: the model does not include any dynamics or clustering. Collisions, which are suppressed by the Pauli principle, are needed to knock these nucleons to the large transverse energies in the spectrum. Also, clustering can cause many participant nucleons to emerge as light clusters rather than free nucleons. However, the trends in the model give some insight into the trends in the data. In both the model and the data, there are always more neutrons emitted from the neutron-rich ^{124}Sn system than from the neutron-poor ^{112}Sn system, for a given energy and impact parameter. More neutrons are also emitted in central collisions than in the corresponding peripheral collisions, which is consistent with a larger portion of the nucleons being participants in the reaction. Interestingly, this effect is smaller in the 50 MeV reactions than in the 120 MeV reactions, which is not expected from the spectator-participant model. In those lower energy reactions, the steeper slope of the mid-peripheral data leads to larger extrapolated values of the spectra at low kinetic energies. Integrating the spectra over just the range shown in Figure 5.1 leads a larger difference between the central and mid-peripheral multiplicities than when the spectra are extrapolated to zero kinetic energy. This may indicate that the exponential fit breaks down for the lowest kinetic energies. Finally, the integrals of a 120 AMeV spectra are larger than the integrals of the corresponding 50 AMeV spectra. This is not indicated by the spectator-participant model. Very likely the increased multiplicity at higher incident energies reflects the expected increased multiplicities for a higher temperature reaction. A higher percentage of neutrons emitted in the transverse direction may indicate an enhanced role for nucleon-nucleon collisions relative to the mean field, as would be expected from transport simulations at these energies.

Next we construct the ratio of neutron spectra between the ^{124}Sn and ^{112}Sn collisions, as shown in Figure 5.2. The uncertainties due to the proton veto efficiency and scattering background are displayed separately for central impact parameters in the top row of plots. The uncertainty due to the proton veto efficiency, which is shown in red, is largest at low energies where more charged particles produce light above the 2 MeVee threshold and below the 24 MeVee cutoff. The uncertainty due to the scattering background is largest at high energies where the statistics of the background measurement are lowest, as shown in Figure 4.21, but they do not vary as much as the proton veto uncertainties. The combined errors are then smaller at high energies, as shown in black.

The bottom plots in Figure 5.2 display data from both impact parameter cuts compared to the ImQMD calculations. Systematic errors are indicated for the central collision data; the uncertainties are dominated by systematics at low energies and statistics at high energies. The ratio of neutrons in the initial collision system $(n_{124}/n_{112})_{syst} = 74/62$ is shown as a dotted line. A departure from this line indicates a sensitivity to isospin-dependent effects. The results of the ImQMD simulations for the different Skyrme potentials listed in Table 5.2 are indicated by the filled regions. These should be compared to the central impact parameter data. Color indicates the sign of the mass splitting, and fill style indicates the density dependence of the symmetry energy. The uncertainties in the data and the uncertainties in the simulations are both large, but some trends are notable.

Both impact parameter cuts, at both beam energies, are significantly different from this initial system ratio. The 50 MeV data (bottom left) displays an impact parameter dependence. While the systematic uncertainties are of a similar size as the splitting between the central and mid-peripheral data, the systematic uncertainties in the two datasets will be in the same direction for any given data point. Therefore, the consistent difference between the two impact parameter selections is not the result of the systematic

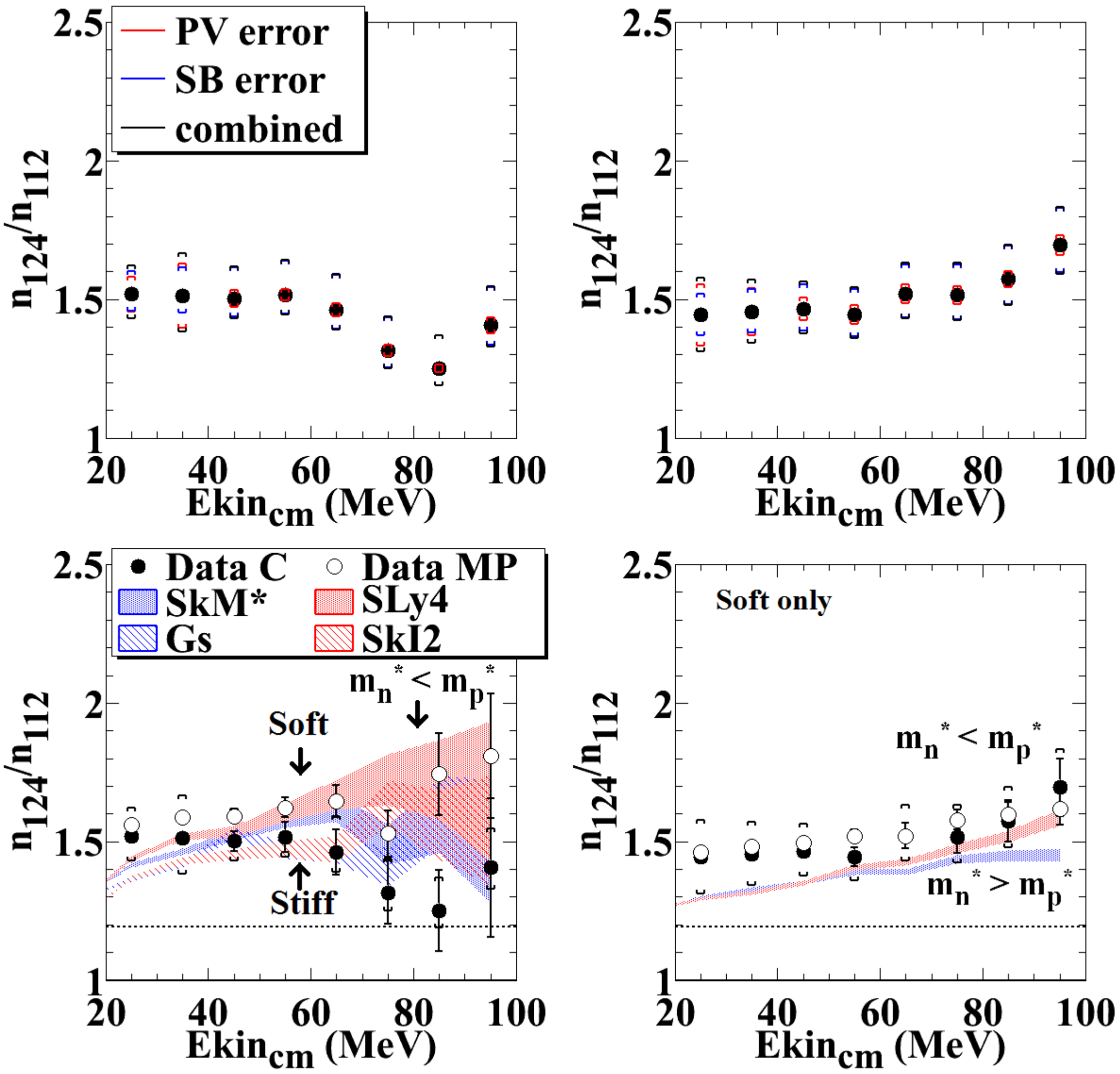

Figure 5.2: Ratio of neutron energy spectrum from the ^{124}Sn + ^{124}Sn reaction to the neutron spectrum from the ^{112}Sn + ^{112}Sn reactions, for the 50 AMeV reactions (left) and 120 AMeV reactions (right). The top row shows the separate contributions to the systematic errors for central collisions, while the bottom row shows both impact parameter cuts and a comparison to simulations. Simulations with a stiff symmetery energy are indicated by diagonal filling and simulations with a soft symmetry energy are indicated by a dotted fill style. Only soft symmetry energy simulations are currently available at the higher beam energy. Simulations employing an effective mass splitting with $m_n^* < m_p^*$ are shown in red, while those with te opposite splitting are shown in blue. The horizontal dashed line is the n/n ratio for the whole reaction system.

uncertainty. Interestingly, this indicates a stronger sensitivity to isospin-dependent effects for larger impact parameters. The reason for this is unclear. It may reflect a larger abundance of clusters at larger impact parameters, which is consistent with a slighter lower temperature. All four simulated interactions under predict the lowest energy data. This discrepancy at low kinetic energies will be a common feature of the ratios, and will be addressed at the end of the chapter. At kinetic energies near 60 MeV, the simulated ratios show a sensitivity to the symmetry energy but not to the mass splitting. The simulations that employ a stiff symmetry energy, i.e. those having a larger slope at saturation density, match the data in this region. At high energies the simulations are more sensitive to the mass splitting than the symmetry energy. The downward trend of the data is better matched by the simulations that employed potentials with $m_n^* > m_p^*$ (blue); the ratios produced with the opposite mass splitting trend upward. The large uncertainties in the simulations and the strong impact parameter dependence of the data make it difficult to draw conclusions from these comparisons.

No strong impact parameter dependence is evident in the 120 MeV data (bottom right). Both the central and mid-peripheral spectra increase slowly with increasing kinetic energy. The statistical uncertainties in both the data and the simulations are much smaller due to increased emission of high energy neutrons. Only simulations with a soft symmetry energy are available, but with both values of the mass splitting. The predicted effect of the mass splitting is seen to be quite small for this observable. Nevertheless, the values of the data at high energy are more consistent with the SLy4 simulation, in which $m_n^* < m_p^*$. However, both simulations systematically under predict the data at low energy, so one can also say that the SkM* simulation better matches the trend of the data, but that there is an offset between the two.

Similar conclusions can be made about the ratios of proton spectra, shown in Figure 5.3. The 50 MeV data is mostly flat at a value around 0.75. The central data is slightly below this value while the data at larger impact parameters is slightly larger. This may be an effect of cluster production, where an increasing fraction of the free neutrons are taken up in the production of the heavier clusters for the more neutron rich system. This impact parameter dependence is opposite that of the neutrons: the central data is further from the equilibrium line, indicating more sensitivity. The ImQMD simulations suggest that the 50 MeV p/p ratio should be more sensitive to the mass splitting than the n/n ratio at the same energy, but that it is not very sensitive to the symmetry energy. However, regardless of which Skyrme potential is employed, the simulations predict a significantly larger p/p ratio at low kinetic energies than is evident in the data. The data points at larger kinetic energies are similar to simulations with $m_n^* < m_p^*$, but the flat trend is better matched by the simulations with the opposite relationship.

The 120 MeV data does not display any impact parameter dependence. Both the central and mid-peripheral spectra increase towards the initial system ratio at large kinetic energies. The sensitivity of the simulations to the mass splitting is reduced at this beam energy compared to the 50 MeV calculations. As is true with the n/n ratio and the 50 MeV p/p ratio, the trend of the 120 MeV p/p ratio is better matched by the simulations where $m_n^* > m_p^*$ (blue), but there is a sizeable offset so that the value of the data is closer to the simulations where $m_n^* < m_p^*$ (red).

The double n/p ratio is constructed from the neutron and proton spectra from both reaction systems:

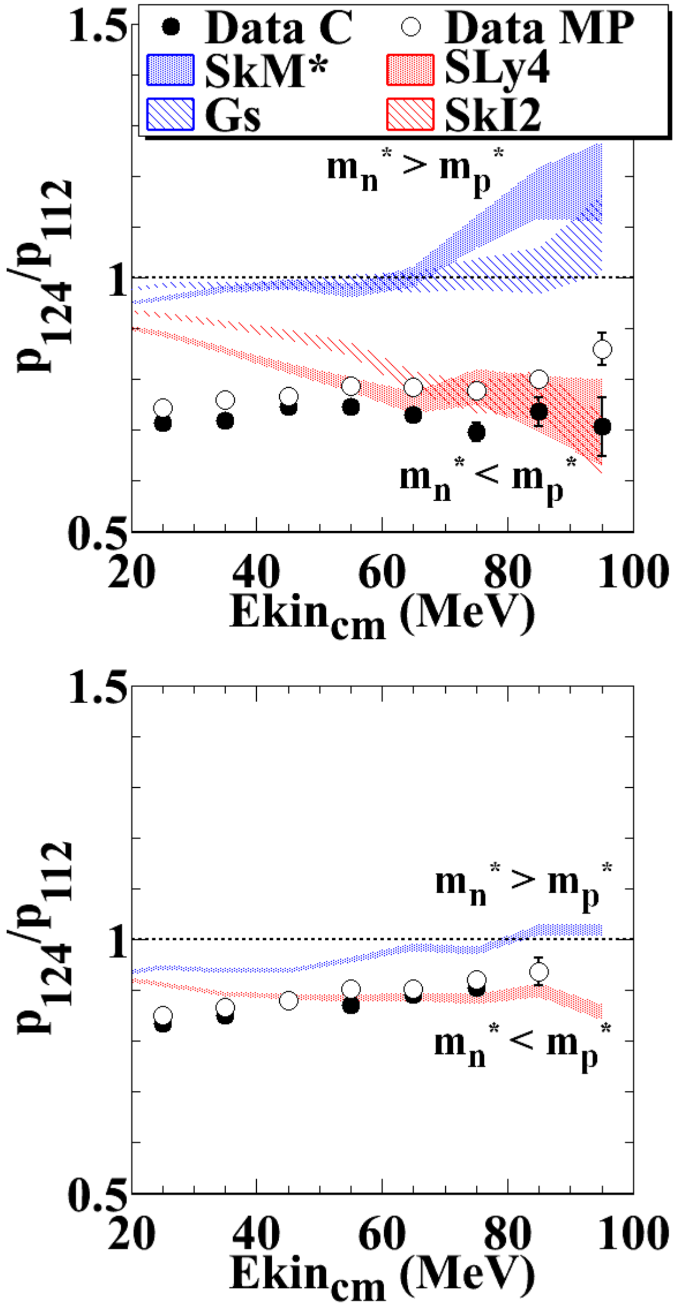

Figure 5.3: Ratio of proton energy spectrum from the ^{124}Sn + ^{124}Sn reaction to the proton spectrum from the ^{112}Sn + ^{112}Sn reactions, for the 50 AMeV reactions (top) and 120 AMeV reactions (bottom). Simulations with a stiff symmetery energy are indicated by diagonal filling and simulations with a soft symmetry energy are indicated by a dotted fill style. Only soft symmetry energy simulations are currently available at the higher beam energy. Simulations employing an effective mass splitting with $m_n^* < m_p^*$ are shown in red, while those with te opposite splitting are shown in blue. The simulations indicate a strong sensitivity to the mass splitting, but they diverge substantially from the data.

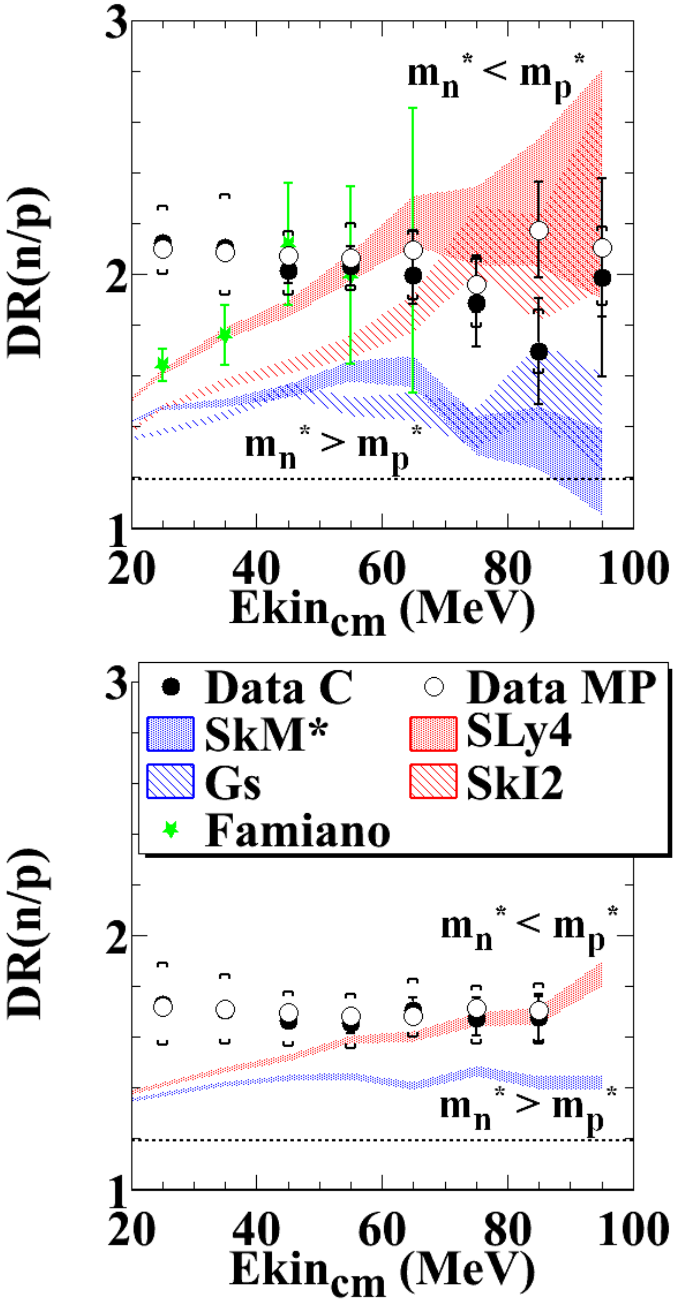

Figure 5.4: Neutron/proton double ratios for the 50 AMeV reactions (top) and 120 AMeV reactions (bottom). Previous data is shown in green. Both the central (C) and mid peripheral (MP) data is displayed, but only the MP data should be compared to the simulations. Simulations with a stiff symmetery energy are indicated by diagonal filling and simulations with a soft symmetry energy are indicated by a dotted fill style. Only soft symmetry energy simulations are currently available at the higher beam energy. Simulations employing an effective mass splitting with $m_n^* < m_p^*$ are shown in red, while those with te opposite splitting are shown in blue.

$$DR(n/p) = \frac{(n/p)_{124}}{(n/p)_{112}} = \frac{n_{124}/n_{112}}{p_{124}/p_{112}} \tag{5.1}$$

and shown in Figure 5.4. The 50 MeV data (top) are mostly flat or slightly decreasing, with a value near 2.1. The impact parameter dependence that was evident in the n/n ratio is mostly canceled by the opposite dependence of the p/p ratio, but the mid-peripheral ratio is somewhat larger than the central ratio at higher kinetic energies. This effect should not be ignored due to the neutron systematic uncertainties, since these uncertainties will act in the same direction on both impact parameter selections. This is contrary to previous ImQMD simulations that predicted a slight decrease in the DR(n/p) at larger impact parameters [55], although other simulations have predicted a slightly increased ratio [96]. The previous double ratio data from Famiano [17] is shown in green. That data set had an impact parameter cut of $b < 5$ fm, which is similar to the combined range of the two impact parameter cuts in the current experiment. Little impact parameter dependence is seen in the current data at the kinetic energies of the Famiano data points, allowing for an easy comparison. The flat trend of the current data is quite a bit different than the upward trend of the Famiano data. This is largely the result of the data between 20 and 40 MeV, where the current data are much higher than the previous analysis. However, the current data are consistent with the previous analysis between 40 and 70 MeV, but with much smaller uncertainties. The trend of the current data also extends to larger kinetic energies than were measured in the Famiano analysis. We do not have a definitive explanation for the discrepancy between the two experiments at low energies. We note that the previous experiment had some difficulties with the CAEN constant fraction discriminators that were borrowed from the MoNA collaboration. These introduced systematic uncertainties into the neutron yields. The comparison in Figure 5.4 suggests that the systematic uncertainties in the previous data may be underestimated. The systematic uncertainties in the current measurement are based on cross-checks within the data that were not possible in the previous experiment due to the nature of the technical difficulties.

At kinetic energies near 60 MeV the simulations show a sensitivity to the symmetry energy, but the effect of the mass splitting is larger. At higher energies there is only a sensitivity to the mass splitting, with a larger DR(n/p) in simulations with $m_n^* < m_p^*$ (red) than those with the opposite mass splitting. This effect is consistent with simple expectations, since a smaller effective mass indicates a more repulsive mean field at high momentum. The magnitude of the effect relative to the effect of the symmetry energy, however, means that the DR(n/p) at beam energies of 50 AMeV is a better observable of the mass splitting than of the symmetry energy. This is similar to the sensitivity of the single n/p ratio reported by Rizzo *et al.* [47].

As was true of the n/n and p/p ratios, the flat trend in the DR(n/p) is matched by the two simulations where $m_n^* > m_p^*$ (blue), but the values of the data at larger kinetic energies better match the simulations with the opposite mass splitting. There is quite a large discrepancy between the data and any of the simulations at low energies, reducing the quality of the comparison.

As in the n/n and p/p ratios, the double ratio at 120 AMeV (bottom) does not display an impact parameter dependence. The trend of the data is quite flat, but the value of the ratio is still well above the double ratio for the initial reaction system (dashed line), indicating that it is still strongly influenced by isospin-dependent effects. The simulations again display increasing sensitivity to the mass splitting at high energies, with a smaller neutron effective mass giving rise to an upward trend while a larger neutron effective mass leads to a flat trend. The sensitivity of the calculations to the symmetry energy was not investigated at this beam energy. However, Rizzo *et al.* [47] reported that the single n/p ratio at a similar beam energy is sensitive to the symmetry energy at mid momentum and to the mass splitting at high momentum. The flat trend of the data is again matched by the SkM* ImQMD calculation, while the high kinetic energy data better matches the SLy4 simulation. There is a striking offset between the data and all the simulations at low kinetic energies. In this region the influence of clusters that deplete the free neutron and proton yields and enhance the difference between them are more important.

Ratios of spectra between reaction systems such as those shown so far are constructed to reduce the sensitivity to systematic uncertainties in the data. However, transport simulations generally show that the single n/p ratio is more sensitive to the symmetry energy. The statistical uncertainties in the data are also smaller when taking the ratio of two spectra rather than taking the ratio of four spectra. The systematic uncertainties due to effects that vary between the reactions such as the Proton Veto efficiency and the scattering background are similarly reduced compared to the double ratio. However, the neutron detection efficiency and the associated uncertainty then contribute to the ratio, as do coverage corrections. At the present we have a neutron efficiency calculation that satisfies some of our basic requirements, therefore we think it may be instructive to explore the single n/p ratio. However we should caution that the results may change as we obtain more sophisticated efficiency calculations. We evaluate the neutron detection efficiency with a 10% uncertainty for illustrative purposes, but this probably understates the issue. Nevertheless, we present the n/p ratios in Figure 5.5. The top two panels show the data

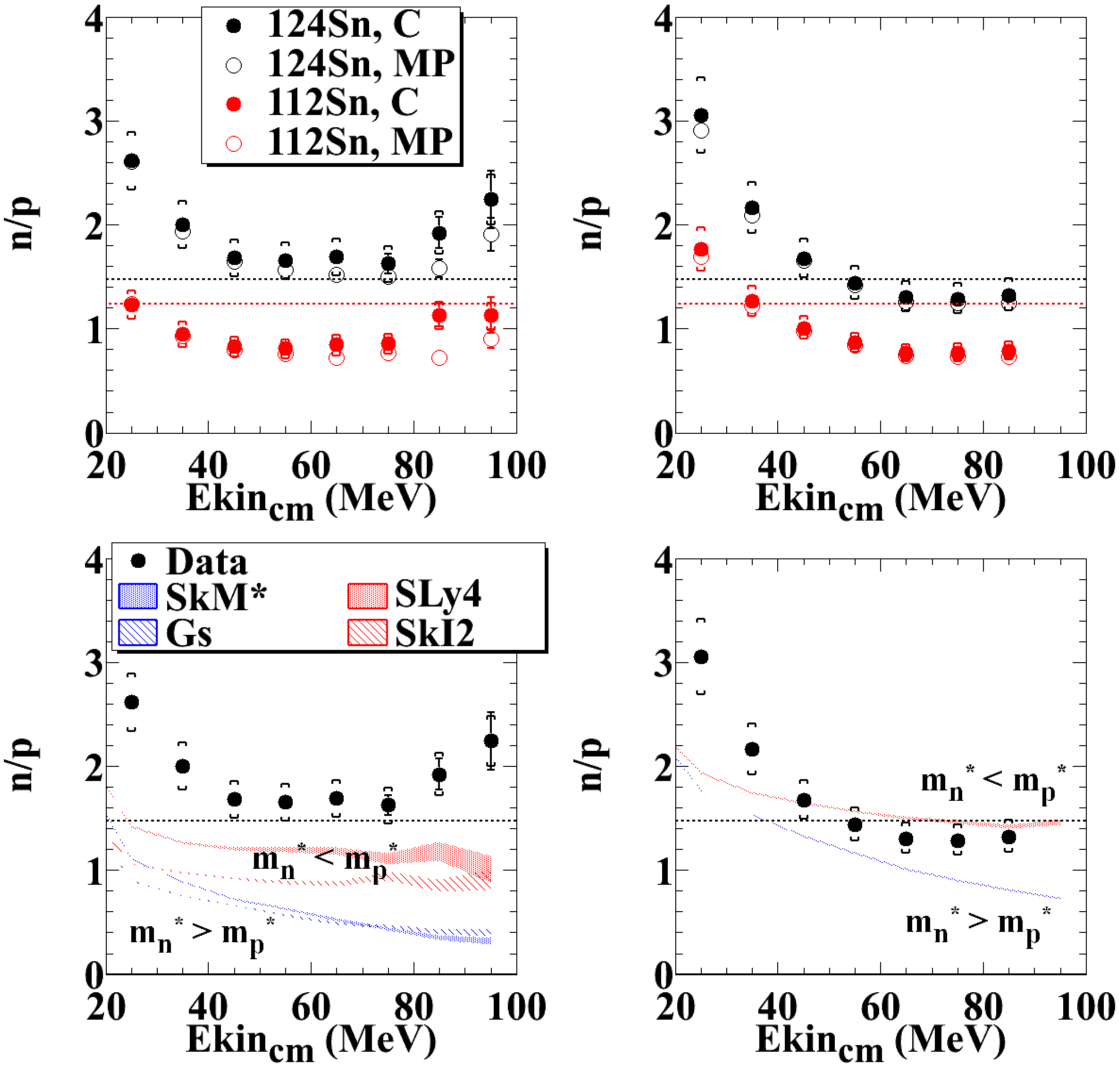

Figure 5.5: The ratio of neutron to proton kinetic energy spectra for the reactions with E_{beam} = 50 AMeV (top left) and E_{beam} = 120 AMeV (top right). On the bottom row, the central ^{124}Sn + ^{124}Sn reactions are compared to ImQMD calculations at both beam energies. Simulations with a stiff symmetery energy are indicated by diagonal filling and simulations with a soft symmetry energy are indicated by a dotted fill style. Only soft symmetry energy simulations are currently available at the higher beam energy. Simulations employing an effective mass splitting with $m_n^* < m_p^*$ are shown in red, while those with te opposite splitting are shown in blue.

separated by impact parameter and reaction system while the bottom compare the central ^{124}Sn + ^{124}Sn data to the corresponding ImQMD calculations. The left two panels depict the reactions with E_{beam} = 50 AMeV while the right panels show E_{beam} = 120 AMeV.

All four 50 AMeV spectra (upper left panel) decrease from low to mid kinetic energies, level out above 40 MeV, and then increase again in the highest energy data points. The origin of the increasing trend at high energies is unclear. The decreasing trend at low energies is an expected consequence of the Coulomb interaction, which shifts protons to higher kinetic energies without affecting the neutrons. The flat portion of the spectrum is the result of the neutron and proton spectra having the same exponential slope above the Coulomb peak; that is, they exhibit the same temperature within a statistical model. Since the neutrons dominate below the Coulomb peak, one might expect the n/p ratio to level out below the initial system ratio (dotted line) in the absence of nuclear isospin-dependent effects. This is what we see in the ^{112}Sn ratio. However, the flat portion of the ^{124}Sn n/p ratio is slightly above the corresponding initial ratio, indicating the sensitivity of the ratio to isospin-dependent effects. One important effect is he production of clusters, which reduces the impact of these neutron and proton number consistency arguments. The mid-peripheral data from both systems is slightly lower than the corresponding central ratio. In a statistical model this would indicate that the difference between the neutron and proton chemical potentials depends on impact parameter.

The n/p ratios derived from the 120 AMeV spectra (upper right panel) have features similar to the 50 AMeV ratios. The Coulomb interaction of the protons with the source causes the proton spectrum to be suppressed at low energies. This leads to a decreasing trend in the n/p ratio at low kinetic energies, which levels out above 60 MeV. At the lowest kinetic energies, the n/p ratios are larger than the corresponding ratios at the lower beam energy, indicating that the Coulomb barrier has a larger effect. This is corroborated by the persistence of the downward trend to larger kinetic energies, indicating that the Coulomb peak is broader and at higher energies. There is no evidence of an increasing trend in the n/p spectral ratio at high energies. The ^{112}Sn ratios flatten out at a similar value to the same ratios at the lower beam energy. On the other hand, the ^{124}Sn n/p ratio reaches a smaller value, which is below the initial system ratio. This indicates the lower sensitivity to isospin dependent effects. For both reaction systems, the mid-peripheral ratios are slightly smaller than the corresponding central ratios. We note that these larger Coulomb effects are cancelled out to first order by constructing the double ratio. This may be another good reason to construct the double ratio.

The bottom left panel of Figure 5.5 compares the lower beam energy central ^{124}Sn n/p ratio to the corresponding simulated ratios. Like the data, the simulations show evidence of a Coulomb peak at low energies, followed by a flatter trend at high energies. The difference between simulations with the same mass splitting (color) but different symmetry energies (fill style) is largest at low kinetic energies, and is either constant or decreases at higher kinetic energies. Meanwhile, the separation between simulations with different momentum dependences starts small but continues to increase at increasing energy, as expected. Only the simulations with $m_n^* < m_p^*$ (red) produce a truly flat trend at intermediate energies that matches the trend of the data. None of the simulations reproduce the increasing trend of the data at higher energies. All of the simulations significantly under predict the data at all kinetic energies.

At the higher beam energy, shown in the bottom right panel, the simulated n/p ratios also indicate a decreasing trend due to the Coulomb interaction. However, the trend is not as sharp as the drop in the data. Again, the ratio produced by $m_n^* > m_p^*$ (blue) continues to decrease at high kinetic energies while the opposite mass splitting levels out to match the trend of the data. Both simulations under predict the low energy data, but the SLy4 interaction is close to the data above 40 MeV. Interestingly, while the flat portion of the experimental n/p ratio is smaller at the higher beam energy, the simulations predict the opposite trend.

Every comparison made above between the experimental spectral ratios and the simulated ratios indicates the same discrepancy. The simulation underpredicts neutron production and overpredicts proton production from the ^{124}Sn system. This is certainly true at low kinetic energies. This can be a consequence of cluster production that subtracts roughly equal amounts of protons and neutrons from the free nucleon yields. At higher kinetic energies the n/n and p/p ratios could match the simulations, depending on the Skyrme interaction used, but in the n/p ratio at the 50 AMeV beam energy the discrepancy persists at large kinetic energies. The magnitude of the effect is smaller for the 120 AMeV beam energy, and depending on the employed Skyrme interaction, the discrepancy at that beam energy may disappear entirely at higher kinetic energies. This kinetic energy and beam energy dependence suggests that one major source of the discrepancy is the production of light clusters, particularly alpha particles. Binding protons and neutrons into alphas will increase the neutron-proton asymmetry of the remaining free nucleons. The alpha spectrum drops off more quickly as a function of energy per nucleon than the corresponding neutron and proton spectra, so the effect decreases as high nucleon kinetic energy. The production of alphas is also less favorable at high temperatures compared

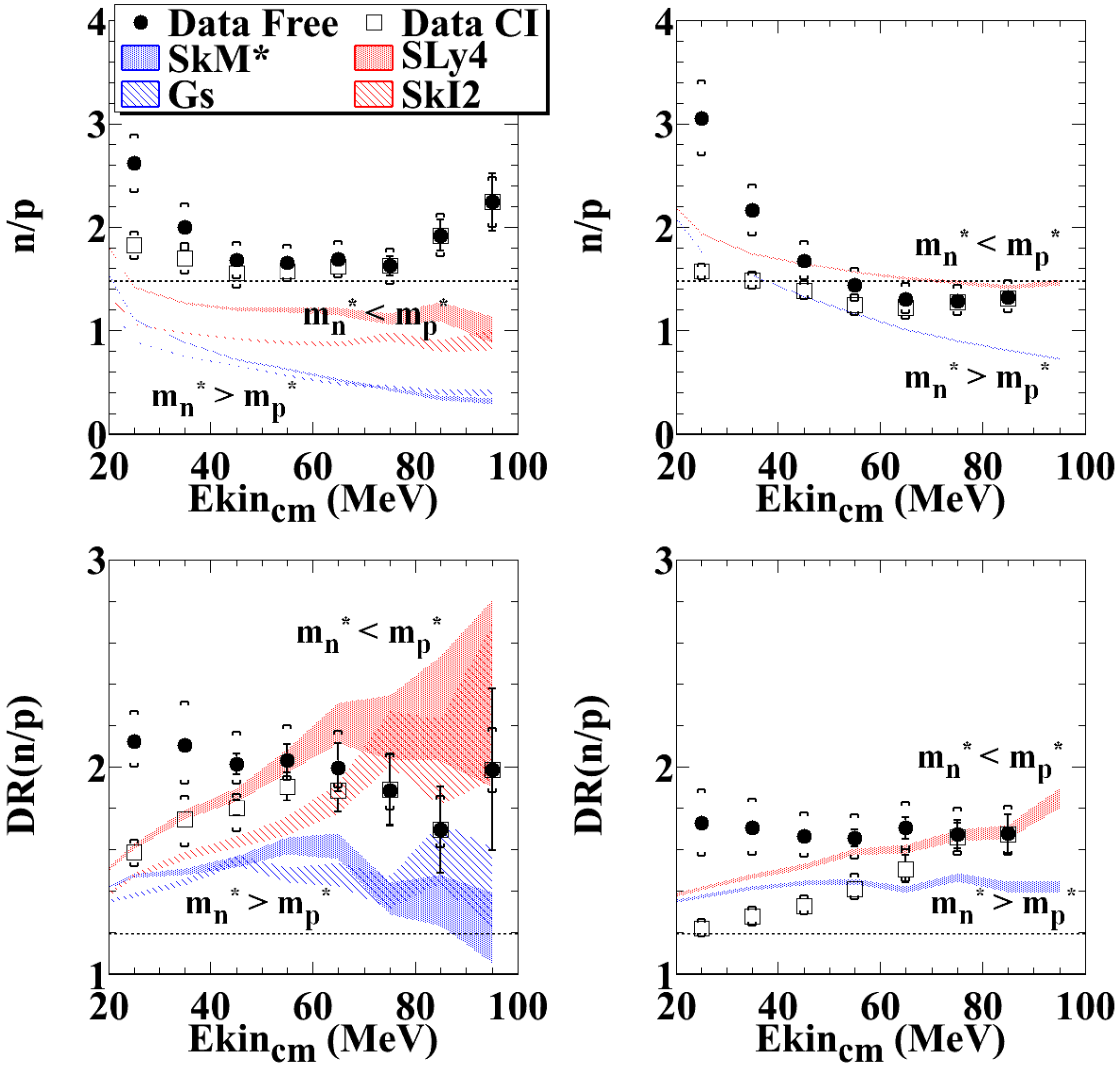

Figure 5.6: Comparison of coalescence-invariant (CI) single n/p ratios (top) and DR(n/p) (bottom) to free ratios and ImQMD simulations. The left column contains the 50 AMeV beam energy data and the right column contains the 120 AMeV data. The difference between the free and CI ratios indicates the importance of clustering in those data points. The fact that the CI ratios are in better agreement with the simulations than the free data shows that the simulations can not completely account for clustering effects. Simulations with a stiff symmetery energy are indicated by diagonal filling and simulations with a soft symmetry energy are indicated by a dotted fill style. Only soft symmetry energy simulations are currently available at the higher beam energy. Simulations employing an effective mass splitting with $m_n^* < m_p^*$ are shown in red, while those with te opposite splitting are shown in blue.

to free nucleons, which explains the smaller effect for the 120 AMeV beam energy. The ImQMD calculation does not accurately produce light clusters.

One way to demonstrate the possible effect of clustering is to consider coalescence invariant (CI) spectra, which are constructed by considering all detected nucleons, whether they are free or part of light clusters. Ratios constructed from CI spectra are presented in Figure 5.6, along with the previously presented free nucleon ratios and the ImQMD simulations. The CI spectra should nominally be compared to CI simulations, but those are currently unavailable. As expected, the CI n/p ratios are smaller than the free particle ratios at low kinetic energies. The same is true of the DR(n/p). The single n/p ratio from the 50 AMeV beam energy data still lies well above the ImQMD simulations, indicating some additional discrepancy between the simulation and experiment. However, the CI DR(n/p) at 50 AMeV is comparable to some of the simulations at all kinetic energies. The 120 AMeV single and double CI ratios are actually below the theoretical calculations at low energies, indicating that the comparison made here is only a limiting case. However, it is clear from the effect demonstrated here that clustering needs to be accounted for when comparing the experiment to theory.

Chapter 6

Conclusions and Outlook

6.1 Sensitivity of Isospin Diffusion to Physics Inputs

We have used the pBUU transport model code to explore the effect of various aspects of the input physics and transport description on isospin diffusion. Consistent with previous studies, we found diffusion to be more significant if the symmetry energy is larger at subsaturation densities. This can occur when the symmetry energy is more weakly dependent on density. Turning our attention to the influence of other transport quantities, we found some unexpected sensitivities. For example, we found that the inclusion of momentum dependence in the isoscaler mean field produced density fluctuations in the neck, prolonging the diffusion process and giving rise to IMFs. In addition, the choice of in-medium NN cross section can also affect isospin diffusion, producing both a change in the IMF distribution and altering the balance between a mean-field driven diffusion process and a collision-driven mixing. Depending on the magnitude of the in-medium cross section and density dependence of the mean field, we found that nucleon-nucleon cross sections can enhance diffusion, for very small cross sections, or reduce diffusion, for large cross sections comparable to the values in free space. This study examined for the first time the effect of including in-medium cluster production on the isospin diffusion process. Previous studies have looked at the effect of IMF formation, but have not looked at in-medium cluster production in a way similar to pBUU. We found that cluster production reduced diffusion by causing the neck to become more isospin symmetric.

In all cases that produce IMFs, considering either the residue alone or all forward-moving fragments yield different isospin diffusion signals, with the residue values for the isospin transport ratio consistent with less diffusion. These can be considered two observables of isospin diffusion, each sensitive to the input physics, and they can both be exploited to improve constraints on the symmetry energy from comparisons between data and calculations. To do this, however, it is important to have experimental data which originates unambiguously from the projectile residue, and this is not the case in the published isospin diffusion data. New experiments aim to measure and compare the different diffusion signals from IMFs and large residues, and this should help to constrain the effects studied here.

6.2 Measurement of Transverse Emission of Neutrons and Protons

We have measured the transverse emission of protons and neutrons from collisions of ^{124}Sn + ^{124}Sn and ^{112}Sn + ^{112}Sn at E_{beam} = 50 AMeV and 120 AMeV. At 50 AMeV, the double ratio of neutron to proton kinetic energy spectra consistent with previous experimental results above 40 MeV in the center of mass, but the uncertainties are smaller and the data is extended to higher kinetic energies. However, the lower energy data points are inconsistent with the previous measurement. No previous measurements exist near a beam energy of 120 AMeV. We found a small impact parameter dependence in the 50 AMeV data that was not previously noted, which indicates stronger isospin dependence for larger impact parameters. No such effect is apparent in the 120 AMeV data.

A slight downward trend is observed in the DR(n/p) at E_{beam} = 50 AMeV, while a flat trend is observed at E_{beam} = 120 AMeV. We note that the previous data at 50 AMeV implied an upward trend, due mostly to the low energy points. Transport model calculations employing neutron-proton effective mass splitting of $m_n^* > m_p^*$ in neutron-rich matter are more consistent with these trends than calculations with $m_n^* < m_p^*$. Calculations without mass splitting exhibit an upward trend [55], which is also inconsistent with the current data. However, the values of the data at high energies are more consistent with $m_n^* < m_p^*$. The sensitivity to the symmetry energy, which was the original aim of this work, is not as strong as the sensitivity to the effective mass splitting.

There is an offset between the experimental spectral ratios and all of the simulations, which is largest at low kinetic energies and at the lower beam energy. Because all the simulated spectra demonstrate this offset, regardless of which interaction is used, the offset must arise from an effect other than the mean field. It is likely that part of this offset is due to clustering effects, which are not fully treated in the model. In particular, when some emitted nucleons are bound into isospin-symmetric clusters such as alpha particles, the remaining free nucleons become more isospin-asymmetric. A coalescence-invariant ratio, constructed from all detected nucleons including those bound in light clusters, is smaller than the DR(n/p) constructed only from free nucleons. This effect was only seen for kinetic energies less than 70 MeV, but it is large enough to change the trend of the data and any conclusions about the effective mass splitting. In general, the sensitivity of this data to cluster formation and the discrepancy between the theory and experiment should stimulate additional theoretical efforts to better account for clustering effects in transport simulations.

The DR(n/p) is still quite large in the 120 AMeV data, indicating continued sensitivity to isospin-dependent effects. It would be interesting to see if this persists at even higher beam energies. However, the current experiment indicates that the measurement of neutrons from central heavy ion collisions becomes more difficult at higher beam energies. The high multiplicity of neutrons and charged particles increases the demands on the proton veto array, and the increasing rate of scattering background relative to the rate of direct neutrons necessitates a precise measurement of this background. The design of future experiments at higher beam energies, or even different reaction systems at similar beam energies, should account for this.

Having a large, granular proton veto array near the neutron detector, rather than a small array closer to the target, would improve the charged particle subtraction. The scattering background measurement would be more precise if wider shadow bars were used, which would increase the statistics of the measurement and remove ambiguity due to the position resolution of the neutron walls. It would also be useful to investigate the sources of the scattering background. The floor and walls of the vault are too far away to contribute to most of the interesting range of time of flight. There must be a large amount of material nearer to the reaction target to produce the observed background.

One possibility is the 6 cm thick CsI crystals in LASSA. It may be possible to remove LASSA and detect charged particles in the Neutron Walls. This would remove one source of neutron scattering and would actually increase the maximum identifiable energy of charged particles, which is currently limited by the punch-through energy of the CsI. On the other hand, it would require the removal of more intervening material, and it would remove isotopic resolution for high energy charged particles. As a final note, the pulse shape analysis of the neutron walls shows a strong contribution from gamma-like pulses even in the 120 AMeV data, so it is important to maintain this ability. At the shortest time of flights, however, a large fraction of these may arise from recoil or direct protons escaping the walls without stopping.

6.3 Conclusion

The ultimate goal of many contemporary heavy ion collision experiments is to determine the symmetry energy. This is done by identifying and measuring sensitive observables and comparing them to transport calculations. There are difficulties in both the theoretical and experimental pieces of this approach. On the theoretical side, the transport models are computationally challenging and rely on phenomenological approximations of the underlying physics. The symmetry energy is only one of several incompletely constrained quantities in these simulations. Attempts to constrain the symmetry energy using heavy ion collisions must acknowledge and address these uncertainties. The large effects observed in the isospin diffusion study suggest that more work is needed to pin down the input physics in transport models other than the symmetry energy.

On the experimental side, the measurements continue to increase in complexity, but they are also becoming more precise. The measurement of neutron and proton emission presented here represents a substantial increase in precision over a previous often-cited measurement, as well as an entirely new measurement at a higher beam energy. Comparison of the current data to a transport model sensitivity study shows that this data will be useful in constraining the physics inputs of transport simulations.

REFERENCES

REFERENCES

[1] Tianxiao Liu. *Isospin Dynamics and the Isospin Dependent EOS*. PhD thesis, Michigan State University, 2005.

[2] Philip David Zecher. *Design, Construction, and Use of the Neutron Wall Array in Measuring the ^{8}Li(n,γ)^{9}Li Astrophysics Reaction*. PhD thesis, Michigan State University, November 1996.

[3] M.S. Wallace, M.A. Famiano, M.-J. van Goethem, A.M. Rogers, W.G. Lynch, J. Clifford, F. Delaunay, J. Lee, S. Labostov, M. Mocko, L. Morris, A. Moroni, B.E. Nett, D.J. Oostdyk, R. Krishnasamy, M.B. Tsang, R.T. de Souza, S. Hudan, L.G. Sobotka, R.J. Charity, J. Elson, and G.L. Engel. The high resolution array (hira) for rare isotope beam experiments. *Nuclear Instruments and Methods in Physics Research Section A: Accelerators, Spectrometers, Detectors and Associated Equipment*, 583(23):302 – 312, 2007.

[4] D. H. Youngblood, H. L. Clark, and Y.-W. Lui. Incompressibility of nuclear matter from the giant monopole resonance. *Phys. Rev. Lett.*, 82:691–694, Jan 1999.

[5] A. Schmah, S. Lang, I. Böttcher, F. Dohrmann, A. Förster, E. Grosse, P. Koczoń, B. Kohlmeyer, F. Laue, M. Menzel, L. Naumann, H. Oeschler, W. Scheinast, T. Schuck, E. Schwab, P. Senger, Y. Shin, H. Ströbele, C. Sturm, G. Surówska, F. Uhlig, A. Wagner, W. Waluś, C. Fuchs, Amand Faessler, and H. Mansour. Kaon and pion emission in asymmetric c+au and au+c collisions at 1.0 *A* gev and 1.8 *A* gev. *Phys. Rev. C*, 71:064907, Jun 2005.

[6] P. Danielewicz, R. Lacey, and W. G. Lynch. Determination of the equation of state of dense matter. *Science*, **298**:1592, 2002.

[7] S. Typel and B. Alex Brown. Neutron radii and the neutron equation of state in relativistic models. *Phys. Rev. C*, 64(2):027302, Jun 2001.

[8] Lie-Wen Chen, Che Ming Ko, Bao-An Li, and Jun Xu. Density slope of the nuclear symmetry energy from the neutron skin thickness of heavy nuclei. *Phys. Rev. C*, 82(2):024321, Aug 2010.

[9] A.W. Steiner, M. Prakash, J.M. Lattimer, and P.J. Ellis. Isospin asymmetry in nuclei and neutron stars. *Physics Reports*, 411(6):325 – 375, 2005.

[10] C. J. Horowitz and J. Piekarewicz. Neutron star structure and the neutron radius of ^{208}pb. *Phys. Rev. Lett.*, 86(25):5647–5650, Jun 2001.

[11] Luca Trippa, Gianluca Colò, and Enrico Vigezzi. Giant dipole resonance as a quantitative constraint on the symmetry energy. *Phys. Rev. C*, 77(6):061304, Jun 2008.

[12] A. Klimkiewicz, N. Paar, P. Adrich, M. Fallot, K. Boretzky, T. Aumann, D. Cortina-Gil, U. Datta Pramanik, Th. W. Elze, H. Emling, H. Geissel, M. Hellström, K. L. Jones, J. V. Kratz, R. Kulessa, C. Nociforo, R. Palit, H. Simon, G. Surówka, K. Sümmerer, D. Vretenar, and W. Waluś. Nuclear symmetry energy and neutron skins derived from pygmy dipole resonances. *Phys. Rev. C*, 76(5):051603, Nov 2007.

[13] Andrea Carbone, Gianluca Colò, Angela Bracco, Li-Gang Cao, Pier Francesco Bortignon, Franco Camera, and Oliver Wieland. Constraints on the symmetry energy and neutron skins from pygmy resonances in ^{68}ni and ^{132}sn. *Phys. Rev. C*, 81(4):041301, Apr 2010.

[14] M. Lattimer and M. Prakash. Neutron star structure and the equation of state. *ApJ*, 550:426–442, March 2001.

[15] James M. Lattimer. The nuclear equation of state and neutron star masses. *Annual Review of Nuclear and Particle Science*, 62(1):485–515, 2012.

[16] Hans-Thomas Janka. Explosion mechanisms of core-collapse supernovae. *Annual Review of Nuclear and Particle Science*, 62(1):407–451, 2012.

[17] M. A. Famiano, T. Liu, W. G. Lynch, M. Mocko, A. M. Rogers, M. B. Tsang, M. S. Wallace, R. J. Charity, S. Komarov, D. G. Sarantites, L. G. Sobotka, and G. Verde. Neutron and proton transverse emission ratio measurements and the density dependence of the asymmetry term of the nuclear equation of state. *Phys. Rev. Lett.*, 97(5):052701, Aug 2006.

[18] M. B. Tsang and et.al. Isospin diffusion and the nuclear symmetry energy in heavy ion reactions. *Phys. Rev. Lett.*, **92**:062701, 2004.

[19] T. X. Liu, W. G. Lynch, M. B. Tsang, X. D. Liu, R. Shomin, W. P. Tan, G. Verde, A. Wagner, H. F. Xi, H. S. Xu, B. Davin, Y. Larochelle, R. T. de Souza, R. J. Charity,

and L. G. Sobotka. Isospin diffusion observables in heavy-ion reactions. *Phys. Rev. C*, 76(3):034603, Sep 2007.

[20] Horst Müller and Brian D. Serot. Phase transitions in warm, asymmetric nuclear matter. *Phys. Rev. C*, 52(4):2072–2091, Oct 1995.

[21] S. R. Souza, M. B. Tsang, R. Donangelo, W. G. Lynch, and A. W. Steiner. Probing the symmetry energy from the nuclear isoscaling. *Phys. Rev. C*, 78:014605, Jul 2008.

[22] H. S. Xu, M. B. Tsang, T. X. Liu, X. D. Liu, W. G. Lynch, W. P. Tan, A. Vander Molen, G. Verde, A. Wagner, H. F. Xi, C. K. Gelbke, L. Beaulieu, B. Davin, Y. Larochelle, T. Lefort, R. T. de Souza, R. Yanez, V. E. Viola, R. J. Charity, and L. G. Sobotka. Isospin fractionation in nuclear multifragmentation. *Phys. Rev. Lett.*, 85:716–719, Jul 2000.

[23] M. B. Tsang, C. K. Gelbke, X. D. Liu, W. G. Lynch, W. P. Tan, G. Verde, H. S. Xu, W. A. Friedman, R. Donangelo, S. R. Souza, C. B. Das, S. Das Gupta, and D. Zhabinsky. Isoscaling in statistical models. *Phys. Rev. C*, 64:054615, Oct 2001.

[24] Bao-An Li. Probing the high density behavior of the nuclear symmetry energy with high energy heavy-ion collisions. *Phys. Rev. Lett.*, 88(19):192701, Apr 2002.

[25] B. Alex Brown. Neutron radii in nuclei and the neutron equation of state. *Phys. Rev. Lett.*, 85:5296–5299, Dec 2000.

[26] M. B. Tsang, Yingxun Zhang, P. Danielewicz, M. Famiano, Zhuxia Li, W. G. Lynch, and A. W. Steiner. Constraints on the density dependence of the symmetry energy. *Phys. Rev. Lett.*, 102(12):122701, Mar 2009.

[27] M. B. Tsang, J. R. Stone, F. Camera, P. Danielewicz, S. Gandolfi, K. Hebeler, C. J. Horowitz, Jenny Lee, W. G. Lynch, Z. Kohley, R. Lemmon, P. Möller, T. Murakami, S. Riordan, X. Roca-Maza, F. Sammarruca, A. W. Steiner, I. Vidaña, and S. J. Yennello. Constraints on the symmetry energy and neutron skins from experiments and theory. *Phys. Rev. C*, 86:015803, Jul 2012.

[28] W. Reisdorf, M. Stockmeier, A. Andronic, M.L. Benabderrahmane, O.N. Hartmann, N. Herrmann, K.D. Hildenbrand, Y.J. Kim, M. Kis, P. Koczon, T. Kress, Y. Leifels, X. Lopez, M. Merschmeyer, A. Schttauf, V. Barret, Z. Basrak, N. Bastid, R. Caplar, P. Crochet, P. Dupieux, M. Dzelalija, Z. Fodor, Y. Grishkin, B. Hong, T.I. Kang, J. Kecskemeti, M. Kirejczyk, M. Korolija, R. Kotte, A. Lebedev, T. Matulewicz, W. Neubert, M. Petrovici, F. Rami, M.S. Ryu, Z. Seres, B. Sikora, K.S. Sim, V. Simion, K. Siwek-Wilczynska, V. Smolyankin, G. Stoicea, Z. Tyminski, K. Wisniewski, D. Wohlfarth,

Z.G. Xiao, H.S. Xu, I. Yushmanov, and A. Zhilin. Systematics of pion emission in heavy ion collisions in the 1 agev regime. *Nuclear Physics A*, 781(3-4):459 – 508, 2007.

[29] G. Ferini, M. Colonna, T. Gaitanos, and M. Di Toro. Aspects of particle production in isospin-asymmetric matter. *Nuclear Physics A*, 762(1-2):147 – 166, 2005.

[30] Zhigang Xiao, Bao-An Li, Lie-Wen Chen, Gao-Chan Yong, and Ming Zhang. Circumstantial evidence for a soft nuclear symmetry energy at suprasaturation densities. *Phys. Rev. Lett.*, 102(6):062502, Feb 2009.

[31] Zhao-Qing Feng and Gen-Ming Jin. Probing high-density behavior of symmetry energy from pion emission in heavy-ion collisions. *Physics Letters B*, 683(2-3):140 – 144, 2010.

[32] Y. Leifels, Th. Blaich, Th. W. Elze, H. Emling, H. Freiesleben, K. Grimm, W. Henning, R. Holzmann, J. G. Keller, H. Klingler, J. V. Kratz, R. Kulessa, D. Lambrecht, S. Lange, E. Lubkiewicz, E. F. Moore, W. Prokopowicz, R. Schmidt, C. Schütter, H. Spies, K. Stelzer, J. Stroth, E. Wajda, W. Waluś, M. Zinser, and E. Zude. Exclusive studies of neutron and charged particle emission in collisions of *au*197 +197au at 400 mev/nucleon. *Phys. Rev. Lett.*, 71(7):963–966, Aug 1993.

[33] W. Reisdorf, D. Best, A. Gobbi, N. Herrmann, K. D. Hildenbrand, B. Hong, S. C. Jeong, Y. Leifels, C. Pinkenburg, J. L. Ritman, D. Schll, U. Sodan, K. Teh, G. S. Wang, J. P. Wessels, T. Wienold, J. P. Alard, V. Amouroux, Z. Basrak, N. Bastid, I. Belyaev, L. Berger, J. Biegansky, M. Bini, S. Boussange, A. Buta, R. Caplar, N. Cindro, J. P. Coffin, P. Crochet, R. Dona, P. Dupieux, M. Dzelalija, J. Er, M. Eskef, P. Fintz, Z. Fodor, L. Fraysse, A. Genoux-Lubain, G. Goebels, G. Guillaume, Y. Grigorian, E. Hfele, S. Hlbling, A. Houari, M. Ibnouzahir, M. Joriot, F. Jundt, J. Kecskemeti, M. Kirejczyk, P. Koncz, Y. Korchagin, M. Korolija, R. Kotte, C. Kuhn, D. Lambrecht, A. Lebedev, A. Lebedev, I. Legrand, C. Maazouzi, V. Manko, T. Matulewicz, P. R. Maurenzig, H. Merlitz, G. Mgebrishvili, J. Msner, S. Mohren, D. Moisa, G. Montarou, I. Montbel, P. Morel, W. Neubert, A. Olmi, G. Pasquali, D. Pelte, M. Petrovici, G. Poggi, P. Pras, F. Rami, V. Ramillien, C. Roy, A. Sadchikov, Z. Seres, B. Sikora, V. Simion, K. Siwek-Wilczynska, V. Smolyankin, N. Taccetti, R. Tezkratt, L. Tizniti, M. Trzaska, M. A. Vasiliev, P. Wagner, K. Wisniewski, D. Wohlfarth, and A. Zhilin. Central collisions of au on au at 150, 250 and 400 amev. *Nuclear Physics A*, 612(3-4):493 – 556, 1997.

[34] P. Russotto, P.Z. Wu, M. Zoric, M. Chartier, Y. Leifels, R.C. Lemmon, Q. Li, J. Lukasik, A. Pagano, P. Pawlowski, and W. Trautmann. Symmetry energy from elliptic flow in 197au + 197au. *Physics Letters B*, 697(5):471 – 476, 2011.

[35] S. Abrahamyan, Z. Ahmed, H. Albataineh, K. Aniol, D. S. Armstrong, W. Armstrong, T. Averett, B. Babineau, A. Barbieri, V. Bellini, R. Beminiwattha, J. Benesch, F. Benmokhtar, T. Bielarski, W. Boeglin, A. Camsonne, M. Canan, P. Carter, G. D. Cates, C. Chen, J.-P. Chen, O. Hen, F. Cusanno, M. M. Dalton, R. De Leo, K. de Jager, W. Deconinck, P. Decowski, X. Deng, A. Deur, D. Dutta, A. Etile, D. Flay, G. B. Franklin, M. Friend, S. Frullani, E. Fuchey, F. Garibaldi, E. Gasser, R. Gilman, A. Giusa, A. Glamazdin, J. Gomez, J. Grames, C. Gu, O. Hansen, J. Hansknecht, D. W. Higinbotham, R. S. Holmes, T. Holmstrom, C. J. Horowitz, J. Hoskins, J. Huang, C. E. Hyde, F. Itard, C.-M. Jen, E. Jensen, G. Jin, S. Johnston, A. Kelleher, K. Kliakhandler, P. M. King, S. Kowalski, K. S. Kumar, J. Leacock, J. Leckey, J. H. Lee, J. J. LeRose, R. Lindgren, N. Liyanage, N. Lubinsky, J. Mammei, F. Mammoliti, D. J. Margaziotis, P. Markowitz, A. McCreary, D. McNulty, L. Mercado, Z.-E. Meziani, R. W. Michaels, M. Mihovilovic, N. Muangma, C. Muñoz Camacho, S. Nanda, V. Nelyubin, N. Nuruzzaman, Y. Oh, A. Palmer, D. Parno, K. D. Paschke, S. K. Phillips, B. Poelker, R. Pomatsalyuk, M. Posik, A. J. R. Puckett, B. Quinn, A. Rakhman, P. E. Reimer, S. Riordan, P. Rogan, G. Ron, G. Russo, K. Saenboonruang, A. Saha, B. Sawatzky, A. Shahinyan, R. Silwal, S. Sirca, K. Slifer, P. Solvignon, P. A. Souder, M. L. Sperduto, R. Subedi, R. Suleiman, V. Sulkosky, C. M. Sutera, W. A. Tobias, W. Troth, G. M. Urciuoli, B. Waidyawansa, D. Wang, J. Wexler, R. Wilson, B. Wojtsekhowski, X. Yan, H. Yao, Y. Ye, Z. Ye, V. Yim, L. Zana, X. Zhan, J. Zhang, Y. Zhang, X. Zheng, and P. Zhu. Measurement of the neutron radius of ^{208}Pb through parity violation in electron scattering. *Phys. Rev. Lett.*, 108:112502, Mar 2012.

[36] Andrew W. Steiner, James M. Lattimer, and Edward F. Brown. The equation of state from observed masses and radii of neutron stars. *The Astrophysical Journal*, 722(1):33, 2010.

[37] Bao-An Li, Lie-Wen Chen, and Che Ming Ko. Recent progress and new challenges in isospin physics with heavy-ion reactions. *Physics Reports*, 464:113, Aug 2008.

[38] G.F. Bertsch and S. Das Gupta. A guide to microscopic models for intermediate energy heavy ion collisions. *Physics Reports*, **160**(4):189, 1988.

[39] P. Danielewicz. Determination of the mean-field momentum-dependence using elliptic flow. *Nuclear Physics A*, **673**:375, 2000.

[40] K. A. Brueckner. Two-body forces and nuclear saturation. iii. details of the structure of the nucleus. *Phys. Rev.*, 97:1353–1366, Mar 1955.

[41] G.E. Brown, J.H. Gunn, and P. Gould. Effective mass in nuclei. *Nuclear Physics*, 46(0):598 – 606, 1963.

[42] C Mahaux, P.F Bortignon, R.A Broglia, and C.H Dasso. Dynamics of the shell model. *Physics Reports*, 120(14):1 – 274, 1985.

[43] J. Dobaczewski. Structure of nuclei at extreme values of the isospin. *Acta Physica Polonica B*, 30:1647, 1999.

[44] H. A. Bethe. Supernova mechanisms. *Rev. Mod. Phys.*, 62:801–866, Oct 1990.

[45] M. Farine, J.M. Pearson, and F. Tondeur. Skyrme force with surface-peaked effective mass. *Nuclear Physics A*, 696(34):396 – 412, 2001.

[46] J. Rizzo, M. Colonna, M. Di Toro, and V. Greco. Transport properties of isospin effective mass splitting. *Nuclear Physics A*, 732(0):202 – 217, 2004.

[47] J. Rizzo, M. Colonna, and M. Di Toro. Fast nucleon emission as a probe of the momentum dependence of the symmetry potential. *Phys. Rev. C*, 72:064609, Dec 2005.

[48] O. Sjberg. On the landau effective mass in asymmetric nuclear matter. *Nuclear Physics A*, 265(3):511 – 516, 1976.

[49] W. Zuo, I. Bombaci, and U. Lombardo. Asymmetric nuclear matter from an extended brueckner-hartree-fock approach. *Phys. Rev. C*, 60:024605, Jul 1999.

[50] W. Zuo, A. Lejeune, U. Lombardo, and J.F. Mathiot. Microscopic three-body force for asymmetric nuclear matter. *The European Physical Journal A - Hadrons and Nuclei*, 14:469–475, 2002.

[51] F. Hofmann, C. M. Keil, and H. Lenske. Density dependent hadron field theory for asymmetric nuclear matter and exotic nuclei. *Phys. Rev. C*, 64:034314, Aug 2001.

[52] B. Liu, V. Greco, V. Baran, M. Colonna, and M. Di Toro. Asymmetric nuclear matter: The role of the isovector scalar channel. *Phys. Rev. C*, 65:045201, Mar 2002.

[53] V. Greco, M. Colonna, M. Di Toro, and F. Matera. Collective modes of asymmetric nuclear matter in quantum hadrodynamics. *Phys. Rev. C*, 67:015203, Jan 2003.

[54] M. Colonna, A. Ono, and J. Rizzo. Fragmentation paths in dynamical models. *Phys. Rev. C*, 82(5):054613, Nov 2010.

[55] Yingxun Zhang, D.D.S. Coupland, P. Danielewicz, Zhuxia Li, Hang Liu, Fei Lu, W.G. Lynch, and M.B. Tsang. The influence of transport model parameters on the isospin sensitive observables. *arXiv:1009.1928v1, Submitted to Phys. Rev. C*, 2011.

[56] D. D. S. Coupland, W. G. Lynch, M. B. Tsang, P. Danielewicz, and Yingxun Zhang. Influence of transport variables on isospin transport ratios. *Phys. Rev. C*, 84:054603, Nov 2011.

[57] L. Shi and P. Danielewicz. Nuclear isospin diffusivity. *Phys. Rev. C*, 68(6):064604, Dec 2003.

[58] V. Baran, M. Colonna, M. Di Toro, M. Zielinska-Pfabé, and H. H. Wolter. Isospin transport at fermi energies. *Phys. Rev. C*, 72(6):064620, Dec 2005.

[59] F. et al. Rami. Isospin tracing: A probe of nonequilibrium in central heavy-ion collisions. *Phys. Rev. Lett.*, 84(6):1120–1123, Feb 2000.

[60] Bao-An Li and Lie-Wen Chen. Nucleon-nucleon cross sections in neutron-rich matter and isospin transport in heavy-ion reactions at intermediate energies. *Phys. Rev. C*, 72(6):064611, Dec 2005.

[61] P. Danielewicz and G. F. Bertsch. Production of deuterons and pions in a transport model of energetic heavy-ion reactions. *Nuclear Physics A*, **533**:712, 1991. http://dx.doi.org/10.1016/0375-9474(91)90541-D.

[62] P. Danielewicz. Formation of composites emitted at large angles in intermediate and high energy reactions. *Nuclear Physics A*, **545**:21c, 1992.

[63] P. Danielewicz. Hadronic transport models. *Acta. Phys. Pol. B*, **33**:45, 2002.

[64] G. D. Westfall, W. Bauer, D. Craig, M. Cronqvist, E. Gaultieri, S. Hannuschke, D. Klakow, T. Li, T. Reposeur, A. M. Vander Molen, W. K. Wilson, J. S. Winfield, J. Yee, S. J. Yennello, R. Lacey, A. Elmaani, J. Lauret, A. Nadasen, and E. Norbeck. Mass dependence of the disappearance of flow in nuclear collisions. *Phys. Rev. Lett.*, 71(13):1986–1989, Sep 1993.

[65] J. Cugnon, D. L'Hote, and J. Vandermeulen. Simple parameterization of cross-sections for nuclear transport studies up to the gev range. *NIM B*, **111**:215, 1996.

[66] H.-J. Schulze, A. Schnell, G. Röpke, and U. Lombardo. Nucleon-nucleon cross sections in nuclear matter. *Phys. Rev. C*, 55(6):3006–3014, Jun 1997.

[67] A. Schnell, G. Röpke, U. Lombardo, and H.-J. Schulze. Elastic nucleon-nucleon cross section in nuclear matter at finite temperature. *Phys. Rev. C*, 57(2):806–810, Feb 1998.

[68] J. Rizzo, M. Colonna, V. Baran, M. Di Toro, H.H. Wolter, and M. Zielinska-Pfabe. Isospin dynamics in peripheral heavy ion collisions at fermi energies. *Nucl. Phys. A*, 806:79–104, June 2008.

[69] L. Shi and P. Danielewicz. Effect of cluster formation on isospin asymmetry in the liquid-gas phase transition region. *Europhys. Lett.*, 51(1):34–40, July 2000.

[70] R.T. De Souza, N. Carlin, Y.D. Kim, J. Ottarson, L. Phair, D.R. Bowman, C.K. Gelbke, W.G. Gong, W.G. Lynch, R.A. Pelak, T. Peterson, G. Poggi, M.B. Tsang, and H.M. Xu. The msu miniball 4p fragment detection array. *Nuclear Instruments and Methods in Physics Research Section A: Accelerators, Spectrometers, Detectors and Associated Equipment*, 295(12):109 – 122, 1990.

[71] P.D Zecher, A Galonsky, J.J Kruse, S.J Gaff, J Ottarson, J Wang, F Dek, Horvth, Kiss, Z Seres, K Ieki, Y Iwata, and H Schelin. A large-area, position-sensitive neutron detector with neutron/?-ray discrimination capabilities. *Nuclear Instruments and Methods in Physics Research Section A: Accelerators, Spectrometers, Detectors and Associated Equipment*, 401(23):329 – 344, 1997.

[72] Saint-Gobain Crystals. Bc-501/bc-501a/bc519 liquid scintillators. http://www.detectors.saint-gobain.com/uploadedFiles/SGdetectors/Documents/Product_Data_She 501A-519-Data-Sheet.pdf. Accessed: 11/02/2012.

[73] Glenn F. Knoll. *Radiation Detection and Measurement*. John Wiley and Sons, Inc., 3 edition, 2002.

[74] B Davin, R.T de Souza, R Yanez, Y Larochelle, R Alfaro, H.S Xu, A Alexander, K Bastin, L Beaulieu, J Dorsett, G Fleener, L Gelovani, T Lefort, J Poehlman, R.J Charity, L.G Sobotka, J Elson, A Wagner, T.X Liu, X.D Liu, W.G Lynch, L Morris, R Shomin, W.P Tan, M.B Tsang, G Verde, and J Yurkon. Lassa: a large area silicon strip array for isotopic identification of charged particles. *Nuclear Instruments and Methods in Physics Research Section A: Accelerators, Spectrometers, Detectors and Associated Equipment*, 473(3):302 – 318, 2001.

[75] George L. Engel, Muthukumar Sadasivam, Mythreyi Nethi, Jon M. Elson, Lee G. Sobotka, and Robert J. Charity. A multi-channel integrated circuit for use in low- and intermediate-energy nuclear physicshinp16c. *Nuclear Instruments and Methods in Physics Research Section A: Accelerators, Spectrometers, Detectors and Associated Equipment*, 573(3):418 – 426, 2007.

[76] Andrew Michael Rogers. *Study of ^{6}9Br Grand State Proton Emission and Effects on the rp-Process ^{6}8Se Waiting Point*. PhD thesis, Michigan State University, 2009.

[77] C. Cavata, M. Demoulins, J. Gosset, M.-C. Lemaire, D. L'Hôte, J. Poitou, and O. Valette. Determination of the impact parameter in relativistic nucleus-nucleus collisions. *Phys. Rev. C*, 42:1760–1763, Oct 1990.

[78] O.B. Tarasov and D. Bazin. Lise++: Radioactive beam production with in-flight separators. *Nuclear Instruments and Methods in Physics Research Section B: Beam Interactions with Materials and Atoms*, 266(1920):4657 – 4664, 2008. ¡ce:title¿Proceedings of the XVth International Conference on Electromagnetic Isotope Separators and Techniques Related to their Applications¡/ce:title¿.

[79] Richard J. Kurz. A 709/7090 fortran ii program to compute the neutron-detection efficiency of plastic scintillator for neutron energies from 1 to 300 mev. Technical report, Lawrence Radiation Laboratory, University of California, 1964. UCRL-11339.

[80] Robert Reid Doering. *Isobaric Analog State Transitions in (p,n) Reactions on 48Ca, 90Zr, 120Sn, and 208Pb at 25, 35, and 45 MeV*. PhD thesis, Michigan State University, 1975.

[81] V.V. Verbinski, W.R. Burrus, T.A. Love, W. Zobel, N.W. Hill, and R. Textor. Calibration of an organic scintillator for neutron spectrometry. *Nuclear Instruments and Methods*, 65(1):8 – 25, 1968.

[82] Jon Justin Kruse. *Dissociation of Lithium 11*. PhD thesis, Michigan State University, 1999.

[83] Lawrence Harvey Heilbronn. *Production of Neutron-Unbound States in Intermediate-Mass Fragments from ^{14}N + Ag Reactions at E/A = 35 MeV*. PhD thesis, Michigan State University, 1990.

[84] T.M. Amos, R.R. Doering, A. Galonsky, R. Jolly, and M.K. Zigrang. Production of neutrons with protons of 22, 30, and 40 mev in stopping targets of carbon, aluminum, copper, silver, tantalum, and lead. *Nuclear Science and Engineering*, **147**(1):73, 2004.

[85] S. Agostinelli, J. Allison, K. Amako, J. Apostolakis, H. Araujo, P. Arce, M. Asai, D. Axen, S. Banerjee, G. Barrand, F. Behner, L. Bellagamba, J. Boudreau, L. Broglia, A. Brunengo, H. Burkhardt, S. Chauvie, J. Chuma, R. Chytracek, G. Cooperman, G. Cosmo, P. Degtyarenko, A. Dell'Acqua, G. Depaola, D. Dietrich, R. Enami, A. Feliciello, C. Ferguson, H. Fesefeldt, G. Folger, F. Foppiano, A. Forti, S. Garelli, S. Giani,

R. Giannitrapani, D. Gibin, J.J. Gmez Cadenas, I. Gonzlez, G. Gracia Abril, G. Greeniaus, W. Greiner, V. Grichine, A. Grossheim, S. Guatelli, P. Gumplinger, R. Hamatsu, K. Hashimoto, H. Hasui, A. Heikkinen, A. Howard, V. Ivanchenko, A. Johnson, F.W. Jones, J. Kallenbach, N. Kanaya, M. Kawabata, Y. Kawabata, M. Kawaguti, S. Kelner, P. Kent, A. Kimura, T. Kodama, R. Kokoulin, M. Kossov, H. Kurashige, E. Lamanna, T. Lampn, V. Lara, V. Lefebure, F. Lei, M. Liendl, W. Lockman, F. Longo, S. Magni, M. Maire, E. Medernach, K. Minamimoto, P. Mora de Freitas, Y. Morita, K. Murakami, M. Nagamatu, R. Nartallo, P. Nieminen, T. Nishimura, K. Ohtsubo, M. Okamura, S. O'Neale, Y. Oohata, K. Paech, J. Perl, A. Pfeiffer, M.G. Pia, F. Ranjard, A. Rybin, S. Sadilov, E. Di Salvo, G. Santin, T. Sasaki, N. Savvas, Y. Sawada, S. Scherer, S. Sei, V. Sirotenko, D. Smith, N. Starkov, H. Stoecker, J. Sulkimo, M. Takahata, S. Tanaka, E. Tcherniaev, E. Safai Tehrani, M. Tropeano, P. Truscott, H. Uno, L. Urban, P. Urban, M. Verderi, A. Walkden, W. Wander, H. Weber, J.P. Wellisch, T. Wenaus, D.C. Williams, D. Wright, T. Yamada, H. Yoshida, and D. Zschiesche. Geant4a simulation toolkit. *Nuclear Instruments and Methods in Physics Research Section A: Accelerators, Spectrometers, Detectors and Associated Equipment*, 506(3):250 – 303, 2003.

[86] Z. Kohley, E. Lunderberg, P.A. DeYoung, B.T. Roeder, T. Baumann, G. Christian, S. Mosby, J.K. Smith, J. Snyder, A. Spyrou, and M. Thoennessen. Modeling interactions of intermediate-energy neutrons in a plastic scintillator array with geant4. *Nuclear Instruments and Methods in Physics Research Section A: Accelerators, Spectrometers, Detectors and Associated Equipment*, 682(0):59 – 65, 2012.

[87] B Luther, T Baumann, M Thoennessen, J Brown, P DeYoung, J Finck, J Hinnefeld, R Howes, K Kemper, P Pancella, G Peaslee, W Rogers, and S Tabor. Monathe modular neutron array. *Nuclear Instruments and Methods in Physics Research Section A: Accelerators, Spectrometers, Detectors and Associated Equipment*, 505(12):33 – 35, 2003. ¡ce:title¿Proceedings of the tenth Symposium on Radiation Measurements and Applications¡/ce:title¿.

[88] T. Baumann, J. Boike, J. Brown, M. Bullinger, J.P. Bychoswki, S. Clark, K. Daum, P.A. DeYoung, J.V. Evans, J. Finck, N. Frank, A. Grant, J. Hinnefeld, G.W. Hitt, R.H. Howes, B. Isselhardt, K.W. Kemper, J. Longacre, Y. Lu, B. Luther, S.T. Marley, D. McCollum, E. McDonald, U. Onwuemene, P.V. Pancella, G.F. Peaslee, W.A. Peters, M. Rajabali, J. Robertson, W.F. Rogers, S.L. Tabor, M. Thoennessen, E. Tryggestad, R.E. Turner, P.J. VanWylen, and N. Walker. Construction of a modular large-area neutron detector for the nscl. *Nuclear Instruments and Methods in Physics Research Section A: Accelerators, Spectrometers, Detectors and Associated Equipment*, 543(23):517 – 527, 2005.

[89] S. Mouatassim, G.J. Costa, G. Guillaume, B. Heusch, A. Huck, and M. Moszynski. The light yield response of ne213 organic scintillators to charged particles resulting from neutron interactions. *Nuclear Instruments and Methods in Physics Research Section A: Accelerators, Spectrometers, Detectors and Associated Equipment*, 359(3):530 – 536, 1995.

[90] D. Satoh, T. Sato, N. Shigyo, and K. Ishibashi. Scinful-qmd: Monte carlo based computer code to calculate response function and detection efficiency of a liquid organic scintillator for neutron energies up to 3 gev. Technical report, Japan Atomic Energy Agency, 2006. JAEA-Data/Code 2006-023.

[91] Yingxun Zhang. private communication, 2013.

[92] Yingxun Zhang and Zhuxia Li. Probing the density dependence of the symmetry potential with peripheral heavy-ion collisions. *Phys. Rev. C*, 71:024604, Feb 2005.

[93] Yingxun Zhang and Zhuxia Li. Elliptic flow and system size dependence of transition energies at intermediate energies. *Phys. Rev. C*, 74:014602, Jul 2006.

[94] Yingxun Zhang, Zhuxia Li, and Pawel Danielewicz. In-medium NN cross sections determined from the nuclear stopping and collective flow in heavy-ion collisions at intermediate energies. *Phys. Rev. C*, 75:034615, Mar 2007.

[95] J. Aichelin, A. Rosenhauer, G. Peilert, H. Stoecker, and W. Greiner. Importance of momentum-dependent interactions for the extraction of the nuclear equation of state from high-energy heavy-ion collisions. *Phys. Rev. Lett.*, 58:1926–1929, May 1987.

[96] Zhang Xun-Chao, Li Bao-An, Chen Lie-Wen, and Yong Gao-Chan. Impact parameter dependence of the double neutron/proton ratio of nucleon emissions in isotopic reaction systems. *Chinese Physics Letters*, 26(5):052502, 2009.